

ADVANCED GNSS RECEIVER ARCHITECTURAL MEASURES FOR IMPROVED PERFORMANCE IN INTERFERENCE ENVIRONMENTS

By

David Fernandez Prim

A dissertation submitted to the Dean of Studies of the Faculty of Electrical
Engineering and Information Technology at Graz University of Technology,
in partial satisfaction of the requirements for the degree of

Doctor of Engineering Sciences (Dr. techn.)

Graz, 23 November 2010

Under the advice and review of:

Univ.-Prof. Dipl.-Ing. Dr. Otto Koudelka

Graz University of Technology

Dr. Manuel Hernandez-Pajares

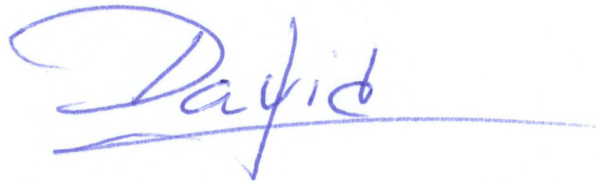
Universitat Politècnica de Catalunya



STATUTORY DECLARATION

Ich erkläre an Eides statt, dass ich die vorliegende Arbeit selbstständig verfasst, andere als die angegebenen Quellen/Hilfsmittel nicht benutzt, und die den benutzten Quellen wörtlich und inhaltlich entnommene Stellen als solche kenntlich gemacht habe.

I declare that I have authored this thesis independently, that I have not used other than the declared sources/resources, and that I have explicitly marked all material which has been quoted either literally or by content from the used sources.

A handwritten signature in blue ink, appearing to read 'David', with a horizontal line underneath it.

(Signed: David Fernandez Prim)

Graz, 23 November 2010

A C K N O W L E D G E M E N T S

The pure reason-to-be of an acknowledgements section in a PhD thesis cannot be understood until its completion. Now I can say I understand it. For this reason, and with special affection, I want to mention here my sister and parents for being always there and supporting me in all possible ways despite the distance, and all my friends for giving always a good reason to proceed.

Furthermore, I would like to recognize the effort and valuable time that Prof. Otto Koudelka (TU Graz, Austria) and Dr. Manuel Hernandez-Pajares (UPC, Barcelona, Spain) have spent with me on this long way, respectively as advisor and reviewer of this thesis.

Additionally, special credits and acknowledgements go to Jean-Jacques Floch (EADS Astrium GmbH, Munich, Germany), who, from his experience and expertise, provided priceless comments, ideas and collaboration for the successful accomplishments of key sections in Chapter 5 and Chapter 6 of this thesis.

Last but not least, I kindly thank each and every one of my colleagues at the Institute of Applied Systems Technology at JOANNEUM RESEARCH *Forschungsgesellschaft mbH* in Graz for their unconditional help and valuable comments.

To all of you, with endless and infinite appreciation.

A B S T R A C T

It is clear at this time that the 21st century Society is becoming progressively more and more addicted to technology in all aspects of life, somehow overtaking the dependency already shown during the late nineties. This statement can be generally applied to every layer of the economic system of the present world, from all sectors of industry to individual life, with effects on transportation, communications, agriculture or the banking business, to mention just a few.

For a clear example, let's consider the number of positioning and navigation-related applications presently available to everyone with a GPS-enabled cell phone or PDA that take advantage of location signals received from the GPS constellation, and that can also download the satellites' ephemeris through GSM or GPRS for a fast acquisition (aided-GPS approach) or even use the range to cellular base stations to refine its position in urban environment. The simple technological possibility highlighted here opens a broad range of possibilities and applications that allows the user not only to know their coordinates but also to obtain information about the environment by querying this information into GIS databases.

With the upcoming commission of the European satellite navigation system Galileo, the concept of 'multiconstellation' will take a broader sense. Within this framework, the author of this thesis is committed to give an insight to the benefits and disadvantages for the user segment derived from the combination of several satellite constellations for positioning and navigation purposes. This information is then to be used to propose solutions to three problems of importance in the field and with high interest from the industry point of view.

In first place, while developing optimized software simulation tools of relevance for subsequent advances, a more computationally efficient method is designed to characterize the Spectral Separation Coefficient between two given navigation signals as a function of the Doppler frequency offset. This technique is shown to substantially reduce the model-based simulation time when evaluating the impact of non-pulsed interference sources on a given navigation receiver.

In second place, a new method applied to the antenna pattern is presented and evaluated to improve the robustness of mass-market GNSS receivers against external interferences and multipath. Through an exhaustive software simulation campaign, it is shown that the elevation masking angle of a GPS+Galileo compatible receiver antenna can be increased to reject the incoming energy from ground-based interference sources as well as from multipath reflected rays.

In third place, a novel technique is developed to detect and reduce the systematic error or bias that can potentially affect the satellite-to-user pseudorange estimation within a GNSS receiver compatible with modern subcarrier-based navigation modulations. In this case, the presented development is accompanied by a detailed analysis on the practicality and applicability of the measure within a user receiver.

All advances here presented have been publically presented in the more relevant GNSS international meetings.

KURZFASSUNG

Bereits heute ist deutlich zu sehen, dass die Gesellschaft des 21. Jahrhunderts in allen Lebensbereichen zunehmend von Technologie abhängig sein wird. Dabei wird jener Grad an Abhängig noch übertroffen, der schon in den späten Neunzigerjahren des vorigen Jahrhunderts sichtbar war. Diese Beobachtung trifft generell auf alle Ebenen unseres Wirtschaftssystems zu, von allen Wirtschaftsbereichen bis hin zum Privatleben, mit Auswirkungen auf Transportwesen und Mobilität, Kommunikation, Land- und Finanzwirtschaft, um nur ein paar Bereiche explizit zu erwähnen.

Als konkretes Beispiel sei hier die Vielzahl von positionierungs- und navigationsbezogenen Anwendungen erwähnt, die gegenwärtig für jedermann mit einem GPS-fähigem Mobiltelefon oder einem PDA mit geeigneter Ausstattung zur Verfügung steht. PDAs nutzen oft die Positionierungssignale der GPS Satelliten und können auch die Ephemerideninformation über GSM oder GPRS für eine rasche Positionierung empfangen, oder sogar auch die Entfernung zu Mobilfunkbasisstationen auswerten. Diese soeben noch überschaubar abgegrenzten technologischen Möglichkeiten und Anwendungen ermöglichen dem Nutzer nicht nur seinen Aufenthaltsort zu bestimmen, sondern bei entsprechender Kombination mit GIS Datenarchiven ebenso Information über seine Umgebung zu erhalten.

Mit der bevorstehenden Inbetriebnahme des europäischen Satellitennavigationssystems Galileo gewinnt das Konzept von Multikonstellationssystemen breite praktische Bedeutung. In diesem Zusammenhang möchte der Autor dieser Dissertation einen Einblick in die Vor- und Nachteile geben, die der Nutzer durch die Kombination mehrerer Konstellationen von Satellitennavigationssystemen erhält. Aufbauend darauf werden Lösungen für drei spezielle Probleme in diesem Technologiebereich vorgeschlagen, die auch von großem Interesse für industrielle Zwecke sind.

Als erste Problemlösung und Technologiefortschritt wurde eine neue Methode entwickelt, den Spectral Separation Coefficient zwischen zwei Navigationssignalen als Funktion der Doppler-Frequenzverschiebung berechnungstechnisch effizienter zu ermitteln, als dies bisher der Fall war. Dies geschah aus praktischem Bedarf während einschlägiger Softwareentwicklung für verbesserte Simulationswerkzeuge. Es wird gezeigt, dass diese Methode die Simulationszeiten für den Einfluß von nicht-gepulsten Störsignalen auf einen Navigationsempfänger substantiell verkürzt.

Als Zweites wird eine neue Methode vorgestellt und untersucht, die es mit Hilfe geeigneter Antennencharakteristik erlaubt, die Robustheit von Grossserien-Navigationsempfängern gegen externe Störsignale und Mehrwegeausbreitung zu verbessern. Mit Hilfe umfangreicher und gründlicher Softwaresimulationen wurde gezeigt, dass der Elevations-Maskierungswinkel eines Navigationsempfängers, der GPS und Galileo gemeinsam empfängt, gegenüber Empfängern für nur ein System vergrößert werden kann. Dadurch werden Signale von terrestrischen Störquellen und der Einfluss von Mehrwegeausbreitung ignoriert.

Als Drittes wird eine neue Methode präsentiert, die die Detektion und Verringerung von systematischen Fehlern erlaubt, die möglicherweise der Bestimmung der Pseudoentfernung

zwischen Satellit und Empfänger anhaftet, wenn dieser moderne Modulationen mit Unterträgerfrequenzen nutzt. Für die gezeigte Methode wurde eine detaillierte Analyse über die Anwendbarkeit für einen alltagstauglichen Empfänger erstellt.

Alle Technologiefortschritte, die hier vorgestellt werden, wurden vom Autor bei einschlägigen internationalen Tagungen präsentiert.

C O N T E N T S

| | |
|---|---------------------|
| Statutory Declaration | <i>i</i> |
| Acknowledgements..... | <i>iii</i> |
| Abstract..... | <i>v</i> |
| Kurzfassung | <i>vii</i> |
| Contents | <i>ix</i> |
| List of Figures..... | <i>xiii</i> |
| List of Tables..... | <i>xix</i> |
| List of Acronyms..... | <i>xxi</i> |
| Numerical Constants..... | <i>xxvii</i> |
| CHAPTER 1 Introduction..... | <i>1</i> |
| 1.1 Motivation..... | <i>1</i> |
| 1.2 Contributions Original to This Work..... | <i>3</i> |
| 1.3 Organization of This Dissertation..... | <i>4</i> |
| 1.4 General Notes and Definitions | <i>4</i> |
| 1.5 Formal Framework of This Work..... | <i>5</i> |
| CHAPTER 2 Current and Future Satellite Radionavigation Systems | <i>7</i> |
| 2.1 Preface | <i>7</i> |
| 2.2 Global and Regional Satellite Navigation Systems | <i>9</i> |
| 2.2.1 GPS | <i>9</i> |
| 2.2.2 GLONASS | <i>14</i> |
| 2.2.3 Galileo | <i>18</i> |
| 2.2.4 Beidou-1, towards COMPASS..... | <i>22</i> |
| 2.2.5 QZSS | <i>26</i> |
| 2.2.6 CAPS | <i>29</i> |
| 2.2.7 Other Systems..... | <i>31</i> |
| 2.3 Regional Satellite Based Augmentation Systems..... | <i>32</i> |
| 2.3.1 EGNOS | <i>33</i> |
| 2.3.2 WAAS..... | <i>36</i> |
| 2.3.3 MSAS | <i>38</i> |
| 2.3.4 GAGAN, towards IRNSS..... | <i>39</i> |
| 2.3.5 SDCM..... | <i>40</i> |
| 2.4 Chapter Summary | <i>41</i> |

| | |
|---|-----------|
| CHAPTER 3 The GNSS Receiver | 43 |
| 3.1 Preface | 43 |
| 3.2 The Navigation Signal | 46 |
| 3.3 The User Antenna..... | 46 |
| 3.4 The RF Frontend..... | 49 |
| 3.5 The Baseband Receiver Channel | 50 |
| 3.5.1 The Satellite Acquisition Phase | 51 |
| 3.5.2 The Carrier and Code Tracking Operation | 52 |
| 3.6 Chapter Summary | 54 |
| CHAPTER 4 A Review of Error Sources and Effects in Satellite Radionavigation Systems | 55 |
| 4.1 Preface | 55 |
| 4.2 Error Sources on the Accuracy of the Reported Position..... | 55 |
| 4.3 Radio Interference Sources on Satellite Navigation Bands | 59 |
| 4.3.1 GNSS Interferences | 61 |
| 4.3.2 Harmonics of Commercial Transmitters of FM Radio and Analog/Digital TV..... | 61 |
| 4.3.3 Analog and Digital Amateur Radio Link Stations..... | 62 |
| 4.3.4 Digital Noise | 62 |
| 4.3.5 JTIDS / MIDS | 62 |
| 4.3.6 Wind Profiler Radar..... | 63 |
| 4.3.7 Inmarsat Downlink | 64 |
| 4.3.8 DME / TACAN | 64 |
| 4.3.9 ARSR | 66 |
| 4.3.10 Globalstar Satellite-to-User Downlink | 66 |
| 4.3.11 The ISM Band | 67 |
| 4.3.12 WiMAX | 69 |
| 4.3.13 SAP/SAB | 69 |
| 4.3.14 MLS..... | 69 |
| 4.3.15 UWB | 71 |
| 4.4 Effects of Error Sources on the Pseudorange Determination..... | 71 |
| 4.5 Chapter Summary | 72 |
| CHAPTER 5 The Simulation Approach Applied to Radionavigation Systems | 73 |
| 5.1 Preface | 73 |
| 5.2 Part 1: The Frequency-Domain GNSS Software Simulator..... | 74 |
| 5.2.1 The Flux Diagram of the Simulator | 74 |

| | | |
|---|--|------------|
| 5.2.2 | Budget of the Generated Data Volume | 76 |
| 5.2.3 | Determination of the Position and Velocity for User and Signal Sources | 78 |
| 5.2.4 | The Visibility of Satellites and Interferers | 79 |
| 5.2.5 | The Simulated Link Budget and Relative Doppler Frequency Offset | 79 |
| 5.2.6 | A More Pragmatic Approach to the Spectral Separation between Signals | 80 |
| 5.2.7 | The Interference Level Computation and the Effective C/N ₀ Evaluation | 91 |
| 5.3 | <i>Part 2: Evaluation of the Receiver Performance</i> | 94 |
| 5.3.1 | The Deterministic Approach | 94 |
| 5.3.2 | The Bit-True Technique | 95 |
| 5.3.3 | A Modified Semi Bit-True Method | 98 |
| 5.4 | <i>Chapter Summary</i> | 101 |
| CHAPTER 6 A Robust Bias Detection Method in the Frequency Domain for Code Delay Estimation Applied to Modern Navigation Modulations | | 103 |
| 6.1 | <i>Preface</i> | 103 |
| 6.2 | <i>Background</i> | 103 |
| 6.3 | <i>Development Methodology</i> | 104 |
| 6.4 | <i>Sources of Bias on the Code Delay Estimation</i> | 104 |
| 6.5 | <i>Classical and State-of-the-Art Techniques</i> | 106 |
| 6.6 | <i>A Novel Technique in the Frequency Domain</i> | 107 |
| 6.7 | <i>Simulations and Results</i> | 111 |
| 6.8 | <i>On the Practicality of This Measure</i> | 115 |
| 6.9 | <i>Chapter Summary</i> | 115 |
| CHAPTER 7 Trade-Off Between Dilution of Precision and Interference Level on a Compatible Receiver Within a Combined GPS+Galileo Scenario | | 117 |
| 7.1 | <i>Preface</i> | 117 |
| 7.2 | <i>Study Logic</i> | 118 |
| 7.3 | <i>Part 1: Preliminary Study over Graz, Austria</i> | 119 |
| 7.3.1 | Background | 119 |
| 7.3.2 | Procedure | 119 |
| 7.3.3 | Definition of Scenarios | 121 |
| 7.3.4 | Satellite Visibility of GPS and Galileo Constellations | 122 |
| 7.3.5 | Determination of GDOP for GPS, Galileo and Combined Constellations | 125 |
| 7.3.6 | GNSS-Induced Interference Levels From and to GPS and Galileo | 126 |
| 7.3.7 | Receiver Performance Degradation Due to Interferences for All Scenarios | 129 |

| | | |
|--|--|------------|
| 7.3.8 | Lessons Learned From Phase 1 | 132 |
| 7.4 | <i>Part 2: Assessment of the Worldwide Applicability of the Proposed Measure</i> | 134 |
| 7.4.1 | Modifications on the Original Procedure..... | 134 |
| 7.4.2 | Definition of Worldwide Scenarios | 135 |
| 7.4.3 | Estimation of the Spectral Separation between Signals | 136 |
| 7.4.4 | Determination of Visibility for GPS and GPS+Galileo Constellations..... | 145 |
| 7.4.5 | Determination of PDOP for GPS and GPS+Galileo Constellations | 145 |
| 7.4.6 | Effective C/N ₀ Due to GNSS-Induced Interference Level | 145 |
| 7.4.7 | Receiver Performance Degradation Due to GNSS-Related Interferences Sources..... | 149 |
| 7.4.8 | Scenario Equivalence Based on Combined Code Tracking Jitter and PDOP | 150 |
| 7.5 | <i>Chapter Summary</i> | 151 |
| CHAPTER 8 General Conclusions and Future Lines of Work | | 153 |
| ANNEX A Envelope PSD of Common Modulation Types in Current Satellite Navigation Systems | | 157 |
| A.1 | <i>BPSK</i> | 157 |
| A.2 | <i>BOC</i> | 158 |
| A.2.1 | <i>BOCsin</i> | 158 |
| A.2.2 | <i>BOCcos</i> | 159 |
| A.3 | <i>AltBOC</i> | 160 |
| A.3.1 | Constant Envelope | 160 |
| A.3.2 | Non-constant Envelope..... | 161 |
| A.4 | <i>MBOC</i> | 163 |
| ANNEX B Representative Clear Sky Link Budgets for GPS and Galileo Constellations..... | | 165 |
| B.1 | <i>Statistic of the Satellite-to-User Range</i> | 165 |
| B.1.1 | GPS | 165 |
| B.1.2 | Galileo | 166 |
| B.2 | <i>Free Space Loss Determination</i> | 167 |
| B.2.1 | Computation for GPS Carriers..... | 167 |
| B.2.2 | Computation for Galileo Carriers..... | 168 |
| B.3 | <i>Received powers from GPS and Galileo constellations</i> | 170 |
| List of References | | 173 |

LIST OF FIGURES

| | |
|---|----|
| Figure 1-1: A likely future multiconstellation scenario..... | 1 |
| Figure 2-1: Usage of frequency bands currently assigned to Space-to-Earth RNSS services (last update on 23 November 2010)..... | 8 |
| Figure 2-2: Artist impression of a GPS Block IIF satellite in orbit..... | 12 |
| Figure 2-3: Artist impression of a GLONASS-K satellite in orbit..... | 17 |
| Figure 2-4: Artist impression of GIOVE-B in orbit. | 18 |
| Figure 2-5: Artist impression of a Beidou-1 satellite in orbit..... | 23 |
| Figure 2-6: Artist impression of the ground track of QZSS. | 26 |
| Figure 2-7: Coverage areas of a number of present and planned SBAS systems. | 33 |
| Figure 3-1: Functional scheme of a multifrequency GNSS receiver. | 43 |
| Figure 3-2: Functional scheme of a single frequency GNSS receiver..... | 44 |
| Figure 3-3: State machine describing the behaviour of the receiver controller..... | 45 |
| Figure 3-4: Functional scheme of the RF frontend. | 49 |
| Figure 3-5: Typical structure of a high resolution GNSS receiver channel..... | 52 |
| Figure 4-1: Conceptual classification of error sources in satellite-based positioning systems. | 55 |
| Figure 4-2: Usage of frequency bands currently assigned to Space-to-Earth RNSS services, with exemplar interfering sources of interest for an arbitrary user (last update on 23 November 2010)..... | 60 |
| Figure 4-3: European radio broadcast and TV bands susceptible to interfere on Galileo services. | 61 |
| Figure 4-4: E-3 AWACS airplanes parked at the NATO european airbase in Geilenkirchen (Germany)..... | 62 |
| Figure 4-5: Transmission spectral mask to which JTIDS/MIDS signals must be compliant with. | 63 |
| Figure 4-6: 1,290 MHz Wind Profiler Radar at Lindenberg, Germany..... | 63 |
| Figure 4-7: Details of the Morse codes within DME/TACAN signal structure. | 65 |
| Figure 4-8: Transmission spectral mask to which DME/TACAN (a) airborne and (b) ground stations must be compliant with. | 65 |
| Figure 4-9: (a) TACAN station. (b) VOR/DME station (VOR antenna on the center pole). | 66 |
| Figure 4-10: Globalstar coverage updated to June 2009..... | 67 |
| Figure 4-11: Theoretical spectral mask for every FDMA channel of the Globalstar downlink..... | 67 |
| Figure 4-12: Theoretical spectral mask to which Bluetooth emissions must be compliant [Ref. 1]..... | 68 |
| Figure 4-13: Example of WLAN spectral mask, which shows the drop of 30 dB at ± 11 MHz off carrier, as required by the standard 802.11. | 69 |
| Figure 4-14: Transmission spectral mask to which MLS stations must be compliant with. | 70 |
| Figure 4-15: MLS station at NASA-operated Wallops Flight Facility. | 70 |
| Figure 5-1: Software flux diagram of a model-based frequency-domain GNSS simulator..... | 76 |
| Figure 5-2: 3D plot of the SSC for fine structured GPS L1 C/A pair, as a function of the absolute Doppler frequency shifts. | 82 |
| Figure 5-3: Representation of the spectral separation coefficient for signals of Type I. (a) BPSK(1) – BPSK(1), (b) CBOCsin(6,1,1/11) – CBOCsin(6,1,1/11)..... | 83 |

| | |
|---|-----|
| Figure 5-4: Representation of the spectral separation coefficient for signals of Type II, obtained for a Doppler offset resolution of 7.8049 Hz. (a) GPS L1 C/A – GPS L1 C/A (no data rate), (b) Galileo L1B – Galileo L1B (no data rate)..... | 85 |
| Figure 5-5: Used PSDs for (a) GPS L1 C/A and (b) Galileo L1B, with a frequency resolution of 7.8049 Hz. | 86 |
| Figure 5-6: Representation of the spectral separation coefficient for signals of Type I and II, obtained for a Doppler offset resolution of 7.8049 Hz and the combination GPS L1 C/A (50 sps data rate) – Galileo L1B (250 sps data rate)..... | 87 |
| Figure 5-7: Representation of the spectral separation coefficient for Galileo L1B – GPS L1 C/A (in blue), estimated in a reduced set of Doppler offset points (in red dots, for $N = 2$). | 88 |
| Figure 5-8: Normalized receiver antenna pattern in elevation, scaled to 4.3 dBi to be used for the application example. | 88 |
| Figure 5-9: Temporal evolution of the error on the effective C/N_0 , when the fast SSC estimation method is in use, as seen by a user in Western Europe, considering the scenario in Table 5-3, with noise level -202 dBW/Hz, atmospheric losses 0.6 dB and displayed for the Galileo satellite (a) SV4, (b) SV10, and (c) SV27. | 89 |
| Figure 5-10: Algorithm for the SSC computation in the frequency domain, used in the reference tool. | 90 |
| Figure 5-11: Code delay estimation jitter versus effective C/N_0 , for a number of receiver architectures (Early-Late spacing values in units of chips). | 95 |
| Figure 5-12: Equivalent scheme for the performance simulation of a single receiver channel, using a bit-true technique. | 96 |
| Figure 5-13: S-curve normalization for a code delay EMLP discriminator, for a value of Early-Late spacing equal to 0.5 chips, as seen for a BOCsin(1,1)..... | 98 |
| Figure 5-14: Simplified model for a bit-true GNSS receiver channel simulator..... | 99 |
| Figure 5-15: Simplified model for a semi bit-true GNSS receiver channel simulator. | 99 |
| Figure 5-16: Equivalent scheme for the performance simulation of a single receiver channel, using a semi bit-true technique. | 100 |
| Figure 6-1: Cross-correlation of (a) BOCcos(10,5) and (b) BOCcos(15, 2.5). | 105 |
| Figure 6-2: Proposed FFT-based code delay bias resolution technique. | 109 |
| Figure 6-3: FFT-based bias estimation method. | 110 |
| Figure 6-4: Biased and bias-free tracking of BOCcos(10,5) with an RF frontend bandwidth of 40 MHz, for successive simulated systematic errors and the parametric configuration in the left column of Table 6-1, with moving average. | 111 |
| Figure 6-5: Biased and bias-free tracking of BOCcos(15,2.5) with an RF frontend bandwidth of 40 MHz, for successive simulated systematic errors (right column of Table 6-1), with moving average. | 112 |
| Figure 6-6: Improved bias removal on the tracking of BOCcos(10,5) with an RF frontend bandwidth of 40 MHz, for successive simulated systematic errors and the parametric configuration in Table 6-1, with low-pass filtering. | 113 |
| Figure 6-7: Improved bias removal on the tracking of BOCcos(15,2.5) with an RF frontend bandwidth of 40 MHz, for successive simulated systematic errors and the parametric configuration in Table 6-1, with low-pass filtering. | 113 |

| | |
|--|-----|
| Figure 6-8: Code delay jitter of BOCcos(10,5) and BOCcos(15, 2.5) for an RF frontend bandwidth of 40 MHz, with and without bias removal..... | 114 |
| Figure 7-1: Concept of the proposed antenna-based protection measure..... | 117 |
| Figure 7-2: Applicable study logic for the developments in Chapter 7. | 118 |
| Figure 7-3: Satellite visibility for scenario 1 (user in Graz). | 123 |
| Figure 7-4: Satellite visibility for scenario 2 (user in Graz). | 123 |
| Figure 7-5: Satellite visibility for scenarios 3 and 4 (user in Graz). | 123 |
| Figure 7-6: Maximum, minimum and mean values of visibility for scenario 1 (user in Graz). | 124 |
| Figure 7-7: Maximum, minimum and mean values of visibility for scenario 2 (user in Graz). | 124 |
| Figure 7-8: Maximum, minimum and mean values of visibility for scenarios 3 and 4 (user in Graz)..... | 124 |
| Figure 7-9: GDOP in a GPS-only scenario, for elevation cut-off angles between 0° and 25° (user in Graz)..... | 125 |
| Figure 7-10: GDOP in a Galileo-only scenario, for elevation cut-off angles between 0° and 25° (user in Graz)..... | 125 |
| Figure 7-11: GDOP in a GPS+Galileo scenario, for elevation cut-off angles between 0° and 35° (user in Graz)..... | 126 |
| Figure 7-12: Mean desired power received from the GPS constellation..... | 127 |
| Figure 7-13: Mean desired power received from the Galileo constellation..... | 127 |
| Figure 7-14: Mean I_{ref} received from the GPS system in scenario 1. | 127 |
| Figure 7-15: Mean I_{ref} received from the Galileo system in scenario 2 | 128 |
| Figure 7-16: Mean I_{ref}/I_{int} received from GPS and Galileo constellations for scenario 3. | 128 |
| Figure 7-17: Mean I_{ref}/I_{int} received from Galileo and GPS constellations, for scenario 4. | 128 |
| Figure 7-18: Mean C/N_0 seen by a GPS receiver channel, applicable to scenarios 1&3..... | 129 |
| Figure 7-19: Mean C/N_0 seen by a Galileo receiver, applicable to scenarios 2&4..... | 129 |
| Figure 7-20: Mean $(C/N_0)_{eff}$ seen by a GPS receiver channel in scenario 1..... | 130 |
| Figure 7-21: Mean $(C/N_0)_{eff}$ seen by a GPS receiver channel in scenario 3..... | 130 |
| Figure 7-22: Mean $(C/N_0)_{eff}$ seen by a Galileo receiver channel in scenario 4..... | 130 |
| Figure 7-23: Jitter of the code delay estimate for a typical GPS receiver channel tracking L1 C/A in scenario 1..... | 131 |
| Figure 7-24: Jitter of the code delay estimate for a typical GPS receiver channel tracking L1 C/A in scenario 3..... | 131 |
| Figure 7-25: Jitter of the code delay estimate for a typical Galileo receiver channel tracking E1B in scenario 4..... | 132 |
| Figure 7-26: Fine structured PSDs used within simulations in this section. | 138 |
| Figure 7-27: Envelope PSDs used within simulations in this section. | 139 |
| Figure 7-28: CDF of the Doppler offset difference between satellites of the GPS constellation as specified in Table 7-4..... | 140 |
| Figure 7-29: CDF of the Doppler offset difference between satellites of the Galileo constellation as specified in Table 7-4..... | 140 |
| Figure 7-30: CDF of the Doppler offset difference between satellites of GPS and Galileo constellations as specified in Table 7-4. | 141 |
| Figure 7-31: CDF of the Doppler offset difference between satellites of Galileo and GPS constellations as specified in Table 7-4. | 141 |
| Figure 7-32: SSCs computed for scenarios 5, 6 & 7, with GPS L1 C/A as the desired signal..... | 142 |

| | |
|---|-----|
| Figure 7-33: SSCs computed for scenario 7, with Galileo E1B as the desired signal. | 143 |
| Figure 7-34: Scenario fitting for combined GPS+Galileo PDOP, relative to GPS-only with θ equal to 10° | 145 |
| Figure 7-35: Minimal visibility obtained for (a) scenario 5 with 10° elevation masking angle, and scenario 6 with (b) 30° and (c) 35° | 146 |
| Figure 7-36: Mean PDOP obtained for (a) scenario 5 with 10° elevation masking angle, and scenario 6 with (b) 15° and (c) 20° | 147 |
| Figure 7-37: Mean $(C/N_o)_{\text{eff}}$ obtained for (a) scenario 5 with 10° elevation masking angle, and (b) scenario 6 with 10° and 15° (c). | 148 |
| Figure 7-38: Code delay jitter versus the Early-Late spacing on the discriminator for a GPS receiver channel with 2.5 MHz RF frontend bandwidth. | 149 |
| Figure 7-39: Jitter of the estimated code delay versus the Early-Late spacing on the discriminator for a Galileo receiver channel with 24.5 MHz RF frontend bandwidth..... | 149 |
| Figure 7-40: Scenario fitting for combined GPS+Galileo tracking code error, relative to GPS-only with θ equal to 10° . Units of vertical axis in meters. | 150 |
| Figure 7-41: Scenario fitting for combined GPS+Galileo tracking code error and PDOP, relative to GPS-only with θ equal to 10° | 151 |
| Figure A-1: Compared PSDs of BPSK(1) and BPSK(10), normalized to power 1W over a bandwidth of 52 MHz. | 157 |
| Figure A-2: Compared PSDs of BOCsin(1,1) and BOCsin(2,5), normalized to power 1W over a bandwidth of 42 MHz. | 158 |
| Figure A-3: Compared PSDs of BOCcos(1,1) and BOCcos(2,5), normalized to power 1W over a bandwidth of 42 MHz. | 159 |
| Figure A-4: Compared PSDs of BOCsin(1,1) and BOCcos(1,1), normalized to power 1W over a bandwidth of 42 MHz. | 160 |
| Figure A-5: Compared PSDs of AltBOC(15,10) and AltBOC(5,2) (constant envelope), normalized to power 1W over a bandwidth of 100 MHz. | 161 |
| Figure A-6: Compared PSDs of AltBOC(15,10) and AltBOC(5,2) (non-constant envelope), normalized to power 1W over a bandwidth of 100 MHz. | 162 |
| Figure A-7: Compared PSDs of AltBOC(15,10) with constant and non-constant envelope, normalized to power 1W over a bandwidth of 50 MHz. | 162 |
| Figure A-8: Compared PSDs of MBOCsin(6,1,1/11) and MBOCsin(6,1,10/11), normalized to power 1W over a bandwidth of 24 MHz. | 163 |
| Figure A-9: Compared PSDs of MBOCcos(6,1,1/11) and MBOCcos(6,1,10/11), normalized to power 1W over a bandwidth of 24 MHz. | 163 |
| Figure A-10: Compared PSDs of MBOCsin(6,1,1/11) and MBOCcos(6,1,1/11), normalized to power 1W over a bandwidth of 24 MHz. | 164 |
| Figure B-1: Probability distribution function of satellite-to-user range for the GPS constellation. | 165 |
| Figure B-2: Probability distribution function of satellite-to-user range for the Galileo constellation. | 166 |
| Figure B-3: Evolution of GPS free space loss for several values of the user antenna cut-off angle. | 167 |

Figure B-4: Evolution of Galileo free space loss for several values of the user antenna cut-off angle. 168

LIST OF TABLES

| | |
|--|----|
| Table 2-1: WGS-84 ellipsoid parameters. | 10 |
| Table 2-2: GPS signal characteristics (complete scheme foreseen for 2013)..... | 10 |
| Table 2-3: GPS minimum RF signal strength expected at the end of life of IIF and IIR-M satellites..... | 11 |
| Table 2-4: GPS history timeline (1/2)..... | 13 |
| Table 2-5: GPS history timeline (2/2)..... | 14 |
| Table 2-6: GLONASS signal characteristics since 2003..... | 15 |
| Table 2-7: Expected minimum signal strength at the end of life of GLONASS and GLONASS-M satellites..... | 15 |
| Table 2-8: PZ-90 ellipsoid parameters. | 16 |
| Table 2-9: GLONASS history timeline (1/2)..... | 17 |
| Table 2-10: GLONASS history timeline (2/2)..... | 18 |
| Table 2-11: Galileo signal characteristics in L-Band..... | 20 |
| Table 2-12: Expected Galileo signal strength..... | 20 |
| Table 2-13: Galileo history timeline (1/2)..... | 21 |
| Table 2-14: Galileo history timeline (2/2)..... | 22 |
| Table 2-15: Detail on Beidou-1 satellites. | 22 |
| Table 2-16: Initial COMPASS signal characteristics..... | 24 |
| Table 2-17: Expected COMPASS signal scheme, as released on July 2009..... | 24 |
| Table 2-18: History timeline of Beidou-1 & -2 (1/2). | 25 |
| Table 2-19: History timeline of Beidou-1 & -2 (2/2). | 26 |
| Table 2-20: Orbital parameters of QZSS. | 27 |
| Table 2-21: GRS80 ellipsoid parameters..... | 27 |
| Table 2-22: QZSS signal characteristics..... | 28 |
| Table 2-23: Expected QZSS signal strength..... | 28 |
| Table 2-24: History timeline of QZSS. | 29 |
| Table 2-25: History timeline of CAPS. | 31 |
| Table 2-26: Detail on EGNOS Satellites..... | 34 |
| Table 2-27: History timeline of EGNOS (1/2). | 35 |
| Table 2-28: History timeline of EGNOS (2/2)..... | 36 |
| Table 2-29: Detail on WAAS space segment..... | 37 |
| Table 2-30: History timeline of WAAS..... | 37 |
| Table 2-31: Detail on MSAS space segment..... | 38 |
| Table 2-32: History timeline of MSAS. | 38 |
| Table 2-33: Detail on GAGAN space segment..... | 39 |
| Table 2-34: History timeline of GAGAN. | 39 |
| Table 2-35: Detail on SDCM space segment. | 40 |
| Table 2-36: History timeline of SDCM..... | 40 |
| Table 3-1: Example of classic code delay error discriminator functions. | 53 |
| Table 5-1: Radio navigation application examples, with estimated simulation complexity. | 74 |
| Table 5-2: Data budget produced within a characteristic simulator. | 77 |
| Table 5-3: Simulation target scenario definition. | 78 |

| | |
|--|-----|
| Table 5-4: Signal and receiver baseband processing channel architecture for which results are depicted in Figure 5-11..... | 94 |
| Table 6-1: Configurations for the simulated behaviour of the developed bias removal technique..... | 111 |
| Table 6-2: Reference configurations for the code jitter extraction..... | 114 |
| Table 7-1: Relevant configurations for the simulation scenarios of Phase 1..... | 121 |
| Table 7-2: SSC values considered within Table 7-1 (in dB/Hz)..... | 122 |
| Table 7-3: Summary of numeric results obtained in Phase 1..... | 133 |
| Table 7-4: Relevant configurations for the worldwide simulation scenarios for Phase 2..... | 136 |
| Table 7-5: Doppler difference boundaries obtained from the simulations reported above..... | 141 |
| Table 7-6: SSC values estimated for scenario 5..... | 144 |
| Table 7-7: SSC values estimated for scenario 6..... | 144 |
| Table 7-8: SSC values estimated for scenario 7..... | 144 |
| Table 7-9: Parametric configuration of GPS and Galileo receiver channels for Phase 2..... | 149 |
| Table 7-10: Study results summarized for several values of the reference masking angle in a GPS-only case..... | 151 |
| Table B-1: Boundary values for the satellite-to-user range for the GPS constellation..... | 166 |
| Table B-2: Boundary values for the satellite-to-user range for the Galileo constellation..... | 166 |
| Table B-3: Free space loss computed for L1 carrier in GPS..... | 167 |
| Table B-4: Free space loss computed for L2 carrier in GPS..... | 168 |
| Table B-5: Free space loss computed for L5 carrier in GPS..... | 168 |
| Table B-6: Free space loss computed for E1 carrier in Galileo..... | 169 |
| Table B-7: Free space loss computed for E5a carrier in Galileo..... | 169 |
| Table B-8: Free space loss computed for E5b carrier in Galileo..... | 169 |
| Table B-9: Free space loss computed for E6 carrier in Galileo..... | 169 |
| Table B-10: Transmitted power levels and satellite antenna gain for the GPS signal components in L1..... | 170 |
| Table B-11: Transmitted power levels and satellite antenna gain for the Galileo signal components in E1..... | 170 |
| Table B-12: Minimum received power on GPS L1 for an on-ground user receiver with an RHCP antenna of 0 dBi..... | 170 |
| Table B-13: Minimum received power on Galileo E1 for an on-ground user receiver with an RHCP antenna of 0 dBi..... | 171 |

LIST OF ACRONYMS

| | |
|--------|--|
| ACF | Auto-Correlation Function |
| ADC | Analog-to-digital Converter |
| AGPS | Aided GPS |
| AltBoc | Alternate Binary Offset Carrier |
| AOR | Atlantic Ocean Region |
| ARSR | Air Route Surveillance Radar |
| ASIC | Application-Specific Integrated Circuit |
| ATV | Amateur Television |
| AWACS | Airborne Warning And Control System |
| AWGN | Additive White Gaussian Noise |
| BER | Bit Error Rate |
| BOC | Binary Offset Carrier |
| BPSK | Binary Phase shift Keying |
| CAPS | Chinese Area Positioning System |
| CAPSTS | CAPS Time System |
| CAST | China Academy of Space Technology |
| CCF | Cross-Correlation Function |
| CDF | Cumulative Density Function |
| CDMA | Code Division Multiple Access |
| CLS | Collected Localization Satellites |
| CNAGA | China National Administration of GNSS and Applications |
| CNES | <i>Centre National d'Études Spatiales</i> (French) |
| COSPAS | <i>COsmicheskaya Sistyema Poiska Avariynich Sudov</i> (Russian), Space System for the Search of Vessels in Distress. |
| CRF | Celestial reference frame |
| CRLB | Cramer-Rao Lower Bound |
| CS | Commercial Service |
| CSNPC | China Satellite Navigation Project Centre |
| DGPS | Differential GPS |
| DLL | Delay-Locked Loop |
| DME | Distance Measurement Equipment |
| DOP | Dilution of Precision |
| DORIS | Doppler Orbitography and Radio Positioning Integrated by Satellite |

| | |
|---------|--|
| DPSK | Differential Phase Shift Keying |
| DS-CDMA | Direct Sequence CDMA |
| DSP | Digital Signal Processor |
| DVB-T | Digital Video Broadcast - Terrestrial |
| ECAC | European Civil Aviation Conference |
| ECEF | Earth-centred Earth-fixed reference frame |
| ECI | Earth-centred inertial reference frame |
| EGNOS | European Geostationary Navigation Overlay Services |
| EMLP | Early Minus Late Power discriminator |
| EOL | End of Life |
| ESA | European Space Agency |
| ESTB | EGNOS System Test Bed |
| EWAN | EGNOS Wide-area Network |
| FAA | Federal Aviation Administration |
| FDMA | Frequency Division Multiple Access |
| FER | Frame Error Rate |
| FFT | Fast Fourier Transform |
| FIR | Flight Information Regions |
| FM | Frequency Modulated |
| FOC | Full Operational Capability |
| FPGA | Field-Programmable Gate Array |
| GAGAN | GPS Aided, Geo-Augmented Navigation (System) |
| GBAS | Ground-Based Augmentation System |
| GDOP | Geometric Dilution of Precision |
| GEO | Geosynchronous Earth Orbit |
| GFSK | Gaussian Frequency Shift Keying |
| GGSP | Galileo Geodetic Service Provider |
| GIOVE | Galileo In-Orbit Validation Element |
| GJU | Galileo Joint Undertaking |
| GLONASS | <i>GLO</i> bal' <i>n</i> aya <i>NA</i> vigatsionnaya <i>S</i> putnikovaya <i>S</i> istema (Russian), Global Navigation Satellite System. |
| GLS | Global Navigation Satellite System Landing System |
| GMS | Ground Monitoring Stations |
| GNSS | Global Navigation Satellite System |
| GPRS | General Packet Radio Service |
| GPS | Global Positioning System |

| | |
|-------|--|
| GPST | Global Positioning System Time |
| GSA | GNSS Supervisory Authority |
| GSM | Global System for Mobile communication |
| GST | Galileo System Time |
| GSTB | Galileo System Test Bed |
| GTRF | Galileo Terrestrial Reference Frame |
| HDOP | Horizontal Dilution of Precision |
| HEO | Highly-inclined elliptical orbits |
| HRC | High Resolution Correlator |
| ICAO | International Civil Aviation Organization |
| ICD | Interface Control Document |
| ICG | International Committee on Global Navigation Satellite Systems |
| IDS | International DORIS Service |
| IFFT | Inverse Fast Fourier Transform |
| IGSO | Inclined GeoSynchronous Orbit |
| ILS | Instrument Landing System |
| INLUS | Indian Navigation Land Uplink Station |
| INMCS | Indian Master Control Station |
| INRES | Indian Reference Stations |
| IOC | Initial Operational Capability |
| ION | Institute of Navigation |
| IOR | Indic Ocean Region |
| IOV | In-Orbit Validation |
| ISRO | Indian Space Research Organization |
| ISS | International Space Station |
| ITRF | International Terrestrial Reference Frame |
| ITU | International Telecommunications Union |
| JAXA | Japan Aerospace Exploration Agency |
| JCAB | Japan Civil Aviation Bureau |
| JGS | Japanese Geodetic System |
| LAAS | Local Area Augmentation Systems |
| LEO | Low Earth Orbit |
| LHCP | Left Hand Circular Polarized |
| LNA | Low Noise Amplifier |
| LORAN | LONg RANge Navigation |

| | |
|-------|---|
| LOS | Line-of-Sight |
| MBOC | Multiplexed Binary Offset Carrier |
| MCC | Master Control Centre |
| MCS | Master Control Stations |
| MEO | Medium Earth Orbit |
| MLS | Microwave Landing System |
| MRS | Monitoring and Ranging Stations |
| MSAS | MTSAT Satellite-based Augmentation System |
| MTSAT | Multi-functional Transport Satellite |
| NAOC | National Astronomical Observatories of China |
| NASA | National Aeronautics and Space Administration |
| NATO | North Atlantic Treaty Organization |
| NCO | Numerically-Controlled Oscillator |
| NLES | Navigation Land Earth Stations |
| NLOS | Non-Line-of-Sight |
| NOAA | National Oceanic and Atmospheric Administration |
| NTSC | National Time Service Center |
| OFDM | Orthogonal Frequency Division Multiplexing |
| OOK | On-Off Keying |
| OS | Open Service |
| PDOP | 3D positional Dilution of Precision |
| PLL | Phase-Locked Loop |
| PPP | Public-Private Partnership |
| PRF | Pulse repetition frequency |
| PRN | Pseudorandom Noise |
| PRS | Public Regulated Service |
| PVT | Position-Velocity-Time solution |
| QAM | Quadrature Amplitude Modulation |
| QPSK | Quadrature Phase Shift Keying |
| QZSS | Quasi Zenith Satellite System |
| RAIM | Receiver Autonomous Integrity Monitoring |
| RHCP | Right Hand Circular Polarized |
| RIMS | Receiver Integrity Monitoring Station |
| RNSS | Radio Navigation Satellite System |
| RTK | Real-Time Kinematics |

| | |
|--------|---|
| SAB | Services Ancillary to Broadcasting |
| SAIF | Submeter-class Augmentation with Integrity Class |
| SAP | Services Ancillary to Programming |
| SAR | Search And Rescue |
| SARSAT | Search And Rescue Satellite-Aided Tracking |
| SBAS | Satellite-Based Augmentation System |
| SDCM | System of Differential Correction and Monitoring |
| SECOR | Sequential Collation of Range |
| SIGSO | Slightly Inclined Geostationary-Satellite Orbit |
| SIS | Signal In Space |
| SOFDM | Scalable Orthogonal Frequency Division Multiplexing |
| SoL | Safety of Life |
| SRRC | Square Root Raised Cosine |
| SSC | Spectral Separation Coefficient |
| SSPA | Solid-State Power Amplifier |
| SSR | Secondary Surveillance Radar |
| SV | Space Vehicle |
| TACAN | Tactical Air Navigation system |
| TAI | <i>Temps Atomique International</i> (French) |
| TDMA | Time Division Multiple Access |
| TDOA | Time Difference Of Arrival |
| TDOP | Time Dilution of Precision |
| TEC | Total Electron Content |
| TOA | Time Of Arrival |
| TRF | Terrestrial reference frame |
| TWTA | Travelling Wave Tube Amplifier |
| USERE | User Equivalent Range Error |
| UHF | Ultra High Frequency |
| USSR | Union of Soviet Socialist Republics |
| UTC | Universal Time Coordinated |
| VDOP | Vertical Dilution of Precision |
| VHF | Very High Frequency |
| VOR | VHF Omnidirectional Range |
| WAAS | Wide-Area Augmentation System |
| WLAN | Wireless Local Area Network |

| | |
|-----|-----------------------------|
| WMS | WAAS Master Station |
| WPR | Wind Profiler Radar |
| WRS | Wide-area Reference Station |

NUMERICAL CONSTANTS

| Symbol | Value | Description |
|----------------|-----------------------|--|
| c | 299,762,458 m/s | Speed of light in vacuum. |
| π | 3.14159265359 | Pi value used in this document. |
| f_o | 1.023 MHz | Fundamental frequency of GPS. |
| f_{L1} | 1,575.42 MHz | Centre frequency of GPS L1 band. |
| $f_{E1/L1/E2}$ | f_{L1} | Centre frequency of Galileo L1 band. |
| f_{L2} | 1,227.60 MHz | Centre frequency of GPS L2 band. |
| f_{L5} | 1,176.45 MHz | Centre frequency of GPS L5 band. |
| f_{E5} | 1,191.795 MHz | Centre frequency of Galileo E5 band. |
| f_{E5a} | f_{L5} | Centre frequency of Galileo E5a band. |
| f_{E5b} | 1,207.14 MHz | Centre frequency of Galileo E5b band. |
| f_{E6} | 1,278.75 MHz | Centre frequency of Galileo E6 band. |
| f_{G1} | 1,602.00 MHz | Centre frequency of GLONASS G1 band. |
| f_{G2} | 1,246.00 MHz | Centre frequency of GLONASS G2 band. |
| f_{G3} | 1,204.704 MHz | Centre frequency of GLONASS G3 band. |
| R_E | 6,371 Km | Mean Earth radius. |
| L | 1,164.0 – 1,610.0 MHz | Frequency range in L-band, reserved for Satellite Navigation according to ITU regulations [Ref. 56]. |
| S | 2,483.0 – 2,500.0 MHz | Frequency range in S-band, reserved for Satellite Navigation according to ITU regulations [Ref. 56]. |
| C | 5,010.0 – 5,030.0 MHz | Frequency range in C-band, reserved Satellite Navigation, according to ITU regulations [Ref. 56]. |

CHAPTER 1

INTRODUCTION

1.1 Motivation

Although for a long time GPS and GLONASS were synonyms for global navigation systems, with both developments initiated during the late 1960s, and which consolidation was mainly sparked by political and military tensions during the Cold War, the near future envisages a rather more complex scenario in which multiple additional satellite navigation constellations will be added to the pool by several countries in an attempt to improve the quality of service offered to all kind of users, or simply to gain a priceless strategic advantage in case of international military conflict.

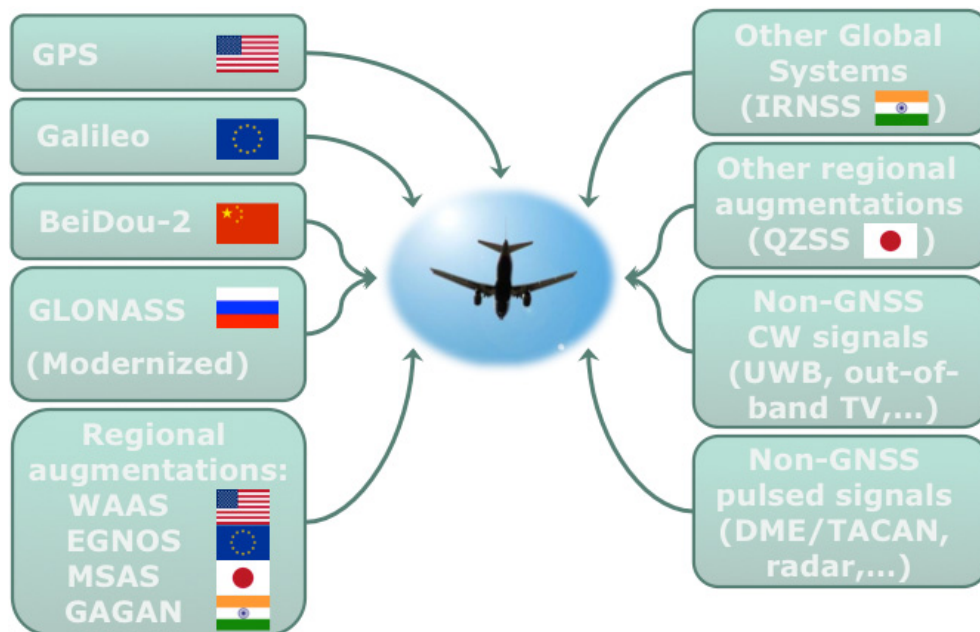


Figure 1-1: A likely future multiconstellation scenario.

For whatever reason, it is presently out of contestation that the present satellite positioning and navigation technology is clearly evolving towards an aggregate system of systems. In the near future, a number of GNSS constellations will be orbiting the Earth (i.e. the North American GPS, the Russian GLONASS, the European Galileo or the Chinese COMPASS, among the most relevant), and several additional navigation signals will be made available to both civilian and military users to complement currently existing services. Furthermore, the presence of several regional augmentations (the North American WAAS, the European EGNOS and the Japanese MSAS), and the upcoming constitutions of a number of new systems (i.e. the Japanese QZSS or the Indian GAGAN -towards the global system IRNSS-) will introduce additional complexity to this composite global scheme.

For the sake of completeness, and besides the satellite-based signal sources implicitly mentioned above, we must also consider a range of non-navigation related interfering sources in certain radio navigation bands. To this respect, take for instance an especially crowded band around 1,176.45 MHz, shared by systems like GPS L5, Galileo E5a, COMPASS L5, QZSS L5 or the modernized CDMA GLONASS on L5, and co-occupied by non-navigation related interferers such as Distance Measurement Equipments (DME) and their military equivalent TACAN, or the physical layer of Multifunction Information Distribution Systems (MIDS, a tactical inter-computer communication network). Or a band centred on 1,278.75 MHz becoming of importance with Galileo E6 and under consideration for COMPASS B3 or QZSS LEX signals, and being currently in use for Aeronautical En-Route Secondary Radars and Wind Profiler Radars in L-band. Other examples of interest that might initiate discussions in the near future are the partial spectral overlapping of Galileo SAR (Search and Rescue) service and the INMARSAT satellite downlink (at least, as far as out-of-band emissions are concerned), or the effects of Microwave Landing Systems (MLS) or Ultra Wide Band (UWB) transmissions in a band under study for future C-band navigation services.

In such a complex scenario outlined above, provided that compatibility and interoperability is maintained in all cases, users of positioning and navigation applications will have to expect a number of drawbacks directly related to the co-existence of multiple GNSS systems¹:

- Additional signals (mainly spread spectrum) will contribute to increase the noise power density level at the receiver antenna, degrading the quality of the signal at user position and finally the accuracy of position and velocity determinations.
- All present and planned systems are showing the same vulnerabilities, for they rely on the same principles and are subject to the same weaknesses and error sources.

However, a number of advantages will also be offered (and presently are, with GPS/GLONASS receivers) to those future users equipped with multisystem GNSS receivers. Take for example:

- A higher number of satellites will be visible from virtually every point on or near the Earth surface. This fact will constitute a significant advantage not only for users seeking knowledge of their position but also to scientific operations using radio signals in navigation bands for indirect measures of i.e. atmospheric parameters or ground reflectivity conditions.
- The geometry of satellites in view will be statistically improved all over the planet with the consideration of additional constellations.
- The use of more than one independent GNSS will provide improved robustness against satellite/system failure, adding reliability to the PVT solution.

All in all, this thesis is focused towards the exploitation of benefits and the solution of drawbacks on selected topics within the described scenario.

¹ These drawbacks here noted are directly worsened by the presence of interference signal sources in the vicinity of the receiver and multipath due to atmospheric and environmental causes. Note that these points are not mentioned here since they are not attributable to the presence of multiple GNSS constellations transmitting on overlapping frequency bands.

1.2 *Contributions Original to This Work*

The most relevant contributions of this PhD dissertation are concentrated on the preliminary study of the present and future GNSS scene, the improvement of simulation techniques applied to the radionavigation field, and the development of receiver-based measures to increase the reliability of the PVT solution in a broad range of scenarios. The specific original developments in this dissertation are listed below and detailed all along this document.

1. Review of all present and planned global and regional satellite navigation systems from a technological point of view in order to set coherent and realistic simulation conditions for subsequent studies in this document. A joint historical revision gives an insight into the evolution of satellite-based positioning and navigation, which covers from the early times of Transit, predecessor of GPS, to the present developments taking place during the construction of Galileo and COMPASS, and the modernization of GLONASS.
2. A detailed investigation is as well conducted and documented in this thesis to identify potential external interference sources on navigation services in L-, S- and C-bands, and the threat that they might pose to the reliability of the navigation solution. Note that this study is not limited to L-band, on which traditionally all existent navigation services are transmitted, but extended to higher bands (S and C) which presently are regarded as good candidates for future Galileo extensions.
3. Design and development of a model-based software simulation tool for GNSS-related and external interference studies, appropriate to characterize the effects of these factors on the quality of the solution obtained from a given navigation receiver. Additionally, a computationally efficient method is designed here to compute the spectral separation coefficient between two arbitrary navigation signals as a function of the Doppler frequency offset.
4. By using the tool outlined in 3, the feasibility of a new approach to the interference robustness is studied, based on the increase of the user receiver antenna masking angle in a GPS+Galileo scenario in order to further reject ground-based interferences and multipath reflected rays in urban canyons, for instance. For this purpose, the dichotomy between benefits and disadvantages provided by the combination of GNSS systems will be studied and evaluated.
5. Design and development of a semi-bit-true GNSS receiver software simulator to assess the extent of dynamic factors on the low level functions of such a device.
6. The application of a modified version of the simulator developed in 5 allows developing and demonstrating a novel technique to detect and reduce the systematic error or bias that can potentially affect the code delay estimation within a GNSS receiver compatible with modern subcarrier-based navigation modulations. Exhaustive examples on how this technique performs on Galileo E1a and E6a signals are provided.

1.3 Organization of This Dissertation

The present document is divided in two well defined parts. The first one, included here to establish a solid base for the succeeding developments, will include three chapters. A complete review of present and futures satellite-based navigation systems of regional and global coverage will be available from **Chapter 2** in order to understand the needs and requirements from the user point of view, and to set coherent simulation scenarios. **Chapter 3** will be devoted to the review of the technology related to the implementation and function of receivers for extremely weak signal reception, with special highlight to classical structures and techniques used in the processing of GNSS signals. From the two preceding chapters, **Chapter 4** will give an overview of error sources and vulnerabilities in satellite-based navigation applications, also providing references to counter techniques and measures of special interest in the high accuracy user segment. From the spectral usage point of view, an exhaustive analysis covered in this chapter will list potential RF sources to potentially interfere the broadcast, reception and usage of navigation signals in L-, S- and C-bands.

As a natural evolution, once the basics are covered, the second part of the document is dedicated to the understanding and optimization of the modern software simulation techniques applied to the design, characterization, and performance troubleshooting of satellite based navigation systems and receivers (**Chapter 5**). Particular efforts will be applied to the fast estimation of the Spectral Separation Coefficients (SSC) between navigation signals within model-based signal quality simulations, and to the runtime reduction of bit-true GNSS receiver simulators. Novel developments in **Chapter 5** will then be used in **Chapter 6** to study an innovative receiver design approach to eliminate the risk of DLL false lock for subcarrier-based modulations, and in **Chapter 7** to the detailed description of the trade-off between the satellite geometry and the interference level as seen by a receiver within a multisystem GNSS scenario, a study that is not available in the literature at the moment of writing.

Finally, **Chapter 8** will summarize the set of conclusions and results reached during the present dissertation, and will propose highly interesting lines of work for a future follow-on.

1.4 General Notes and Definitions

In the following, the term ‘receiver’ will be generically used to denote a navigation receiver designed to acquire and track DS-CDMA navigation signals. Similarly, the operator of such a receiver will be simply named the ‘user’ all throughout this document, assuming that the context of this work is understood to be framed in the GNSS field.

As a general premise in this contribution, special interest will be put to measures applicable to mass-market receivers. Due to this fact, only CDMA systems based on Time-of-arrival (TOA) range determination will be considered, excluding from relevant analysis those systems requiring receivers with an active role.

Furthermore, some more definitions must be clarified in order to establish a coherent and common understanding:

Accuracy. As defined by the Encyclopedia Britannica, the accuracy of a measurement ‘*is the degree of agreement between the experimental result and the true value*’. In other words, the

accuracy of a set of measures corresponds to the difference between the average of all measured values and the actual value to be observed.

Precision. Again, according to Encyclopaedia Britannica, precision is defined as '*the degree of agreement among a series of measurements of the same quantity*'. Then, it can be said that precision is a measure of the reproducibility of results rather than their correctness. In mathematical terms can be seen as a synonymous of the number of significant digits used to express a quantity.

GNSS vs. RNSS. GNSS and RNSS are acronyms often indiscriminately used in the literature to designate satellite constellations of global coverage with positioning and navigation purposes. However, it must be understood that, for the sake of accuracy, RNSS will be generally used within this document and GNSS will be reserved to designate satellite systems with global coverage, to the detriment of regional augmentation systems. Therefore, GNSS will be considered a subset of RNSS.

Interference. As defined by ITU [Ref. 56], '*Effect of unwanted energy due to one or a combination of emissions, radiations, or inductions upon reception in a radio communication system, manifested by any performance degradation, misinterpretation, or loss of information which could be extracted in the absence of such unwanted energy*'.

1.5 *Formal Framework of This Work*

All innovative procedures shown in this thesis have been developed during the nominal course of real research and development projects awarded by the European Space Agency (ESA) to *JOANNEUM RESEARCH Forschungsgesellschaft mbH* (Graz, Austria), acting either as prime or subcontractor. Therefore, given the confidential nature of these projects, the results shown in this document have been obtained for scenarios modified from the originally designed for the mentioned projects.

From the previous statement, it is specifically understood that the author of this PhD dissertation has been directly involved in either the proposal phase and/or in the actual realization of such ESA projects, and that all techniques here exposed have been entirely developed by the author unless otherwise specified. Note that this remark serves to complement the formal Statutory Declaration signed at the beginning of this document.

CHAPTER 2

CURRENT AND FUTURE SATELLITE RADIONAVIGATION SYSTEMS

2.1 *Preface*

As a starting point, and following a historical line, it is appropriate to discuss the origins of GPS and GLONASS global navigation system, whose basic functional concepts were developed through precursor systems during the Cold War by the two world superpowers of that moment. This was the case, for instance, of the *U.S. Navy Transit Doppler system*, whose first satellite (Transit 1B) was successfully launched in 1960, one year after the launching failure of Transit 1A. *Transit*, composed of 3 operational satellites, allowed the user position determination from the Doppler frequency shifts of the received signals. This system was open to civil users from 1967 to 1996, year of its decommission after almost thirty years of service.

The *U.S. Army SECOR*, was an all-weather geodetic survey system composed of 13 satellites launched from 1964 to 1969. This system was used to fix the location of many Pacific islands and required three portable ground stations in accurately known locations to determine the position of a forth receiver.

In 1967, the first satellite of *U.S. Navy Timation* technology program was launched, carrying a highly stable quartz-crystal clock and thus laying the way for the first atomic clock in space in the payload of later models. This program was designed to advance the development of high-stability clocks, time-transfer, two-dimensional navigation, and demonstrate the technology for three-dimensional navigation. Despite the noticeable sensitivity of *Timation* to jamming, it helped to build the basis for GPS as we know it today. In fact, the last two *Timation* satellites were used as prototype GPS space vehicles. From 1968 to 1971, within the U.S. Air Force program code-named *621B*, tests from airplanes assessed the effectiveness of pseudorandom PRN codes as a suitable option to implement robustness against jamming.

Still in the frame of the Cold War, and as an answer to U.S. advances in the field, the former Soviet Union also developed early navigation systems for both military and civilian users based on the Doppler frequency shift principle of *Transit*. The civil and military branches of the system (named *Tiskada* and *Parus* -also known as *Tiskada M-*) are presently active since 1976. Last known launches of *Tiskada* and *Parus* took place in 1995 and 2003 respectively.

It is obvious that the contemporary GNSS scenario is a direct inheritance of past historical developments, and that a number of new players are sitting on the bench waiting for its opportunity to enter the game. Many clues suggest nowadays that the early future GNSS scheme is evolving towards an enormous system of navigation systems with an American modernized GPS, a Russian

refurbished GLONASS, an European brand new Galileo and a Chinese COMPASS or an Indian IRNSS being under preparation, and a number of regional ground- and space-based augmentation systems taking an active role. Therefore, given the limited frequency bands and bandwidths reserved for RNSS use, it is more and more complicated for the respective task forces to keep the interoperability and mutual independence between systems. As an example of this complexity, Figure 2-1 depicts the usage of the currently allocated RNSS frequency bands, expected when a number of new systems come into operation.

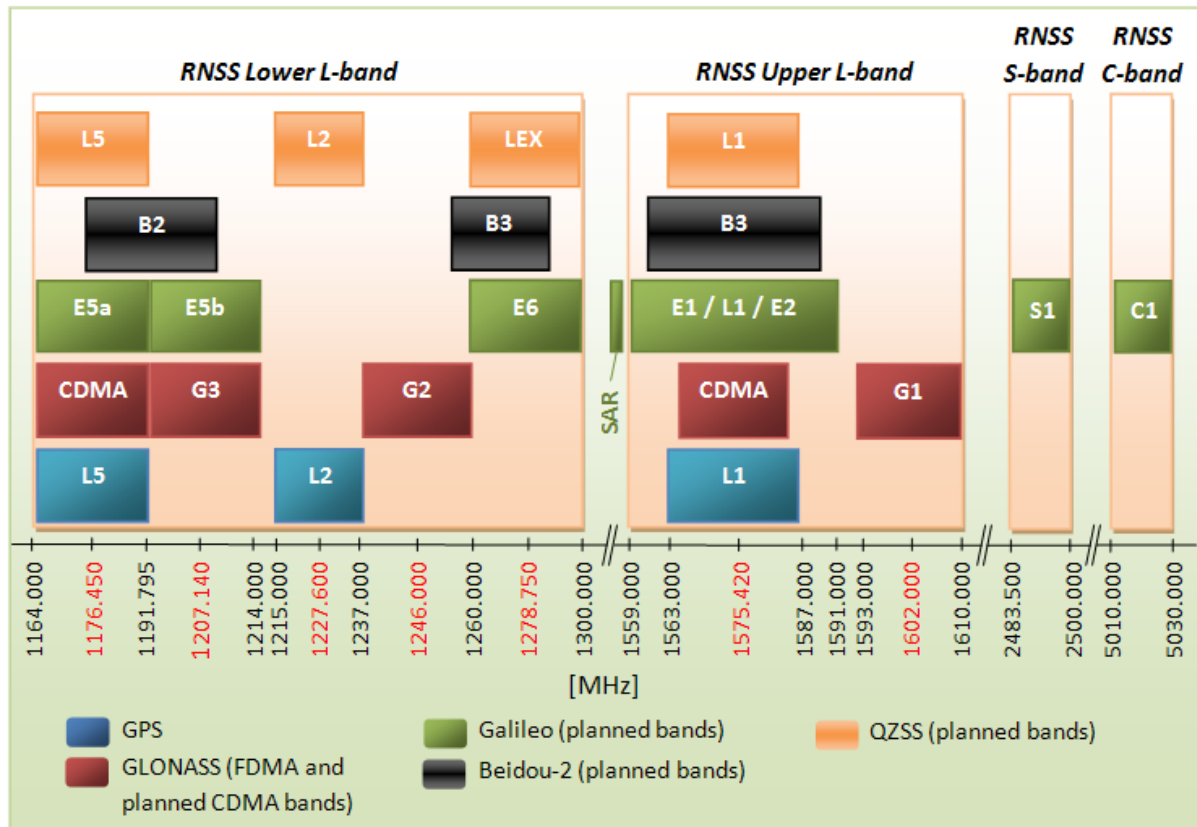


Figure 2-1: Usage of frequency bands currently assigned to Space-to-Earth RNSS services (last update on 23 November 2010).

Figure 2-1, complemented in Chapter 4 with a range of non-navigation related interfering radio sources, shows an especially crowded band around 1,176.45 MHz, shared by a number of signals like GPS L5, Galileo E5a, COMPASS L5, QZSS L5 or the modernized CDMA GLONASS on L5, or a band centred on 1,278.75 MHz becoming of importance with Galileo E6 and under consideration for COMPASS B3 or QZSS LEX. According to current developments, and as per today, S- and C-bands are in the target of the next generation satellite navigation systems, providing a relatively navigation-related interference-free frequency band yet affected by higher atmospheric attenuations among other drawbacks. It is worth to point out here that mainly because of this inconvenience, the possibility of Galileo services in C-band is very well in risk to be discarded.

2.2 *Global and Regional Satellite Navigation Systems*

2.2.1 GPS

Outline. GPS is currently regarded as the first fully operational global navigation satellite system (GNSS), a clear evolution of the accurate clocks of *Timation*, the jamming resistance of 612B, and the Time-of-Arrival (TOA) ranging measurement method of the terrestrial radio navigation system LORAN¹. Developed by the U.S. Air Force, Department of Defence, GPS was originally envisaged as a continuously available navigation satellite system with clear military purposes, originally designed for precise ballistics delivery and nuclear weapon explosions detection². At the present, GPS is a dual-use system (since 1984, by announcement of the formerly U.S. President Reagan), which broadcasts spread spectrum navigation signals in a number of L-band frequencies to support both military (encrypted) and civil open positioning services, and to disseminate a form of Universal Coordinated Time (UTC).

Space Segment. Although according to the official specifications, a constellation of 24 MEO satellites (distributed in 6 orbital planes with offset 55°, nominal altitude 20,200 Km, orbital revolution period equal to 11 hours and 58 minutes) is required for Full Operational Capability (FOC), as much as 31 satellites have been simultaneously in orbit. Through the nominal constellation, as much as 4 to 8 satellites are guaranteed to be visible worldwide above 15° of elevation relative to the receiver horizon. All operative SVs (Space Vehicles), simultaneously transmitting RHCP signals in L1, L2 and L5 bands, are identified by means of different Pseudorandom Noise Codes (PRN) (designed to display minimum cross-correlation and maximum auto-correlation properties) that support the satellite-to-user ranging measurements. In the GPS satellite payload, two different PRN ranging codes (a short, coarse acquisition C/A code and a long, precise P(Y) encrypted code) are generated and combined with the navigation data prior to its modulation, and used at reception (and after decoding of the embedded navigation data stream) to estimate the satellite-to-user propagation time of the signal, and hence to determine the satellite-to-user pseudorange. TOA (time-of-arrival) to at least 4 different satellites in line-of-sight (LOS) to the user are needed for the determination of the main user unknowns: its longitude, latitude, height and the receiver clock offset relative to the GPS time base (the reader is kindly referred to [Ref. 9] for a classic example of this computation).

As the GPS receiver has a passive role in the system, service can be provided simultaneously to an unlimited number of users by means of the TOA ranging method. All navigation signals and carriers are synchronized to the Global Positioning System Time (GPST) (used to adjust the highly accurate on-board atomic clocks of the satellites), and used to broadcast the necessary information for the receiver to determine the health and accuracy of every visible satellite, their orbital position at the time of signal transmission, the behaviour of on-board clocks and ionospheric correction parameters

¹ More accurately, LORAN provides 2-dimensional positioning by combining differential TOA measurements (TDOAs) over at least two pairs of paths between at least three fixed stations (one master and two or more secondary stations) and the target to locate [Ref. 66].

² As a reminder of the capabilities shown by the group of U.S. *Vela* satellites, a secondary payload, named NDS after *Nuclear Detonation Detection System*, has been continuously included in every GPS satellite launched since 1983 to provide reliable and real-time detection of Earth-based and atmospheric nuclear detonations taking place worldwide. The NDS includes optical, x-ray and electromagnetic pulse (EMP) sensors, and a data processing unit able to locate the event with accuracy better than 100 m [Ref. 57].

in order for single-frequency receiver to reduce the pseudorange error due to ionospheric propagation (see Chapter 4 for further descriptions).

Reference Systems. The GPST time reference used in and disseminated by GPS was initiated at 00:00 hours UTC, January 6, 1980 (GPS standard epoch) and is delayed exactly 19.000 s relative to the international atomic time (TAI). The GPS time is counted in weeks relative to the standard epoch, and seconds within the current week, numbers that are included in the navigation data stream. Note that, as only 10 bits are reserved for the week number transmission, a roll-off occurs every 1,024 weeks.

The coordinate reference system within GPS is the World Geodetic System 1984 (WGS-84). The last revision of this reference system took place in 2002, originating WGS-84(G1150), which is virtually identical to the International Terrestrial Reference Frame (ITRF). The ellipsoid of revolution associated to this reference frame is completely defined by the parameters listed in Table 2-1.

| Description | Symbol | Value |
|-------------------------------------|------------|---|
| Semimajor axis of the ellipsoid | a | 6,378,137.0 m |
| Flattening of the ellipsoid | f | 1/298.257223563 |
| Angular velocity of the Earth | ω_e | $7,292,115 \cdot 10^{-11}$ rad/s |
| Gravitational constant of the Earth | μ | $3,986,004.418 \cdot 10^8$ m ³ /s ² |

Table 2-1: WGS-84 ellipsoid parameters.

Signal Structure. A summary of the present and modernized GPS signal configurations in every band is exposed in the table below.

| Frequency band | PRN code | Code rate [Mcps] | Code Length [chips] | Modulation | Bandwidth [MHz] | Data rate [sps] |
|----------------|-------------------|------------------|---|--------------------|-----------------|-----------------|
| L1 | C/A | 1.023 | 1,023 | BPSK(1) | 2.046 | 50 |
| | P ^(c) | 10.23 | Aprox. $6.2 \cdot 10^{12}$ ^(d) | BPSK(10) | 20.46 | 50 |
| | M | 5.115 | ^(b) | BOCsin(10,5) | 30.69 | ^(b) |
| | L1 C _D | 1.023 | 10,230 | BOCsin(1,1) | 4.092 | 100 |
| | L1 C _P | 1.023 | 10,230 | TMBOCsin(6,1,1/11) | 4.092 | pilot |
| L2 | P ^(b) | 10.23 | Aprox. $6.2 \cdot 10^{12}$ ^(c) | BPSK(10) | 20.46 | 50 |
| | L2C | 0.5115 | 10,230 | BPSK(1) | 2.046 | 50 |
| | M | 0.5115 | 767,250 | BPSK(1) | 2.046 | pilot |
| | M | 5.115 | ^(a) | BOCsin(10,5) | 30.69 | ^(a) |
| L5 | L5-I | 10.23 | 10,230 | BPSK(10) | 20.46 | 100 |
| | L5-Q | 10.23 | 10,230 | BPSK(10) | 20.56 | pilot |

(a) According to the last update of [Ref. 4], as per 23 August 2010.

(b) Not published for confidentiality reasons.

(c) Encrypted.

(d) Segments of a master sequence of $2.35 \cdot 10^{14}$ chips long.

Table 2-2: GPS signal characteristics (complete scheme foreseen for 2013).

C/A and P signals in L1, L5-I and L5-Q, and CM and CL in L2 in GPS are multiplexed following a phase/quadrature approach. L1 C_D and L1 C_P are multiplexed on the L1 carrier through BOCsin(1,1) and TMBOCsin(6,1,1). However, at the moment of writing, the multiplexing schemes selected to combine all signals in modernized GPS on L2 are not yet defined (see [Ref. 4]).

Note in Table 2-2 the GPS legacy signals in L1 (C/A and P) and L2 (P) and a set of modernized components. The applicability of the complete set is foreseen for 2013, target date of GPS-III. To complement Table 2-2, the minimum RF power levels to be expected by a terrestrial user for all signals at the end of life of IIR-M and IIF GPS satellites are presented in Table 2-3. These values are defined as received above 10° elevation by an on-ground user receiver with a hemispherical antenna of 0 dBi and ideally matched to the transmitted RHCP polarization [Ref. 3].

| Frequency band | Signal | Signal strengths [dBW] |
|----------------|----------|------------------------|
| L1 | C/A | -158.5 |
| | P | -161.5 |
| | M | ^(a) |
| | L1 C_D | -163 |
| | L1 C_P | -158.25 |
| L2 | P | -161.5 |
| | L2CM | -163.0 |
| | L2CL | -163.0 |
| | M | ^(a) |
| L5 | L5-I | -157.9 |
| | L5-Q | -157.9 |

(a) Not available.

Table 2-3: GPS minimum RF signal strength expected at the end of life of IIF and IIR-M satellites.

Offered Services. Two kinds of GPS positioning services are available, known as SPS and PPS:

- Standard Positioning Service (SPS): Available without restrictions and free of direct charges to all civil users worldwide, this is the service of predominant use for millions of users. In GPS, this service is based on C/A code, exclusively on L1. The availability of this service can be modified under control of the Department of Defence of the United States, depending on the geopolitical circumstances of the country. With this service, the global average user range accuracy is guaranteed to be better than 30 m the 99.94% of the time, with time accuracies¹ better than 40 ns the 95% of the time [Ref. 1].
- Precise Positioning Service (PPS): Intended for U.S. military and authorized users only. The use of this service, mainly supported by the signal component P on L1 and L2 bands, requires certain initial knowledge of the pseudorandom code sequence. The performance of this service is currently secured through cryptographic methods as an anti-spoofing measure. The observation of accuracies of this service, considerably higher than in SPS, is used to monitor the quality of the standard service.

¹ These values assume no Selective Availability (SA) activated, current situation since May 2000 (see [Ref. 12]).

System Administration. The complete GPS infrastructure, including space, ground, and military user-equipment segments have been managed by the GPS Wing (formerly NAVSTAR GPS Joint Program Office) of the Space and Missile Systems Centre at Los Angeles Air Force Base, California). It has been also a competence of the GPS Wing to maintain and update the GPS Interface Control Document (ICD), being IS-GPS-200, revision E [Ref. 3] the current official issue.

Since November 10, 2010, the GPS Directorate is in effect, replacing the U.S. Air Force GPS Wing at Los Angeles Air Force Base. This new organism will assume all competences formerly assigned to the GPS Wing.

GPS Modernization. The modernization process of GPS, already initiated in 1998 with an announcement of the White House has as the main target the implementation of new ground stations and the launching of modernized satellites by 2013. These updates will provide additional signals available to civilian and military users, improving accuracy and availability worldwide as well as interoperability with Galileo and future systems.



Figure 2-2: Artist impression of a GPS Block IIF satellite in orbit.
(source: NASA)

For safety-of-life applications, a new signal in L5 [Ref. 2] was initially planned to be available for SPS users by 2008, transmitting longer spreading codes with higher bandwidth and power than current L1 and L2. However, due to delays of varied nature, the first two satellites broadcasting this signal (IIR(M)-20 and IIR(M)-21, with respective PRN 1 and 5) are available since late 2009, with more delays to be expected towards the FOC of GPS in L5.

Furthermore, L2C [Ref. 3], a new civilian signal in L2 for non-safety-of-life applications, will be introduced in order to allow SPS dual frequency receivers to determine and compensate for the ionospheric delay without relying upon generic models and thus more precisely. An improved version of the GPS signal in L1, named L1C [Ref. 4] will be available by 2013, designed for backward compatibility to all existent GPS receivers on L1, and featuring more spectrally efficient modulation schemes than L1 C/A. Additionally, a new signal for PPS users, implementing the so-called M code, will be transmitted in both L1 and L2, to increase resistance to interference and jamming relative to the legacy P(Y) code.

GPS History. In an effort to summarize the most important milestones in the development and modernization of GPS, the tables below present its timeline extended to the future, according to reliable and official sources of information.

| | |
|-----------------------|---|
| Late 1960s | The system concept is developed by the U.S Army. |
| 1972 | First prototypes of GPS receivers tested over White Sands Missile Range, using ground-based pseudo-satellites. |
| February 1978 | First experimental Block-I GPS satellite launched on an Atlas-F booster. |
| 1984 | U.S. President Reagan announces that the GPS system will be available for civilian uses upon its completion. |
| 1985 | Last of ten Block-I GPS satellites is launched. |
| 1986-1989 | Launch program stopped due to the disaster of STS-51L mission (space shuttle Challenger). |
| February 1989 | A revived program: first second-generation GPS satellite (Block-II) launched. |
| 1991 | GPS is validated during the Persian Gulf War. |
| July 1991 | Selective accuracy activated. |
| July 1993 | U.S. Federal Aviation Administration approves use of GPS on civil aviation. |
| December 1993 | GPS achieves initial operational capability. |
| January 1994 | 24 GPS satellites in orbit. |
| February 1994 | FAA announces that GPS is now operational and is an integrated part of the U.S. air traffic control system. |
| April 1995 | GPS declared of full operational capability by NAVSTAR |
| December 1996 | TRANSIT satellite system ceases operations. |
| January 1999 | The U.S. government announces the GPS modernization. |
| 1996 | U.S. President Clinton issues a directive declaring GPS of dual civilian and military use. |
| 1997 | The rocket carrying the first of GPS Block-IIR satellites explodes after lift-off. |
| 1998 | U.S. Vice President Al Gore announces plans for GPS upgrade. |
| May 2000 | Selective Availability mechanism disabled as per presidential directive of 1996. [Ref. 12] |
| 2004 | Agreement between the U.S. government and the European Community signed, regarding interoperability of GPS and planned Galileo. |
| 2004 | U.S. President Bush issues an updated policy to keep civilian GPS free of direct charges for users. |
| September 2005 | First modernized GPS satellite launched (Block IIR-M). |
| December 2005 | First modernized GPS satellite declared operative, and broadcasting L2C beside the legacy signals. |

Table 2-4: GPS history timeline (1/2).

| | |
|-------------------------|---|
| April 2009 | After substantial delays, the ITU spectrum filling for GPS in L5 signal is secured through a transmission from the IIR(M)-20 satellite. |
| August 2009 | The last IIR GPS satellite (IIR(M)-21) is declared operational 10 days after successful launching. |
| May 2010 | First GPS IIF satellite launched from Cape Canaveral. |
| August 27, 2010 | First GPS IIF satellite (identified through the PRN 25) is set to healthy state. |
| November 9, 2010 | The GPS Directorate enters into effect, replacing the U.S. Air Force GPS Wing at Los Angeles Air Force Base. |
| 2013 | New L1C signal is to be available to civilian users. Modernization of GPS, GPS-III, scheduled to reach target date. |

Table 2-5: GPS history timeline (2/2).

2.2.2 GLONASS

Outline. Also in the frame of the Cold War, the developments and lessons learned from the programmes *Parus* and *Tiskada* enabled the former Union of Soviet Socialist Republics to respond to GPS with an alternative under exclusive military control and use, known as GLONASS after the Russian *GLobal'naya NAVigatsionnaya Sputnikovaya Sistema*.

December 1976 is considered the official program kick-off date, in which a detailed plan for GLONASS development was presented to and accepted by the former *Council of Ministers of the USSR*. In this plan, an FDMA¹ system of 21 active satellites (plus 3 spare units) orbiting at 19,100 Km of altitude and distributed in 3 orbital planes with 64.8° inclination, was foreseen to reach FOC by 1991. By design, GLONASS was meant to provide a continuous 4-satellite visibility at any point on Earth the 97% of the time [Ref. 7], and especially on the northern regions of the present Russian territory.

In 1991, though, after nine years and 48 successful launchings, only twelve GLONASS satellites were remaining operational, still under exclusive military management. It was not until 1996 when the full 24-satellite nominal constellation was complete, and the Russian government initiated a disclosure process to make of GLONASS a dual-use system, allowing public access to signal specifications (see [Ref. 5] for a current release of this information) for users and industry. Due to the collapse of the Russian economy, the system rapidly fell in disrepair and the number of operative satellites in orbit was rapidly reduced.

Signal Structure. As already stated earlier in this section, every GLONASS satellite has assigned unique carrier frequencies in each sub-band, with a channel separation of 562.5 kHz in G1, or 437.5 kHz in G2. See equations in 2-1.

$$\begin{aligned}
 f_{k1} &= 1602 + k \cdot 0.5625 & [MHz] \\
 f_{k2} &= 1246 + k \cdot 0.4375 & [MHz]
 \end{aligned}
 \tag{2-1}$$

¹ In here, FDMA makes reference to the carrier-based satellite identification method used in GLONASS. The range from satellite to user, as in GPS, is determined through TOA applied to PRN codes transmitted on every frequency.

Since 2005, GLONASS satellites have been broadcasting RHCP signals only in channels $k \in \{-7, \dots, 4\}$ (see equations in 2-1, with k unique for every satellite) in order to limit interferences on satellite communication and radio astronomy services. Note that the aforementioned frequency restriction left only 12 unique carriers to be used for the 21+3 satellites in the GLONASS constellation. This limitation was overcome by assigning equal frequencies to satellites on antipodal positions over the Globe.

| Frequency band | PRN code | Code rate [Mcps] | Code length [chips] | Modulation | Bandwidth [MHz] | Data rate [sps] |
|-------------------|------------------|------------------|---------------------|------------------|-----------------|-----------------|
| G1 | C/A | 0.511 | 511 | BPSK(0.511Mcps) | 1.022 | 50 |
| | P ^(b) | 5.11 | $5.11 \cdot 10^6$ | BPSK(5.11Mcps) | 10.22 | 50 |
| G2 | C/A | 0.511 | 511 | BPSK(0.511Mcps) | 1.022 | 50 |
| | P ^(b) | 5.11 | $5.11 \cdot 10^6$ | BPSK(5.11Mcps) | 10.22 | 50 |
| G3 ^(a) | | | | | | |

(a) Not yet in space. The configuration of the GLONASS transmission in this band has not yet been made available.

(b) Not encrypted

Table 2-6: GLONASS signal characteristics since 2003.

| Frequency band | Signal | Signal strength [dBW] |
|-------------------|--------|-----------------------|
| G1 | C/A | -161 |
| | P | -161 |
| G2 | C/A | -167 |
| | P | -167 |
| G3 ^(a) | | |

(a) Not yet in space. The configuration of the GLONASS transmission in this band has not yet been made available.

Table 2-7: Expected minimum signal strength at the end of life of GLONASS and GLONASS-M satellites¹.

Two navigation messages at a data rate of 50 bps are modulo-2 added to P and C/A PRN codes, and used to modulate the satellite carriers. Table 2-6 summarizes the characteristics of the Signal-In-Space of GLONASS since 2003, and Table 2-7 presents the minimum RF strength to be expected from GLONASS and GLONASS-M satellites at the end of their life.

Since February 15th 2008, preliminary CDMA signals for GLONASS open service include BOC(2,2) and BOC(4,4) centred in GPS L1 and L5 respectively. Additionally, a third GLONASS FDMA band will be allocated in 1,197.648 MHz – 1,212.255 MHz, just below GPS L2 [Ref. 8]. A refined CDMA signal and frequency plan in G1, G2 and G3 was made available in November 2010 by Russian authorities. However, due to the preliminary nature of this information no note has been taken of such contributions in this thesis.

¹ The values in this table are defined as received above 5° elevation by an on-ground user receiver with a hemispherical antenna of 0 dBi and ideally matched to the transmitted RHCP polarization [Ref. 5].

Offered Services. The organization of services provided by GLONASS is similar to GPS. In this case, GLONASS is designed to provide two positioning services, known as SPS ('Standard Precision Service', the civilian service of GLONASS) and HPS ('High Precision Service', access granted only to Russian military and authorized users), in two frequency bands (G1 and G2). Initially, SPS was mainly supported on G1 C/A and it was not until 2003 that an additional C/A code was offered as well on G2, making of GLONASS the first GNSS system to provide dual-frequency operation to non-military users. Transmissions on G3 are foreseen as a backup in safety-of-life applications.

Reference Systems. The reference coordinate system used within GLONASS is denoted as PZ-90 after the Russian translation of 'Parameters of the Earth 1990' (*Parametry Zemli 1990*). Table 2-8 defines the ellipsoid characteristic to this coordinate reference system.

The realizations of WGS-84 and PZ-90 present certain bias due to the use of different sets of stations for their determination. In the past, many authors presented transformations from GLONASS to GPS reference frames (see table 2 in [Ref. 11]). Nevertheless, according to [Ref. 10], it is internationally accepted to reduce the transformation to a rotation of the Z-axis of -0.343 arc seconds.

| Description | Symbol | Value |
|-------------------------------------|------------|---|
| Semimajor axis of the ellipsoid | a | 6,378,136.0 m |
| Flattening of the ellipsoid | f | 1/298.257839303 |
| Angular velocity of the Earth | ω_e | $7,292,115 \cdot 10^{-11}$ rad/s |
| Gravitational constant of the Earth | μ | $3,986,004.418 \cdot 10^8$ m ³ /s ² |

Table 2-8: PZ-90 ellipsoid parameters.

A revision of PZ-90, named PZ-90.02, was released in 2008 as an amendment to GLONASS ICD version 5.1 [Ref. 5] and specifying minimal variations to the content of Table 2-8.

The difference of the GLONASS time base relative to UTC has two major components: (a) a constant delay equal to the difference between the time in Moscow and Greenwich, this is, 3 hours, and (b) an additional component τ due to the time keeping by means of non-synchronized clocks. This last parameter, obtainable from the data broadcasted within the GLONASS navigation messages, allows the determination of UTC from GLONASS time dissemination by using the relation in equation 2-2.

$$t_{UTC} = t_{GLONASS} + \tau - 3 \text{ hours}$$

2-2

GLONASS Modernization. A presidential decree of 2001 signed by the former Russian President Vladimir Vladimirovich Putin is ensuring up to present days the refurbishment and modernization of the system, which is expected to recover the nominal constellation and continuous worldwide coverage by 2011. Third-generation GLONASS satellites (also known as GLONASS-K, to be incorporated to the modernized fleet) are expected to implement a change in GLONASS current

access technique and broadcast signals in CDMA as a first step towards the full interoperability with GPS and Galileo, and the design simplification of an eventual combined receiver.



Figure 2-3: Artist impression of a GLONASS-K satellite in orbit. (source: NASA)

GLONASS Timeline. Table 2-10The tables below depict the history of GLONASS since its conceptual beginnings.

| | |
|----------------------|---|
| Early 1960s | The former USSR develops <i>Tiskada</i> and <i>Parus</i> . |
| December 1976 | The development of the GLONASS officially begins, with a goal of global coverage by 1991. |
| October 1982 | The first GLONASS satellite is launched. |
| May 1985 | The second phase of GLONASS deployment starts. |
| 1991 | The Soviet Union is dismantled. Only twelve functional GLONASS satellites are operative in two orbital planes. |
| March 1995 | GLONASS declared available to civilian users. |
| January 1996 | Full constellation and FOC achieved. |
| August 1996 | ICAO responds favourably to the Government of the Russian Federation's proposal to present GLONASS as part of an international aviation navigation resource. |
| 1996-1998 | Due to lack of funding, the GLONASS system is no longer maintained. |
| August 2001 | President Putin initiates GLONASS modernization. |
| 2003 | New GLONASS satellites start to transmit a second C/A code in G2. |
| January 2004 | Agreement signed between the Russian Space Agency and the Indian Space Research Organization for collaboration in the restoration and modernization of GLONASS. |

Table 2-9: GLONASS history timeline (1/2).

| | |
|------------------------------|--|
| May 2007 | Presidential decree signed by President Putin to officially provide free-of-charge access to GLONASS signals to civil users. |
| October-December 2007 | Six new second-generation GLONASS-M satellite successfully launched. |
| 2008 | First launch of third-generation GLONASS satellites (GLONASS-K) scheduled. Reported to be already transmitting on G3 band. |
| February 2010 | 19 active GLONASS-M satellites are reported to be in the air by Russian official authorities. |
| November 2010 | Preliminary configuration of the GLONASS CDMA signal plan revealed by Russian authorities. |
| December 2010 | Scheduled launch of first CDMA capable GLONASS-K satellite. |
| 2012-2013 | Full deployment for continuous worldwide coverage scheduled. |

Table 2-10: GLONASS history timeline (2/2).

As a curiosity, it is interesting to compare these tables against the correspondent data in section 2.2.1, and observe the parallel evolution of GPS and GLONASS.

2.2.3 Galileo

Outline. The importance of an independent GNSS was early noticed in Europe. As an initial step towards the European independence from existent GNSS (namely GPS and GLONASS), a resolution of the European Council signed on December 19, 1994 defined the contributions of Europe to the satellite navigation scenario in two main lines of actions. A first statement of this text represented the aim to enhance GNSS-1 with a new and independent space-based augmentation, the European Geostationary Navigation Overlay Service, also known as EGNOS (see section 2.3.1).



Figure 2-4: Artist impression of GIOVE-B in orbit.
(source: ESA)

In second place, this document stated the intention to contribute to GNSS-2 with the initiation of preliminary works that will lead to a fully functional Galileo system in a near future.

With the early development managed by the GJU (Galileo Joint Undertaking), and later transferred to the GSA (GNSS Supervisory Authority) after its dissolution, Galileo is envisaged as a 30-satellite constellation distributed in three different orbital planes of 56° inclination, with a nominal altitude of 23,222 Km. Every orbital plane will contain a reserve satellite, thus producing the nominal constellation of 27 active satellites.

Offered Services. The differential fact of Galileo relative to the pre-existing systems is the amount and variety of positioning services that will make available, targeted to mass market, governmental, scientific or commercial applications. A total of 5 services are foreseen, with one of them entirely dedicated to Search and Rescue operations:

- **Open Service (OS):** free-of-charge positioning and time dissemination for all kinds of users and mass-market applications. This service will allow relatively reduced accuracy to be achieved for single-frequency receivers, or more precise positioning through the combination of instances of the same signal in three different frequencies on which OS will be broadcasted. In all cases though, the quality of the service will be guaranteed, and no integrity information will be embedded within the signal.
- **Public Regulated Service (PRS):** Only for government-authorized members in any of the EU Member States. This service is planned to be continuously available, even in time of crisis, and designed for robustness against intentional interference (spoofing or jamming).
- **Commercial Service (CS):** Accessible through key-protected receivers only, this service will provide higher accuracy than OS with two additional signals, and a number of payable added value services based on the global broadcast of system information data.
- **Safety-of-Life Service (SoL):** The use of certified dual-frequency receivers (in E1 and E5) will grant access to this Galileo service, designed for those applications where safety is a must.
- **Search and Rescue Service (SAR):** Galileo SAR, service interoperable with COSPAS-SARSAT, will permit near real time reception of distress messages from all over the Earth, and the location of the victim with an accuracy of a few meters.

Signal Structure. An accurate study of the requirements for every service led to a subtle combination of bands and modulation schemes. Descriptions in Table 2-11 (complemented with Table 2-12) are to be most likely expected in the final deployment phase of Galileo in L-band. However, values contained in this table should be taken with caution, as specifications are not definitive at the time of writing.

As per 2010 [Ref. 6], E1 and E5b Galileo bands are designed to support OS and SoL services, and to broadcast system integrity data. E5b will broadcast freely accessible navigation data to support OS services. And the E6 band will serve to disseminate a commercial navigation message to give support to CS service. Regarding the downlink of the SAR service, it will be supported on 1,544 – 1,545 MHz.

| Frequency band | PRN code | Code rate [Mcps] | Primary code length ^(a) [chips] | Secondary code length ^(a) [chips] | Modulation ^(a) | Receiver Reference Bandwidth [MHz] ^(b) | Data rate [sps] ^(a) |
|----------------|----------|------------------|--|--|---------------------------|---|--------------------------------|
| E1 | E1A | 2.5575 | ^(c) | ^(c) | BOCcos(15, 2.5) | 24.552 | 110 |
| | E1B | 1.023 | 4,092 | N/A | MBOCsin(6,1,1/11) | | 250 |
| | E1C | 1.023 | 4,092 | 25 | MBOCsin(6,1,1/11) | | pilot |
| E5 | E5a-I | 10.23 | 10,230 | 20 | AltBOC(15,10) | 20.460 | 50 |
| | E5a-Q | 10.23 | 10,230 | 100 | AltBOC(15,10) | | pilot |
| | E5b-I | 10.23 | 10,230 | 4 | AltBOC(15,10) | | 250 |
| | E5b-Q | 10.23 | 10,230 | 100 | AltBOC(15,10) | | pilot |
| E6 | E6a | 5.115 | ^(c) | ^(c) | BOCcos(10,5) | 40.920 | 110 |
| | E6b-I | 5.115 | 5,115 | 1 | BPSK(5) | | 1,000 |
| | E6b-Q | 5.115 | 5,115 | 100 | BPSK(5) | | pilot |

(a) Not definitive.

(b) [Ref. 6].

(c) Not published.

NOTE: I (in-phase), Q (quadrature).

Table 2-11: Galileo signal characteristics in L-Band.

| Frequency band | Signal | Signal strength [dBW] |
|----------------|--------|-----------------------|
| E1 | E1A | -160 |
| | E1B | -160 |
| | E1C | -160 |
| E5 | E5a-I | -158 |
| | E5a-Q | -158 |
| | E5b-I | -158 |
| | E5b-Q | -158 |
| E6 | E6a | -158 |
| | E6b-I | -158 |
| | E6b-Q | -158 |

NOTE: I (in-phase), Q (quadrature).

Table 2-12: Expected Galileo signal strength¹.

¹ The values in this table are defined as received above 10° elevation by an on-ground user receiver with a hemispherical antenna of 0 dBi and ideally matched to the transmitted RHCP polarization [Ref. 6].

Reference Systems. The Galileo terrestrial reference frame (GTRF) is expected to be related to the ITRF, with a difference smaller than or equal to 3 cm. This quality that will be ensured by the GGSP (Galileo Geodetic Service Provider).

Regarding the time reference system for Galileo (GST), it will present a constant integer offset in seconds relative to TAI and a variable difference relative to UTC. Both offsets as well as the difference from GPS to Galileo will be included within the broadcasted message, and the correspondent adjustments made at user receiver level.

Galileo Timeline. Table 2-13 and Table 2-14 introduce the history of Galileo up to the present. Please note that, due to uncertainties in the development of the program, the expected date for FOC might be extended.

| | |
|----------------------|---|
| December 1994 | The European Commission signs a resolution, introducing the intention of Europe to contribute to GNSS-2 with an independent GNSS. |
| June 1995 | ESA announces plans for an independent GPS augmentation system under European civil control. |
| June 1999 | The Transport Council of the EU accords the development of an independent GNSS-2, provisionally named 'Galileo' after the Italian scientist and astronomer. |
| March 2002 | The development of Galileo obtains both political and economical support from the Council of Heads of State and the EU Council respectively. |
| 2003 | An important milestone is achieved in the Galileo programme, with the signature of an international cooperation agreement. The Galileo Joint Undertaking is established, to manage the initial development of Galileo. The Galileo definition phase is completed. |
| 2004 | Agreement signed between EU and US to ensure the compatibility between GPS and Galileo, and allow their combined use. The agreement foresees the use of MBOC modulation within Galileo E1. Start of validation of on-ground algorithms within the GSTB-V1 project. |
| May 2005 | The Public-Private Partnership (PPP) is constituted. |
| December 2005 | First Galileo experimental satellite, code name GSTB-V2/A (also known as GIOVE-A), successfully launched. This milestone indicates the starting point of the Galileo IOV phase. |
| January 2006 | First transmission of GIOVE-A from MEO orbit received ⁸ . |
| May 2006 | First draft of the Galileo Open Service ICD made available by ESA and GJU. |
| December 2006 | The Galileo Joint Undertaking is dissolved, and competences transferred to the European GNSS Supervisory Authority. |

Table 2-13: Galileo history timeline (1/2).

⁸ The successful launch and operation of GIOVE-A served to secure the frequency bands that were allocated by ITU for the Galileo operation. Besides, it was designed to demonstrate the critical technology and to characterize the radiation environment at Galileo orbits.

| | |
|------------------------|---|
| April 2007 | Galileo envisages a political peril, with the collapse of the PPP. |
| February 2008 | Second draft of the Galileo Open Service ICD made available by ESA and GSA. |
| April 2008 | GIOVE-B successfully launched. |
| May 2008 | First transmission of GIOVE-B received. |
| June 2009 | Contract signed between ESA and Arianespace for the launching of 4 IOV satellites on board of Soyuz ST-B rockets. |
| January 2010 | The constitution of the operational structure of Galileo is started with the signature of the first contracts between ESA and the industry. |
| February 2010 | First issue of the Galileo Open Service ICD made available by the European Union. |
| 2014 (or later) | Expected FOC of Galileo. |

Table 2-14: Galileo history timeline (2/2).

2.2.4 Beidou-1, towards COMPASS

Outline. Investigations on positioning and navigation technology in China started in late 1960s, and derived into the development and testing (in 1980s) of the positioning concept known as *Twin Star* [Ref. 7], which showed precisions comparable to those achieved with civil services in GPS. In 1993, Chinese authorities commissioned a program for the constitution of an independent navigation system based on the two-way *Twin Star* theory and denominated *Compass Satellite Navigation Experimental System*, or Beidou-1.

At a cost several orders of magnitude lower, in 2000 an alternative programme was initiated to produce the Chinese Area Positioning System (CAPS) through the use of commercial communication satellites. This SBAS will be treated in section 2.2.6.

Space Segment. Beidou-1 was developed by China Academy of Space Technology (CAST) to provide 2D positioning and navigation services initially only to military users and also, since April 2004, to civilian users. This system is envisaged as a 3 GEO satellite constellation (2 active, at 139.9° E and 80.2° E, and one spare at 110.4°E, named Beidou-1A to 1C) with a regional coverage area limited between 70°E – 140°E longitude, and 5°N – 55°N latitude. A fourth satellite, Beidou-1D has been added to the constellation since 2007 to complement operations, and a fifth one (Beidou-1E) is expected to be launched to complete the GEO section of COMPASS.

| Description | Longitude | Comments |
|-------------|-----------|------------------|
| Beidou-1A | 140°E | Not active |
| Beidou-1B | 80°E | Active |
| Beidou-1C | 110.5°E | Backup |
| Beidou-1D | 58.75°E | Active |
| Beidou-1E | 160°E | Not yet launched |

Table 2-15: Detail on Beidou-1 satellites.



Figure 2-5: Artist impression of a Beidou-1 satellite in orbit.
(source: CAST)

Ground Segment. The ground segment of Beidou-1 contains the following elements:

- A control station situated in Beijing, which communicates with the satellites through a link at $2,491.75 \pm 4.08$ MHz (S-band)
- Three orbit monitoring ground stations in Jamushi, Kashi and Zhanjiang, precisely determining the small variations of the GEO orbit of all satellites.
- A number of calibration stations throughout China that compute corrections to the errors in the transmission time determination.
- And the user receiver, which in this system takes an active role, transmitting back to the satellite on 1,615.68 MHz (L-Band)

Reference Systems. The Beijing 1954 coordinates system was selected as coordinates reference frame for Beidou-1 and the time reference was extracted from the China UTC as determined in Beijing.

Towards the Global Coverage. Beidou-1 is serving, at the time of writing, as the base for the *Compass Satellite Navigation System*, codename Beidou-2/COMPASS, which is scheduled to provide navigation and positioning services to China and part of the neighbouring countries by 2010, and to expand then the coverage to worldwide.

The program, initiated by China military forces and presently managed by China Satellite Navigation Project Centre (CSNPC), foresees a space segment comprising⁹ 30 MEO satellites at 21,500 Km of altitude (distributed in 3 orbital planes with an inclination of 55°) and 5 GEO satellites (at 58.75°E, 80°E, 110.5°E, 140°E and 160°E) to transmit in the bands 1,195.14 – 1,219.14 MHz,

⁹ A number of IGSO satellites may most likely be added to the system to complement a nominal 35-satellite constellation by 2020.

1,256.52 – 1,280.52 MHz, 1,559.05 – 1,563.15 MHz, 1,587.69 – 1,591.79 MHz, and L5 with a barely defined signal scheme. The lack of a public draft ICD available at the time of writing has initially suggested the scheme in Table 2-16 to be applicable in a first design iteration. Associated to these signals, two kinds of services will be made available for regular and authorized users, this last offering more accurate positioning, velocity and time dissemination services, and integrity information. The same sources releasing the initial modulation scheme of COMPASS ([Ref. 20] locate the open service in B1-In phase, B1-BOC, B2-In phase, B2-BOC, and L5. B1-Quadrature, B1-2, B2-Quadrature, B3, and B3-BOC are then allocated to authorized services.

| Signal | Carrier frequency [MHz] | Bandwidth [MHz] | PRN code rate [Mcps] | Signal modulation | Navigation data bit rate [bps] |
|--------|-------------------------|-----------------|----------------------|---------------------|--|
| B1 | 1,561.098 | 4.092 | 2.046 | QPSK(2) | I(GEO) : 500 I(MEO) : 50 Q : 500 |
| B1-2 | 1,589.742 | 4.092 | 2.046 | QPSK(2) | |
| B2 | 1,207.14 | 24 | 10.23 | QPSK(10) | |
| B3 | 1,268.52 | 24 | 10.23 | QPSK(10) | |
| B1-BOC | 1,575.42 | 16.368 | 1.023 | MBOCsin(6, 1, 1/11) | 50 |
| B2-BOC | 1,207.14 | 30.69 | 5.115 | BOC(10, 5) | |
| B3 | 1,268.52 | 35.805 | 2.5575 | BOC(15, 2.5) | |
| L5 | 1,176.45 | 24 | 10.23 | QPSK(10) | |

Table 2-16: Initial COMPASS signal characteristics.
(source [Ref. 20])

A new and unexpected update of the COMPASS signal scheme was released in July 2009 in the ICG Workshop on GNSS Interoperability [Ref. 28], which brought the new configuration to the one summarized in Table 2-17. In this case, the open service is supported through multiplex BOC and AltBOC modulations, respectively supported on GPS L1 and Galileo E5b, and the authorized service broadcasted on B1, B3 and B3-A, with considerable spectrum overlap with Galileo PRS service.

| Signal | Carrier frequency [MHz] | PRN code rate [Mcps] | Signal modulation | Navigation data bit rate [bps] |
|-------------------|-------------------------|----------------------|-------------------|--------------------------------|
| B1-C _D | 1,575.42 | 1.023 | MBOCsin(6,1,1/11) | 50 |
| B1-C _P | | | | pilot |
| B1 _D | 1,575.42 | 2.046 | BOCsin(14,2) | 50 |
| B1 _P | | | | pilot |
| B2a _D | 1,191.795 | 10.23 | AltBOCsin(15,10) | 25 |
| B2a _P | | | | pilot |
| B2b _D | | | | 50 |
| B2b _P | | | | pilot |
| B3 | 1,268.52 | 10.23 | QPSK(10) | 500 |
| B3-A _D | | 2.5575 | BOCsin(15,2.5) | 50 |
| B3-A _P | | | | pilot |

Table 2-17: Expected COMPASS signal scheme, as released on July 2009.
(source [Ref. 28])

According to Chinese official information sources, the system is intended to be fully compatible with GPS, GLONASS and Galileo, assuming from this point that the Twin Star positioning technique will not be continued. Nevertheless, no details on the coordinate reference frame and the time reference system to be implemented have been disclosed at the time of writing.

Time Outline of the Beidou Programme. Table 2-18 and Table 2-19 present the complex timeline of COMPASS until present times.

| | |
|-------------------------|---|
| 1989 | The <i>Twin Star</i> theory is successfully tested through two DFH-2A communication satellites. |
| 1993 | An independent Chinese satellite navigation system obtains governmental approval. |
| October 2000 | Beidou-1A, 1 st satellite of the Beidou-1 experimental navigation system successfully launched. |
| December 2000 | Beidou-1B successfully launched. |
| 2001 | Beidou-1 starts to broadcast positioning and navigation services. |
| May 2003 | Beidou-1C is positioned in orbit as a backup space vehicle. |
| April 2004 | Positioning and navigation services of Beidou-1 are open to civilian users. |
| February 2007 | Beidou-1D launched. |
| April 2007 | 1 st MEO satellite of BeiDou-2, codename Compass-M1, successfully launched. |
| June 19, 2008 | First details on signal definition for COMPASS are made public by Chinese authorities during the ICG 2008 (Montreal, Canada). |
| April 2009 | 2 nd Beidou-2 Satellite (code name Beidou-G2) successfully launched, and positioned into GEO orbit. |
| July 2009 | CNAGA reveals an updated COMPASS signal plan. |
| January 2010 | 3 rd Beidou-2 Satellite (code name Beidou-G1) successfully launched, and positioned into GEO orbit. |
| June 2, 2010 | 4th Beidou-2 Satellite (code name Beidou-G3) successfully launched, and positioned into a GEO orbit on 84.6°E. Broadcast on three frequencies from this satellite started by June 11, 2010. |
| August 1, 2010 | 5th Beidou-2 Satellite (code name Beidou-I1) successfully launched, and positioned into IGSO orbit. This is the first IGSO satellite in the COMPASS constellation. |
| November 1, 2010 | 6th Beidou-2 Satellite (code name Beidou-G4) successfully launched, and positioned into GEO orbit. |

Table 2-18: History timeline of Beidou-1 & -2 (1/2).

| | |
|-----------------------|--|
| December, 2010 | The second IGSO Beidou-2 Satellite (code name Beidou-I2) Scheduled to be launched. |
| 2012 | COMPASS scheduled to provide initial service to users within Chinese territory, through a 14-satellite constellation (5 GEOs, 4 MEOs and 5 IGSOs). |
| 2020 | Target 35-satellite (27 MEOs, 3 IGSOs and 5 GEOs) nominal constellation expected to be completed. |

Table 2-19: History timeline of Beidou-1 & -2 (2/2).

2.2.5 QZSS

Outline. Even though the Quasi-Zenith Satellite System is being designed with a regional coverage to provide GPS augmentation¹⁰ services over East Asia and Oceania, it constitutes the basis for a completely autonomous Japanese CDMA positioning system. It is important to note that all details provided here are based on the very last version of QZSS SIS-ICD [Ref. 21], which is being reviewed at the moment of writing.



Figure 2-6: Artist impression of the ground track of QZSS.
(source: JAXA)

Space Segment. According to the baseline in [Ref. 21], three satellites placed in three HEO orbits with geosynchronous periods will ensure high elevation visibility of at least one satellite for a user on Japanese territory, and hence providing advantageous performance against multipath in canyon-like urban environments and mountainous areas. Table 2-20 provides an outline of the orbital parameters for this system, that yields an eight-shaped ground track plot and reduced Doppler frequency offset (± 3 kHz for L1 carrier frequency).

¹⁰As a GPS augmentation, QZSS provides improved availability and enhanced accuracy and reliability by transmitting signals very similar to modernized GPS before they are readily available.

| Description | Symbol | Value |
|-----------------------------------|----------|---|
| Semimajor axis of the ellipsoid | a | 42,164 Km (average) |
| Eccentricity | e | 0.075 ± 0.015 |
| Orbital inclination | i | $43^\circ \pm 4^\circ$ |
| Argument of perigee | ω | $270^\circ \pm 2^\circ$ |
| Central longitude of ground track | | $135^\circ \text{ east} \pm 5^\circ$ |
| Right ascension of ascending node | Ω | Computed, for every satellite, to keep the central longitude of ground track (120° apart) |

Table 2-20: Orbital parameters of QZSS.

Ground Segment. The basic scheme of the QZSS ground segment has major similarities with other systems. A number of monitoring stations situated over East Asia, Japan, and Oceania linked to a master control station provide the state of signals transmitted from satellites of QZSS and other GNSS. This information is then used for orbit resolution, time synchronization, integrity determination, and as a basis for the generation of the navigation message, which will be uploaded to the satellites by means of the tracking control stations. The navigation message is modulated into the ranging signal in L-band at the satellite, and prepared for broadcast.

Reference Systems. The time reference system envisaged for QZSS is synchronized with TAI, being approximately 19 seconds behind it. It is also foreseen to include in the navigation message, as part of the QZSS interface to GPS and Galileo, the exact time offset relative to both systems.

Regarding the coordinates reference frame in QZSS (known as JGS), it will be based on the GRS80 (Geodetic Reference System 1980) ellipsoid, summarized in Table 2-21. According to [Ref. 21] and [Ref. 22], JGS and all reference frames used in other GNSS will converge towards ITRF in the future.

| Description | Symbol | Value |
|-------------------------------------|------------|---|
| Semimajor axis of the ellipsoid | a | 6,378,137.0 m |
| Flattening of the ellipsoid | f | $1/298.257222107$ |
| Angular velocity of the Earth | ω_e | $7,292,115.1467 \cdot 10^{-11}$ rad/s |
| Gravitational constant of the Earth | μ | $3,986,005 \cdot 10^8$ m ³ /s ² |

Table 2-21: GRS80 ellipsoid parameters.

Signal Characteristics. In order to support positioning, time dissemination, and augmentation services, a set of ranging signals (see Table 2-22) are to be expected from QZSS in several frequency

bands, multiples of 10.23 MHz (shifted approximately $5.523 \cdot 10^{-3}$ Hz to compensate for relativistic effects¹¹).

To ensure interoperability with modernized GPS and to exploit the potential availability improvement offered in QZSS, compatible RHCP signals are structured in L1C/A, L1C, L2C and L5. An additional signal in L1, named SAIF (Submeter-class Augmentation with Integrity Class) is introduced for complete interoperability with GPS-SBAS services and targeted to augmentation services only.

Finally, a second native experimental signal with high data rate is being developed for interoperability with Galileo in E6 band. Up-to-date further details to this respect can be found in [Ref. 21].

| Frequency band | PRN code | Code rate [Mcps] | Modulation | Bandwidth [MHz] | Data rate [sps] |
|----------------|-------------------|------------------|-------------|-----------------|-----------------|
| L1 | L1 C/A | 1.023 | BPSK(1) | 24 | 50 |
| | L1 C _D | 1.023 | BOCsin(1,1) | 24 | 100 |
| | L1 C _P | 1.023 | BOCsin(1,1) | 24 | Pilot |
| | L1-SAIF | 1.023 | BPSK(1) | 24 | 500 |
| L2 | L2C | 1.023 | BPSK(1) | 24 | 50 |
| L5 | L5I | 10.23 | BPSK(10) | 25 | 100 |
| | L5Q | 10.23 | BPSK(10) | 25 | Pilot |
| E6 | LEX | 5.115 | BPSK(5) | 42 | 2000 |

Table 2-22: QZSS signal characteristics.
(source [Ref. 21])

Additionally, Table 2-23 includes the expected power levels for all QZSS signals, that for compatibility with GPS, present values for L1C/A, L1C, L2C and L5 which are identical to the content of Table 2-3.

| Frequency band | Signal | Signal strength [dBW] |
|----------------|-------------------|-----------------------|
| L1 | L1 C/A | -158.5 |
| | L1 C _D | -163.0 |
| | L1 C _P | -158.25 |
| | L1-SAIF | -161.0 |
| L2 | L2C | -160 |
| L5 | L5I | -157.9 |
| | L5Q | -157.9 |
| E6 | LEX | -155.7 |

Table 2-23: Expected QZSS signal strength.
(source [Ref. 21])

¹¹ Note that the non-constant velocity of a satellite in elliptical orbit produces a variable relativistic effect on the perception of the on-board time reference frequency. Complementary fine compensations for this effect will be also broadcast within QZSS navigation message.

Also here, the values in Table 2-23 are defined as received above 10° elevation by an on-ground user receiver with a hemispherical antenna of 0 dBi and ideally matched to the transmitted RHCP polarization.

QZSS History Timeline. In Table 2-24, an approximated list of events and milestones are presented to define the timeline of the Japanese navigation satellite system.

| | |
|-----------------------|--|
| 2002 | GPS-QZSS Technical Working Group established |
| 2003 | QZSS conceptual study phase started. |
| January 2007 | First draft of the QZSS SIS-ICD released. |
| July 2007 | COMPASS-QZSS RF compatibility coordination started |
| June 2008 | First version of QZSS SIS-ICD officially released. |
| September 2010 | First satellite namely QZS-1 (<i>Michibiki</i>) successfully launched from Tanegashima Space Centre, and positioned into quasi zenith orbit. |

Table 2-24: History timeline of QZSS.

2.2.6 CAPS

Outline. By the time when Beidou-1 was already being constituted under military management, the civilian Chinese Area Positioning System (CAPS) was initiated in 2002 from a proposal of the National Astronomical Observatories of China (NAOC) to cover the complete country territory. This regional positioning system, based on the one-way range determination method¹², is essentially based on existing communication GEO and IGSO satellites that act as transponders for the broadcasting in C-band of the signal and message uploaded from the on-ground navigation facilities.

With this disposition, degraded 3D positioning is achieved. A barometric altimeter integrated within the receiver provides an accurate estimation of the height and is considered an additional virtual satellite in the CAPS constellation. The calibration of this element is accomplished from temperature and pressure information collected all over the coverage area and embedded within the navigation message.

In this system, and in contrast with all satellite-based navigation systems reviewed so far in this document, the user receiver measures pseudoranges relative to the ground station that generates the navigation message. The pseudorange from satellite to user is obtained by applying the concept of virtual clock. The modelling of a virtual clock that could hypothetically be located on board the satellite is obtained from measurements of the round trip delay by observation of the broadcasted message from the ground station. The coefficients of this modelling are included in the navigation data message, and the virtual clock correction applied at receiver level.

Space Segment. In order to achieve reasonable values of PDOP, the initial constellation of CAPS could not be uniquely formed of GEO satellites, as all of them would be located in the same equatorial plane. In order to improve the satellite geometry in the north-south direction, a number of IGSO satellites with a ‘figure-8’ ground track were added to the system.

¹² In contrast with the two-way *Twin Star* method used in Beidou-1 (see 2.2.4).

Initial trials, reported in [Ref. 62], observed two GEO satellites at 87.5°E and 110.5°E and two decommissioned GEO drifting to SIGSO¹³, located at 134°E and 142°E. However, the final constellation is foreseen to contain 3 GEO, 3 SIGSO and 3 IGSO.

The rent of bandwidth in commercial GEO satellites is a key factor for the fast deployment and reduced initial costs of CAPS. Nevertheless, other drawbacks are derived from the same design decision. Take, for instance, the restriction of the available navigation broadcasting carriers to C-band, typically used for Space-to-Earth communication services and affected of larger rain attenuation and a tropospheric delay higher than in L-band.

Signal Characteristics. Two downlink carriers in C-band are used to broadcast navigation messages from the satellites ($C1_d$ at 4,143.15 MHz and $C2_d$ at 3,826.02 MHz), and can be combined at receiver level to reduce the ionospheric delay.

The observed signal structures in CAPS are similar to GPS. A C/A Gold code at 1.023 Mcps and a special P code at a rate of 10.23 Mcps are BPSK-modulated, and a BOC implementation is currently under implementation [Ref. 63]. The embedded data message includes information about predicted satellite ephemeris, signal transmission time and offset relative to NTSC at the Chinese Academy of Science, virtual clock parameters, local area differential corrections, integrity information regarding other GNSSs and information for the calibration of the receiver barometer.

Ground Segment. A master station in Lintong (and a backup in Xishuangbanna) coordinates the system's operation, and implements the following functionalities: (1) measurements for virtual clock characterization, (2) time reference synchronization with NTSC, (3) gathering of meteorological data from more than 1,860 weather stations over China, (4) computation of differential corrections, (5) integration of orbital determination data from 8 stations over China, (6) processing and data message configuration, and (7) RF baseband synthesis.

The upload to satellites takes place from two communication stations (located in Beijing and Xishuangbanna) through two uplink carriers in C-band ($C1_u$ at 6,368.15 MHz, $C2_u$ at 6,051.02 MHz).

Reference Systems. The CAPS time system (CAPSTS) is synchronized with UTC on midnight of December 27, 2003, and presents a constant delay of 32 s relative to IAT. Presently, CAPSTS maintains a bias equal or lower than 10 ns with UTS as maintained by NTSC at the Chinese Academy of Science.

Regarding the coordinates reference system in CAPS, it is based on an improved evolution of ITRF2000.

History Timeline. In Table 2-25, a brief history of CAPS is illustrated, here included for completeness. It is important to note that, due to the importance that COMPASS is taking in the

¹³ When station-keeping operations of a GEO satellite are ceased, its orbit experiences a drift in the north-south direction higher than in the east-west axis due to gravitational perturbations. This fact can be used for orbital conversion to SIGSO of GEO satellites decommissioned when the level of remaining fuel in the on-board tanks is low but still enough to keep the orbital position in the east-west direction. Note that this operation takes only up to 10% of the consumed fuel, while the 90% is generally invested on the station-keeping on the perpendicular direction.

GNSS international scene at the time of writing, CAPS is feared to lose priority in the budget assignments of the Chinese government for the upcoming years.

| | |
|------------------|-------------------------------------|
| 2002 | CAPS programme is initiated |
| July 2005 | First validation system constituted |

Table 2-25: History timeline of CAPS.

2.2.7 Other Systems

Besides all major global satellite navigation and positioning systems outlined above, other examples with extremely specialized applications exist. Some of them will be briefly described in this separate section as a non-exhaustive list of examples, not due to their lack of importance in the global scene but because of them not being of relevance for the purpose of the present study.

Argos. Designed as a global satellite-based location and data collection system for environmental purposes, Argos is the result of the Franco-American cooperation between CNES, NOAA and operated by CLS (*Collected Localization Satellites*). Since 2006, Eumetsat is co-operator of the system. At the time of writing, Argos instruments are flying on-board of 4 active satellites plus 1 backup, on polar orbits at 850 Km of altitude, and projecting a visibility circle on the Earth surface of around 5,000 Km of diameter. This configuration allows the Earth to be scanned several times a day, with every satellite visible during 10 minutes in average for any given beacon.

All Argos-certified transmitting platforms (characterized through a unique identifier) transmit a specific message on a stable $401.650 \text{ MHz} \pm 30 \text{ kHz}$ uplink carrier and can be as light as 20 g, in order to allow their use on live specimens. The data recorded by all satellites from beacons in view is retransmitted in L-band to nearly 50 global and regional receiving stations on cross-over, and delivered to two redundant processing centres (Washington D.C., United States and Toulouse, France), where positions are computed for every platform by processing the observed Doppler frequency shifts of the uplink carrier, and the messages are processed and classified. The resulting data is made available to registered users with a typical latency of 20 minutes.

The expected positioning error with this system is of 300 m and can be significantly reduced when GPS positioning data is embedded within the Argos message at beacon level, and decoded at the user end.

Updated information and further details relative to this system can be obtained from [Ref. 23].

COSPAS-SARSAT. Also a Doppler-based location system, COSPAS-SARSAT is a joint venture of United States, Russia, France and Canada with the single purpose to assist the location of distressed users using certified beacons. These user platforms, for aviation, marine, and personal applications, have been originally using two uplink frequencies (121.5 MHz and 406 MHz) with different associated location accuracies (13 Km and 2 Km respectively). After January 2009, however, service to 121.5 MHz must be considered discontinued and no message in this band will be processed by COSPAS-SARSAT.

The space segment of this system includes a number of LEO and GEO satellites, balanced in a trade-off between coverage (global for LEO satellites) and latency to alert (instantaneous for GEO satellites). The LEO constellation (a similar approach to Argos) is nominally composed of 4 satellites. Two of them, placed on quasi-polar orbit at 1,000 Km of altitude and equipped with SAR instrumentation, are supplied by Russia. The rest, USA-supplied, are placed in a sun-synchronous, near polar orbit at 850 Km, and equipped with SAR instruments of French and Canadian production. The GEO constellation, at the time of writing, is formed by units provided by USA, India and Eumetsat.

The SAR messages recorded and repeated by the whole constellation are received by a complete network of ground local user terminals, and transferred to Mission Control Centres that process the message content and forwards it to the Search and Rescue Point of Contact or other Mission Control Centres.

The Galileo SAR service (see 2.2.3) has been designed to enhance the performance of COSPAS-SARSAT in terms of accuracy and latency to alert also providing a downlink to distressed user as a means for signal acknowledgment. Updated information relative to this system and interesting statistics on the effectiveness of the system can be obtained from [Ref. 24].

DORIS. Developed and maintained by CNES, DORIS is a positioning and orbit determination satellite system based on the Doppler principle, like other systems here exposed. However, in this case the mode of operation has been reversed, as the satellites measures, over a short period of time, the Doppler frequency shift of a stable carrier transmitted through any of the 50 uniformly located ground beacons on 2,036.25 MHz (and 401.25 MHz, in order to remove the effect of ionospheric delay). The acquired data is accurately time-tagged and stored in an on-board memory and regularly retransmitted to the mission control centre of the system in Toulouse (France), from where it is made available to the scientific and operational community through the IDS.

Nowadays, DORIS payloads are installed in 9 satellites (Envisat, Jason-1 and 2,...) with a confirmed expansion of the system to 4 more space vehicles (Cryosat-2, Sentinel-3A,...). This configuration makes of DORIS an ideal tool for orbitographic, positioning, and Earth Observation application, among many others.

Updated information relative to this system and its applications can be obtained from [Ref. 25] and [Ref. 26].

2.3 Regional Satellite Based Augmentation Systems

In order to improve the quality of the positioning determination¹⁴ (normally in terms of both accuracy and precision) over a relatively reduced area, the navigation signal (in a general sense) can be monitored from a well known and stable position, and the error vector extracted to produce a correction that will be broadcasted and processed by augmentation-enabled receivers. This

¹⁴ Increased accuracy and precision are required for Safety-of-life applications, mainly in the transport market.

correction data will then be integrated in the user position computation to compensate for positioning errors (see Chapter 4 for details on error sources in GNSS).

This is the approach locally exploited, for instance, in DGPS, or in a broader region by SBAS. The particular architecture of every Satellite-based Augmentation Systems may vary, but the common constituent elements are (1) a network of monitoring stations spread all over the coverage area¹⁵, (2) a number of master stations that will generate the correction based on data collected by the monitoring stations, (3) one or more satellites (in general, but not necessarily with a GEO orbit) that will broadcast the augmentation data to the final users, and (4) a uniform or non-uniform data transport network that will link monitoring stations to master stations, and provide a means to uplink correction data to the satellites. The characteristics of other features (i.e. signal scheme, redundancy or availability of integrity dissemination) are particular to every system and are mainly discussed in the following for a number of present and planned regional augmentation systems providing service in several regions worldwide (see Figure 2-7).

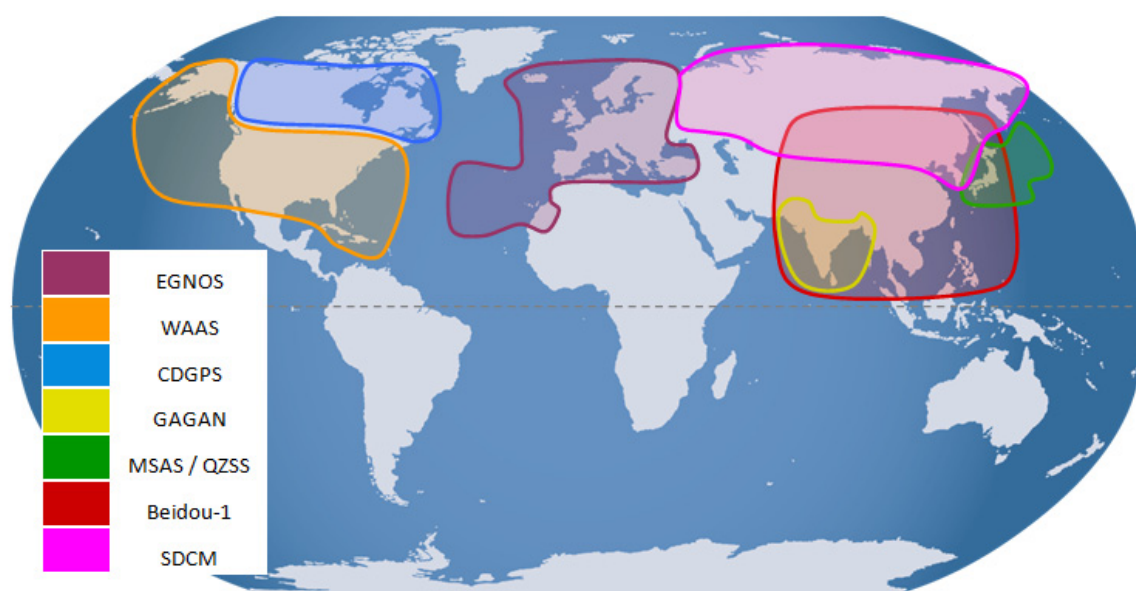


Figure 2-7: Coverage areas of a number of present and planned SBAS systems.

In order to ensure interoperability and compatibility between SBAS, ICAO has developed standards that guarantee this very same objective (see [Ref. 14], [Ref. 15] or [Ref. 16]) and to allow the combined use of different systems with minimal receiver modifications.

2.3.1 EGNOS

A resolution of the European Council signed on December 19, 1994, defined the contributions of Europe to the satellite navigation scene in two main lines of actions. In first place, this document stated the intention to contribute to GNSS-2 with an independent GNSS, named Galileo some years later (see 2.2.3 for further details). A second point of this text represented the aim to enhance GNSS-1 with a new and independent space-based augmentation, the European Geostationary Navigation

¹⁵ The coverage area of a SBAS is not defined by the area of influence of the satellites, but delimited by the location of the monitoring stations.

Overlay Service (EGNOS), jointly undertaken by the European Commission, the European Space Agency, and European Organization for the Safety of Air Navigation (Eurocontrol).

The EGNOS first signal in space was available in 2000 (4 years after the kick-off of the project), transmitted as ESTB, (EGNOS System Test Bed) and relayed from Inmarsat-3/AOR-E, a geostationary satellite situated over the Atlantic Ocean Region. The Initial Operational Capability (IOC) of the overall system was declared on July 2005 and FOC was achieved in 2007, with an expected lifetime of 20 years.

In an initial state, EGNOS is expected to cover the European Civil Aviation Conference (ECAC) area with augmentations for GPS and GLONASS. In subsequent developments, however, the provision of service will most likely be extended to Africa and East Europe countries, giving also support to GPS L5 and modernized GLONASS, and obviously to Galileo when active.

Ground Segment. Approximately 34 Receiver Integrity Monitoring Stations (RAIMs) spread all over the coverage area make observations of the GPS, GLONASS and EGNOS signal. The data collected is transferred through the EGNOS wide-area network (EWAN) to 4 Master Control Centres (MCC, one active, one as a hot backup, and 2 that will be activated only in case of catastrophic circumstances affecting the previous two). The information is then processed in the MCC and, integrity and corrections of pseudoranges, ionospheric delay models and ephemeris are determined for every satellite. The correction information is sent (again through the EWAN) to the so called Navigation Land Earth Stations (2 NLES are foreseen for every EGNOS satellite, one active and one as a backup) and uploaded from there to the space segment.

Space Segment. The augmentation data is embedded in a message frame, modulated at a rate of 250 bps onto a ranging GPS C/A-like signal, and uploaded to 3 GEO satellites (Table 2-26) that will act as relay transponders, broadcasting on L1 band. Although EGNOS is designed as a SBAS, the development by the European Space Agency of SISNeT allows the provision of highly accurate, real-time EGNOS corrections through Internet or any other means of data communication (GSM, GPRS), to enabled receivers.

| Description | PRN | Longitude |
|---------------------|-----|--|
| Inmarsat-3-F2/AOR-E | 120 | 15.5°W (East of Atlantic Ocean Region) |
| ESA Artemis | 124 | 21.5°E (Over Africa) |
| Inmarsat-3-F5/IOR-W | 126 | 25.0°E (West of Indic Ocean Region) |

Table 2-26: Detail on EGNOS Satellites.
(source [Ref. 13])

Benefits and Offered Services. Among the benefits provided by EGNOS we find the improved continuity and availability of navigation services over the EGNOS coverage area, yield by the use of GEO satellites¹⁶. Additionally, the broadcast of integrity information allows the user to discern a

¹⁶ Besides, signals received from a GEO space vehicle exhibit minimum Doppler frequency offset on the received signal, which makes acquisition and tracking easier at receiver level.

malfunction of GPS, GLONASS or EGNOS itself with a minimal latency of 6 seconds¹⁷. Finally, the use of EGNOS allows enhanced positioning accuracy of about 4 m and 6 m in the horizontal and vertical axes respectively.

Below are listed the EGNOS services available after the certification of the system, ongoing at the moment of writing.

- **EGNOS Open Service:** This service is available free of charge to all users with an EGNOS-enabled receiver within the EGNOS open service coverage area. As such, no guarantee will be given to its performance.
- **EGNOS Commercial Data Distribution Service:** For all those professional users with a need for enhanced performances, this service will be offered in a controlled basis only, through terrestrial data networks by means of SISNeT [Ref. 18].
- **EGNOS Safety-of-Life Service:** After the certification of the system for Safety of Life applications, EGNOS will offer a service liable to costs to support safety critical operations, mainly in the transport market (i.e. non-precision approach in civil aviation). The access to this service will be limited to those users with a certified receiver within the EGNOS SoL area. Service and performance guarantee in this case will be agreed between the service provider (the European Satellite Services Provider) and the final customer.

Timeline. Table 2-27 and Table 2-28 here enclosed show a high level description of the timeline of EGNOS history, from the initial kick-off of the project until its certification for SoL applications.

| | |
|----------------------|---|
| December 1994 | A resolution of the European Commission is signed, mentioning the European contribution to GNSS-1, EGNOS. |
| June 1996 | Kick-off of the development of EGNOS. |
| February 2000 | ESTB begins the transmission of experimental EGNOS SIS through Inmarsat-3-F2/AOR-E. |
| November 2003 | ESTB broadcast is switched to Inmarsat-3-F5/IOR with PRN 131. |
| May 2005 | ESTB signal transmission with PRN 131 is stopped. |
| June 2005 | ESTB signal broadcast resumed, now with PRN 120. |
| July 2005 | EGNOS enters initial operational capability. |
| June 2006 | Broadcast of ESTB signal definitively stopped. |

Table 2-27: History timeline of EGNOS (1/2).

¹⁷ At the present, it can take as long as 3 hours to declare a malfunctioning GPS satellite as 'unhealthy'. Therefore, the faster response of EGNOS introduces additional positioning confidence.

| | |
|---------------------|---|
| 2007 | EGNOS full operational capability achieved. |
| 2008 | Certification of EGNOS for Safety of Life applications. |
| April 2009 | EGNOS ownership transferred to the European Commission. |
| October 2009 | EGNOS Open Service made available. |
| 2010 | EGNOS SoL and Commercial services expected to be available. |

Table 2-28: History timeline of EGNOS (2/2).

2.3.2 WAAS

The development of the Wide-Area Augmentation System started in 1994, as a joint venture of the United States Department of Transport (USDOT) and the Federal Aviation Administration (FAA), to obtain a suitable system to support precision flight approach operations over US continental territory¹⁸ with performances comparable to the traditional category 1 ILS scheme¹⁹. As the exclusive use of GPS was not meeting aviation requirements for integrity, accuracy, and availability for this kind of operations, FAA considered a SBAS that could broadcast augmentation and integrity information over a wide area. This consideration led to the design and commission of WAAS, the first space-based augmentation system developed throughout the world²⁰. FOC of WAAS was already reached in late 2008.

Ground Segment. Information about the quality of the GPS positioning is collected by 38 Wide-area Reference Stations (WRS) of precisely surveyed position. All data is then transferred via a terrestrial network to two WAAS master stations or WMS (one on every coast) where the correction is computed (to counteract the effect of atmospheric and ionospheric delays, and orbit and on-board clock drifts) and the augmentation data message generated. The correction message is then embedded in a GPS-like signal and uplinked to the satellites of the system for its broadcast to the user segment.

Space Segment. WAAS's space segment is currently formed by two GEO satellites with navigation payloads in GPS L1 and L5 bands used as transponders (one of them in test mode at the time of writing). The system was formerly constituted with two Inmarsat-3 space vehicles that ceased WAAS transmissions in 2007 due to the end of the Inmarsat lease contract. In the present, and under a FAA's contract with Lockheed Martin, two new GEO satellites have been provided with PRN 135 and 138, to support the system (see Table 2-29 for details).

WAAS History Timeline. The evolution of WAAS is summarized in Table 2-30. It is interesting to note here that the service provided by WAAS at the present is evolving towards a global coverage in its next phase of deployment as Global Navigation Satellite System Landing System (GLS). GLS is expected to be operational coinciding with the FOC of GPS III, giving to GLS additional measures against natural and artificial interferences [Ref. 17].

¹⁸ The coverage of WAAS has been extended, at the time of writing, to Alaska, Canada, Hawaii, Mexico and Puerto Rico.

¹⁹ WAAS is not achieving accuracies comparable to category 2 and 3 ILS, for which it needs to be complemented with a local area augmentation system (LAAS)

²⁰ In fact, the scheme of WAAS is used as a case for development of present and planned SBAS systems.

| Description | PRN | Longitude |
|---------------------|-----|-----------------------------------|
| Inmarsat-3-F3/POR | 134 | 178°E (Ceased WAAS transmissions) |
| Inmarsat-3-F4/AOR-W | 122 | 142°W (Ceased WAAS transmissions) |
| Intelsat Galaxy XV | 135 | 133°W |
| Telesat Anik-F1R | 138 | 107.3°W |
| Inmarsat-4-F3 | 133 | 98°W (Currently under test) |

Table 2-29: Detail on WAAS space segment.

| | |
|-----------------------|--|
| 1994 | WAAS development starts. |
| December 1996 | Inmarsat-3-F3 launched from Kourou Space Centre. |
| June 1997 | Inmarsat-3-F4 launched from Kourou Space Centre. |
| December 1999 | First WAAS transmitted, for experimentation purposes only. |
| August 2000 | WAAS signal made available for non safety-of-life applications. |
| July 2003 | WAAS is authorized by FAA for aviation use. |
| June 2005 | First international WRS installed in Canada. |
| September 2005 | Telesat's Anik-F1R launched from Baikonur Cosmodrome. |
| October 2005 | Intelsat Galaxy XV launched from Kourou Space Centre. |
| July 2007 | Inmarsat-3-F3 and F4 cease to broadcast WAAS signal. Service now switched to Galaxy XV and Anik-F1R. |
| September 2007 | WAAS service officially available in Canada and Mexico. |
| January 2008 | FOC of WAAS reached. |
| August 2008 | Inmarsat-4-F3 launched from Baikonur Cosmodrome. |
| September 2008 | Navigation data from Galaxy XV and Anik-F1R flagged as suitable for precision approach. |
| April 2010 | Loss of control of Intelsat Galaxy XV confirmed by Intelsat S.A. |
| March 2010 | Inmarsat-4-F3 starts WAAS transmission in test mode. |
| 2013 | Next generation of WAAS, referred as GNSS Landing System (GLS) available, scheduled to coincide with the FOC of GPS III. |

Table 2-30: History timeline of WAAS.

2.3.3 MSAS

Based on the WAAS system scheme, MSAS was developed by the Japan Civil Aviation Bureau (JCAB) to augment the GPS performance for civil aviation use on non-precision approach operations²¹ over the Japanese airspace.

Ground Segment. The scheme of the MSAS's ground segment is very similar to the one observed in WAAS and EGNOS, but with some particularities. GPS survey data collected by four Ground Monitoring Stations (GMS) spread over Japan domestic territory (in Sapporo, Tokyo, Fukuoka, and Naha), plus two Monitoring and Ranging Stations (MRS) in Hawaii and Canberra, is continuously delivered to two Master Control Stations (MCS) in Kobe and Hitachiota for its processing.

Space Segment. The augmentation data is then modulated in GPS-like signals and uplinked on Ku-band from the MCSs to two redundant MTSAT satellites in GEO orbit (from the MCS in Kobe to MTSAT-1R, and from the MCS in Hitachiota to MTSAT-2), in which one of the payloads is dedicated to the broadcast of MSAS augmentation signal in L1 to users in the area of coverage of the system²². By 2008, the specified augmentation signal is foreseen to broadcast on 1,575.45 MHz, with a bandwidth of 2.2 MHz and with a data rate of 500 bps (FEC code included). The signal is expected to be received on-ground with a minimum power of -161 dBW [Ref. 19].

| Description | PRN | Longitude |
|-------------|-----|-----------|
| MTSAT-1R | 129 | 140°E |
| MTSAT-2 | 137 | 145°E |

Table 2-31: Detail on MSAS space segment.

Once more, in MSAS increased reliability and continuity of service is given to the system by design through redundancy of key elements. In this sense, it is foreseen that, if either one of the uplink stations or satellites suffers from failure, the other branch of the system takes over, transmitting signal on both PRN [Ref. 19].

Time History. A brief history is displayed in Table 2-32, given the short time MSAS project has been ongoing and the classified nature of the related information.

| | |
|-----------------------|---|
| February 2005 | MTSAT-1R launched from Tanegashima Space Centre |
| February 2006 | MTSAT-2 launched from Tanegashima Space Centre |
| September 2007 | MSAS is certified for aviation use. |
| 2015 | EOL estimated for MTSAT-1R |
| 2016 | EOL estimated for MTSAT-2 |

Table 2-32: History timeline of MSAS.

²¹ Plans to improve MSAS performance for its use on precision approach phase are undergoing [Ref. 19].

²² As shown in Figure 2-7, the coverage area of MSAS includes the Japanese FIRs (Flight Information Regions). Note that this is only a portion of the actual coverage of MTSAT satellites.

2.3.4 GAGAN, towards IRNSS

The GPS Aided, Geo-Augmented Navigation (GAGAN) Program is currently under development by the Union Ministry of Civil Aviation with support from the Indian Space Research Organization (ISRO) and in close collaboration with the Department of Defence of the United States to ensure compatibility with GPS and WAAS²³. This system intends to provide GPS augmentation over the region between EGNOS and MSAS coverage areas to be used within Indian aerospace.

Ground Segment. The installation of eight networked Reference Stations (INRES) evenly distributed over Indian territory have been foreseen at Delhi, Ahmedabad, Calcutta, Jammu, Portblair, Guwahati, Trivendrum and Bangalore, where also the Master Control Station (INMCS) and the uplink station (INLUS) of the system will be located.

| Description | PRN | Longitude |
|-------------|-----|--------------------|
| GSAT-4 | 127 | 82°E (tentatively) |
| GSAT-8 | 128 | 55°W (tentatively) |

Table 2-33: Detail on GAGAN space segment.

Space Segment. The augmentation signal will be broadcasted by two GEO satellites (GSAT-4 and GSAT-8), most likely positioned between 82°E and 55°E [Ref. 27]. A third satellite, code name GSAT-10, would be added to the constellation as an in-orbit back-up.

Time History. The joint table provides an overview of the project schedule, as seen by the author of [Ref. 27].

| | |
|---------------------------------------|---|
| September 2008 | Indian government approves the implementation of GAGAN. |
| April 2010 | Failure of the launching vehicle carrying GSAT-4, with on-board GAGAN payload. |
| Last quarter of 2010 (delayed) | GSAT-8 originally scheduled to launch with on-board GAGAN payload. This milestone was delayed due to the GSAT-4 launching failure. |
| 2011 (delayed) | GSAT-10 originally scheduled to launch, and positioned as in-orbit spare. This milestone was delayed due to the GSAT-4 launching failure. |
| 2012 (delayed) | Foreseen FOC of GAGAN. This milestone was delayed due to the GSAT-4 launching failure. |

Table 2-34: History timeline of GAGAN.

A Brief Glimpse into IRNSS. According to [Ref. 27] the lessons learned from GAGAN are enabling India to develop the Indian Regional Navigation Satellite System, with a nominal constellation of seven to nine GEO and non-GEO satellites. Open and restricted services would be provided on L- and S-bands, with modulation schemes most likely based on GPS L2C, L5 and L1C.

²³ Compatibility with Galileo, EGNOS, MSAS is equally being considered.

2.3.5 SDCM

At the time of writing, and as part of the GLONASS refurbishment, a SBAS support system is under preparation as a counterpart of EGNOS or WAAS, to give coverage to the Russian federation territory.

According to preliminary details made public by Sergey Revnivykh (Deputy General Director of the Central Research Institute for Machine Building) on December 2008 during the 3rd meeting of the International Committee on GNSS (ICG) [Ref. 49], SDCM is meant to provide integrity monitoring of GPS and GLONASS satellites, and real time differential corrections for GLONASS, providing positioning accuracies of up to 1.5 m and 3 m respectively on the horizontal and vertical axes, plus high precision positioning at centimetre level (2 and 6 cm on horizontal and vertical axes) within the 200 Km area around every ground reference station.

Ground Segment. Presently, the designed augmentation ground structure consists on a dozen of monitoring stations distributed all over the Russian federation territory (Moscow, Pulkovo, Norilsk, Irkutsk, ...) currently under test since 2007, and a dozen more to come to complete the coverage. Following an approach similar to all the augmentation systems here reviewed, all monitoring stations are linked to one or two redundant central processing facilities and the computed corrections uploaded to the space segment from several uplink stations.

Space Segment. According to [Ref. 49], the space segment of SDCM will be composed of three GEO satellites, Luch-5A, 5B and 4, respectively situated at 16°W, and 95°E and 167°E, to support the broadcast of the correction signals over the coverage area of the system.

| Description | Longitude |
|-------------|-----------|
| Luch-5A | 16°W |
| Luch-5B | 95°E |
| Luch-4 | 167°E |

Table 2-35: Detail on SDCM space segment.

Time History. Due to scarce details available at the time of writing, the timeline of SDCM is difficult to determine. However, Table 2-36 summarizes the most relevant moments of the SDCM history presently known.

| | |
|-------------|--|
| 2007 | Test of preliminary SDCM ground monitoring network starts. |
| 2011 | Luch-5A scheduled to be launched with on-board SDCM payload. |
| 2012 | Luch-5B scheduled to be launched with on-board SDCM payload. |
| 2013 | Luch-4 scheduled to be launched with on-board SDCM payload. |

Table 2-36: History timeline of SDCM.

2.4 Chapter Summary

This second chapter has been committed to the consolidation of the reference future multisystem scenario (briefly introduced in the preface of Chapter 1) which will be taken as a pivotal point for all developments in this document. To this respect, this chapter has presented an exhaustive list of existing and planned satellite-based positioning and augmentation systems with global or regional extent. This list is providing, already at this point in the document, a clear idea of the high complexity that future compatibility and interoperability studies will show.

Note that this chapter is mainly meant to provide support to subsequent sections. Therefore, and due to the practical approach selected by the author of this study for the drawing of all conclusions, the presentation of technical aspects concerning the constellation orbital parameters, the signal definitions, and the received power levels for all relevant systems have been considered a priority.

CHAPTER 3

THE GNSS RECEIVER

3.1 Preface

Among the main tasks to be performed by a GNSS receiver, the acquisition and tracking of the weak received signals, the bit synchronization and navigation data bit extraction are the most important. Additionally, depending on its applications, a GNSS receiver must implement other features, i.e. mitigation measures against multipath, interference and/or intentional jamming, or integration of other sources of data for assisted navigation.

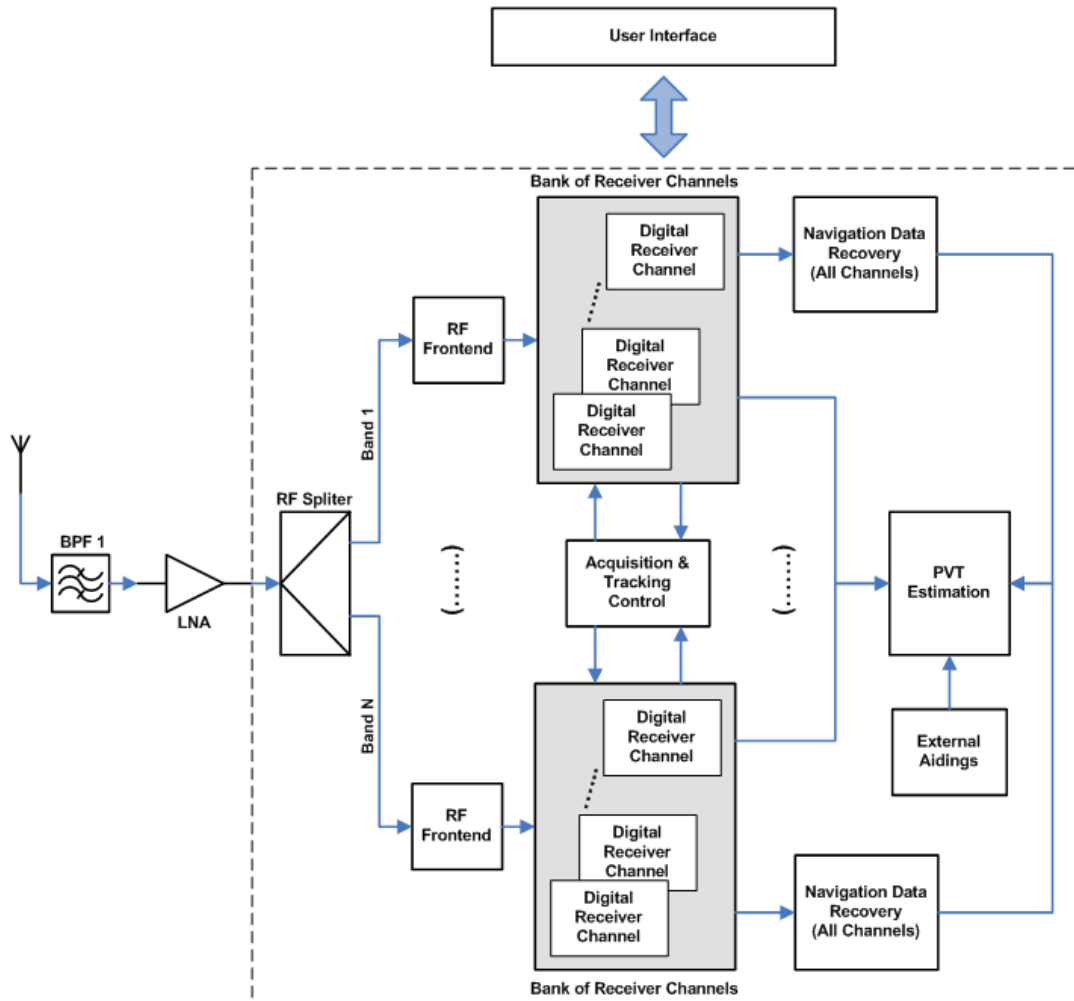


Figure 3-1: Functional scheme of a multifrequency GNSS receiver.

In this chapter, a functional description of the GNSS receiver structure is given, increasing the level of detail down to component level when required for the sake of conciseness. The inputs given here will be used to support further explanations in subsequent chapters, understanding in all circumstances that the material given here is valid not only for L-band positioning signals but can also be considered for S- and C-band future navigation signals foreseen for Galileo, for instance. Obviously, even though the kernel of the receiver can be considered valid in all cases, the pertinent redevelopments will be required for bands other than L, especially in the antenna, RF and IF sections, and most likely in the application section of the receiver. These modifications are explicitly excluded from this chapter.

As the structure of a GNSS receiver is highly dependent on the application, it is extremely complex to come up with a generic model to support the analysis in this chapter. However, the functional scheme in Figure 3-1, corresponding to a multifrequency GNSS receiver²⁴, seems to be the most appropriate for this matter. However, for practical reasons, the functional behaviour of such a specialized receiver will be equivalently explained from Figure 3-2, which depicts a single frequency GNSS receiver and basically obtained from one of the RF branches of Figure 3-1.

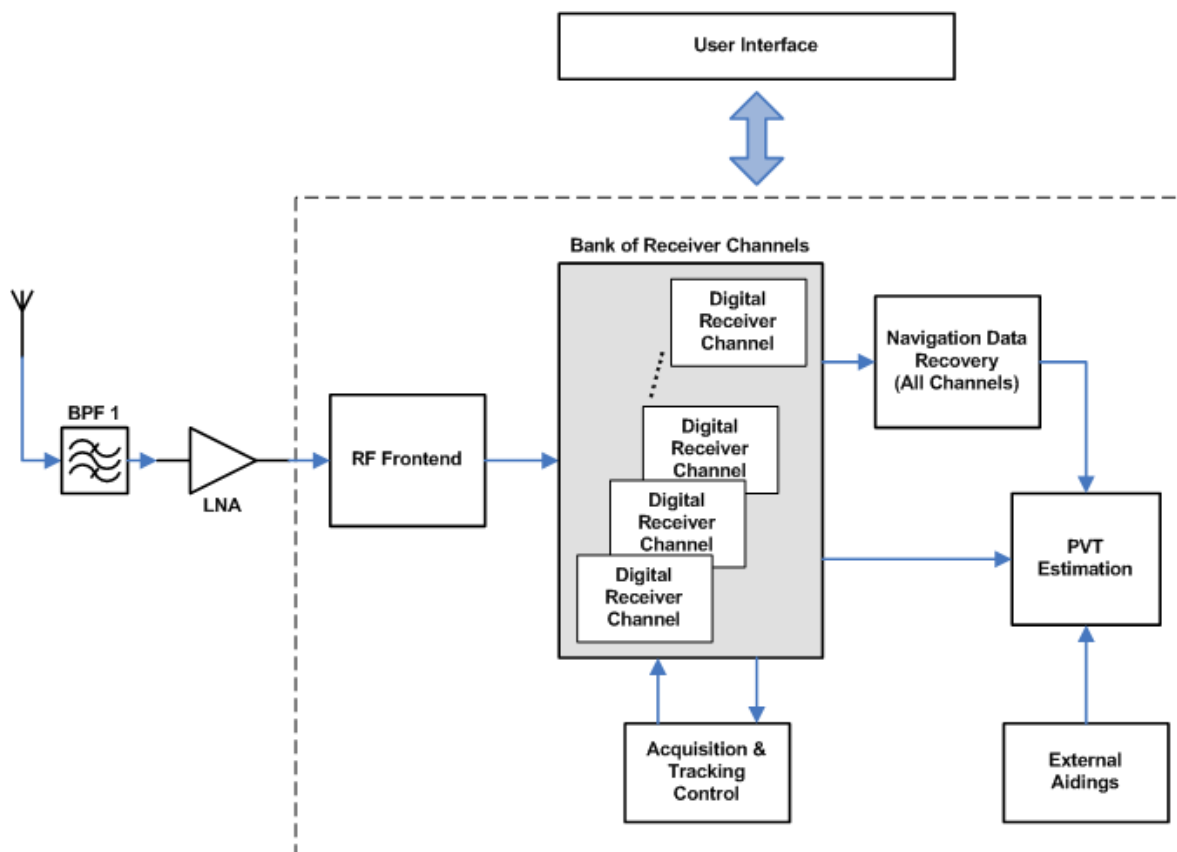


Figure 3-2: Functional scheme of a single frequency GNSS receiver.

²⁴ Multifrequency receivers are employed in high accuracy applications, mainly to minimize the impact of the ionospheric delay on the estimated satellite-to-user pseudorange by receiving signals on two or more frequencies. This procedure is extensively treated in the classic literature and will not be reproduced here.

As an outline, the receiver here exposed is used to acquire and track the navigation signals broadcasted by all different navigation satellites in view from the user position. A series of derived parameters from every tracked satellite such as the code delay and the carrier phase observations are then combined by the application module of the receiver with the demodulated navigation data from every channel in order to estimate the PVT solution for the user location.

Given a particular user position, the radiated power from all visible satellites propagates through the space and the atmosphere, and is collected by the antenna by inducing a combined voltage signal between its terminals. This extremely weak received RF signal is then adequately band-pass filtered (with bandwidth BW_{RF} centred on f_{RF}) and amplified to be ready for its down conversion to an intermediate frequency f_{IF} more appropriate for its analog-to-digital transformation. The digitalized data is then transferred to a bank of digital receiver channels that will separately acquire and track a number of code multiplexed signals under the management of a control unit responding to the state diagram depicted in Figure 3-3, which applies in general for every digital receiver channel.

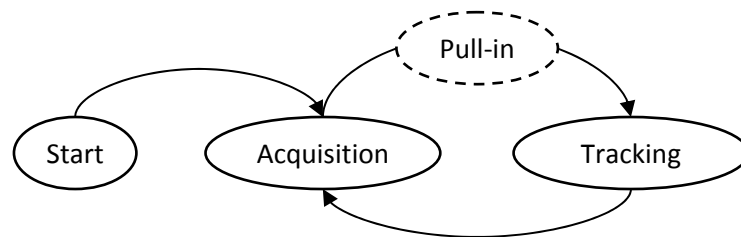


Figure 3-3: State machine describing the behaviour of the receiver controller.

Once the signal from a particular space vehicle is identified, coarse estimations of code delay and carrier phase are feed to a free tracking channel in the so called ‘pull-in’ transition phase. These preliminary estimations are used to initialize the local code and carrier generators to effectively track the received spreading code and Doppler frequency shift from this particular satellite. During tracking, the navigation data is recovered and combined with the output of other locked channels or external aiding data (such as inertial systems) to estimate the position and velocity of the receiver user. These data are then passed to the operator and application interface for their post processing or representation in a graphical user interface.

Traditionally, GNSS receivers have presented a well defined hardware-to-software balance in their implementation, with a clear predominance of hardware within the RF frontend and of software in the definition of user interfaces. However, a diffuse agglomerate of technologies have been used in the past within the digital receiver channel, in which critical sections in terms of processing runtime have been deployed on ASIC or FPGA, or even DSPs.

Despite the past tendency, the evolution of RF technology is drifting the fuzzy division line towards the antenna, bringing the software into the RF frontend for mass market production receivers, and thus providing a more cost effective solution reconfigurable at all levels.

3.2 The Navigation Signal

Before going deeper into the GNSS receiver structure and functional blocks, we should develop further to determine the structure of the signal compound obtained at the receiver antenna output, for a receiver in a multi-constellation scenario. For this matter, let us start by considering one single arbitrary target constellation of satellites, each one transmitting a multi-component signal per frequency band allocated to this particular GNSS. Then, equation 3-1 represents, in the time domain, the navigation signal modulated with power P_{ij}^{Tx} (measured at the satellite antenna input) on a defined carrier frequency f_c , and transmitted by the i -th space vehicle of the constellation, on its j -th component.

$$s_{ij}^{Tx}(t) = (\sqrt{2P_{ij}^{Tx}}) \cdot c_{ij}(t) \cdot d_{ij}(t) \cdot \cos(2\pi f_c t) \quad 3-1$$

In equation 3-1, $d_{ij}(t)$ is the navigation message embedded within the signal with data rate $1/T_d$ and data pulse shape $p_j(t)$, and $c_{ij}(t)$ is the spreading code sequence (shaped through the pulse $g_j(t)$) for the i -th satellite, on the j -th signal component, of chipping rate $1/T_c$ and time duration T_d limited by the window $w_{T_d}(t)$ (assuming T_d/T_c an integer).

$$c_{ij}(t) = w_{T_d}(t) \cdot \sum_k c_{ijk} \cdot g_j(t - k \cdot T_c) \quad 3-2$$

$$d_{ij}(t) = \sum_k d_{ijk} \cdot p_j(t - k \cdot T) \quad 3-3$$

At this point, any satellite payload impairment or non-linearity will result in a spectrum of the transmitted signal with distorted bandwidth or symmetry relative to the carrier frequency.

Following the notation introduced above, the expression for the j -th signal component received at the u -th user location, from the i -th satellite, with power P_{iju}^{Rx} measured at the output of the user receiver antenna is as presented in equation 3-4, with τ_{iu} the time delay due to the signal propagation towards the user and other errors specified in Chapter 4, f_{iu} the Doppler carrier phase shift introduced by the relative dynamics of the i -th satellite and receiver, and θ_{oi} the initial phase of the j -th satellite on-board frequency reference.

$$s_{iju}^{Rx}(t) = (\sqrt{2P_{iju}^{Rx}}) \cdot c_{ij}(t - \tau_{iu}) \cdot d_{ij}(t - \tau_{iu}) \cdot \cos(2\pi \cdot (f_c + f_{iu}) \cdot (t - \tau_{iu}) + \theta_{oi}) \quad 3-4$$

3.3 The User Antenna

In the main part of GNSS applications, the quality of the positioning is directly related to the electromagnetic characteristics of the reception antenna at the user's end. The position determined by a navigation receiver is not that of the location of the receiver itself, but the position of the

antenna phase centre, defined as the point in space in the proximities of the antenna for which the electromagnetic field of the incident signal exactly matches the signal at the output of antenna terminals²⁵. Consequently, for high accuracy applications, a precise knowledge of the position of the antenna phase centre (a function of the direction of arrival of every signal, among other parameters) is crucial, and achievable by means of calibration or the use of differential strategies.

The antenna in use is also an important factor with effect on the number of visible satellites from a particular user position, for it is not only a function of the user position itself but also of the antenna radiation pattern (generally given with dependency on elevation and azimuth) and its polarization adaptation. Other factors apply, such as the sensitivity of the receiver that is mainly driven by its noise figure (effectively established by the characteristics of the LNA of the active antenna, or by first stages of the RF frontend in case of a passive antenna).

For marine or aeronautical applications, the gain of the antenna is extended to cover the upper and lower hemispheres to compensate for the dynamics of the user vehicle on all its axes. However, for other applications where the user is static or its dynamics allows constant pitch and roll, the antenna radiation pattern is designed with revolution symmetry relative to the zenith-nadir axis, and to concentrate its gain to the upper hemisphere (or above a predefined elevation masking angle), and thus rejecting in some measure multipath reflected rays and low elevation ground-based interference signals. A similar principle is exploited through multibeam antennas, which provide the means to dynamically steer the position of gain nulls of their reception pattern towards the direction of maximal interfering radiation sources and most likely directions of arrival of NLOS rays (given the position of the user and the structure of its surroundings).

Additional (although not complete) rejection of multipath effects is provided when the antenna is designed with low gain at LHCP and targeted to RHCP signals, since GNSS are generally RHCP²⁶ and signals other than LOS rays may suffer polarization rotation when reflected. Moreover, due to atmospheric effects the polarization of the received signal is not purely circular but slightly elliptic, a loss factor L_{pol} must be considered in the link budget to account for polarization mismatches.

With all considerations exposed above, the received power at the antenna output can be computed through the link budget as in equation 3-5 (all values in linear units), where $G_{ij}^{Tx}(\theta_{iu})$ is the antenna gain of the i -th satellite towards the user, $G_{ju}^{Rx}(\theta_{ui})$ the antenna gain of the user receiver towards the i -th satellite. For all development below, an active antenna with an LNA of gain G_u^{LNA} and complementary band-pass filtering will be considered part of this functional block, without loss of generality.

²⁵ Equivalently, the phase centre of an antenna is the point in space that closer approximates the centre of curvature of the radiating waveform [Ref. 46].

²⁶ Even though the production of linearly polarized antennas is easier and more cost effective, circularly polarized antennas are selected for GNSS applications in order to eliminate the need for an exact orientation of transmission and reception antennas for optimal reception conditions. For further argumentation, note that the optimal orientation does not only depend on the relative geometric disposition of the antennas, but also on the effect of the ionosphere on the polarization plane of the transionospheric signal.

In the link budget, also a loss factor L_{iu} will be considered to account for the free space propagation through the satellite-to-receiver range d_{iu} (see equation 3-6), and L_{other} to include losses related to the signal propagation through the atmospheric layers, foliage, vegetation and building penetration, and even internal receiver losses induced by its implementation.

$$P_{iju}^{Rx} = P_{ij}^{Tx} \cdot G_{ij}^{Tx}(\theta_{iu}) \cdot \left(\frac{1}{L_{iu}} \right) \cdot G_{ju}^{Rx}(\theta_{ui}) \cdot G_u^{LNA} \quad 3-5$$

$$L_{iu} = \left(\frac{4\pi \cdot d_{iu} \cdot f_c}{c} \right)^2 \cdot L_{other} \quad 3-6$$

Now, if we expand the scenario initiated in section 3.1 to consider an arbitrary number N_C of satellite constellations, and assume that the geographical position of the receiver at a given instant allows the visibility of N_n^{vis} satellites from the n -th constellation, the compound signal present at the output of the antenna can be described, for every particular signal component, as the addition of

$N^{vis} = \sum_{n=1}^{N_C} N_n^{vis}$ contributions from GNSS satellites (see equation 3-7).

$$S_j^{Rx}(t) = \sum_{k=1}^{N_C} \sum_{i=1}^{N_k^{vis}} S_{ijk}^{Rx}(t) \quad 3-7$$

For a single frequency band, then, with a number N_{Comp} of signal components received from all constellations in this band, equation 3-8 represents the most generalist form of the voltage signal measured at the antenna output terminal.

$$S^{Rx}(t) = \sum_{j=1}^{N_{Comp}} \sum_{k=1}^{N_C} \sum_{i=1}^{N_k^{vis}} S_{ijk}^{Rx}(t) + \sum_{m=1}^{N_{pulsed}^{vis}} i_m^{pulsed}(t) + \sum_{p=1}^{N_{non-pulsed}^{vis}} i_p^{non-pulsed}(t) + n(t) \quad 3-8$$

Note in the representation above the inclusion of a number of external interfering sources of different nature, the received power from which is already affected by the receiver antenna gain towards its direction of arrival. And obviously, a level of noise that can be considered originated from the receiver's environment and the electronic components of the signal preconditioning analog stages (in case an active antenna is in use, with integrated band-pass filter and LNA). Noise at this stage can be considered Additive White and Gaussian (AWGN) on the bandwidth of the signal of interest, by definition of zero-mean and variance σ_n^2 . For the convenience of the development in this chapter, $\sigma_n^2 = 1$ is assumed, and the amplitude of signals received from satellites are chosen according to the value of C/N_0 at every point of the receiver signal flow.

Given the extremely low power of GNSS signals received by users on the Earth surface²⁷ and the fact that interferences can be several orders of magnitude more powerful than these signals, special care must be taken at receiver level to guard the integrity of the receiver. The implementation of protection measures within the RF-frontend of the receiver against saturation and overload is therefore necessary, together with the study of the effect of such non-desired signals on the acquisition and tracking performance and on the quality of the navigation solution²⁸.

3.4 The RF Frontend

The output of the antenna is delivered to one RF frontend per every band of interest, and the GNSS signal is brought through several processing stages to condition it for the baseband acquisition and tracking. Special attention must be paid to the design and component selection of this section, as it effectively sets the noise figure of the whole receiver (according to the Friis formula for noise figure [Ref. 67]) and consequently its sensitivity and the C/N_0 of the received RF signal. The C/N_0 of the down-converted signal in Figure 3-4, as it will be discussed in the following sections, will be one of the performance drivers of the receiver in both tracking and acquisition operation modes.

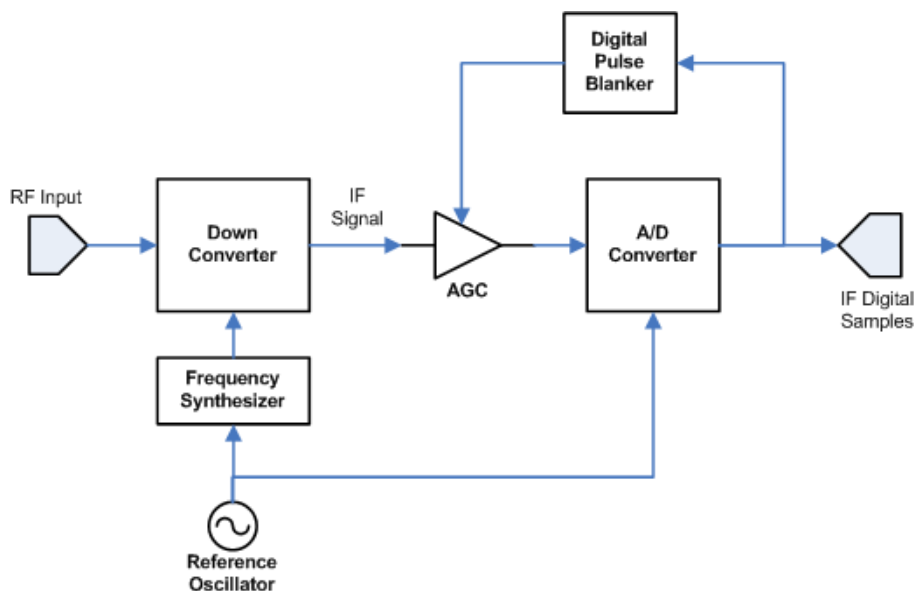


Figure 3-4: Functional scheme of the RF frontend.

The compound signal at the output of the active antenna (described in equation 3-8) is then conducted to the down-conversion stage (see Figure 3-4), in which $s^{Rx}(t)$ is down-converted to an intermediate frequency f_{IF} and conditioned to be then converted into the digital domain. Nowadays, to this very same regard, extensive research is being conducted in the field of software receivers to make of the direct RF sampling a reality. Although the present technology already supports the direct analog-to-digital conversion and processing of signals in L-band, the associated band-pass filters require high quality factors that are not practical. As an instance, the direct

²⁷ Rated, for instance, not greater than -154 dBW for GPS L1C [Ref. 4]. For additional values, see Chapter 2.

²⁸ Extensive developments have already been made to this respect in the available literature (take [Ref. 29], [Ref. 33] or [Ref. 35] for instance) and will not be reproduced here.

sampling of GPS L1 C/A would require band-pass filters with a Q factor higher than 700 in order to avoid a degraded C/N_0 .

At this point, as discussed in [Ref. 31], a pulse blanker (or a structure with similar purpose) is included in order to mitigate the effect of pulsed interferences. The combined band-pass filtering effect of the RF frontend, symbolized as an impulse response $h_{RF}(t)$ or a transfer function $H_{RF}(f)$ is considered in here as obtained from the contribution of the antenna LNA and the RF frontend itself, as the most representative factors. B_{RF} is taken as the 3 dB bandwidth²⁹ of $H_{RF}(f)$, and f_S as the sampling frequency used within the ADC. Note here that, for compliance with the Nyquist-Shannon Sampling Theorem, the relationship $f_S \geq 2 \cdot (f_{IF} + B_{RF} / 2)$ must be fulfilled.

3.5 *The Baseband Receiver Channel*

In order to analyze the elements of the complex signal at the output of the RF frontend, from now on in this chapter (unless otherwise noted), we will focus our attention to a single baseband processing arm targeted to acquire and track the j -th signal component from a single satellite in a particular GNSS constellation. In this simplified scenario, the voltage described in equation 3-8 can be considered the addition of the following components, classified for compliance with [Ref. 30]:

- The j -th signal component received from the target satellite.
- Other visible satellites in the target constellation transmitting the same desired signal component (obviously with different spreading codes), in order to account for the finite code isolation between different PRN.
- Other navigation signal components transmitted in the same band of interest by all visible satellites orbiting the target GNSS constellation.
- Other navigation signal components transmitted in the same band of interest by all visible satellites orbiting a constellation not belonging to the target system.
- Pulsed and non-pulsed, non-GNSS signals transmitted in the frequency band of the desired signal component, and extensively studied in Chapter 4.

In the conditions described by the expression in 3-7, a single frequency, single component navigation receiver specifically designed for operation on the n -th constellation is to independently and simultaneously acquire and track the maximum number of visible satellites (ideally, all of them) in order to combine their observables into the PVT solution. For this purpose, a sufficient number of channels or baseband processing arms are to be enabled within the device, after the down-conversion stage, to fulfil the processing requirements presented above.

²⁹ By design, B_{RF} must be sufficient to minimize the distortion on the received spread spectrum signal. Note that the bandwidth of the received compound signal will be a function of the spreading code rate used in every signal [Ref. 32].

3.5.1 The Satellite Acquisition Phase

During the acquisition phase, the receiver searches within the received compound signal for all satellites from the n -th constellation that are in view. This is a 3-dimensional search process in which all (or a reduced set of) PRN codes assigned to the n -th constellation are sequentially applied to the received signal with a range of expected code and carrier phases explored to maximize the cross-correlation. An extensive description of several classic acquisition techniques applied to CDMA systems is available from [Ref. 9] and [Ref. 47]. These will not be reproduced here, as the acquisition operation is not within the focus of this thesis.

Through pull-in, the local code replica generator of a number of available baseband channels are initialized with the PRN codes of the identified space vehicles, and the corresponding code delay and carrier phase tracking loops fed with coarse initial estimations of code and carrier phases for their posterior tracking.

With no previous knowledge, the search process of satellites in view is a highly time consuming operation. In order to ease the acquisition, in the memory of every GNSS navigation receiver several information points are internally stored: the set of visible satellites and their almanacs, the disseminated time, and the previously computed user position. Depending on the validity and/or availability of these sets of data, this mode of operation and its duration can vary:

- **Cold start:** In this state, the receiver assumes that either some or all of the stored data is not valid or unavailable, and performs an exhaustive search through all spreading codes reserved for the n -th constellation in an attempt to identify the PRN of visible satellites and initialize the tracking loops for code delay and carrier phase. This mode is in general the most time-consuming, and can be sensibly reduced by enabling the receiver to obtain valid sets of almanacs for visible satellites from other sources than the satellites themselves. Alternative means include for instance GSM/GPRS as in AGPS, after the coarse triangulation of the user location within the mobile telephony network.
- **Warm start:** If the internal memory of the device does not contain information about the set of visible satellites (or it is out of date), but remembers its previously calculated position, almanacs and time, the receiver intends to use this partial information to identify which satellites are visible in the sky and initiate the tracking process. This mode takes generally less time than the previous state.
- **Hot start:** In this case, the receiver has available a precise knowledge of valid almanacs, time, and position, information that is used to initialize the receiver channels for all visible satellites. Clearly, this is the fastest acquisition mode.

The acquisition process is periodically repeated in order to update the set of visible satellites, and to enable the tracking of the maximum amount of space vehicles at every time. Therefore, the state diagram depicted in Figure 3-3 must be considered dynamic, this is, frequent state jumps may occur, and acquisition and tracking modes can take place simultaneously in different baseband channels.

3.5.2 The Carrier and Code Tracking Operation

Once a set of visible satellites has been acquired, every one of them is then independently tracked. The temporal evolution of code delay and carrier phase of every target satellite are extracted and transferred to the microprocessor of the receiver, which will compute the evolution of the range and the user velocity relative to the target satellite. These quantities are also used for complete and accurate spreading code and carrier removal from the received signals in order to enable the optimal demodulation of the embedded navigation data frame.

The satellites obtained after the acquisition process, coarsely characterized in terms of initial code delay (τ_{0L}) and carrier phase (ϕ_{0L}), are pulled into the tracking channels to follow the evolution of the carrier phase and code delay of the received signals from each of the acquired space vehicles.

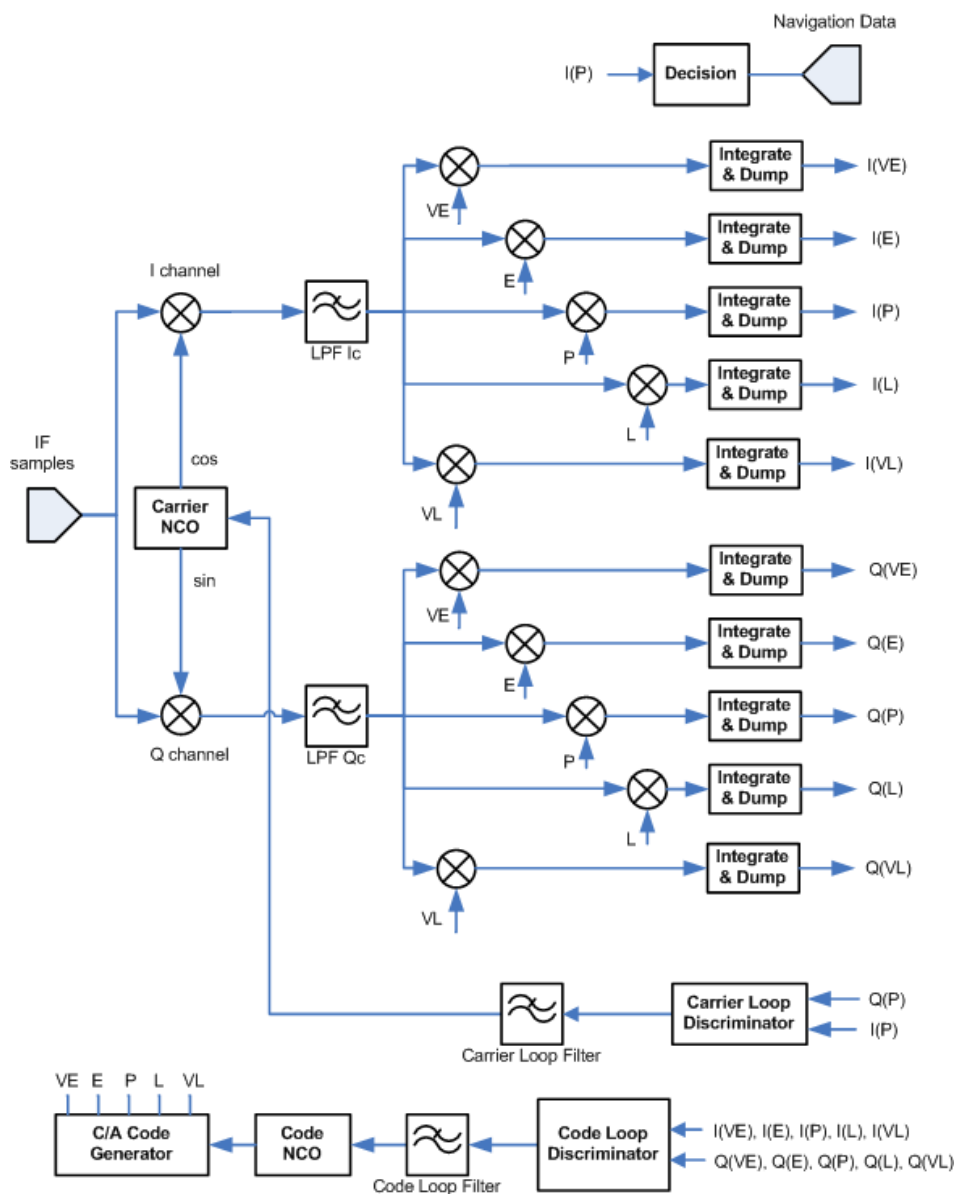


Figure 3-5: Typical structure of a high resolution GNSS receiver channel.

During the tracking stage of a particular channel, the carrier phase (ϕ_L) and the code delay (τ_L) of the locally generated replicas are matched to the respective parameters of the received signal from a particular satellite (ϕ_{Rx}, τ_{Rx}), and followed in closed loop over time through a classical GNSS tracking structure. Figure 3-5, to this respect, serves to exemplify both code and carrier phase tracking loops implementing a 5-correlator HRC (High Resolution Correlator) approach. A statistical characterization of the TOA estimation provided by this classical structure is available in the relevant literature. Take, for instance, [Ref. 58] and [Ref. 59] where Betz and Kolodziejewski develop on the theoretical CRLB of the code delay estimation jitter for coherent and noncoherent operations, in presence of AWG noise and interferences. Additionally, in [Ref. 34] Holmes provides a refined theory accounting for frontend-related impairments and their effect on the TOA tracking performance.

Essentially, the goal of the code and carrier closed loops in tracking is to minimize the errors $\Delta\phi = \phi_{Rx} - \phi_L$ and $\Delta\tau = \tau_{Rx} - \tau_L$. These error quantities are typically estimated from the output of a reduced number of integrators that complete the signal correlation with delayed copies of the locally generated spreading code. Generally, the discrimination of $\Delta\tau$ is performed following an Early-Late approach, by combining signals from the output of three or five correlators (see Table 3-1 for some examples).

| Name | Number of correlators | Discriminator function |
|-----------------------------------|-----------------------|--|
| Early minus late power | 3 | $\Delta\tau = (I_e^2 + Q_e^2) - (I_l^2 + Q_l^2)$ |
| Normalized Early minus Late Power | 3 | $\Delta\tau = \frac{(I_e^2 + Q_e^2) - (I_l^2 + Q_l^2)}{(I_e^2 + Q_e^2) + (I_l^2 + Q_l^2)}$ |
| Non-coherent double delta | 5 | $\Delta\tau = I_{HRC} + Q_{HRC}$ $I_{HRC} = (I_e - I_l) - 0.5 \cdot (I_{ve} - I_{vl})$ $Q_{HRC} = (Q_e - Q_l) - 0.5 \cdot (Q_{ve} - Q_{vl})$ |

Table 3-1: Example of classic code delay error discriminator functions.

Estimated errors ($\Delta\phi, \Delta\tau$) are then low-pass filtered in order to limit the loop noise (obtained from the receiver input and the inherent operation of the closed loop), and fed into code numerically controlled oscillators (NCO) to close the loop and complete the transient phase. The output of the code NCO is then applied to disperse the received signal and, in last instance, to demodulate the embedded navigation data.

For all intents and purposes, the code delay tracking phase can be seen as an optimization operation during which the delay of the spreading code replica is driven to locally maximize the cross-correlation between the received signal and the output of the code NCO. In this process however, if the cross-correlation of the spreading code pulse shaping function presents multiple lobes, several factors are susceptible to cause a suboptimal lock of the loop that will induce a certain degradation of the PVT solution accuracy. This precise problem is on the focus of Chapter 6, where a novel technique to overcome this drawback is presented.

3.6 *Chapter Summary*

Given the needs for subsequent chapters in this thesis, this chapter has been added to provide a detailed knowledge of the generic structure of the GNSS receiver tracking channels. This information will be used in forthcoming chapters to understand the effects of error factors that can potentially affecting the satellite-to-user pseudorange estimation, and to coherently design and implement software simulators for the evaluation of performances in Chapter 6 and Chapter 7.

Note that the description in this chapter does not contemplate the receiver data delivery subsystem that demodulates and decode de navigation data frame from the tracked signal. This subsystem has been deliberately excluded, as it is not of interest for the proposed performance measurements in Chapter 6 and Chapter 7. For details on this matter, the reader is kindly referred to classical texts on the topic like [Ref. 9].

CHAPTER 4

A REVIEW OF ERROR SOURCES AND EFFECTS IN SATELLITE RADIONAVIGATION SYSTEMS

4.1 Preface

It is a clear statement that all developments presented in Chapter 2 are making reference to nominal performances for all described systems. However, due to several sources of errors mainly affecting the satellite-to-user range determination, accuracies of positioning and time dissemination are limited. This very same fact is also applicable to non-satellite-based positioning systems, although the nature of the error sources in this case can be slightly different.

In this section of the document, a review of the error sources and effects on the estimation of the PVT solution will be conducted according to the objectives of this investigation. For further details, the reader is kindly referred to the classic literature.

4.2 Error Sources on the Accuracy of the Reported Position

The factors that can potentially degrade the quality of the positioning service can be classified in many ways. In this document, the categorization will respond to the origin of the cause within the signal path, as depicted in Figure 4-1.

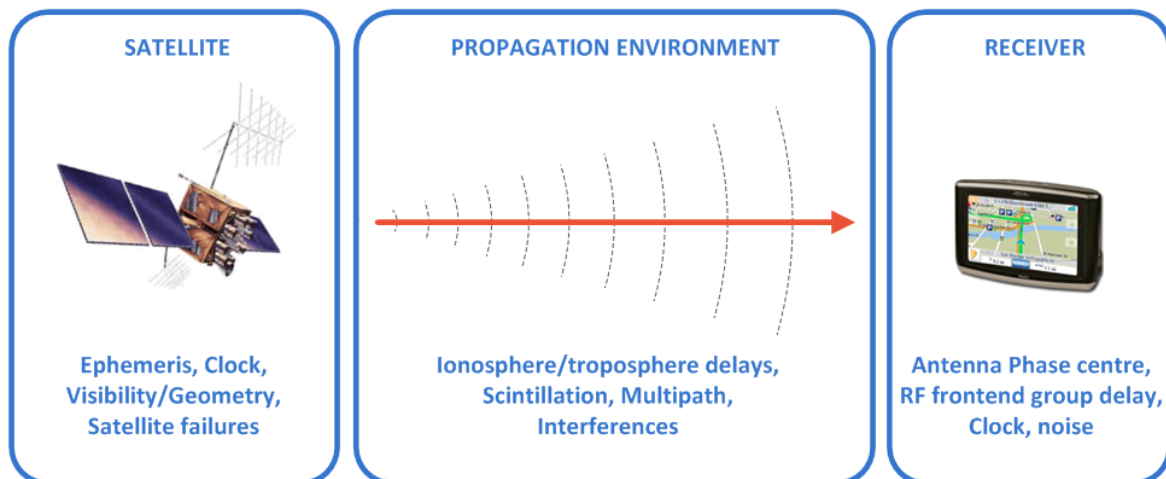


Figure 4-1: Conceptual classification of error sources in satellite-based positioning systems.

Sources Related to the Space Segment. Uncertainties based on the satellite or directly related to the behaviour of the constellation include the broadcast of imprecise ephemeris, the intentional

degradation of the quality of the on-board time base or the broadcasted ephemeris data (i.e. Selective Availability in GPS, disabled since 2000) or satellite conditions affecting, i.e. the precision of on-board atomic clocks. To this regard, and as an example, all Galileo satellites will transmit the deviation of their local clock relative to GST to the receiving equipments through continuously updated³⁰ clock correction parameters within the broadcast navigation data. These clock correction parameters allow a Galileo-compatible user receiver to correct the measured time of transmission, used to derive the satellite-to-user pseudorange. The correction method recommended for this procedure is documented in [Ref. 6].

Additional important factors also attributable to the space segment of a GNSS are an insufficient number of satellites in view (related to the shadowing caused by the environment surrounding the user receiver) or a deficient satellite geometry. The concept of dilution of precision in this context is a measure of the satellite geometry quality; the closer the dilution of precision to the unit, the optimal the geometry for a higher precision of the estimated position³¹.

The linear model for point positioning through code ranges is represented in equation 4-1

$$\mathbf{L} = \mathbf{A} \cdot \mathbf{x} \quad 4-1$$

With:

$$\mathbf{L} = \begin{bmatrix} L^1 \\ L^2 \\ L^3 \\ L^4 \end{bmatrix} \quad \mathbf{A} = \begin{bmatrix} a_x^1 & a_y^1 & a_z^1 & c \\ a_x^2 & a_y^2 & a_z^2 & c \\ a_x^3 & a_y^3 & a_z^3 & c \\ a_x^4 & a_y^4 & a_z^4 & c \end{bmatrix} \quad \mathbf{x} = \begin{bmatrix} \Delta X_{Rx} \\ \Delta Y_{Rx} \\ \Delta Z_{Rx} \\ \delta_{Rx} \end{bmatrix} \quad 4-2$$

Where (a_x^s, a_y^s, a_z^s) for $s \in \{1,2,3,4\}$ are the unitary vectors from four visible satellites to a known approximate user receiver position $(X_{Rx0}, Y_{Rx0}, Z_{Rx0})$, c is the speed of light, $(\Delta X_{Rx}, \Delta Y_{Rx}, \Delta Z_{Rx})$ are the unknown coordinate increments between the approximate $(X_{Rx0}, Y_{Rx0}, Z_{Rx0})$ and the actual receiver position, approximated by $(X_{Rx0} + \Delta X_{Rx}, Y_{Rx0} + \Delta Y_{Rx}, Z_{Rx0} + \Delta Z_{Rx})$, δ_{Rx} represents the unknown receiver clock bias, and L^s for $s \in \{1,2,3,4\}$ is given by equation 4-3

$$L^s = R_{Rx}^s - \rho_{Rx0}^s + c \cdot \delta^s \quad 4-3$$

³⁰ The clock correction parameters to be broadcasted within the Galileo navigation data frame have a validity of approximately 100 minutes. After this period, an update is uploaded to every satellite in the system.

³¹ An optimal geometry is obtained with a satellite on the zenith of the user, and other uniformly distributed over the receiver coverage area [Ref. 7].

With R_{Rx}^s the observed code pseudorange from the receiver to the s -th satellite, ρ_{Rx0}^s the geometric range from $(X_{Rx0}, Y_{Rx0}, Z_{Rx0})$ to the s -th satellite, and δ^s the clock bias of the s -th satellite (known, as it is transmitted within the navigation data frame).

From the 3D position of all visible³² satellites and the user, determined in an Earth Centred-Earth Fixed (ECEF) frame, the GDOP (Geometric Dilution of Precision) is calculated as in 4-5 from the trace of the cofactor matrix \mathbf{Q} in equation 4-4.

$$\mathbf{Q} = (\mathbf{A}^T \mathbf{A})^{-1} = \begin{bmatrix} q_{XX} & q_{YX} & q_{ZX} & q_{TX} \\ q_{XY} & q_{YY} & q_{ZY} & q_{TY} \\ q_{XZ} & q_{YZ} & q_{ZZ} & q_{TZ} \\ q_{XT} & q_{YT} & q_{ZT} & q_{TT} \end{bmatrix} \quad 4-4$$

$$GDOP = \sqrt{q_{XX} + q_{YY} + q_{ZZ} + q_{TT}} \quad 4-5$$

Similarly, the PDOP (Position Dilution of Precision) can be computed also from the cofactor matrix \mathbf{Q} as in 4-6.

$$PDOP = \sqrt{q_{XX} + q_{YY} + q_{ZZ}} \quad 4-6$$

In these conditions, then, to obtain the best instantaneous GDOP or PDOP from a given user position to the four minimal satellites, all combinations of visible satellites must be taken into account, and the lowest value of GDOP or PDOP kept as a result. In effect, this is one of the satellite selection methods of choice in low-cost, mass-market GPS receivers available at the moment of writing.

Given these words on the Dilution of Precision, it is clear that a high visibility as offered by a multiconstellation system provides more chances for a low GDOP. More details on the standard procedure for the GDOP, HDOP, VDOP, TDOP and PDOP calculations can be found in [Ref. 7] and [Ref. 9].

Propagation and Geometry-Related Causes. Many other factors can be related to the signal propagation environment. We find in this group, for instance, the ionospheric and tropospheric delays due to non-constant speeds of the signals through the atmosphere. The ion density and temperature agitation of the ionosphere³³ is affected by the solar radiation (mainly ultraviolet rays), being the total electron content (TEC) higher at latitudes close to the Equator with high variability as

³² In this context, the satellite visibility is considered to include the effect of the globe surface curvature and physical geography, plus the local blockage due to the user environment (buildings, vegetation and foliage, etc).

³³ Dispersive atmospheric layer (at navigation frequencies) situated at altitudes between 50 Km and multiple Earth radii.

well at high latitudes, and dependent on other factors like the year, the season, and even the time of the day. The interaction with the cloud of electrons resulting from the gas ionization in this layer reduces the propagation speed of the pseudorange signals and increases the speed of the carrier phase signals. The pseudorange error yielded by the consequential delay for a particular satellite in view increases at low elevations due to, among other terms, the longer path of the GNSS signals to the user receiver and the higher influence of reflected signals. Therefore, this error will be more important for a satellite close to the horizon than in a zenithal position. The troposphere³⁴, lowest layer of the atmosphere whose effective height varies from 7 to 40 Km, induces an error on pseudoranges dependent on pressure, temperature, humidity, the relative elevation of the satellite, and even the altitude of the user receiver. It is considered the addition of a 'dry' factor, quite predictable and independent of atmospheric conditions and which effect yields the 90% of the total influence, and a 'wet' component directly given by the water vapour content, which quickly fluctuates with the atmospheric parameters.

Presently, two approaches are known to have a positive impact on these error components:

- When signals in two different frequency bands are available to a particular user type (i.e. GPS L1P+L2P for military users or GLONASS G1C/A-G2C/A for civilian users), the use of dual-frequency receivers, although more expensive, help to virtually eliminate the ionospheric component of this error (more than 99.9% of it is explained by the first order approximation of the ionospheric delay).
- Where only single-frequency receivers are available, mathematical models of the atmospheric layers are employed to predict the effects on the pseudorange. A well known model used against the ionospheric delay is the Klobuchar model [Ref. 39], which parametric definition through a set of 8 coefficients is embedded in the navigation message of GPS, GLONASS and Galileo, and is able to eliminate, on average, 50% of the error at midlatitudes. Models for the tropospheric delay used in GPS, GLONASS, and studied for Galileo are based on the work of Saastamoinen and Hopfield [Ref. 7]. In this case, the parameters of the compensation model are implemented within the user receiver.

Another effect closely related to the activity within the ionosphere is known as ionospheric scintillation. A regional³⁵ irregularly structured electron density can cause diffraction and scattering of navigation signals propagating across this layer. Constructive and destructive interferences derived from this fact in the range of 0.3 – 10.0 GHz produce random temporal fluctuations of signal amplitude, phase or angle of arrival that, in extreme, can lead to temporal loss of either code or carrier phase lock if the dynamics of amplitude fading or phase variation is not supported by the tracking loops within the receiver.

A very important factor directly related to the atmospheric propagation and the user receiver environment is known as multipath. For a given satellite, the multipath induces a certain time-

³⁴ Non-dispersive medium below 20 GHz.

³⁵ Ionospheric scintillation regions are more probable to appear in the vicinity of the geomagnetic equatorial region (between $\pm 20^\circ$ latitude) after sunset, with a temporal correlation with the 11-years solar cycle. More persistent (but less severe) manifestations of this phenomenon can be also found at high altitudes [Ref. 9] (respectively above and below 55° and -55°).

variable distortion of the cross-correlation between the chip shaping function of the received PRN and the pulse characteristic of the locally generated spreading code replica, mainly caused by the reception of the addition of LOS and reflected signals³⁶ from the same reference satellite. In this context, and due to the fact that the code delay loop embedded in the bit synchronization structure of the tracking receiver channel is susceptible to lock on one of the multiple generated suboptimal stable points of the aforementioned cross-correlation, the time evolution of the code delay estimation and the corresponding range determination may be affected of a systematic error or bias, that can additionally lead to inaccurate code removal from the compound received signal and increased bit error rate measured on the navigation data stream recovered from the tracked satellite.

Other biases on the code delay estimation may be produced by the instability or miss-calibration of the antenna phase centre, relevant for high accuracy applications, or by the group delay of the RF frontend filters.

Receiver-Based Error Sources. Once the signal reaches the user, and due to the fact that the clock at the receiver is not as precise as the on-board reference (for obvious reasons of price and weight, mass market receivers use built-in quartz clocks, cheaper and lighter than on-board atomic clocks), timing errors appear from both the instability and biases of this component, or from the imperfect synchronization with the target GNSS time base.

A last source of error, theoretically assigned to the receiver, is designated with the generic term 'noise' and includes not only the thermal noise, which is inherently generated by the electronic components of the receiver, but also all received power from external sources of a random nature.

Additionally, even the presence of interfering signals within the bandwidth of the RF- frontend of the user receiver have an impact on the performance of the receiver and, naturally, on the accuracy and precision of the positioning solution. Although all error factors briefly summarized above are known to cause important errors in the determination of the PVT solution delivered to the user, and given the nature of this document, this last source of error will be considered of special relevance and, as such, the entire section 4.3 in this chapter will be dedicated to the detailed study of interference sources in GNSS bands susceptible to affect different types of users and services.

4.3 *Radio Interference Sources on Satellite Navigation Bands*

Early in this document (see 1.1, for instance), a reduced set of interfering sources has already been suggested and briefly set into the context of the multiconstellation scenario. In this section, however, a detailed study of the most usual signal sources susceptible to affect satellite navigation services in L-, S- and C-bands will be introduced, focusing the analysis in all cases towards the satellite to user downlink used to broadcast the navigation signals, and considering of relevance both in-band and out-of-band interference sources on RNSS frequencies in the aforementioned bands, as potentially observed within European territory.

³⁶ As discussed in Chapter 3, reflected signals will alternatively switch between RHCP and LHCP polarizations. Therefore, and due to the gain characteristics of the GNSS receiver antenna, mainly even-order reflections should be theoretically accounted for.

All signal sources here mentioned are set into context in Figure 4-2, where the spectral co-occupation of satellite GNSS frequency bands and non-navigation related signal sources is depicted. It is important to note that the common spectral occupation of two signals is not a sufficient condition for interference to take place. Besides, other factors such as the received power spectral density and polarization, modulation or multiplex access method must be taken into account for this evaluation.

All interference sources highlighted below are assumed to affect the victim GNSS receiver by entering the system through the antenna, and to reach the bank of receiver channels through the RF frontend. This is correct in all cases if sufficient design measures to ensure the electromagnetic compatibility and robustness of the GNSS receiver have been considered. This assumption will also apply to the rest of this document.

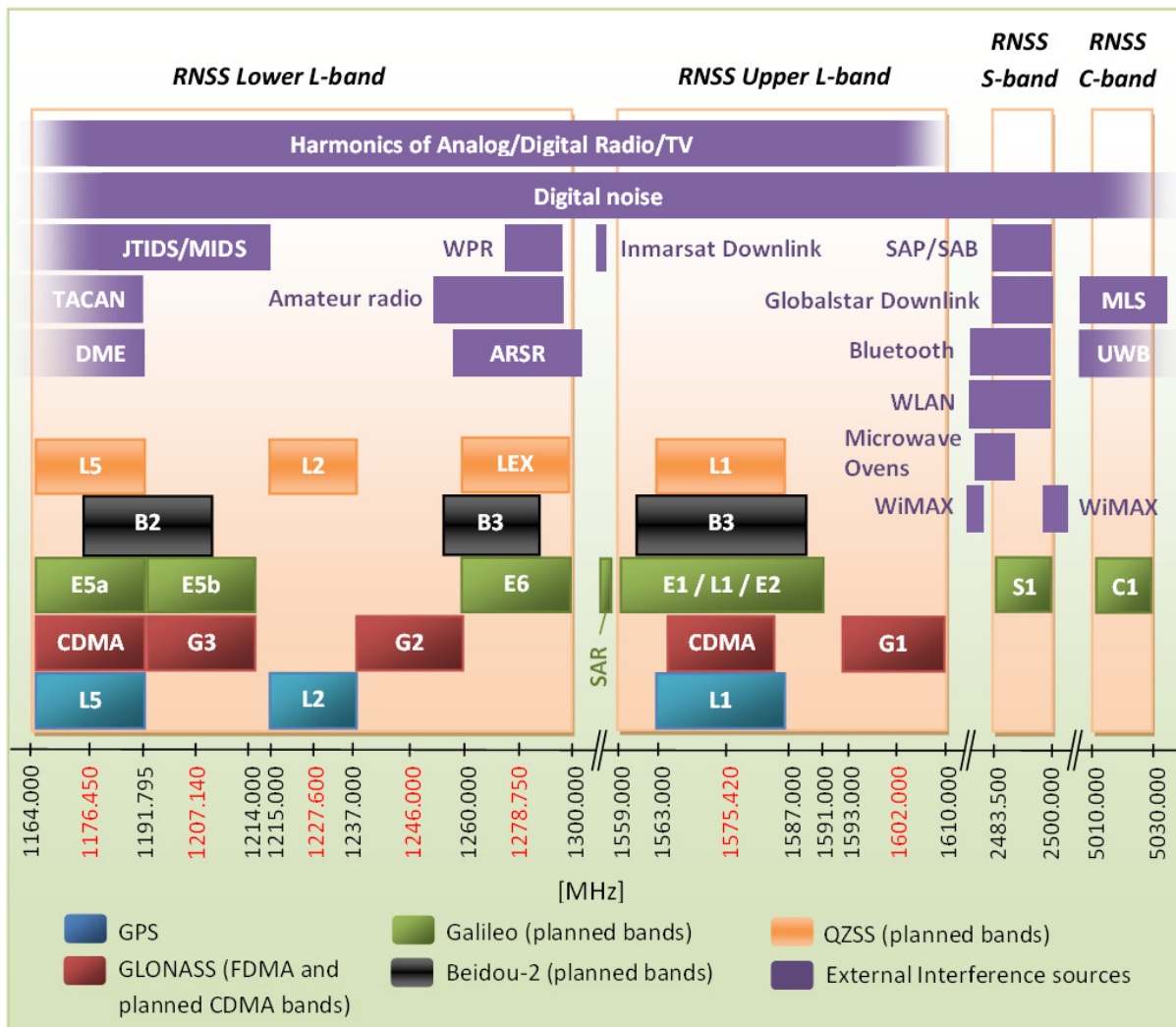


Figure 4-2: Usage of frequency bands currently assigned to Space-to-Earth RNSS services, with exemplar interfering sources of interest for an arbitrary user (last update on 23 November 2010).

4.3.1 GNSS Interferences

This category includes GNSS navigation radiations other than the target signal transmitted by the satellite whose PRN is being tracked by the receiver channel of reference. A complete classification is introduced in section 5.2.7 and will not be reproduced here.

4.3.2 Harmonics of Commercial Transmitters of FM Radio and Analog/Digital TV

Although interference from analogue radio transmitters is very unlikely because of the high suppression of unwanted high order harmonics (typically larger than 120 dB), a theoretical out-of-band emission could occur at several high order harmonics of any FM radio transmitter station. Another possible source of radio interference in this category would be caused by the high order harmonics from the mixer of a (low cost) transistor radio or the local oscillators in VHF super-heterodyne receivers.

Out-of-band harmonics from UHF Analog and Digital TV transmitters have special presence in RNSS bands. Depending on the TV channel considered, the third order (for channels in the lower half of the UHF band) or second order (for upper frequencies) harmonic of such radiations, if not filtered out, can be present with enough power to disturb the operation of a GNSS receiver. As an example, take channel 27, whose video carrier is broadcasted on 519.25 MHz (with 8 MHz bandwidth) over Western Europe, and whose third harmonic will overlap Galileo E1 band. Or channel 36, transmitted on 591.25 MHz in the same region, with a second harmonic overlapping GPS L5 and Galileo E5a.

| Galileo band | Harmonic Order | Band/Frequency (MHz) | Usage |
|--------------|--------------------------------------|----------------------|-------------------|
| E5 | 13 th | 89.70 – 93.70 | FM broadcast |
| | 12 th | 97.20 – 101.70 | FM broadcast |
| | 11 th | 106.00 – 108.00 | FM broadcast |
| | 18 th to 25 th | 47.00 – 67.70 | TV band I |
| | 6 th | 194.30 – 203.00 | TV band III |
| | 3 rd | 388.67 – 406.00 | TV band IV |
| | 2 nd | 582.00 – 609.00 | TV band V |
| E6 | 0 | 1,296.89 | Amateur Beacon |
| | 0 | 1,279.40 – 1,281.70 | FM-ATV Relay |
| | 0 | 1,284.00 – 1,286.80 | FM-ATV Relay |
| | 0 | 1,240.00 – 1,300.00 | Packet-Radio Node |
| | 2 nd | 658.00 | TV broadcast |
| | 14 th | 101.83 | Radio broadcast |
| E1 | 15 th | 104.76 – 105.29 | FM broadcast |
| | 16 th | 98.21 – 98.71 | FM broadcast |
| | 2 nd | 785.71 – 788.71 | UHF TV |
| | 3 rd | 523.80 – 526.47 | UHF TV |
| | 8 th | 196.42 – 197.42 | VHF TV |
| | 9 th | 174.60 – 175.49 | VHF TV |

Figure 4-3: European radio broadcast and TV bands susceptible to interfere on Galileo services.

(source: [Ref. 43])

4.3.3 Analog and Digital Amateur Radio Link Stations

Several amateur radio services are allocated within RNSS bands. For instance the FM-ATV transmission around 1.2 GHz, or 23 cm Radio Amateur band in the range 1,240 MHz – 1,300 MHz could very well affect the performance of positioning receivers tracking Galileo satellite signals transmitted on E6.

4.3.4 Digital Noise

Digital devices available nowadays are susceptible to produce impulsive broadband noise at RNSS frequency bands. In this category, personal or industrial computers, laptops or any other digital equipment will emit a certain noise power level (due to the transistor switching mechanism among other causes) in frequencies close to the oscillator of the main clock or bus clock of the system. Therefore, as current technologies are offering clock frequencies between 1 and 2.5 GHz, these signals are more likely to affect RNSS receivers operating on L-band, and/or on an eventual S-band.

4.3.5 JTIDS / MIDS

JTIDS is an old version of MIDS, the communication layer of the military inter-computer data exchange network of NATO, known as Link-16. JTIDS is an UHF TDMA system (396,288 pulses of 6.4 ms in 12-seconds frames, divided into 1,536 slots/frame), with resistance to jamming provided by means of a frequency-hopping approach according to which the transmission frequency of every terminal is allocated (in a pseudorandom pattern, unique to every station) on one of 51 3-MHz-channels between 960 and 1,215 MHz at a rate of 77,000 hops/s [Ref. 42].

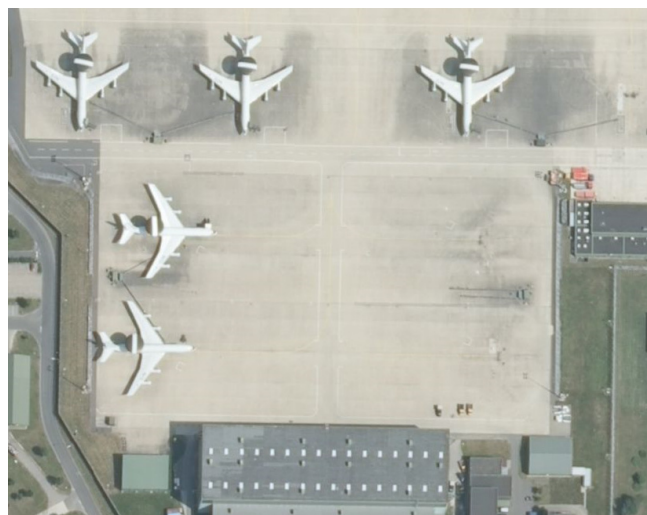


Figure 4-4: E-3 AWACS airplanes parked at the NATO European Airbase in Geilenkirchen (Germany).
(source: www.bing.com).

JTIDS/MIDS signals are transmitted with an RF power ranging from 200 (small terminals) to 1,000 W (fixed ground assets, Frigates and E-3 AWACS), compliant with the spectral mask in Figure 4-5. The signal scheme noted above highlights the pulsed nature of this interference source, as seen by a navigation receiver in GPS L5 and Galileo E5a/E5b bands.

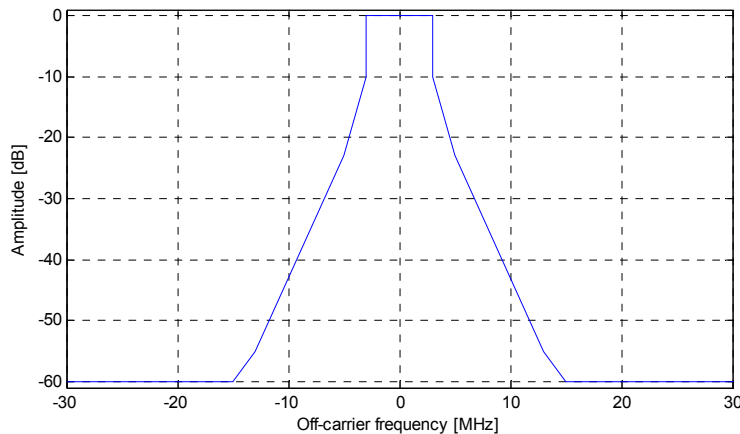


Figure 4-5: Transmission spectral mask to which JTIDS/MIDS signals must be compliant with.
(source: Eurocontrol).

4.3.6 Wind Profiler Radar

This type of radar makes use of a multi-beam antenna, every beam of which provides information about the radial velocity (based on Doppler offset determination) in one single direction. Measurements in at least three directions are needed in order to compose the wind vector. This type of radar is able to measure, among other variables, the wind speed in the atmosphere at heights between 500 and 16,000 m, depending on the frequency band in use. Of special relevance here, the use of WPR in the band 1,270 – 1,295 MHz, posing a pulsed type of interference directly on Galileo E6.



Figure 4-6: 1,290 MHz Wind Profiler Radar at Lindenberg, Germany
(source: German Meteorological Service (DWD)).

In theory, this type of radar is not susceptible to interfere on any on-ground navigation receiver due to the fact that generally transmits to high elevations. However, the side lobes of the antenna pattern might derive interfering power to low elevations, to affect an eventual GNSS receiver in the vicinity of the radar site.

4.3.7 Inmarsat Downlink

Direct or out-of-band emissions from the Inmarsat Downlink, located between 1,530 and 1,546 MHz and transmitting on RHCP with a Narrowband FM modulation (25 kHz bandwidth), are susceptible to interfere on the Galileo SAR service.

4.3.8 DME / TACAN

These aeronautical aiding systems can be received with the spectral masks in Figure 4-8 within the band 960 – 1,215 MHz and are considered of special importance in the interference evaluation on all present and planned GNSS systems in E5a/L5, especially for aeronautical users. Every DME/TACAN station transmits on any of the different channels within the range 1,025 – 1,150 MHz, with a bandwidth of 100 kHz, and a channel separation of 1 MHz. The response signals will return on a frequency differing ± 63 MHz of the received carrier, within the range of 962 – 1,213 MHz.

In the time domain, the DME/TACAN signal is characterized by a train of Gaussian envelope pulse pairs (as described by equation 4-7, with α equal to $4.51 \cdot 10^{11} \text{ s}^{-2}$), with pulse width of $3.5 \mu\text{s}$ (measured at 50% voltage level), a pulse separation δ of $12 \mu\text{s}$ (for X channels) or $30 \mu\text{s}$ (for Y channels), and a maximal PRF (Pulse Repetition Frequency) in static conditions of 2,700 pps for DME and 3,600 pps for TACAN transponders.

$$p(t) = P_{pk} \cdot (e^{-\alpha \cdot t^2} + e^{-\alpha \cdot (t-\delta)^2}) \quad 4-7$$

As a means for identification, every DME/TACAN ground station periodically substitutes the transmission of interrogation and reply pulses for pulse pairs at a fixed rate of 1,350 pps, modulated in amplitude by a baseband OOK signal defining the Morse-code identifier of the station. This coded word, audible from the aircraft cockpit, follows the timing summarized in the list below for the definition of dots and dashes (according to ICAO specifications):

- Dots have a duration in the range [0.1, 0.160] seconds.
- Dash duration is 3 times the dot duration.
- The separation between dots/dashes is equal to a dot duration $\pm 10\%$.
- Letter spacing shall not be less than 3 dot durations.
- The duration of a code group shall not be higher than 10 seconds.
- Identification words repeat every 30 s and 40 s for DME and TACAN stations respectively.

DME (Distance Measurement Equipment) and TACAN (Tactical Air Navigation system) are, due to the nature of the transmitted signal, considered pulsed sources of interference. As such, and in order to account for collisions between pulses from different stations, the approach in [Ref. 40] should be applied to the computation of the total C/N_0 degradation provided by these sources on a user within a given scenario.

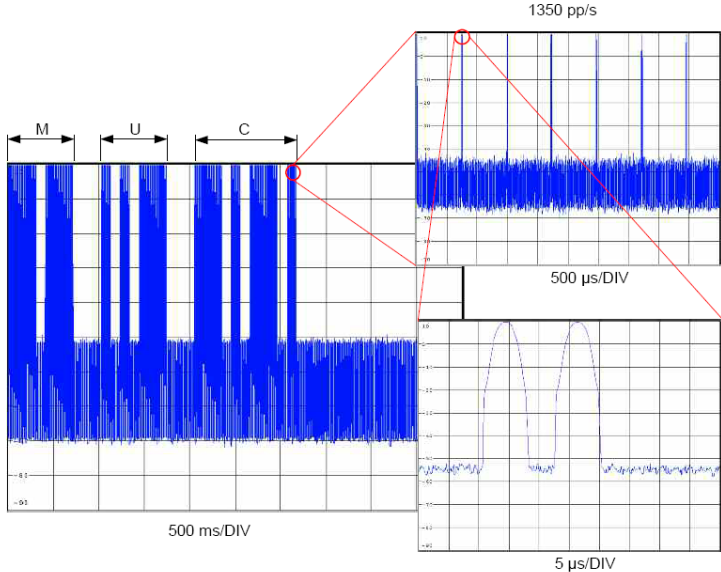


Figure 4-7: Details of the Morse codes within DME/TACAN signal structure. (source: [Ref. 64]).

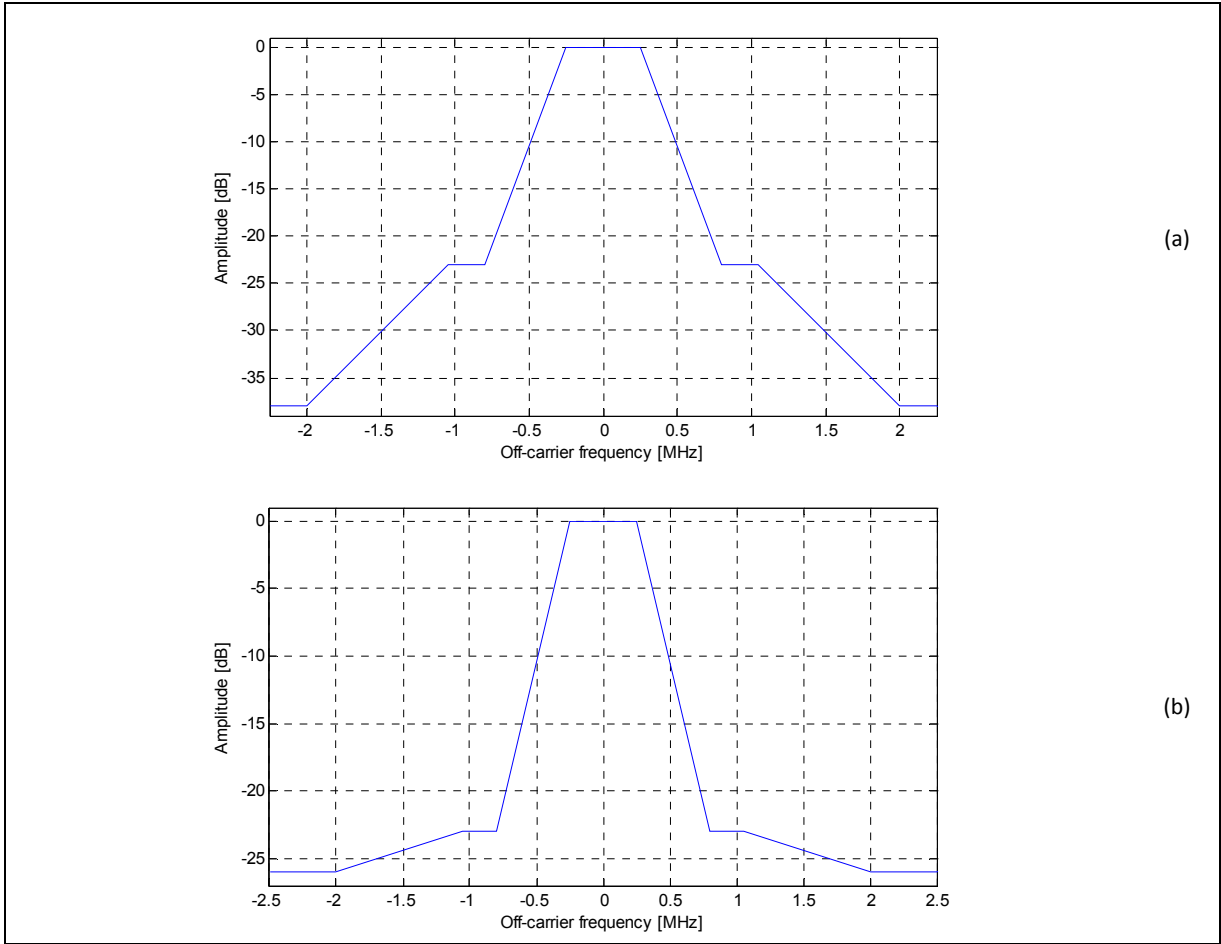


Figure 4-8: Transmission spectral mask to which DME/TACAN (a) airborne and (b) ground stations must be compliant with. (source: Eurocontrol).



Figure 4-9: (a) TACAN station. (b) VOR/DME station (VOR antenna on the center pole).
(source: US Air Force)

4.3.9 ARSR

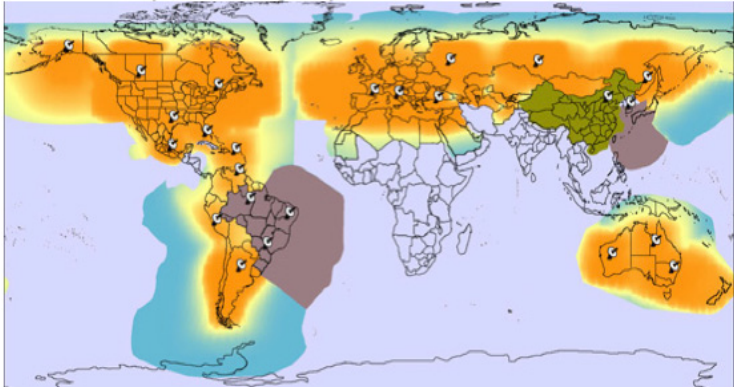
Air Route Surveillance Radar (ARSR) is the FAA civilian denomination for a type of scanning long-range radar in L-band, used in air traffic management operations to plot an aircraft's position and course while en route between control areas. The newest ARSR model, denominated ARSR-4, allows radar coverage areas of over 400 Km of diameter, with a dual-channel frequency hopping technology supported in the frequency range between 1,215 and 1,400 MHz, with bandwidths in the range 0.5 to 2.5 MHz [Ref. 48]. This configuration enables the operator to detect small targets with minimal multipath and weather effects.

4.3.10 Globalstar Satellite-to-User Downlink

Globalstar Inc. provides, since its launching in 1991, access to mobile voice and data services over its coverage area (see Figure 4-10) through a constellation of 48 active LEO satellites, which act as 'bent pipe' repeaters within a global network of ground gateway stations.

Of special relevance for this study, the downlink from satellite to Globalstar terminals is allocated in the band 2,483.5 – 2,500 MHz and provided by multibeam antennas. In every beam of the coverage, 13 FDMA channels 1.23 MHz wide can support up to 128 CDMA signals per channel following a DS-SS BPSK modulation with a chipping rate of 1.2288 Mcps.

Prior to modulation, a SRRC (Square Root Raised Cosine) filter is applied at chip level, with a roll-off factor of 0.2. This combined scheme is shown to provide high spectral separation (low SSC values) relative to eventual Galileo signals in S-band.



Last update June, 2009



Figure 4-10: Globalstar coverage updated to June 2009. (Source: www.globalstar.com)

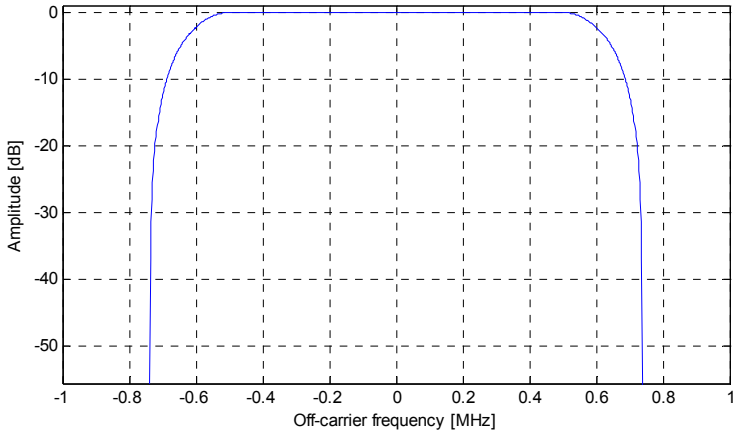


Figure 4-11: Theoretical spectral mask for every FDMA channel of the Globalstar downlink.

4.3.11 The ISM Band

The ISM band in the frequency range 2,400 – 2,500 MHz is mainly shared by unlicensed robust wireless standards such as *Bluetooth* (IEEE 802.15) or *WLAN* (IEEE 802.11). The unintentional use of this band is also a known issue, especially from out-of-band radiations from home microwave ovens operating at 2.45 GHz and other unregulated devices.

4.3.11.1 Bluetooth

In Europe (except for Spain and France), Bluetooth can operate on 79 channels centred at carriers equal to $2,402+k$ MHz, $k = 0, \dots, 78$, with 1 MHz bandwidth. In Spain and France, 23 channels in $2,449+k$ MHz, $k = 0, \dots, 22$ and $2,454+k$ MHz, $k = 0, \dots, 22$ are respectively allocated.

Reduced sensitivity to interferences is achieved in Bluetooth by implementing a frequency hopping spread spectrum method in combination with time-division duplex for the time-slot based transmission of data packets. The duration of every slot is of $625 \mu\text{s}$, therefore frequency hops occur up to 1,600 times per second in a single slot duration. The hopping sequence is pseudorandom, with an approximate period of 23.3 hours.

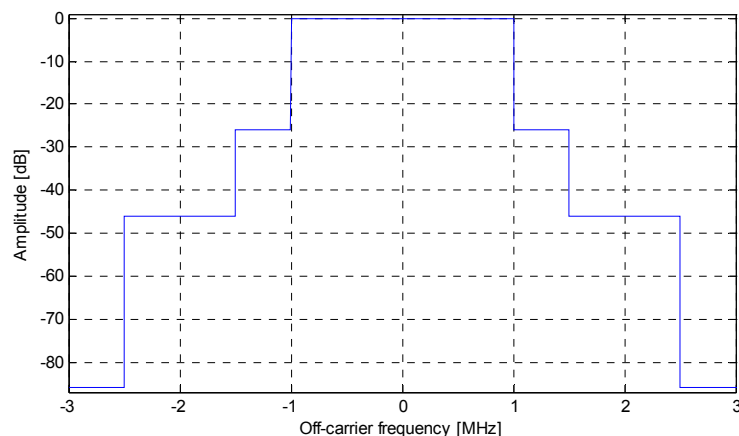


Figure 4-12: Theoretical spectral mask to which Bluetooth emissions must be compliant [Ref. 1].

The data packets are GFSK-modulated, with the product between the Gaussian filter bandwidth and the signal symbol period equal to 0.5, and the modulation index between 0.28 and 0.35 [Ref. 1]. Figure 4-12 depicts the standard transmission mask of Bluetooth.

4.3.11.2 WLAN

Wireless Local Area Network IEEE standards 802.11b/g/n foresee 14 channels 22 MHz wide in the band 2,401 – 2,495 MHz. In this band, the interchannel separation is of 5 MHz (and exceptionally of 12 MHz between channels 13 and 14). For this fact, it is recommended to use channels 1, 6, 11 and 14 in order to avoid interchannel interferences.

The last version of IEEE 802.11n of 2009 specifies several combinations of modulation (BPSK, QPSK, 16-QAM and 64-QAM), data coding rates, spatial diversity and broader channel bandwidths to provide higher throughputs. All these feature combinations must yield signals with spectral characteristics compliant with the mask in Figure 4-13 or similar.

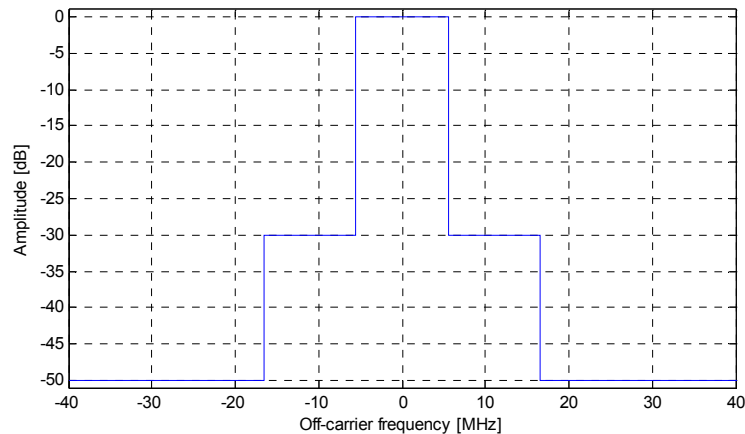


Figure 4-13: Example of WLAN spectral mask, which shows the drop of 30 dB at ± 11 MHz off carrier, as required by the standard 802.11.

4.3.12 WiMAX

WiMAX is an implementation of the wireless networks standard 802.16 oriented to provide broadband connectivity to mobile devices or to substitute cable, DSL or optic fiber through the last mile for fixed broadband access. The current version of this standard defines an OFDM / SOFDM access to an air interface [Ref. 68] with certain uplink and downlink RF channels directly above or below the band 2,400 – 2,500 MHz that should be considered for completeness as potential out-of-band interfering sources to the target future navigation frequencies in S-band. This is the case of the upper channels of band class groups 1.A and 1.B (with 5, 8.75 and 10 MHz uplink and downlink channels in the band 2,300 – 2,400 MHz), the lower uplink and downlink channels in band class group 3.A (with 5 or 10 MHz bandwidth, in the band 2,496 – 2,690 MHz) and the lower uplink channels of band class group 3.B (5 or 10 MHz bandwidth, between 2,496 and 2,572 MHz).

4.3.13 SAP/SAB

Within the Services Ancillary to Broadcasting (SAB) and Programming (SAP), the use of wireless cameras, portable video links and mobile video links on-board aircrafts and vehicles in Europe for the on-spot reporting of media contents is licensed to the 2,483.5 – 2,500 MHz band.

Typically, these are digital OFDM-modulated transmissions with 8 MHz bandwidth, compatible with the DVB-T standard.

4.3.14 MLS

The Microwave Landing System (MLS) was developed in the late 1980s as a standard high precision and all-weather replacement for ILS, to overcome the reduced number of available channels and the high vulnerability to multipath through the use of microwave carriers (200 channels between 5,031 and 5,090.6 MHz). Although the core MLS band presently in use over Europe is allocated between 5,030 and 5,091 MHz, the complete band 5,000-5,150 MHz is currently reserved for this application [Ref. 41]. For this reason, current developments on SIS for C-band Galileo consider MLS as an important potential threat.

This system acts as a rotation radio lighthouse with a very narrow beam (typically, of 2°), to provide azimuth, elevation and range guidance (the last information, provided by means of DME-like operation) to aircrafts in approximation phase. This particular characteristic makes of the MLS signal a pulsed interference as seen by the guided user.

MLS elevation, azimuth and data communications are transmitted on the same frequency channel, multiplexed in time according to a defined TDMA scheme. The spectral characteristics of the MLS transmission (see Figure 4-14) are conditioned by the DPSK-modulated data frame. This frame is used to broadcast the station identifier, the exact locations of azimuth and elevation, and the ground equipment performance level among other important details. Exceptionally, the MLS system is designed to provide runway and weather conditions through an auxiliary data transfer time slot.

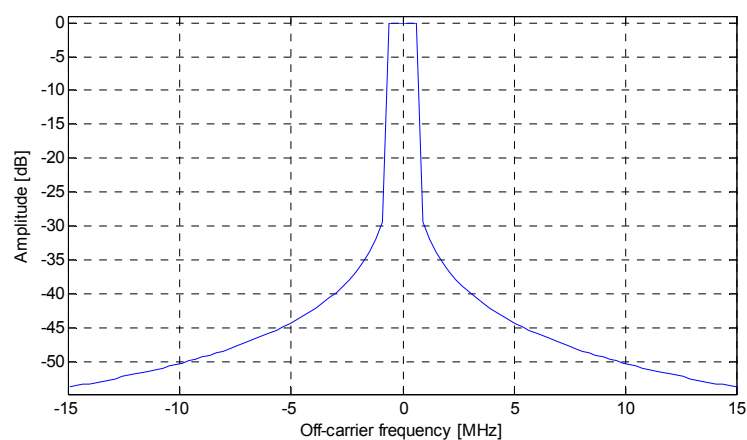


Figure 4-14: Transmission spectral mask to which MLS stations must be compliant with.

(Source: Eurocontrol).



Figure 4-15: MLS station at NASA-operated Wallops Flight Facility.

(Source: NASA).

The future of MLS is uncertain. Although at the present it is in decommission phase in benefit of GNSS and their augmentations, still two active instances are being respectively maintained in Heathrow Airport (UK) and Canberra Airport (Australia).

4.3.15 UWB

Ultra wide-band emissions are generally defined by ITU as signals with a bandwidth exceeding 500 MHz or the 20% of the centre frequency. The band from 3.1 to 10.6 GHz is currently regulated for the unlicensed use of UWB transmitters, provided that they operate with a power spectral density below -41.3 dBm/MHz. Under this category, pulsed transmitters with an instantaneous contiguous or non-contiguous bandwidth occupation higher than 500 MHz are included, with applications in radar and short-range communications as a few examples.

Due to the spectral usage reserved for UWB, a certain level of interference is to be expected on a future Galileo service broadcasted on C-band, minimized due to the spread spectrum nature of both RNSS and UWB signals under consideration.

4.4 *Effects of Error Sources on the Pseudorange Determination*

The causes summarized in 4.2 have varied effects on the accuracy and precision of the computed satellite-to-user pseudo range.

From 4-8, the pseudorange from the user to a particular space vehicle (SV) is obtained from the geometric slant distance from receiver to satellite (ρ_{rxToSv}), affected by a series of error factors.

$$\rho = \rho_{rxToSv} + \Delta\rho_{noise} + \Delta\rho_{int} + \Delta\rho_{rx} + \Delta\rho_{mp} + \Delta\rho_{atmos} + \Delta\rho_{\Delta clk} + \Delta\rho_{eph} \quad 4-8$$

The contributions to ρ in 4-8 are attributable to:

- White noise at the antenna output ($\Delta\rho_{noise}$).
- Interference signals observed at the input of the receiver, $\Delta\rho_{int}$. This factor includes GNSS and non-GNSS interfering signals, and have been previously treated in this chapter.
- Equipment-related delays and biases ($\Delta\rho_{rx}$). This part includes factors ranging from the non-calibrated antenna phase centre until unbalanced hardware delays affecting signals from different satellites. Also in this category, the systematic error due to false lock of the DLL working point. This particular problematic will be addressed in detail in Chapter 6.
- Delays due to multipath ($\Delta\rho_{mp}$).
- Additional delays accumulated during ionospheric and tropospheric propagation ($\Delta\rho_{atmos}$). Note that power variations during ionospheric/tropospheric propagation contribute to additionally degrade the effective C/N₀ at the receiver input, and are not accounted in this factor.
- Receiver and satellite clock uncertainties and errors ($\Delta\rho_{\Delta clk}$).

- Uncertainties on the broadcasted satellite ephemeris ($\Delta\rho_{eph}$).

The combined effect of all sources above on the precision of the single point positioning is estimated in 4-9, through the standard deviation over time of the so-called User Equivalent Range Error (UERE).

$$\sigma_{UERE} = \sqrt{(\sigma_{noise}^2 + \sigma_{int}^2 + \sigma_{rx}^2 + \sigma_{mp}^2 + \sigma_{atmos}^2 + \sigma_{\Delta clk}^2 + \sigma_{eph}^2)} \quad 4-9$$

The standard deviation of the UERE weighted by the PDOP (σ_p in equation 4-10) indicates an estimation of the 3D position precision after all corrective measured applied at receiver level to compensate, for instance, the ionospheric and tropospheric delay error, or the receiver to satellite clock uncertainty.

$$\sigma_p = PDOP \times \sigma_{UERE} \quad 4-10$$

When the UERE is weighted by the GDOP, (σ_{pt} in equation 4-11), the resulting figure of merit estimates the geometric precision in position and time.

$$\sigma_{pt} = GDOP \times \sigma_{UERE} \quad 4-11$$

These expressions are also valid in a multiconstellation scenario (say, GPS plus Galileo), in which case σ_{UERE} takes the form in 4-12 [Ref. 60], and PDOP is computed from all visible satellites in the combined constellation.

$$\sigma_{UERE} = \sqrt{\frac{2 \cdot \sigma_{UERE(GPS)}^2 \cdot \sigma_{UERE(Galileo)}^2}{\sigma_{UERE(GPS)}^2 + \sigma_{UERE(Galileo)}^2}} \quad 4-12$$

4.5 Chapter Summary

This fourth chapter is regarded as an introductory text to the causes and effects of errors that can potentially affect the pseudorange estimation from satellite to the user, and the end of the day, the PVT solution determination.

Given the unpredictability of this particular cause of pseudorange precision degradation, special interest has been drawn to the study of non-intentional in-band RF interference sources to be expected in navigation frequencies within L-, S- or C-bands, with additional details on signal sources of out-of-band emissions that can potentially fall in the bands of interest within European territory only.

CHAPTER 5

THE SIMULATION APPROACH APPLIED TO RADIONAVIGATION SYSTEMS

5.1 *Preface*

It is understood from previous chapters of this document that the engineering activities related to the design, parametrical configuration and characterization of radio navigation systems show a considerable complexity. This level of complication ranges from the relative simplicity of a local indoor positioning and navigation system based on pseudolites, to the extreme intricacy of the multiconstellation scenario depicted in Figure 1-1.

In Table 5-1, different applications are presented to exemplify the degree of complexity that an eventual software or hardware simulator can involve in this field. A first approach to radiolocation and positioning can be achieved through ground-based static reference transmitters such as GPS pseudolites in a GBAS network, or by using already existing communications and broadcasting means with stations of precisely known position. These examples are rated with low simulation complexity due to the static nature of the signal sources and the generally local area of coverage.

More elaborate instances that require an intermediate simulation effort include the more innovative idea of ad-hoc, multiagent 2-dimensional navigation, or the Doppler-based navigation concept provided by Argos among other systems.

For a pseudorange-based satellite navigation system in an arbitrary scenario, given the amount of parameters that lead to the determination of their performances, comprehensive preliminary studies (during the design phase or troubleshooting investigations within the deployment or exploitation phases) are only possible through complex software/hardware simulations.

In the first part of this chapter, the attention will be focused to the software implementation of computational kernels exploiting the mathematical and formalistic behavioural modelling of all systems and subsystems considered in a multiconstellation GNSS scenario, for the determination of the effects of the complete system on the quality of the signal delivered to the navigation receiver in terms of carrier-to-noise ratio. The content of this first part will be directly applied in Chapter 7 for the determination of the interference level and satellite geometries seen by a given GNSS receiver.

The second section of this chapter will deal with the bit-true modelling of the tracking operation within the GNSS receiver itself, and with the determination of the code-based satellite-to-user range estimation quality in statistical terms. Note that a simulator implemented according to this section is to be used in Chapter 6.

It is understood that this chapter presents a generalist approach to the simulation activities in the field of the radio navigation technologies. Therefore, and as such, all explanations here comprised can and should be particularized to any problem by applying the necessary minor modifications.

| Examples | Application | Complexity |
|---|--|--|
| Positioning based on a dedicated network of GPS pseudolites. | Warehouse management, emergency indoor location, and navigation for emergency teams in limited visibility (fire/smoke) | Low. Transmitters are supposed to be static, and user velocity is expected to be low. However, multipath is an issue to be studied |
| Positioning based on ranging from transmitters of known position (GSM/GPRS base stations, radio and TV stations,...). | Indoor or local area in urban environments. | Low. Transmitters are supposed to be static. However, multipath is an issue to be studied |
| Positioning based on ad-hoc networking between user receivers through Wi-Fi, ZigBee, Bluetooth, GSM or GPRS. | Indoor commercial positioning and navigation, in conditions of limited visibility to GNSS satellites. | Medium. Multiagent simulators needed to model the independent behaviour of a number of users in range. |
| Argos-supported, Doppler-based positioning system to track the migration of endangered animal species. | Global positioning and tracking for environmental applications | Medium. One satellite in view at every given instant. Time tagging of the signal necessary. |
| Galileo constellation, on E1 mass-market receivers, global coverage. | Global use for commercial navigation | High. High number of satellites to be modelled. Many interfering factors. |
| Galileo constellation on E1 signals, plus GBAS ground-based stations. | Regional commercial navigation, with expected improved performance within urban canyons. | Very high. High number of satellites and ground-based stations to be modelled. Many interfering signals to be considered on every tracking channel. |
| GPS constellation, plus satellite-based augmentation system. | Aeronautical and safety-of-life applications | Very high. High total number of satellites to be modelled in GPS and SBAS constellations. Many interfering signals to be considered on every tracking channel. Simulator of high accuracy required for SoL. |
| Several GNSS constellations with global coverage. | Global use for commercial navigation, with expected improved performance within urban and non-urban canyons. | Very high. High number of satellites stations to be modelled in every constellation. Complex computation of the interference scenario. |

Table 5-1: Radio navigation application examples, with estimated simulation complexity.

5.2 Part 1: The Frequency-Domain GNSS Software Simulator

5.2.1 The Flux Diagram of the Simulator

Figure 5-1 depicts the tasks to be performed in a model-based, frequency-domain GNSS software simulator. In a preliminary step, in the most general case, the software simulator is configured by the operator, which will define:

- Global or regional satellite constellations to be simulated through valid ephemeris.
- Signals transmitted by every of the satellites in each active constellation, in terms of their carrier frequency, access method (CDMA or FDMA), modulation and bandwidth, spectral and/or temporal properties of the transmitted signal, transmitted power, antenna gain and normalized pattern as a function of elevation and azimuth, the frequency response of the transmission filter and any other parameter of relevance.
- Non-navigation related sources, specified through their location or trajectory, frequency and transmitted power, frequency response of the transmission filter, antenna gain and normalized transmission pattern, the spectral and/or temporal characteristics of the transmitted signal.
- The configuration of the relevant atmospheric models used to predict additional attenuation suffered by the satellite signal through the different layers of the atmosphere, i.e. the tropospheric and ionospheric delays.
- The type of user under consideration (on-ground static or dynamic, or air/space-borne).
- The architecture of the user navigation receiver, and its antenna and RF frontend, in terms of the RF frontend equivalent frequency response, the antenna gain and normalized pattern, the elevation masking angle, the LNA saturation level and time (for use in the processing of pulsed interferers), the protection measure against pulsed interferences, if any (saturating or blanking receiver), the thermal noise PSD, receiver specific losses (implementation losses, correlation losses), the ADC resolution and any other relevant parameter, as exhaustively seen in Chapter 3, to configure the acquisition, tracking and navigation data performance. It is also necessary to specify the navigation signal targeted by the receiver, as other than these signals³⁷ will be considered interferences by the embedded mathematical models.
- A range of user positions and velocities on or above the Globe, through a trajectory or area of coverage (a worldwide coverage, at the limit). Also the user environment could be specified through a reduced number of descriptive parameters or even a precise 3D model, in order to discriminate between urban, rural, mountain and marine scenarios (for instance), with their particular shadowing and/or reflective properties.

Start and stop times of the simulations will also be specified (as well as the time resolution), according to a standard time frame (UTC as the most convenient selection), and used to configure the simulation time axis.

Once the setup process is completed, the simulation is ready to initiate, starting for the position and velocity determination of all signal sources in the scenario in every point of the simulation time axis. This operation is accomplished by interpolating or extrapolating the instant position and velocity of every satellite or interfering mobile from the relevant updated ephemeris or operator-

³⁷ Strictly speaking, when CDMA navigation signals are taken into account and the simulation is focused on a single channel in the receiver, only one target signal from one target satellite is taken as of interest. The rest are considered additions to the interference and noise budgets.

defined trajectories. Similarly, in case of a mobile user is defined, its instantaneous position and velocity needs to be here determined as well.

After the computation of positions, the visibility of transmitters can be geometrically determined for every user position, according the horizon of the planet and the shadowing of the user environment. Additionally, and in a similar fashion, the Doppler frequency shift of every signal source relative to the receiver is determined and the Doppler-dependent spectral separation determined for every satellite in the target constellation transmitting the desired signal, relative to all other non-pulsed signals in the scenario.

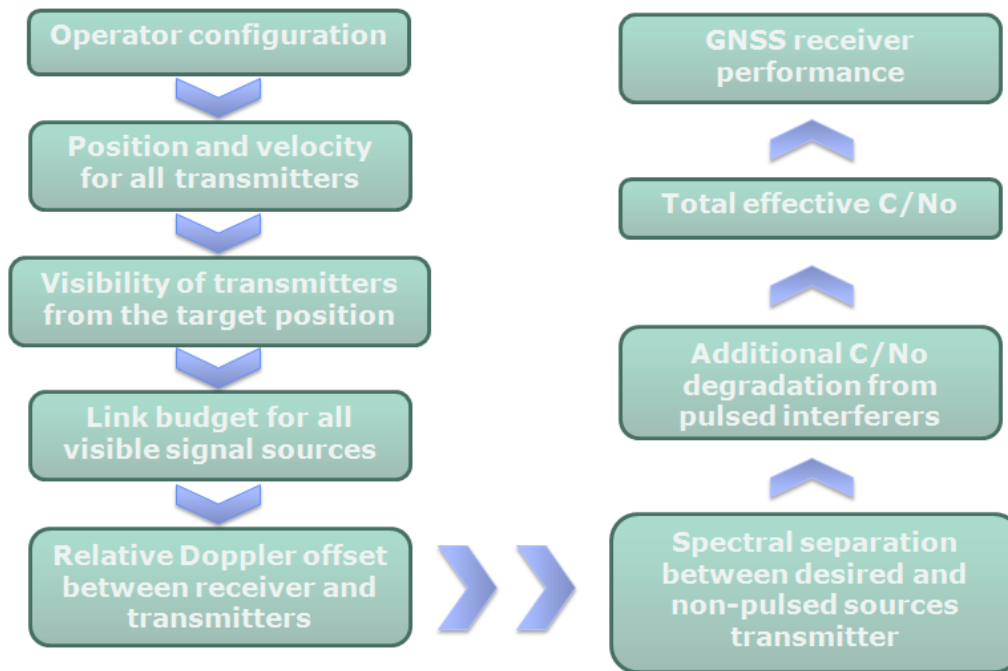


Figure 5-1: Software flux diagram of a model-based frequency-domain GNSS simulator.

For pulsed interferers, however, due to its temporal properties, the analysis approach should be based on statistical methods. Take, for instance, the broadly and officially accepted techniques reported in [Ref. 40]. These methods allow computing the additional degradation drawn onto the effective C/No, $(C/N_o)_{\text{eff}}$ by a set of visible heterogeneous pulsed sources.

Once the total instantaneous $(C/N_o)_{\text{eff}}$ is determined for every user position accounting for all interfering effects in the scenario, the receiver performance can be extracted from the available receiver model and data.

5.2.2 Budget of the Generated Data Volume

All processing steps previously described generate a certain amount of data that, if carefully studied, can help to identify the bottleneck of the process, and to provide hints to the optimization of the simulator in terms of required processing time and/or data storage.

To formalize the data budget breakdown, consider a scenario with a number $S = S_{\text{SAT}} + S_{\text{OTHER}}$ of navigation signal sources, consisting of S_{SAT} RNSS satellites (belonging to global or regional

constellations) and/or transmitters used (possibly not only) for navigation purposes³⁸, and S_{INT} non-navigation related signal sources exclusively acting as interferers. In any case, and as described in Chapter 3, every channel in an arbitrary GNSS receiver will be tracking one of the acquired navigation sources, and subject to $(S - 1) + S_{INT}$ interferers. Within this scenario, the simulation will be run for a number N_{POINT} of points on or above the Earth at N_T time instants.

According to this scenario and nomenclature, every processing stage in Figure 5-1 will produce the amount of data outlined in Table 5-2, and represented in numerical units. From this table, it is evident that, while other stages produce in the most cases a limited amount of values to be stored as intermediate results, the SSC computation is a highly time consuming phase of the simulation due to not only the amount of data here generated but also to the nature of the mathematical operators involved in their computation (see 5.2.6 for the mathematical definition of SSC). Let's see an illustrated example of this fact.

| Processing stage | Data budget |
|--|---|
| Position and velocity | $N_T \cdot [S + S_{INT}]$ |
| Visibility determination | $P \cdot N_T \cdot [S + S_{INT}]$ |
| Link budget calculation | $P \cdot N_T \cdot [S + S_{INT}]$ |
| Doppler frequency offset determination | $P \cdot N_T \cdot [S + S_{INT}]$ |
| Spectral separation determination | $P \cdot N_T \cdot S \cdot [(S - 1) + S_{INT}]$ |
| Total $(C/N_o)_{eff}$ | $P \cdot N_T \cdot S$ |

Table 5-2: Data budget produced within a characteristic simulator.

Given a particular scenario, set as in Table 5-3 to perform a $(C/N_o)_{eff}$ worldwide analysis with 2° grid spacing for both longitude and latitude axes, and a 10-day time span with a 2-minutes time resolution, about 117.95 million space-time points are to be processed to compute the link budget and the frequency Doppler shift from every visible satellite.

Assuming average numbers of visible satellites per RNSS system as in Table 5-3 (an extremely pessimistic case, for a typical receiver antenna elevation mask of 15°), it turns out that the total number of SSC values to be computed here (if Doppler-dependent SSCs are considered for all desired-interfering signal combinations in the scenario) exceeds 9.9×10^9 !. Therefore, even though the present computational technology is more than able to handle this processing load, the necessary calculation time might be excessive for certain applications, for which a faster estimation is required.

³⁸ Signal sources other than navigation satellites are assumed to transmit code-based ranging signals, compatible with the receiver structure developed in Chapter 3. Other types of ranging signals are considered out of the scope of this document. This decision has been taken based on the current tendency in radio navigation systems.

| Parameter | Value |
|--|---|
| Longitude span | [180E, 180W] |
| Latitude span | [90N, 90S] |
| Longitude grid spacing | 2° |
| Latitude grid spacing | 2° |
| Simulated time | 240 hours |
| Time step | 120 seconds |
| Desired RNSS signal | Galileo L1B (tracked PRN) |
| Interfering RNSS signals | Galileo L1B (other PRN) GPS L1 C/A CDMA GLONASS in L1 |
| Average number of visible satellites over time and user position | 6 (Galileo) 5 (GPS) 4 (Modernized GLONASS) |

Table 5-3: Simulation target scenario definition.

5.2.3 Determination of the Position and Velocity for User and Signal Sources

The first step of the frequency-domain GNSS software simulator shown in Figure 5-1 corresponds to the determination of positions and velocities for signal sources and users considered in the analysis, all values expressed on a common UTC time reference system. In case the time reference frame of the systems to be simulated diverges from UTC, as it is the case when simulating several of the GNSS systems outlined in Chapter 2, the correspondent time corrections [Ref. 7] would be applied for compatibility into UTC. It is imperative, then, to express both user and signal sources' position and velocities in a common time frame, which will be generally specified by the software operator, in terms of start (t_{start}) and end (t_{end}) times and an increment (Δt), to yield the N_T time instants referenced in Table 5-2.

Similarly, the positions and velocities of users and signal sources will be determined in a common coordinate reference frame of choice. For this application, the two reference systems considered more appropriate are ECI (or CRF) and ECEF (or TRF). ECI, or Earth-centred inertial, is a geocentric celestial frame, while ECEF (Earth-centred, Earth-fixed) is a terrestrial reference frame. The transformation between the two systems, extensively developed in [Ref. 7], implies four rotations to account for Greenwich sidereal time, nutation, polar motion, and precession. Additionally, the representation of the vector satellite-to-user in a local reference level is also of interest, especially to determine the gain of the user receiver and satellite antennas on the direction to target. Again, [Ref. 7] can be considered classical literature for all transformations here outlined.

User Position and Velocity. From the operator settings, the user position/trajectory and velocity are interpolated on the N_T time instants and respectively represented in a common coordinate reference system as $X_u^{Rx}(t)$ and $V_u^{Rx}(t)$ for the u -th simulated user or grid point (in case a user or worldwide analysis is set).

Signal Source Position. In a similar fashion, the position and velocity of every satellite to be simulated can be obtained on its orbit, computed from the correspondent instantaneous Keplerian and perturbed elements, if available, or broadcasted information. The particular algorithm for the recuperation of orbital information is different for GPS, Galileo, GLONASS and every SBAS, and can be extracted from the relevant ICDs. As an outcome of this process, the time evolution of position and velocity for the i -th satellite or signal source is represented on the common reference frame as $X_i^S(t)$ and $V_i^S(t)$.

5.2.4 The Visibility of Satellites and Interferers

In a simplified approach, the visibility of satellites and interference sources from every user point of view at any time is determined by applying a coordinate transformation of the user vector, from an ECI or ECEF system to a local level coordinate. In this resulting reference system, the vector from user to every signal source is defined and the visibility matrix formed with only those signal sources seen by the user with an elevation above 0° . Further rejection of signal sources is intrinsically added during the computation of the link budget (see 5.2.5) by the user antenna pattern, characterized by a certain elevation masking angle (typically, ranging from 10° to 15° for a typical GPS L1 C/A receiver).

5.2.5 The Simulated Link Budget and Relative Doppler Frequency Offset

The data available from the steps performed above allows the determination of satellite-to-user ranges, and the received power at the u -th user position, from the j -th signal component transmitted by the i -th satellite, $P_{iju}^{Rx}(t)$, as described in equation 3-5. Special attention should be paid here, as a transformation to a user based coordinate reference system is necessary to extract the gain of the user receiver antenna in the direction of the satellite, and an analogous operation is required to interpolate the gain of the satellite antenna towards the user.

The relative radial velocity, $V_{ui}(t)$, between the u -th user and the i -th signal source is defined by the position of the receiver $X_u^{Rx}(t)$ and satellite (or interferer) $X_i^S(t)$, and by the respective velocities $V_u^{Rx}(t)$ and $V_i^S(t)$. In these conditions, and omitting the time dependency for clarity of the equations,

$$V_{ui} = \frac{(X_u^{Rx} - X_i^S)}{\|X_u^{Rx} - X_i^S\|} \cdot (V_u^{Rx} - V_i^S) \quad [\text{m/s}] \quad 5-1$$

The relative radial velocity from equation 5-1 is used to compute the Doppler shift³⁹:

$$\Delta f = f_r - f_s \approx -\frac{V_{ui}}{c} f_s \quad [\text{Hz}] \quad 5-2$$

³⁹ Note that, according to this definition of Doppler frequency shift, $\Delta f > 0$ when receiver and transmitter approach each other and $\Delta f < 0$ when they move away.

where f_s [Hz] denotes the frequency of the transmitted signal, and f_r [Hz] the received frequency. Note that equation 5-2 describes the real theoretical shift due to the relative movement of transmitter and receiver, and not the Doppler frequency shift observed through an appropriate GNSS receiver, which might be affected by clock errors, ionospheric and tropospheric delays among other factors.

The equation introduced in 5-2 is a first approximation considered appropriate for the purpose of this software, and more detailed formulation (splitting the different relativistic effects and introducing potential theory) can be found in [Ref. 50].

As a final note, Δf is a function of the frequency, thus, every frequency underlies a different frequency shift and the frequency spectrum of the transmitted signal is rather compressed than simply shifted. As a simplification, however, the same value of Doppler frequency shift, computed from the carrier frequency, is applied to all frequency points of a particular PSD, prior to its use in the determination of the SSC between two particular signals over time, treated in the following section of this chapter.

5.2.6 A More Pragmatic Approach to the Spectral Separation between Signals

In 5.2.2, it has already been noted that the SSC computation is one of the main bottlenecks to be expected in the simulator under study. For this reason, several possibilities are here outlined, in an attempt to relieve this problem.

As a first option, in order to reduce the required computational cost, in some cases constant SSCs are used, without any loss of generality, but with a consequent numerical error on the output results, which can be of considerable magnitude (consider, for instance, the SSC of GPS L1 C/A – GPS L1 C/A, with values oscillating between -75 and -50 dB/Hz).

Although more time consuming, a more appropriate second option in terms of accuracy implies the computation of all necessary instantaneous SSC per user location, given a known set of Doppler frequency offset values. This technique, however, offers accuracy at the expenses of processing time.

A third approach to effectiveness, optimized within this section, consists of the offline calculation of the corresponding Doppler-dependent SSCs for all relevant signal combinations, for reasonable resolution and ranges of Doppler offset values (typical values are, for a static ground-based user, [-4, +4] kHz, or [-30, +30] kHz for a space-borne user like the ISS), and the interpolation of the necessary values from this data sets. It is important to note that extremely high resolutions in the Doppler offset axes are needed (in general, below 10 Hz) in order to obtain a clear representation of the effect on the SSCs of the spectral lines within the PSDs. This effect will be discussed later in this section, after the necessary mathematical definition of the SSC.

In the frame of this simulator, the effect of non-pulsed sources on the $(C/N_o)_{\text{eff}}$ is accounted by following the SSC-based approach. Given a pair of desired-interfering signals, s and j , with power spectral densities $\Phi_s(f)$ and $\Phi_j(f)$, the corresponding spectral separation coefficient, K_{js} , and the normalized power of the desired signal s through the receiver's filter, μ_s , are computed as:

$$K_{js}(\Delta f_s, \Delta f_j) = \int_{-\infty}^{+\infty} \Phi_{Tj}(f - \Delta f_j) \cdot \Phi_{Ts}(f - \Delta f_s) \cdot |H_R(f)|^2 df \quad 5-3$$

$$\mu_s(\Delta f_s) = \int_{-\infty}^{+\infty} \Phi_{Ts}(f - \Delta f_s) \cdot H_R(f) df \quad 5-4$$

Where the following definitions apply:

- K_{js} [1/Hz]: Spectral separation coefficient between signals s and j .
- μ_s [1]: Normalized power of the desired signal s through the receiver's filter.
- $\Phi_s(f)$ [W/Hz]: Power spectral density (PSD) of the signal s .
- $H_{Ts}(f)$ [1]: Frequency response of the transmission filter for signal s .
- $\Phi_{Ts}(f)$ [1/Hz]: Normalized power spectral density for power 1W transmitted through $H_{Ts}(f)$.

$$\Phi_{Ts}(f) = \Phi_s(f) \cdot |H_{Ts}(f)|^2, \text{ by definition } \int_{-\infty}^{+\infty} \Phi_{Ts}(f) df = 1W \quad 5-5$$

- Δf_s [Hz]: Doppler frequency offset of the desired signal s .
- $\Phi_j(f)$ [W/Hz]: Power spectral density (PSD) of the signal j .
- $H_{Tj}(f)$ [1]: Frequency response of the transmission filter for signal j .
- $\Phi_{Tj}(f)$ [1/Hz]: Normalized power spectral density for power 1W transmitted through $H_{Tj}(f)$.

$$\Phi_{Tj}(f) = \Phi_j(f) \cdot |H_{Tj}(f)|^2, \text{ by definition } \int_{-\infty}^{+\infty} \Phi_{Tj}(f) df = 1W \quad 5-6$$

- Δf_j [Hz]: Doppler frequency offset of the non desired signal j .
- $H_R(f)$ [1]: Frequency response of the frontend filter at the receiver.

On special occasions, especially when phenomena affecting the symmetry of the received post-correlation PSDs with respect to the carrier frequency are to be modelled (i.e. on-board payload and/or receiver impairments), or the signals under consideration are not centred on the very same carrier frequency, formulas in 5-3 and 5-4 must be used due to the non-symmetry of the 3-dimensional space $K_{sj}(\Delta f_s, \Delta f_j)$. The very same statement is also valid when the Doppler frequency offset in a particular scenario is expected to take unusually high values that can cause excessive filtering losses in the receiver RF frontend for any of the navigation signals. A potentially delicate case in this respect could be obtained in simulations involving space-borne target user.

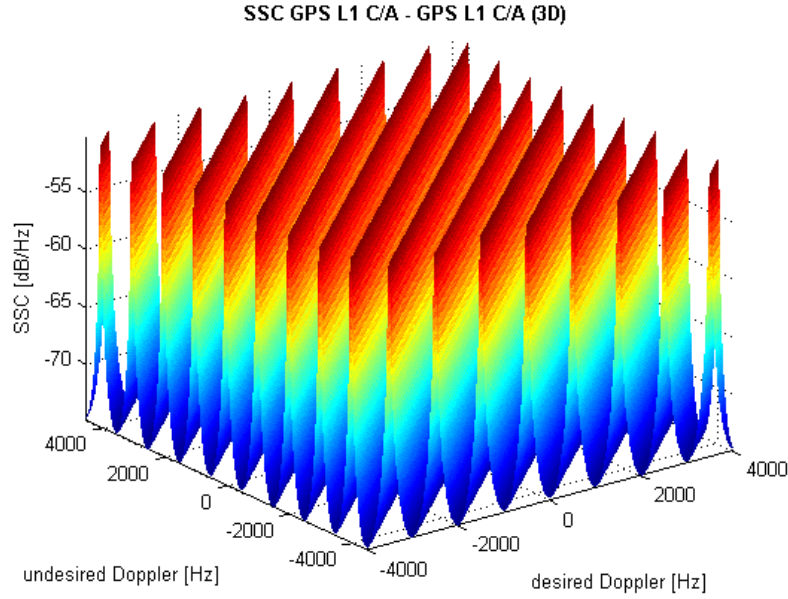


Figure 5-2: 3D plot of the SSC for fine structured GPS L1 C/A pair, as a function of the absolute Doppler frequency shifts.

In the vast majority of cases, however, the more general approach represented through the previous equations lacks practicality because of the symmetry of K_{sj} relative to the plane $\Delta f_s - \Delta f_j = 0$ (see Figure 5-2), and the definition of the spectral separation coefficient simplifies to $K_{sj}(|\Delta f_s - \Delta f_j|)$. The filtering losses affecting the desired signal (directly given by μ_s) can also be neglected in a well-engineered RF frontend.

To extend the practicality of this definition, and for the sake of completeness, let us remember now that the signal PSDs and the filter characteristic are usually available in tabulated form (and given as an input to the simulator), as a finite list of discrete points, equally separated in the frequency domain (respectively obtained from their measure by means of spectrum or network analyzers). Under this assumption, previous equations in this section can only be numerically approximated (obviously with a certain error) from the corresponding discrete versions of $H_R(f)$, $\Phi_{Ts}(f - \Delta f_s)$ and $\Phi_{Tj}(f - \Delta f_j)$ respectively, evaluated on a common frequency axis $f = \{f_0, f_1, \dots, f_{M-1}\}$, with $f_n = f_0 + n \cdot \delta f$, and δf the frequency resolution. By also assuming that discrete PSDs have been obtained taking all precautions to avoid any kind of distortion (spectral leakage, dispersion of spectral lines, etc.), it can be ensured that the estimation errors are only a function of the numerical methods used in the integration/interpolation processes, and the resolution of the Doppler offset axis.

At this point, it is appropriate to establish a navigation signal classification that will apply to all statements in this section unless otherwise specified and that will be used as a basis for comparisons. As similarly introduced in [Ref. 36], and accordingly adapted for the present purpose:

- Power spectral densities of ‘Type I’ are originated from navigation signals with non-periodical codes, regardless of their data modulation contents.

- ‘Type II’ will be used to identify PSDs of signals with periodic codes, from either Data or Pilot channels, this is to say, with or without data modulation.

In the following, two generic examples will be presented, for which the previous simplifications apply. When the PSDs of both navigation signals involved in the operation are of Type I, its correspondent SSC will show a global maximum when $\Delta f_s = \Delta f_j$ for all values of Doppler offset. An illustration can be found in Figure 5-3, which depicts the well known $K_{Sj}(|\Delta f_s - \Delta f_j|)$ of CBOCsin(6,1,1/11) – CBOCsin(6,1,1/11) and BPSK(1) – BPSK(1) for $H_R(f)$ an ideal brick-wall filter of bandwidth 20 MHz, and a Doppler offset resolution of 10 Hz.

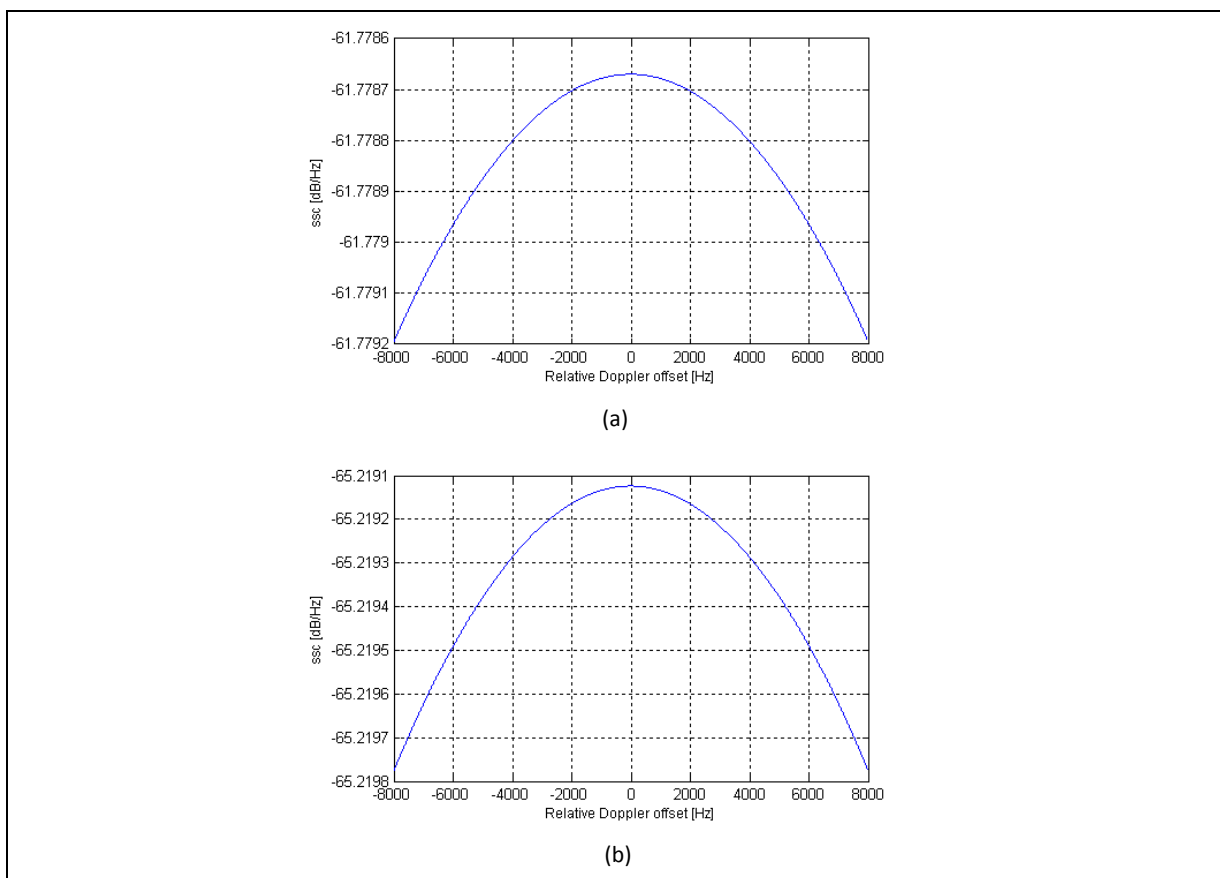


Figure 5-3: Representation of the spectral separation coefficient for signals of Type I.
(a) BPSK(1) – BPSK(1), (b) CBOCsin(6,1,1/11) – CBOCsin(6,1,1/11).

From the range of values in Figure 5-3, it is evident that the use of the constant value $K_{Sj}(0)$ gives enough confidence on the computation of the $(C/N_o)_{\text{eff}}$, and there is no practical need to increase the complexity of the algorithm.

On the other hand, when the PSDs under analysis are of Type II, the superposition of spectral lines originates an oscillatory pattern on $K_{Sj}(|\Delta f_s - \Delta f_j|)$ (initially mentioned in [Ref. 36]) that needs to be studied here with some more attention.

5.2.6.1 Study on the Frequency Pseudoperiodicity of the SSC Computed from Fine Structured Power Spectral Densities

The main objective of this subsection is the characterization of the oscillatory pattern observed in the preface of 5.2.6 and present in the SSC representation as a function of the Doppler frequency offset, when the considered signals use spreading pseudorandom codes of finite periods, and the data bit stream is considered of random nature. From the expression of the PSD for a navigation signal with periodic codes and navigation data in the most general case (previously derived in [Ref. 36] also assuming a random data stream) and assuming a receiver RF frontend of bandwidth β_r , the expression of K_{sj} equivalently expands to equation 5-8 where, for each PSD, L is the code length in chips, T_c is the chip period in seconds (and thus $L \cdot T_c$ is the code duration in seconds), f_d is the data rate in Hz and $w[]$ is a discrete series that weights the PSD spectral lines (a function of the code pulse shape, the code characteristics and the transmission and reception filter amplitude characteristics among other factors).

$$G_s(f) = \sum_{k=-\infty}^{+\infty} w_s[k] \cdot \text{sinc}^2 \left(\frac{f - \frac{k}{L^S \cdot T_c^S}}{f_d^S} \right); \quad G_j(f) = \sum_{n=-\infty}^{+\infty} w_j[n] \cdot \text{sinc}^2 \left(\frac{f - \frac{n}{L^j \cdot T_c^j}}{f_d^j} \right) \quad 5-7$$

From equations in 5-7, the PSD of a navigation signal can be seen as the addition of weighted sincs, regularly shifted and separated $1/(L \cdot T_c)$ Hz. Additionally, the width of all sincs is proportionally driven by the data rate in each case.

Under these conditions and after the proper analysis applied to K_{sj} (see equation 5-3), it is easy to understand that the observed oscillatory effect is due to the superposition of the spectral lines, and that the main period of the effect can be equivalently studied from equation 5-8, which represents the integrated superposition of two shifted delta combs of arbitrary periods and reference origins.

$$R = \int \left[\sum_{k=-\infty}^{+\infty} \delta \left(f - \frac{k}{L^S \cdot T_c^S} - \Delta f_s \right) \cdot \sum_{n=-\infty}^{+\infty} \delta \left(f - \frac{n}{L^j \cdot T_c^j} - \Delta f_j \right) \right] df =$$

$$= \sum_{k=-\infty}^{+\infty} \sum_{n=-\infty}^{+\infty} \delta \left(\frac{n}{L^j \cdot T_c^j} + \Delta f_j - \frac{k}{L^S \cdot T_c^S} - \Delta f_s \right) \quad 5-8$$

Restricting the study to the case in which both navigation signals have proportional spreading code durations (referred to a common fundamental frequency, as an extended practice nowadays), peak values of R will occur when condition in 5-9 applies, with $\text{GCD}(\bullet)$ the greatest common divisor operator, and γ an integer proportionality constant.

$$\left| \Delta f_S - \Delta f_j \right|_{peak} = \gamma \cdot GCD \left(\frac{1}{L^S \cdot T_c^S}, \frac{1}{L^j \cdot T_c^j} \right) \quad 5-9$$

This conclusion can be particularized as in equation 5-10 when both signals use codes of the same durations, i.e. $L^S \cdot T_c^S = L^j \cdot T_c^j = L \cdot T_c$. This situation is applicable during the computation of I_{ref} interference levels (see 5.2.7 for a definition).

$$\left| \Delta f_S - \Delta f_j \right|_{peak} = \gamma \cdot \frac{1}{L \cdot T_c} \quad 5-10$$

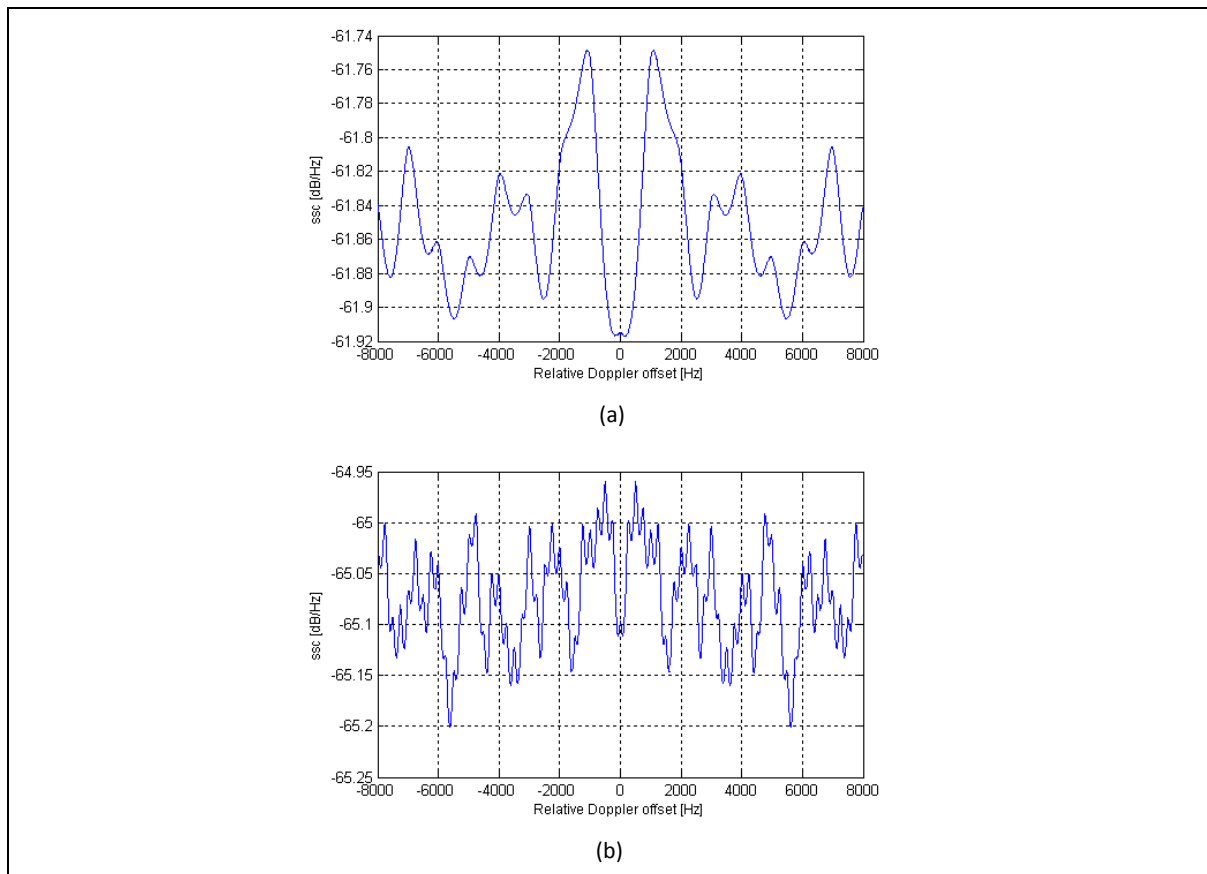


Figure 5-4: Representation of the spectral separation coefficient for signals of Type II, obtained for a Doppler offset resolution of 7.8049 Hz. (a) GPS L1 C/A – GPS L1 C/A (no data rate), (b) Galileo L1B – Galileo L1B (no data rate)

As such, this is a model valid to some extent, for it assumes that both delta combs are weighted with similar discrete amplitude series. This is the case when computing SSCs for the determination of the intrasystem interference level, or in a more general sense, when both navigation signals present identical modulations.

A graphical description of this case is shown in Figure 5-4, corresponding to results obtained from the following signals:

- **GPS L1 C/A:** modulated as a BPSK(1), with a ranging code 1,023 chips long, a code rate of 1.023 Mcps and a data rate of 50 sps (considered when specified). Produced for compliance with [Ref. 3], for two different spreading codes.
- **Galileo L1B:** CBOCs $\sin(6,1,1/11)$ modulated, with a Primary Code of 4,092 chips, a code rate of 1.023 Mcps and a data rate of 250 sps (considered unless otherwise noted). Generated according to specifications in [Ref. 6] for different spreading codes.

The reader can find a graphical display of these PSDs in Figure 5-5. Note that the reference PSDs (in red in these figures) are compliant with Annex A.

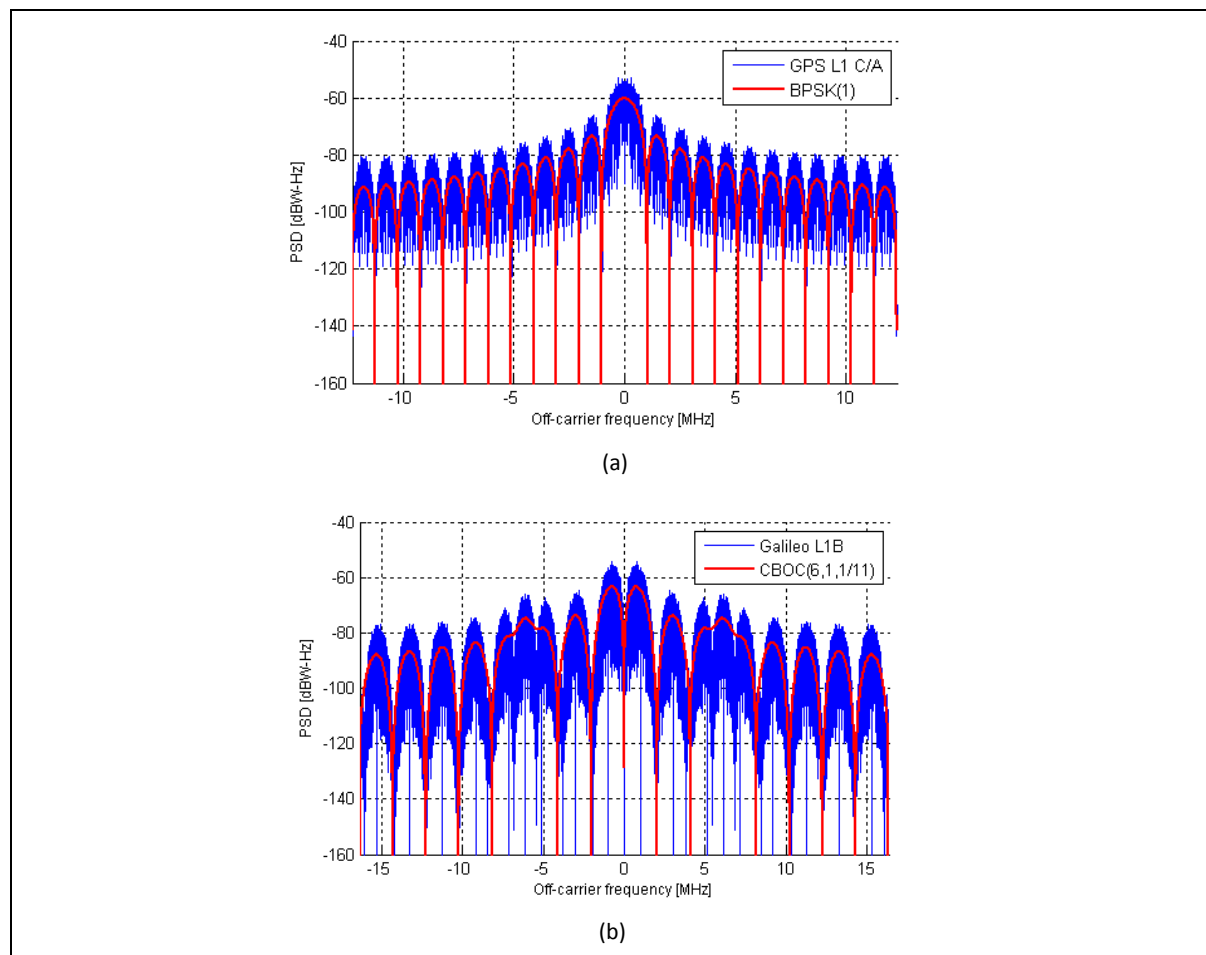


Figure 5-5: Used PSDs for (a) GPS L1 C/A and (b) Galileo L1B, with a frequency resolution of 7.8049 Hz.

For both pictures in Figure 5-4, ideal filters have been taken to model transmitters and receiver RF frontend filters, with 22 MHz and 20 MHz of respective bandwidth. Additionally, the used PSDs have been generated with of 7.8049 Hz resolution, and no data modulation. This configuration has been found more than adequate to confirm predictions here outlined. It is interesting to observe how peaks (or inflexion points in some occasions, due to insufficient resolution of the used PSDs) of

the corresponding SSC are located at multiples of 1 kHz and 250 Hz (as can be respectively seen in Figure 5-4a and Figure 5-4b). These numbers are equal to the inverse of GPS L1 C/A and Galileo L1B respective spreading code durations.

As depicted in Figure 5-6, when the SSC is computed between heterogeneous signal types, a second order more accurate analysis (including the data rate of the signals) is necessary in order to visually locate the effects of the spectral lines of the PSDs. Nevertheless, conclusions previously drawn can also be applied here, with oscillatory peaks appearing at multiples of 250 Hz.

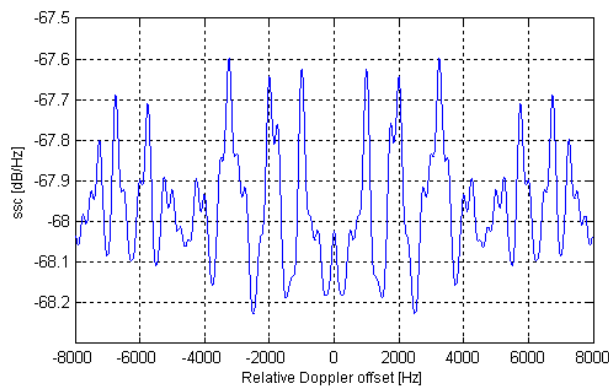


Figure 5-6: Representation of the spectral separation coefficient for signals of Type I and II, obtained for a Doppler offset resolution of 7.8049 Hz and the combination GPS L1 C/A (50 sps data rate) – Galileo L1B (250 sps data rate).

Note that the knowledge on the SSC fine structure here deduced goes beyond pure curiosity, as it is the key to accurate SSC computations for reliable model-based software simulations. The development here presented can even be intelligently exploited in the calculation of $K_{Sj}(|\Delta f_s - \Delta f_j|)$ in order to reduce the required computation time when a fast estimation is required. Along the same line, an algorithm proposed here to exploit this knowledge computes the SSC within a reduced set D of smartly selected relative Doppler offset points. Then the required values are interpolated from this data set through a low order algorithm.

Peaks of SSC versus the relative Doppler offset occur as specified in expressions 5-9 and 5-10. In a first approximation to also include the position of local minima (assumed to be located midway between local maxima) the set D is extended to equation 5-11, with N a positive integer different of 0, to more accurately describe the evolution of the SSC as a function of the relative Doppler offset.

$$D = \left\{ \frac{1}{2N} \cdot |\Delta f_s - \Delta f_j|_{peak} \right\} \quad 5-11$$

By using this methodology, the SSCs in Figure 5-6 would be respectively described, for N equal to the unit, through 32 and 128 Doppler offset points, with the correspondent reduction on computation and interpolation time (98.5% and 95.5% faster in each case), at the expense of a certain lack of numerical accuracy.

For the example provided in Figure 5-7, for instance, the error in the SSC value (for relative Doppler shifts in the range [-4 kHz, 4 kHz]) associated to the use of its fast estimation (with N equal to 2) stays below 0.014 dB in the 95% of the points, never being greater than 0.024 dB when linear interpolation is used. When cubic interpolation is considered, the percentile 95 and the maximum value of the error are 0.005 dB and 0.011 dB respectively.

It is imperative to highlight here that the numerical errors obtained in this example are negligible for many applications, especially when high data rates and codes of long duration are considered in the navigation signals involved. This is despite the fact that the set D proposed in equation 5-11 is suboptimal, because only local maxima of the SSC evolution are precisely located.

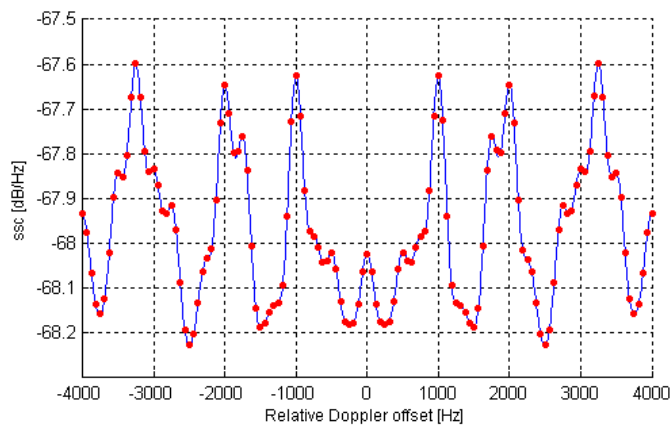


Figure 5-7: Representation of the spectral separation coefficient for Galileo L1B – GPS L1 C/A (in blue), estimated in a reduced set of Doppler offset points (in red dots, for $N = 2$).

As usual, it is left to the reader to decide whether a higher level of accuracy is required for her or his analysis. Obviously, further accuracy can be achieved with higher valued N , specially recommended when SSCs are computed between signals of short code duration and low data rates (i.e. between GPS L1 C/A - GPS L1 C/A).

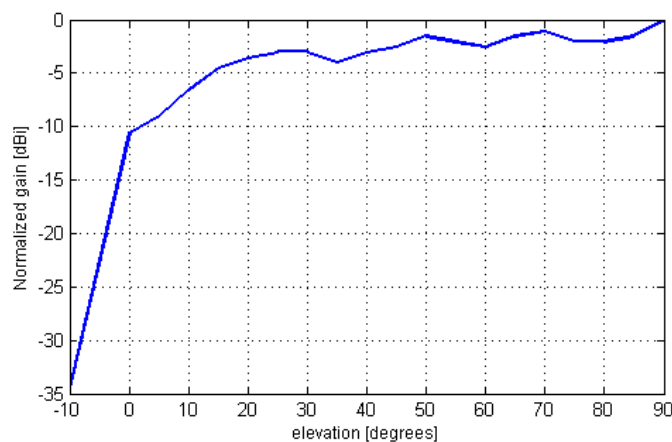


Figure 5-8: Normalized receiver antenna pattern in elevation, scaled to 4.3 dBi to be used for the application example.

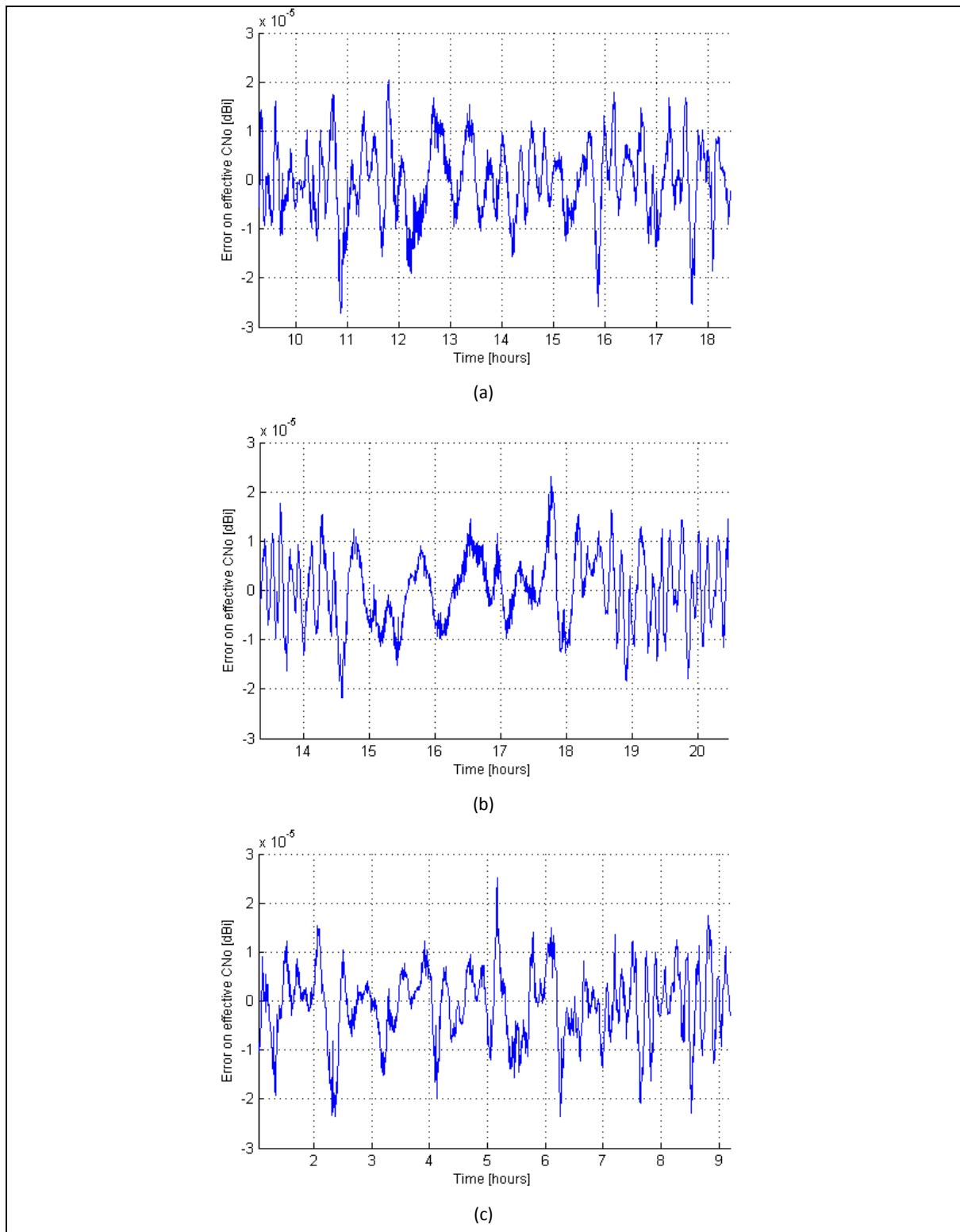


Figure 5-9: Temporal evolution of the error on the effective C/N_0 when the fast SSC estimation method is in use, as seen by a user in Western Europe, considering the scenario in Table 5-3, with noise level -202 dBW/Hz, atmospheric losses 0.6 dB and displayed for the Galileo satellite (a) SV4, (b) SV10, and (c) SV27.

As a final assessment, Figure 5-9 depicts the temporal evolution of the error on the computation of $(C/N_0)_{\text{eff}}$ with Galileo SV 4, 10 and 27 as source of the target desired signal, when the fast SSC estimation method is in use. For a static ground-based user receiver situated on Western Europe,

within the scenario in Table 5-3, a constant valued SSC has been taken equal to -65.1 dB/Hz for the signal combination Galileo L1B – Galileo L1B, and a Doppler dependent SSC specified for Galileo L1B – GPS L1 C/A (Figure 5-5, for both blue and red curves). GLONASS CDMA signals in L1 are deactivated for this example. Moreover, all signals and transmitted powers in the simulation are again compliant with specifications in [Ref. 3] and [Ref. 6] and an elevation mask of 0° has been applied on the receiver antenna pattern of Figure 5-8. In all these conditions, then, the error on the $(C/N_o)_{\text{eff}}$ in logarithmic units remains in the fifth decimal position for all Galileo satellites and time shots in this scenario, confirming the legacy of the proposed technique for the estimation of $(C/N_o)_{\text{eff}}$, a figure of merit with low sensitivity to numerical errors on SSCs.

At this point of the study, separate conclusions can be drawn for PSDs of ‘Type I’ and ‘II’. When the PSD of signals involved in the SSC computation can be approximated through the power spectral density of the code pulse shape, constant SSC values can be practically used without loss of generality. This conclusion can be extrapolated to navigation signals of high data rate relative to the separation of spectral lines.

However, the picture dramatically changes if the navigation signals are defined with codes of limited length and low data rate. In this case, special care must be taken in the selection of relative Doppler offset where the SSC is computed. As an application, a more effective method in terms of computational time is here proposed for a faster estimation of SSCs in a software-based analysis, when the spreading code durations are known for all relevant signals in the scenario. Further extension of this method is also suggested for the fast estimation of the code delay tracking jitter in a GNSS receiver of arbitrary architecture.

START

STEP_1: Read operator settings.

STEP_2: Load RF frontend filter characteristic.

STEP_3: Load PSD for desired and interfering signal.

STEP_4: Load transmission filter for desired and interfering signal.

STEP_5: Normalize PSDs for power 1W over the corresponding transmission bandwidth.

STEP_6: Apply next Doppler offsets to resultant PSDs.

STEP_7: Apply transmission filters on shifted PSDs.

STEP_8: Compute SSC over the RF frontend filter transfer function.

IF all values of Doppler offsets considered

GOTO EXIT

ELSE

GOTO STEP_6

END

EXIT

Figure 5-10: Algorithm for the SSC computation in the frequency domain, used in the reference tool.

All results presented relative to SSCs have been obtained through a highly configurable software tool coded in MATLAB© (only built-in commands used for numerical integration and interpolation) by the author of this work and based on the pseudo-code flow reported in Figure 5-10. This algorithm describes the calculation of spectral separation coefficients in the frequency domain from discretized power spectral densities and filter transfer functions. A critical step of the SSC computation, sometimes omitted, is the normalization of the PSDs of signals over the transmission filter bandwidth, for unitary transmitted powers.

Note that the previously introduced tool has been calibrated for maximal reliability against literature results, finding in [Ref. 37] and [Ref. 38] exemplar references.

5.2.7 The Interference Level Computation and the Effective C/N_0 Evaluation

Focusing our attention to one single baseband channel in the receiver, tracking one particular SV, and in a basic scenario in which no pulsed interferences are defined, the relevant formulation for the calculation of the effective carrier to noise power density at the input of the receiver, $(C/N_0)_{\text{eff}}$, is provided in the following.

For a given user position p and time instant t , the contribution of a set of N visible undesired non-pulsed signal sources on the overall interfering power density is given as:

$$I(p,t) = \sum_{j=1}^{N(p,t)} C_j(p,t) \cdot K_{js}(\Delta f(t)_s, \Delta f_j(t)) \quad 5-12$$

Where:

- C_j [W]: Received power of the non-desired signal source j , from the position p of the receiver, at time instant t .
- N [1]: Number of undesired non-pulsed signals sources visible from the user receiver.
- I [W/Hz]: Contribution of non-pulsed interferers to the noise power spectral density.
- K_{js} [1/Hz]: Spectral separation coefficient, as previously defined in 5.2.6.

Equations 5-3 and 5-12, are used to compute the interfering components listed below. Note that every term in this classification has been slightly modified from [Ref. 30], and every one of them shows a dependency with time and user position (here omitted for the sake of clarity).

- I_{ref} [W/Hz]: Equivalent noise power spectral density due to the aggregate interference from all signals transmitted by each satellite in the reference constellation, except from the target satellite whose PRN is being tracked.
- I_{int} [W/Hz]: Equivalent noise power spectral density due to the aggregate interference from all signals transmitted in the frequency band of interest by all satellites other than those in the reference constellation. This component can be seen as the addition of:

- I_{alt} [W/Hz]: Equivalent noise power spectral density due to the aggregate interference from all the signals transmitted in the frequency band of interest by all satellites of a specific alternate constellation.
- I_{rem} [W/Hz]: Equivalent noise power spectral density due to the aggregate interference from all the signals transmitted in the frequency band of interest by all remaining satellites; i.e., those that are not in either the reference constellation or the alternate constellation.
- I_{ext} [W/Hz]: Equivalent noise power spectral density due to the aggregate interference from all radio signals other than those previously accounted. In this case, this component will include the contributions of all non-pulsed interference.

Then, the effective carrier to noise power density ratio (also as a function of time and user position), measured at the output of the receiver frontend in linear units, is derived for every visible satellite in the reference constellation as:

$$\left(\frac{C}{N_o}\right)_{eff,i}(\Delta f_s, \Delta f_j) = \frac{C_S^i \cdot \int_{-\infty}^{+\infty} \Phi_{T_s}(f - \Delta f_s) \cdot H_R(f) df}{\left[N_o \cdot \int_{-\infty}^{+\infty} \Phi_{T_s}(f - \Delta f_s) \cdot H_R(f) df + \sum_j C_j \cdot \int_{-\infty}^{+\infty} \Phi_{T_s}(f - \Delta f_s) \cdot \Phi_{T_j}(f - \Delta f_j) \cdot |H_R(f)|^2 df \right]} = \frac{C_S^i \cdot \mu_s(\Delta f_s)}{N_o \cdot \mu_s(\Delta f_s) + \sum_{j=1}^N C_j \cdot K_{j_s}(\Delta f_s, \Delta f_j)} = \frac{C_S^i \cdot \mu_s(\Delta f_s)}{N_o \cdot \mu_s(\Delta f_s) + I_{total}} \quad 5-13$$

With:

C_S^i [W]: Power level of the useful signal, received from the i -th SV (measured at the antenna output).

N_o [W/Hz]: Total thermal noise power spectral density. Computed as:

$$N_o = N_o^{floor} + N_o^{rx} \quad 5-14$$

N_o^{floor} [W/Hz]: Thermal noise floor from the receiver environment and other white.

N_o^{rx} [W/Hz]: Contribution of receiver to thermal noise power density.

I_{total} [W/Hz]: Total interfering power spectral density. Computed as:

$$I_{total} = I_{ref} + I_{int} + I_{ext} = I_{ref} + (I_{alt} + I_{rem}) + I_{ext} \quad 5-15$$

Following this approach, for every position p and time instant t , this technique estimates the $(C/N_o)_{eff}$ associated to every active satellite in the reference constellation, as seen by any of the tracking channels within the GNSS receiver. It is evident that all formulations and classifications here given can be easily extrapolated to all sorts of scenarios, covering all possibilities in Table 5-1 and beyond.

Although this technique is only suitable for the determination of the interfering effect of non-pulsed interference sources, the correspondent instantaneous degradation of the $(C/N_o)_{eff}$ can be accordingly computed following the well accepted approach described in [Ref. 40], where a particularization for DME/TACAN or JTIDS/MIDS transmitters is presented.

As a final note, it is important to realize that all interfering signal sources here accounted are reduced, through this method, to equivalent sources of flat spectrum transmitted signals.

5.3 *Part 2: Evaluation of the Receiver Performance*

Section 5.2 has presented a generalist approach to the estimation of interfering power spectral densities due to GNSS satellites and other sources on a given user position, and the temporal evolution of the $(C/N_o)_{\text{eff}}$ evaluated at every user location for every satellite in the target constellation.

Taking the $(C/N_o)_{\text{eff}}$ distribution previously computed, and in order to complete the statistical evaluation (in terms of both accuracy and precision) of the receiver performance in tracking operation within the user position, in the following three numerical methods are exposed to obtain values of mean and jitter for both code delay and carrier phase estimations in every of the baseband channels.

Note that all comments and strategies introduced in the following are relative to structures compatible with the one-way range determination method, and always assume a passive role of the receiver.

5.3.1 The Deterministic Approach

This approach happens to be the cheapest one in terms of computation time and power, and it is included here exclusively for the sake of completeness. Despite its simplicity, this approach lacks of flexibility when several receiver channel architectures are to be studied. It foresees the pre-computation of estimated code delay and carrier phase estimation jitter curves through the evaluation of the appropriate mathematical model for a given fixed range of $(C/N_o)_{\text{eff}}$, receiver architecture and signal to be tracked, and the interpolation of such curves for every instantaneous $(C/N_o)_{\text{eff}}$ estimated value.

| Parameter | Value |
|------------------------------|--------------------------------------|
| Signal to track | BOCsin(1,1) |
| $(C/N_o)_{\text{eff}}$ range | 40 to 70 dBHz |
| Discriminator type | Early Minus Late Power (EMLP) |
| Early-Late spacing | 0.01, 0.025, 0.05, 0.1 and 0.5 chips |
| Code Loop bandwidth | 5 Hz |
| Integration time | 4 ms |
| Simulation duration | 10 s |
| RF frontend bandwidth | 4 MHz |

Table 5-4: Signal and receiver baseband processing channel architecture for which results are depicted in Figure 5-11.

As an illustrative example of this trivial methodology, Figure 5-11 depicts the dependency of the code delay estimation jitter with the value of $(C/N_o)_{\text{eff}}$ for a receiver baseband channel with the parametrical characteristics in Table 5-4.

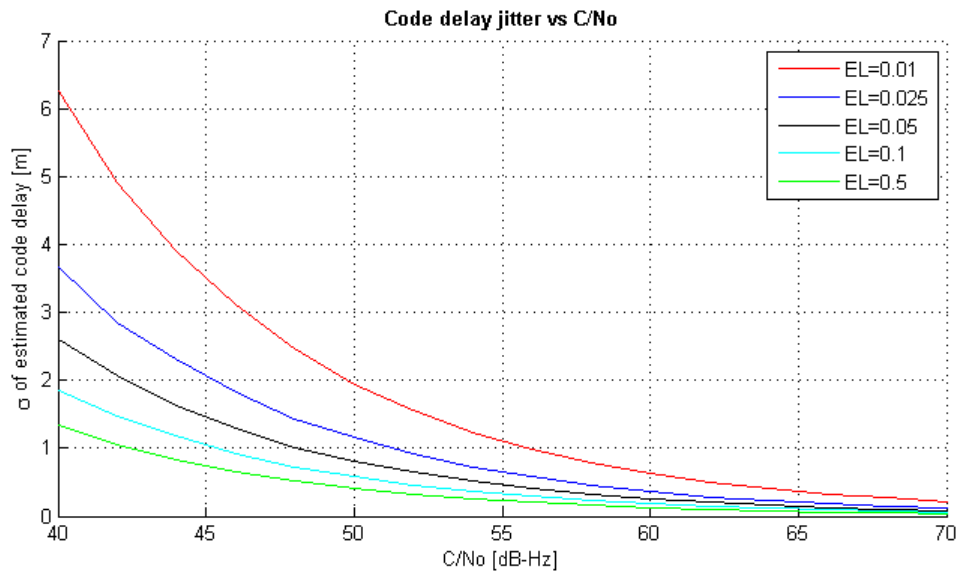


Figure 5-11: Code delay estimation jitter versus effective C/N_0 , for a number of receiver architectures (Early-Late spacing values in units of chips).

Note that in this example, only the precision of the tracked code delay would be statistically determined. Similar plots for the mean value of the estimated code delay (and similar statistics for the estimated carrier phase) as a function of the parametric configuration of the receiver would be required in order to interpolate its value.

5.3.2 The Bit-True Technique

The second simulation technique to be considered for the modelling of a navigation receiver channel is commonly known as ‘bit-true’. This denomination suggests a high degree of similarity between the structure of a real receiver channel and its simulated implementation, which is generically composed of the modules outlined in the following, sequentially called within a continuous loop.

The **Navigation Signal Generator** has as main function the emulation of the satellite broadcasted signal. Depending on the desired level of accuracy and the particular on-board payload impairments to be introduced in the simulation, several factors are to be included in the modelling of the navigation signal. These factors can range from elemental features, such as the carrier frequency, the spreading code, chip rate and pulse shaping, the data rate and navigation frame, to more complex hardware-related characteristics such as the non-linear amplitude and phase responses of TWAs of SSPAs at the satellite payload, the phase noise and stability of the on-board clocks, or the in-phase/quadrature imbalance of the payload. In any way, the navigation signal produced through this approach is represented as a series of samples taken at a regular sampling rate, which is a function of the intermediate frequency selected for the simulation and high enough to account for the spectral spreading due to the non-linear behaviour of on-board high power amplifiers if modelled.

Note that further lower boundaries on the sampling rate are introduced by the variation rate of the propagation models included in the following channel module. As an example, the multipath model considered for GNSS applications consist of 4 rays with delays between 0.25 and 1 ns, and the sampling rate of the signal must be higher than or equal to 4 GHz for consistency. This implication would force the generation of 4 million signal samples to simulate a complete spreading code duration of 1 ms in GPS L1 C/A. However, depending on the application of the simulator itself, the sample rate can be reduced to chip level or even to bit level, reducing in this way the runtime of the simulation and the volume of generated data.

After the signal generation is completed for the overall simulated time, it is transferred to the **Channel Module** and noise, multipath or any other propagation effects characteristic of the satellite channel added to the signal in order to enhance the realistic behaviour of the simulator. In this context, this is most probably the driving module when a Monte Carlo approach is selected, as most of the parameters of random nature are to be found here. Take, for instance, the AWG noise (generated to force a particular value of C/N_0), the direction of arrival of multipath rays (that affects the multipath rejection level induced by the receiver antenna gain), or the power fading due to atmospheric events in the LOS between satellite and receiver.

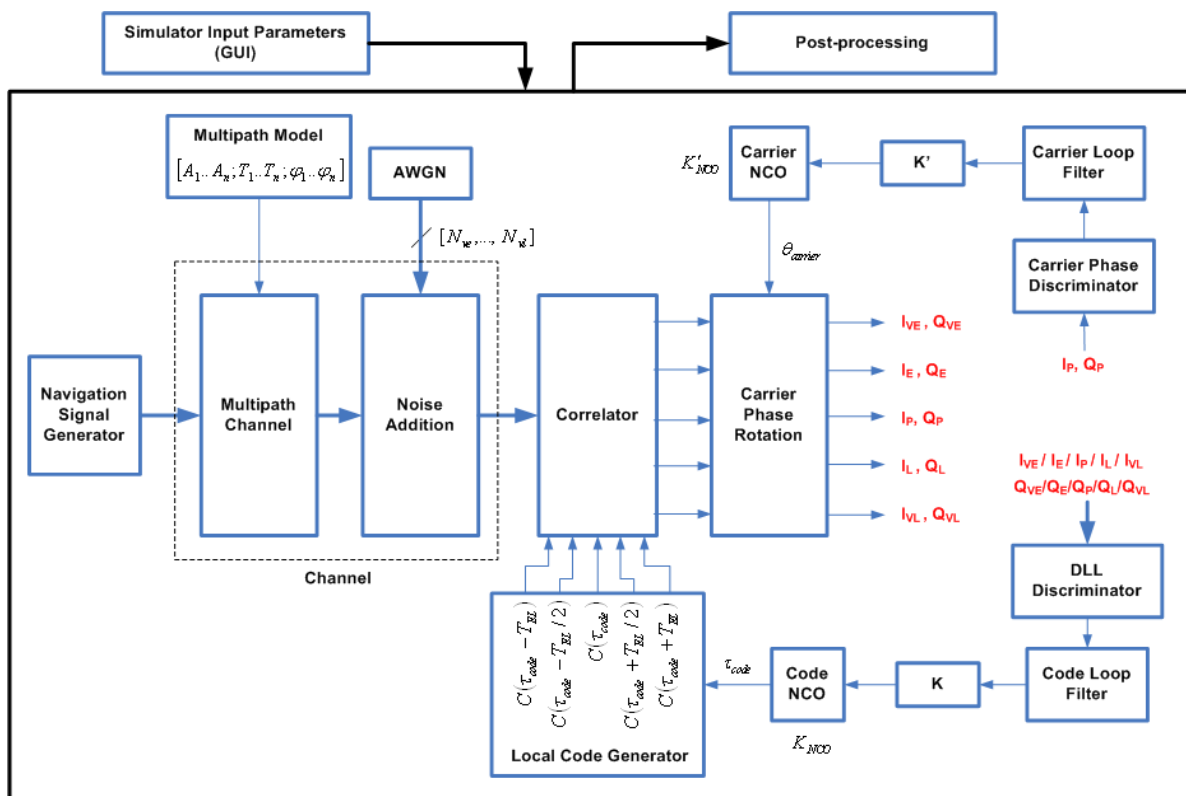


Figure 5-12: Equivalent scheme for the performance simulation of a single receiver channel, using a bit-true technique.

At the output of the channel module, the signal is ready to be processed towards the recovery of all those magnitudes considered of interest for the determination of the user's position in the simulation, i.e. code delay and carrier phase estimates, and demodulated data. The **Carrier Phase Estimation Loop**, essentially used to perform a carrier and Doppler shift conversion to baseband, recursively estimates and reduces the error between the phases of the received carrier and the locally generated signal. The phase recovered from the incoming signal provides information about

the velocity of the tracked satellite and an ambiguous estimation of the user-to-satellite distance, which can be integrated in professional applications to reduce the noise of the code delay unambiguous range determination (obtained from the **Code Delay Estimation Loop**) through methods like the Carrier Smoothing, or to get centimetre error level positioning, such as in RTK techniques. The behaviour and limitations of PLL and Costas Loops, relevant at this point, are extensively treated in the literature, and will not be studied here.

After the carrier removal, the despreading of the received signal is required in the **Code Delay Estimation Loop** as a further step towards the demodulation of the navigation data embedded in the received signal, and in order to obtain a non-ambiguous⁴⁰ estimation of the range to the satellite from the estimated propagation delay of the signal. The code delay estimation loop is based on a classical multicorrelator DLL structure that allows (through the **DLL Discriminator**) the estimation of the error of the delay in the locally generated code replica relative to the observed in the received signal. This estimation is then passed through a low-pass filter of narrow bandwidth that limits not only the noise of the input signal transferred into the estimation of the delay error but also the auto-induced noise level of the closed loop. This signal is then used to command the **Local Code Replica Generator**, which produces a local copy of the spreading code, and replicates it with accumulating delays equal to the correlator spacing $T_{EL}/2$. In Figure 5-12, for instance, a 5-correlator configuration is depicted, receiving local code replicas delayed $-T_{EL}$, $-T_{EL}/2$, 0 , $T_{EL}/2$, and T_{EL} relative to the estimated delay error. It is imperative to note here that the slope of both code delay and carrier phase error discriminators must be normalized to 1, as shown in the example of Figure 5-13, in order to produce an unbiased estimation of these magnitudes. In the real receiver structure, this normalization is done by means of the C/N_0 estimation that can be skipped at simulation time if necessary. In Figure 5-12, this normalization for both code and carrier phase discriminators is respectively accomplished through the gains K and K' .

Code delay and carrier phase estimation loops can be disposed for coherent or non-coherent operation. The first approach requires a correct carrier subtraction before the spreading code of the received signal can be removed. The second disposition, shown in Figure 5-12, combines both closed loops to work simultaneously. More details about the code delay and carrier phase synchronization are given in Chapter 3.

Finally, once the received signal is down-converted to baseband and the spreading code is correctly removed (with code and carrier phases tracked over time), the navigation data frame can be recovered from the output of the code delay estimation loop. Note that this simulation approach is characterized by a long runtime due to the high number of samples to process to obtain reliable statistics for all parameters that characterise the operation of such a receiver (i.e. the jitter of code delay and carrier phase estimations or the bit error rate of the demodulated data). The main proportion of the execution time of a simulator coded according to this method is spent in the operation of all correlators within the DLL. The reduction of the required time for this operation is precisely the idea behind the following simulation technique, outlined in 5.3.3.

⁴⁰ GPS L1 C/A, for instance, does not provide a means for non-ambiguous user-to-satellite distance estimation based on code delay, as the ranging code in this case has a duration of 1 ms, sensibly lower than the minimum range to any visible satellite. Ambiguities of the pseudorange from code delay are to be solved at application level.

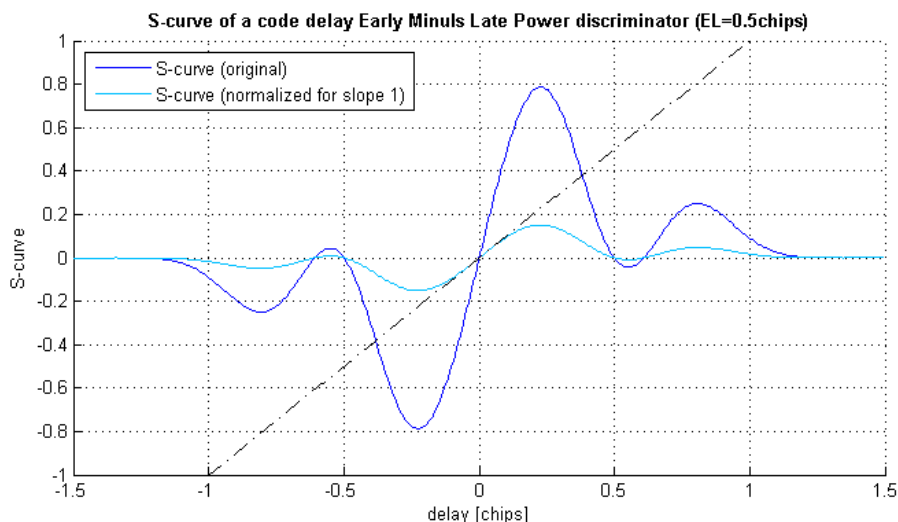


Figure 5-13: S-curve normalization for a code delay EMLP discriminator, for a value of Early-Late spacing equal to 0.5 chips, as seen for a BOCsin(1,1).

5.3.3 A Modified Semi Bit-True Method

The so-called semi bit-true method applied to the simulation of GNSS receiver baseband channels aims to reduce the overall runtime of the simulations by precomputing the cross-correlation function (CCF) of pulse shapes in the received and locally generated spreading codes for an appropriate range of the code delay error. This precomputed function can already contain the effects of, for instance, the bandlimitation and group delay of the RF frontend, and the uncalibrated phase centre of user receiver antenna.

In the **Code Delay Estimation Loop**, the pre-computed CCF is then interpolated at a frequency equal to the chipping rate, at the working point of every correlator in the system (a function of the instantaneous estimated code delay) to yield the input to the **Channel Module**. In the **Channel Module**, the AWGN samples, which in 5.3.2 were added to the generated signal prior the correlation, need to be correlated in every correlator channel with the delayed autocorrelation function (ACF) of the locally generated pulse shape in order to obtain appropriate noise signals to be added at the output of every correlator in the DLL. This step is accomplished through the method outlined by J.K. Holmes in [Ref. 47]. The rest of steps in this approach do not differ from the bit-true method, and are illustrated in Figure 5-16.

Note that this illustration and Figure 5-12 show mathematically equivalent code tracking structures.

On one side, every channel of the system in Figure 5-12 can be modelled in open loop as in Figure 5-14, where $x_R(t)$ is the received signal, a_i and τ_i correspond to the amplitude and delay of every considered multipath ray in the propagation channel, $n(t)$ denotes the AWG noise, $x_L(t)$ is the locally generated signal, and $\phi(t)$ and $\varepsilon(t)$ are the tracked, time-dependent carrier phase and code delay. In these conditions, $x_R(t)$ is obtained from equation 5-16, and fed to equation 5-17.

$$x_R(t) = \sum_i a_i \cdot x_R(t - \tau_i) + n(t) \tag{5-16}$$

$$s(t) = (1/T_{\text{int}}) \int_{T_{\text{int}}} e^{j\phi(t)} \cdot x_L(t - \varepsilon(t)) \cdot x_R(t) dt + (1/T_{\text{int}}) \int_{T_{\text{int}}} e^{j\phi(t)} \cdot x_L(t - \varepsilon(t)) \cdot n(t) dt \tag{5-17}$$

From equation 5-17, and assuming a non-coherent code delay discriminator, the output of the correlator in Figure 5-14 simplifies to:

$$s(t) \cong e^{j\phi} \cdot \left[\sum (a_i \cdot R_{RL}(\varepsilon(t) - \tau_i)) + N_L(t) \right] \tag{5-18}$$

With $R_{RL}(t)$ and $N_L(t)$ the complex CCF of respectively $x_R(t)$ and $n(t)$ and the locally generated signals conveniently delayed for every correlator in the DLL.

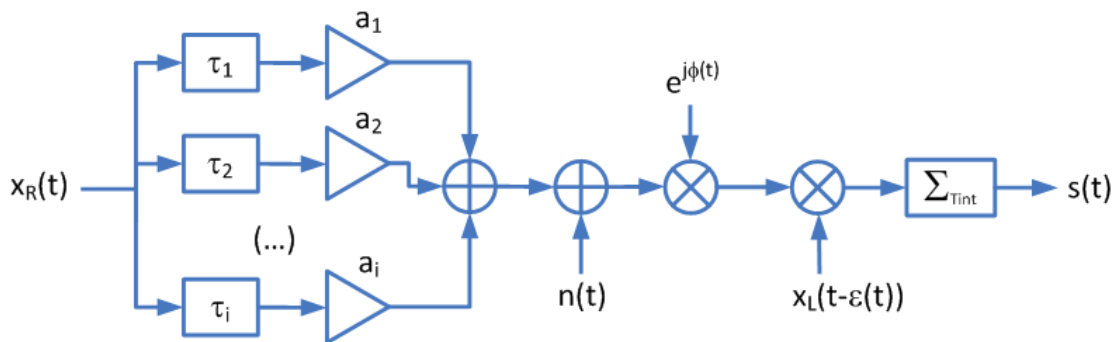


Figure 5-14: Simplified model for a bit-true GNSS receiver channel simulator.

On the other side, the scheme of the semi bit-true simulator in Figure 5-16 can be simplified in open loop as shown below, and with the time response mathematically outlined by equation 5-18.

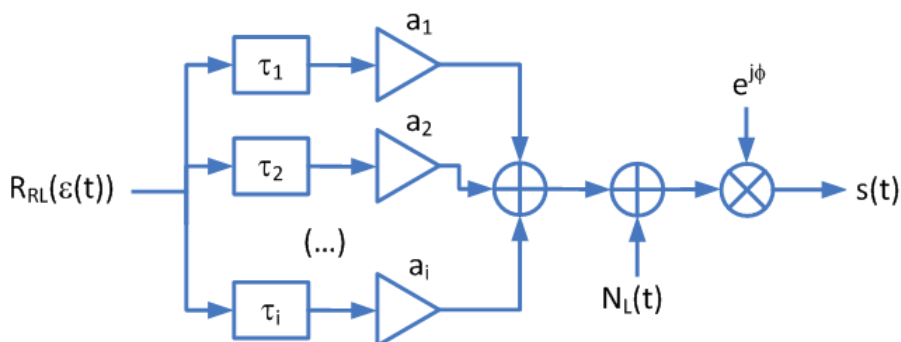


Figure 5-15: Simplified model for a semi bit-true GNSS receiver channel simulator.

This is a simulation technique that performs faster than the one outlined in 5.3.2. Nevertheless, it is affected by a series of limitations. In its current state, this simulation technique is only valid for non-coherent code delay discriminators. Additionally, the results produced by a simulator based on

this technique cannot account for the effects of a data stream modulated in the received signal, and the demodulation of navigation data cannot be emulated. Furthermore, as the sampling rate of the simulation in this case is limited to the chipping rate of the received signal, a secondary loop would be required to include multipath delays shorter than the chipping period.

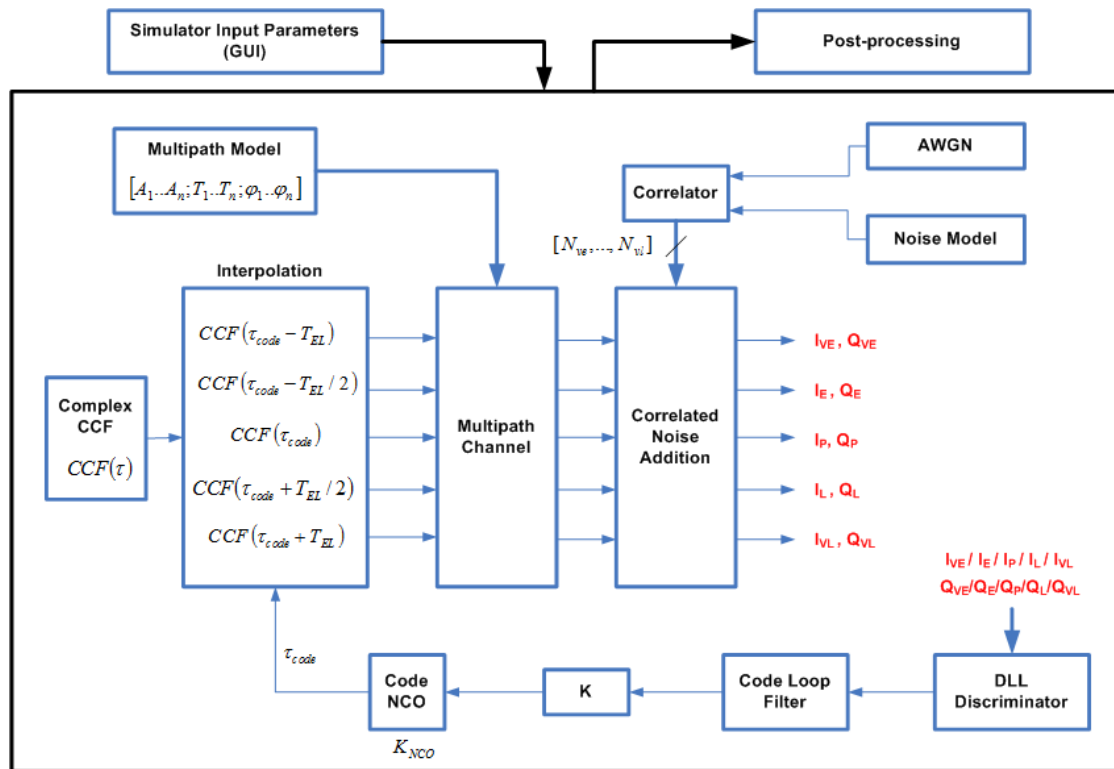


Figure 5-16: Equivalent scheme for the performance simulation of a single receiver channel, using a semi bit-true technique.

Following this very same approach, a software simulator of a navigation receiver baseband channel has been specifically coded to support the developments in Chapter 6 and Chapter 7. This software tool is designed to determine the code delay tracking performance degradation in terms of both accuracy and precision of a parametrically configurable baseband chain, given the following operator-provided information:

- The duration of the simulation and resolution of the time axis, which is equal to the integration time (assumed coherent with the data bit durations).
- Co-polar and cross-polar gain patterns⁴¹ of the antenna in use, given as a function of elevation and azimuth. The co-polar pattern will affect the LOS and the interference signals, while the cross-polar gain will be applied to multipath reflected signals.
- The precomputed complex ACF and CCF functions between received and locally generated spreading codes (also including the effects of the antenna phase centre unknown position, and the phase delay introduced by the RF frontend).

⁴¹ In this case, the terms ‘co-polar’ and ‘cross-polar’ make reference to the antenna gain respectively seen by RHCP and LHCP signals.

- The LOS direction of arrival, to be used to obtain the antenna gain in the direction of the tracked satellite.
- The parametrical configuration of the multipath model (if enabled), given in terms of amplitudes, delays and directions of arrival of all reflected rays (this last parameter randomly generated within user-specified elevation and azimuth ranges), and the relative reflected power factor.
- The flat-spectrum interference source (if enabled), with configurable direction of arrival and power.
- The configuration of the code delay tracking loop.
- The link budget from the satellite antenna output to baseband chain input, and the range of C/N_0 values to sweep for the determination of performances.

In the simulator, a Monte Carlo analysis is combined in two layers to characterize the propagation channel between the user and one given visible satellite. In a first layer, AWG noise series of specific power are generated and correlated with the locally generated code to obtain $N_L(t)$, and eventually added to the output of the correlators to emulate changing channel conditions. In a second layer, the multipath environment is randomly generated following the user-defined distributions for amplitudes, phases, and elevation angles of arrival in every reflected ray. In every execution of the simulator, both levels of the Monte Carlo approach coexist to produce random instances of noise and multipath conditions, later passed to the kernel for its evaluation. Then, the results of multiple executions are taken into account for the extraction of statistical parameters such as the mean and/or the 1-sigma of code delay tracking errors.

5.4 Chapter Summary

This fifth chapter introduces a number of classical and innovative techniques used in the software simulation of GNSS navigation systems and receivers. Part 1, presents a new approach, computationally more efficient, to calculate the spectral separation between navigation signals. Part 2 develops on a fast method for the performance simulation of a code delay tracking loop within a given GNSS receiver channel.

All contents in this chapter have been presented and developed to be used in forthcoming sections of this document, and as such, will be referenced throughout the upcoming chapters of this thesis.

CHAPTER 6

A ROBUST BIAS DETECTION METHOD IN THE FREQUENCY DOMAIN FOR CODE DELAY ESTIMATION APPLIED TO MODERN NAVIGATION MODULATIONS

6.1 *Preface*

The present chapter develops an innovative method in the frequency domain for code delay false lock detection and resolution, applicable to GNSS receivers compatible with subcarrier navigation modulations.

This new technique is based on the cross-spectrum estimation between the cross-correlation of received and locally generated spreading codes, and its well-known theoretical non-shifted auto-correlation. The code delay bias is then obtained back in the time domain, and subtracted in closed loop from the output of the numerically controlled oscillator that generates the delayed code replicas in a classical early-prompt-late GNSS receiver architecture.

Parametrical optimization pending (to be included in a future release), this innovative technique already shows an entire reduction of systematic errors on the estimated code delay in AWGN channels for BOCcos(10, 5) on Galileo E6a and BOCcos(15, 2.5) on Galileo E1a, with virtually no additional performance degradation in terms of code delay estimation jitter.

6.2 *Background*

In the near future, new and improved subcarrier-based navigation modulations such as BOC, AltBOC, TMBOC or CBOC will be implemented (take L1C, L1M or L2M in modernized GPS, or all signals in E1 and E5 in Galileo, for a few examples) and extensively used in order to ensure compatibility and interoperability between existing and planned navigation satellite systems, allowing at the same time sufficient precision and accuracy in the code delay tracking operation⁴². The design of GNSS receivers supporting these types of modulations, however, requires additional considerations due to the structure of the cross-correlation between the chip shaping function of the received PRN and the pulse characteristic of the locally generated spreading code replica.

In this context, and due to the fact that the code delay loop embedded in a given receiver channel bit synchronization structure is susceptible to locally lock on one of the multiple suboptimal stable points of the aforementioned cross-correlation, the time evolution of the code delay

⁴² Although BPSK-like signals do not present multiple cross-correlation lobes and thus they are not likely to cause DLL false lock, the use of this type of modulation yields higher estimated code delay jitter and therefore a lower positioning precision.

estimation and the corresponding pseudorange determination may be affected of a systematic error or bias, which will additionally lead to inaccurate code removal from the compound received signal, and increased BER/FER on the navigation data stream recovered from the tracked satellite.

The strength of the method here proposed resides in the determination of the code delay estimation bias by applying the optimal filtering principle in the frequency domain to resolve eventual systematic errors in a closed-loop structure.

6.3 *Development Methodology*

The development of the proposed technique will start with a formalistic statement of the problem, i.e. the presence of a systematic code delay error, and of its causes and effects on the quality of the positioning solution.

Once the theoretical justifications are completed, a novel approach to the bias detection and resolution will be presented, and its performance determined through a series of experiments on a semi-bit-true GNSS receiver software simulator specially adapted for the occasion (see Chapter 5 for details). Results will then be summarized for a series of relevant scenarios, drawing special attention to the sensitivity of its performance to operational parameters of the receiver such as the code pulse shaping of the incoming signal and the local replica and the sampling frequency of the tracking loops, among others.

Additionally, and as part of the conclusions, the necessary modifications on the classical structure of a DS-CDMA navigation receiver will be studied to support this bias detection method, making of the proposed idea an applicable technique to cope with biases induced by modulation related issues.

6.4 *Sources of Bias on the Code Delay Estimation*

In general, a false lock of the delay locked loop (DLL) on one of the secondary lobes of the autocorrelation function of the received signal code is susceptible to induce a systematic error on the estimation of the code delay. Other factors, out of the scope of this article, are the instability or miss-calibration of the antenna phase centre, relevant for high accuracy applications, or the group delay of the RF frontend filters.

Given the structure of the cross-correlation of a BOCcos(10,5) or a BOCcos(15, 2.5), schemes to respectively support PRS services in future Galileo signals E6A and E1A (see Figure 6-1 for their cross-correlations), a high probability⁴³ exist that the initial values of τ_{0L} used during the pull-in of every satellite to track are forcing the lock of the DLL on a secondary lobe of the cross-correlation.

Additionally, other factors less probable directly related to the dynamics of the received signal can induce the stable lock point of the DLL to jump from the main lobe to a secondary peak.

⁴³ The probability of false lock in this context is inversely proportional not only to the ratio between amplitudes of main and secondary lobes in the CCF but also to the distance in time between main and secondary lobes.

A sudden drop on the effective post-correlation C/N_0 would increase the jitter of the code delay estimation and a permanent bias if not corrected. This condition could be induced by a drop in the received signal power (caused by propagation effects such as shadowing or atmospheric scintillation), or a rise on the effective noise floor due to external interference.

In cases when the relative dynamic between the tracked satellite and the user presents a high gradient, with estimated instantaneous code delay differences higher than the distance in time lag from the main lobe to any of the secondary peaks of the cross-correlation, a false lock might take place, with a higher probability for BOCcos(15, 2.5) than for BOCcos(10,5).

In a similar fashion, changing multipath conditions affecting the shape and position of the main lobe of the cross-correlation function are prone to bring the optimal tracking point close to a suboptimal peak.

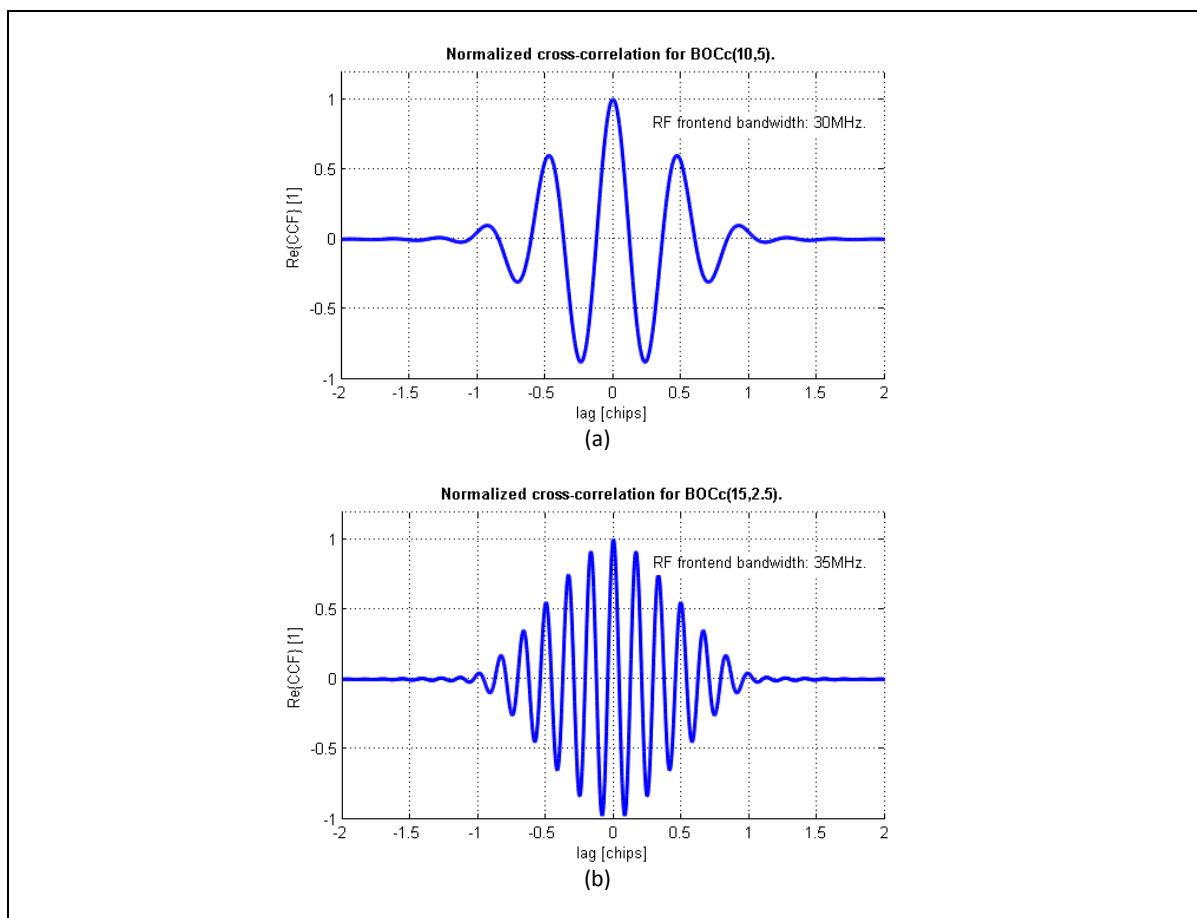


Figure 6-1: Cross-correlation of (a) BOCcos(10,5) and (b) BOCcos(15, 2.5).

To understand the effects of an ambiguity in the code delay estimation, equation 6-1 shows that the pseudorange from the user to a particular SV (Space Vehicle) is obtained from the geometric slant distance from receiver to satellite (ρ_{rxToSv}), affected by a series of error factors due to:

$$\rho = \rho_{rxToSv} + \Delta\rho_{noise} + \Delta\rho_{int} + \Delta\rho_{rx} + \Delta\rho_{mp} + \Delta\rho_{atmos} + \Delta\rho_{\Delta clk} + \Delta\rho_{eph} \quad 6-1$$

- White noise at the antenna output ($\Delta\rho_{noise}$).
- Interference signals observed at the input of the receiver, $\Delta\rho_{int}$. This factor includes GNSS and external, non-GNSS interfering signals.
- Equipment-related delays and biases ($\Delta\rho_{rx}$). This part includes factors ranging from the non-calibrated antenna phase centre till unbalanced hardware delays affecting signals from different satellites.
- Delays due to multipath ($\Delta\rho_{mp}$).
- Additional delays accumulated during the ionospheric and tropospheric propagation ($\Delta\rho_{atmos}$).
- Receiver and satellite clock uncertainties and errors ($\Delta\rho_{\Delta clk}$).
- Uncertainties on the broadcasted satellite ephemeris ($\Delta\rho_{eph}$).

The code delay ambiguity constitutes an important part within the factor $\Delta\rho_{rx}$, with a direct impact on the accuracy of the PVT solution computed by the application layer of the navigation receiver. Besides, as the code delay estimation is directly used to synchronize the spreading code removal and the navigation data demodulation from the received signal, degraded FER/BER and higher time to a reliable PVT solution are to be observed in case of code delay cycle slips.

6.5 *Classical and State-of-the-Art Techniques*

In the classical literature, a number of different techniques have shown to reduce the probability of occurrence of the aforementioned ambiguity with different constraints and success rates.

In 1999, Fine and Wilson [Ref. 51] introduce a multigate-based method called ‘bump-jumping’. According to this technique, prompt, very-early and very-late gate outputs are compared to assess that the prompt correlator tracks the largest cross-correlation peak. In negative case, an iterative process is initiated to ensure that the prompt correlator jumps to track the largest peak.

Fante [Ref. 52] proposes in 2003 a variation of ‘bump-jumping’ that uses a non-ambiguous discriminator monotonic over the range of interest of the cross-correlation function, derived from multiple points of the correlation function sampled at different instants.

In more recent years, several other approaches have been proposed. For instance, Hodgart et al. [Ref. 53] establish a double estimation technique not relying on peak identification, which requires the independent estimation and tracking of code and subcarrier delays. This method introduces a third tracking loop in the classical architecture of the receiver channel to independently track carrier, code and subcarrier phases.

Skournetou et al. [Ref. 54] develop in 2008 on the ‘DiskTracker’, a code delay estimator that shows resistance against initial phase errors by exploiting the advantages of combined feedback and feedforward loops, at the expenses of larger processing windows.

And more recently, De Latour et al. [Ref. 55] propose a code bias detector based on the combination of ambiguous and non-ambiguous discriminators, which operates by defining a threshold on the difference between both estimators. This decision is used to select which discriminator output is fed to the code loop filter at a given time instant.

In this occasion, a novel technique with the concept scheme in Figure 6-2 is presented to detect and eliminate an eventual subcarrier cycle slip observed according to section 3.5.2.

Through an independent third tracking loop (a feature also found in [Ref. 53]), this technique estimates the biased cross-correlation from multiple gates (as similarly introduced in [Ref. 52]), and exploits the well known properties of the direct and inverse Fourier transforms to approximate the systematic error or bias in the code delay estimated by the DLL. However, unlike other techniques serving the same purpose, this approach does not seek to linearize the combined S-curve of the code delay discriminator and code shape in use, as in [Ref. 52]. Besides, in this case the systematic error is directly resolved at the output of the code delay NCO, allowing for prompt and fast recovery of the error condition.

6.6 A Novel Technique in the Frequency Domain

In essence, the concept applied here is founded in the FFT-based active code search technique [Ref. 47] used during the satellite acquisition phase. The proposed strategy offers a means to approximate $E(\tau_{code})$, this is, the code delay estimation bias due to ambiguity, estimated and tracked through a DLL and well studied and consolidated code delay discriminators. In here, τ_{code} is reasonably considered with Gaussian distribution, standard deviation σ_{code} and mean m_{code} .

$$\tau_{code} = m_{code} + \Delta\tau_{code} \quad 6-2$$

$$\sigma_{code} = \sqrt{E(\Delta\tau_{code}^2)} \quad 6-3$$

$$m_{code} = E(\tau_{code}) \quad 6-4$$

For this purpose, the delay between $R_{\hat{x}x}(\tau, \tau_{code})$ and $R_{\hat{x}x}(\tau, \Delta\tau_{code})$ (ideally corresponding to m_{code}) needs to be estimated, where $x(t)$ and $\hat{x}(t)$ are respectively identified with tracked and locally generated reference PRN codes, the $\Delta\tau$ -shifted cross-correlation evaluated when the time lag equals to τ is denoted as $R_{\hat{x}x}(\tau, \Delta\tau)$ (and computed as in equation 6-5, with * the complex conjugate operator), and τ_{code} is the estimated code delay to be integrated in the PVT receiver solution.

$$R_{\hat{X}X}(\tau, \Delta\tau) = \int_{-\infty}^{+\infty} \hat{x}(t)x^*(t - \tau - \Delta\tau)dt \quad 6-5$$

According to the aforementioned technique, a bank of N_{corr} correlators with an inter-correlator separation of Δ_{corr} seconds is used to estimate $R_{\hat{X}X}(\tau, \tau_{code})$, with a rate equal to the inverse of the integration time (T_{int}).

In order for this technique to effectively detect all false locks on the cross-correlation function, $N_{corr} \cdot \Delta_{corr}$ must be bigger than 2 times the total cross-correlation span, D_R . For the two examples in hand, $D_R = 3$ chips is considered a good compromise.

$$N_{corr} \cdot \Delta_{corr} > 2 \cdot D_R \quad 6-6$$

Once estimated, $R_{\hat{X}X}(\tau, \tau_{code})$ is translated into the frequency domain by means of an FFT module of N_{fft} points to extract the power spectrum density $S_{\hat{X}X}(f)$ (see equation 6-7) on a frequency span equal to $1/\Delta_{corr}$ Hz, with a resolution of $1/(\Delta_{corr} \cdot N_{fft})$ Hz.

$$S_{\hat{X}X}(f) = FFT\{R_{\hat{X}X}(\tau, \tau_{code}), N_{fft}\} \quad 6-7$$

In a similar way, the spectrum of the bias-free cross-correlation function corresponds to:

$$S'_{\hat{X}X}(f) = FFT\{R_{\hat{X}X}(\tau, \Delta\tau_{code}), N_{fft}\} \quad 6-8$$

By design, we have knowledge of the theoretical autocorrelation of the locally generated PRN, $R_{\hat{X}\hat{X}}(\tau, 0)$. Therefore, we can write its spectrum as:

$$S_{\hat{X}\hat{X}}^0(f) = FFT\{R_{\hat{X}\hat{X}}(\tau, 0), N_{fft}\} \quad 6-9$$

We define the cross-spectrum of $R_{\hat{X}X}(\tau, \tau_{code})$ and $R_{\hat{X}\hat{X}}(\tau, \Delta\tau_{code})$ as:

$$S(f) = S_{\hat{X}X}(f) \cdot [S'_{\hat{X}\hat{X}}(f)]^* \quad 6-10$$

And by applying the approximation $S'_{\hat{x}\hat{x}}(f) \cong S_{\hat{x}\hat{x}}^0(f)$ to equation 6-10:

$$S(f) \cong S_{\hat{x}\hat{x}}(f) \cdot [S_{\hat{x}\hat{x}}^0(f)]^*$$

6-11

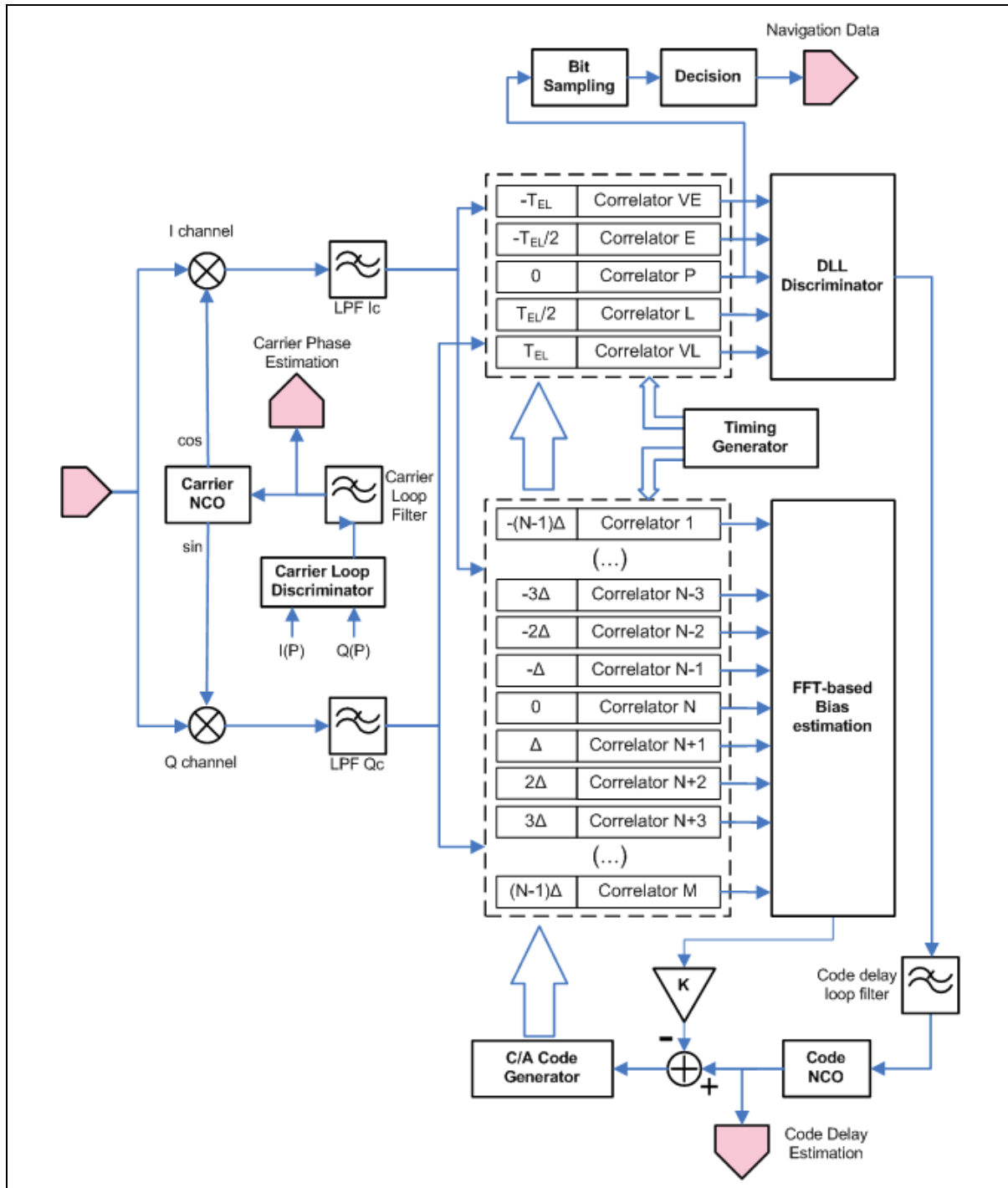


Figure 6-2: Proposed FFT-based code delay bias resolution technique.

Then, the equivalent of equation 6-11 in time domain is computed through its inverse FFT (IFFT) over N_{fft} points, and the position of the peak value of $|R(\tau)|^2$ (represented as in equation 6-12) detected to estimate the relative delay τ_r between $R_{\hat{X}\hat{X}}(\tau, \tau_{code})$ and $R_{\hat{X}\hat{X}}(\tau, 0)$ in terms of τ (see the expression in 6-13).

$$R(\tau) = iFFT\{S(f), N_{fft}\} \quad 6-12$$

$$\tau_r = \{\tau \mid R(\tau_r) = \max[|R(\tau)|^2]\} \quad 6-13$$

For simplicity, in the following N_{fft} and N_{ifft} are assumed equal to N_{corr} . In these conditions, we have that $R(\tau)$ is available in the sampled version $R(n \cdot \Delta_{corr})$, with n an integer in the range $(-N_{corr}/2, +N_{corr}/2)$. Therefore, Δ_{corr} is also the resolution of the bias estimation τ_r , which is weighted by an estimation gain, and subtracted from the output of the code NCO after filtering (see Figure 6-2). Given the approximation introduced in equation 6-11, τ_r will be a noisy estimation of m_{code} , and low-pass filtering will be required to increase its signal-to-noise ratio. In simulation time, two options will be evaluated for such operation: a moving average filter and a first-order low-pass filter.

The estimated bias can be subtracted at a rate lower than the operation frequency of the code delay tracking loop, running at a pace fixed by T_{int} . As will be seen in section 0, this design option will allow reuse of resources and the reduction of the power consumption overhead relative to the classical, non-bias-free architecture. For this purpose, Figure 6-2 includes a timing generator that would act as synchronizer between tracking and bias removal operations.

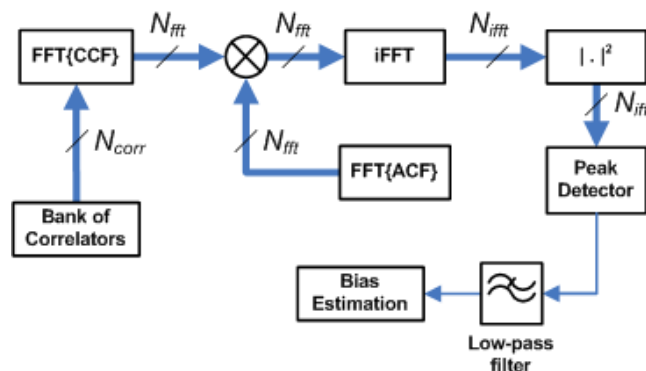


Figure 6-3: FFT-based bias estimation method.

A summary of the reported process is graphically illustrated in the figure above.

6.7 Simulations and Results

In this section, the operation of the developed technique is graphically illustrated, and its performance evaluated through simulations and compared against theoretically predicted behaviours. Special attention is driven to determine the time response of this bias removal technique, and the performance degradation in terms of estimated code delay jitter when this technique is in use.

All simulation results presented in the following have been produced by means of the semi-bit true software simulator developed in Chapter 5, modified to fit the architecture in Figure 6-2. In all simulations performed, coherent integration is assumed, this is, an integer number of chips are integrated at the output of the correlators.

| | BOCcos(10,5) | BOCcos(15,2.5) |
|-----------------------------------|--------------|----------------|
| RF frontend bandwidth | 40 MHz | 40 MHz |
| Integration time | 100 ms | 100 ms |
| Code loop bandwidth | 1 Hz | 1 Hz |
| Code delay discriminator | EMLP | EMLP |
| Early-Late spacing | 0.2 chips | 0.2 chips |
| C/N₀ | 40 dBHz | 40 dBHz |
| Number of bias correlators | 1,025 | 1,025 |
| Bias correlator separation | 0.007 chips | 0.007 chips |
| Bias estimation averaging | 50 samples | 50 samples |
| Bias estimation gain | 0.09 | 0.5 |
| Bias update period | 100 ms | 2 s |

Table 6-1: Configurations for the simulated behaviour of the developed bias removal technique.

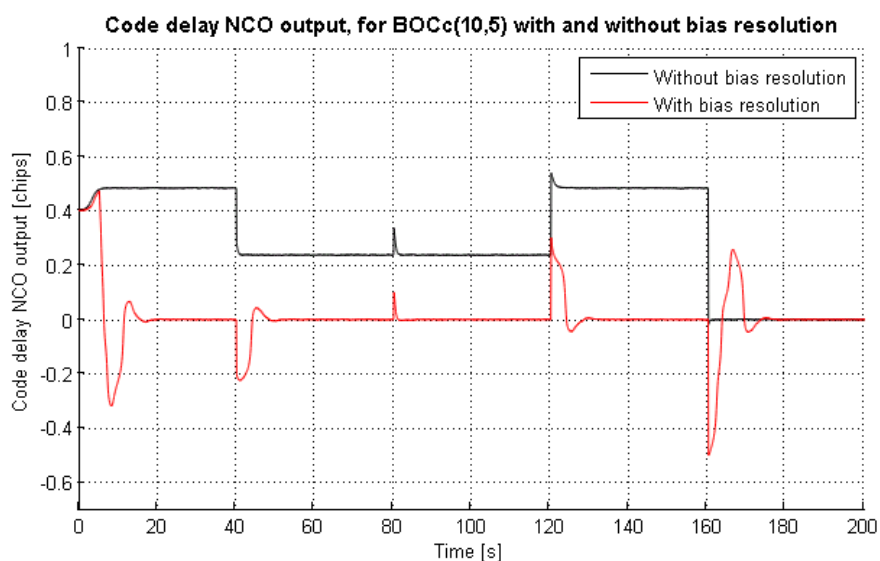


Figure 6-4: Biased and bias-free tracking of BOCcos(10,5) with an RF frontend bandwidth of 40 MHz, for successive simulated systematic errors and the parametric configuration in the left column of Table 6-1, with moving average.

In first place, in order to demonstrate the operation of our technique in simulated scenarios, two plots in the time domain are obtained from the simulation of configurations in Table 6-1 without multipath. In these two cases, the low-pass filtering in Figure 6-3 is performed by means of a moving average filter.

In the figure above, corresponding to the tracking of a BOCcos(10,5), an initial code delay equal to 0.4 chips is introduced to simulate the uncertainty of this value during the pull-in operation of an acquired satellite. While the classical architecture stabilizes on a secondary peak of $R_{\hat{x}x}$ located in the vicinity of 0.5 chips, the enhanced bias resolution scheme forces the loop to lock on the main lobe or $R_{\hat{x}x}$, and thus, to reduce the systematic error on the code delay estimation to zero. Similar responses are observed for other events, with a certain overshoot and a relatively long recovery time (approximately 20 s).

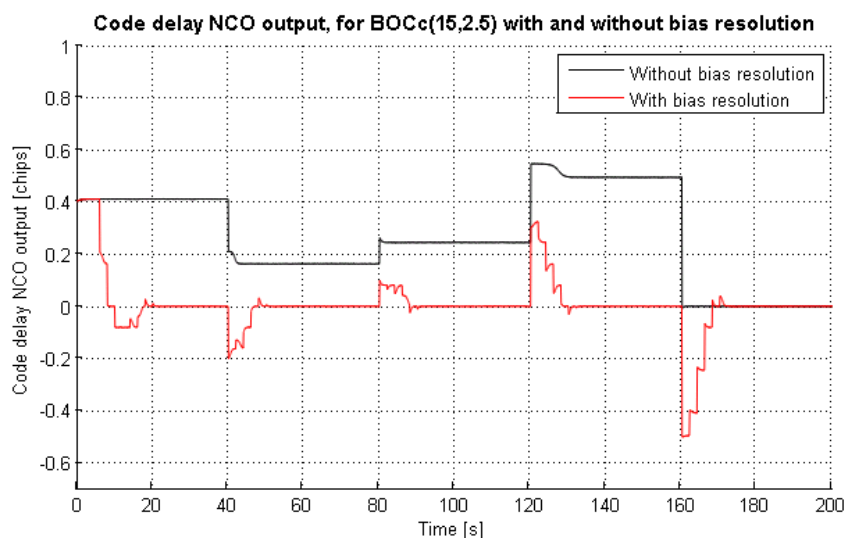


Figure 6-5: Biased and bias-free tracking of BOCcos(15,2.5) with an RF frontend bandwidth of 40 MHz, for successive simulated systematic errors (right column of Table 6-1), with moving average.

Now, if the bias resolution is applied to a rate lower than T_{int} , Figure 6-5 demonstrates the bias resolution on the tracking of a BOCcos(15, 2.5) with a bias update period 20 times higher than the inverse of the code delay loop update rate. Also in this case, complete bias elimination is observed in all events through our enhanced receiver architecture, with lower overshoots and shorter settling times than the previous simulation.

A step further in the design is given by substituting the filtering approach considered in Table 6-1 with a very narrow-band low-pass filter with faster roll-off and higher stop-band attenuation than the moving average filter. This measure serves to simultaneously increase both the closed loop stability of the bias estimator for higher values of the bias estimation gain, and the signal-to-noise ratio of the estimated value.

The application of this variation on the two previously reported cases yield the plots in the figures below, both of them obtained for the reference configurations in Table 6-1, with a bandwidth of the first-order low-pass filter equal to 0.25 Hz, a unit bias estimator gain and a bias update rate of 1 s.

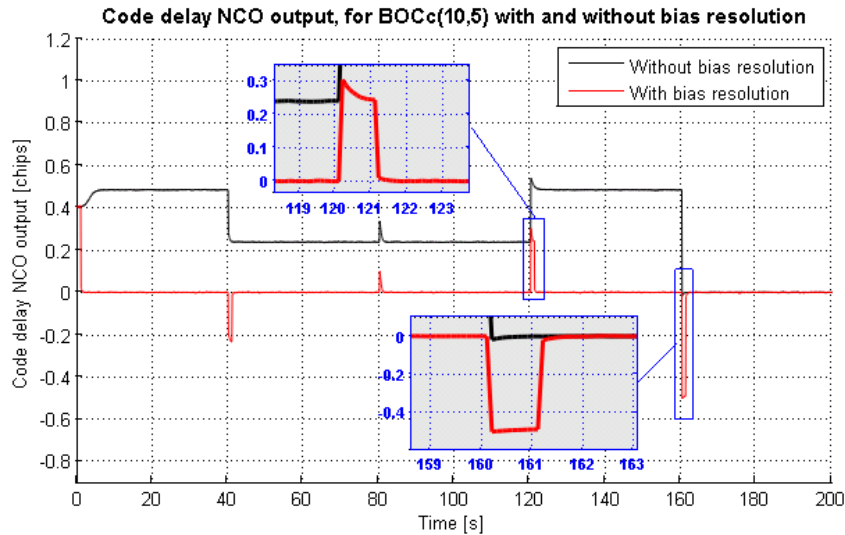


Figure 6-6: Improved bias removal on the tracking of BOCcos(10,5) with an RF frontend bandwidth of 40 MHz, for successive simulated systematic errors and the parametric configuration in Table 6-1, with low-pass filtering.

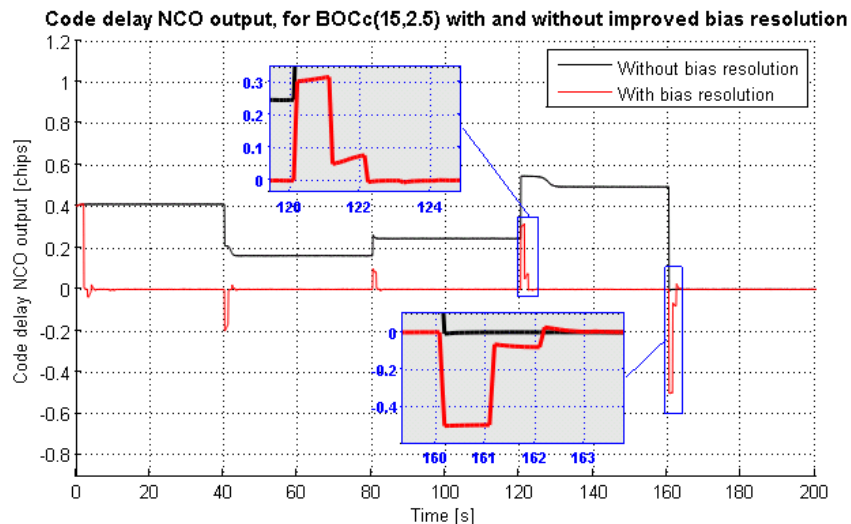


Figure 6-7: Improved bias removal on the tracking of BOCcos(15,2.5) with an RF frontend bandwidth of 40 MHz, for successive simulated systematic errors and the parametric configuration in Table 6-1, with low-pass filtering.

It is observed that, through this simple modification, the worst-case reaction time of our technique is dramatically reduced by a factor of 10 relative to previous results. For the tracked BOCcos(10,5) reported in Figure 6-6, an insight to the zoomed detail rates the reaction time in 1 s, while Figure 6-7 shows that for a BOCcos(15, 2.5), the resolution time is approximately of 2.5 s. This difference in

time is due to the fact that the cross-correlation of a $\text{BOCcos}(15, 2.5)$ provides a higher number of secondary peaks to where the loop can look between two consecutive bias estimation updates (due to the approximation in equation 6-11). However, once the bias resolution forces the estimated code delay difference between the received and locally generated spreading codes close enough to zero, the loop operation inherently drives the working point to lock on the main lobe of the code cross-correlation.

The last set of simulations here included is devoted to quantify the performance degradation, if any, introduced by the exposed bias reduction technique in terms of code delay estimation jitter. To start with, a reference set of calibration curves are obtained to characterize the performance of the simulator without bias reduction for $\text{BOCcos}(10,5)$ and $\text{BOCcos}(15, 2.5)$ in ideal conditions, this is, with an AWGN (Additive White Gaussian Noise) channel, and the architecture parameters listed in Table 6-2.

| | BOCcos(10,5) | BOCcos(15,2.5) |
|---------------------------------|---------------------|-----------------------|
| RF frontend bandwidth | 40 MHz | 40 MHz |
| Integration time | 100 ms | 100 ms |
| Code loop bandwidth | 1 Hz | 1 Hz |
| Code delay discriminator | EMLP | EMLP |
| Early-Late spacing | 0.2 chips | 0.2 chips |
| C/N₀ | 40 – 70 dBHz | 40 – 70 dBHz |

Table 6-2: Reference configurations for the code jitter extraction.

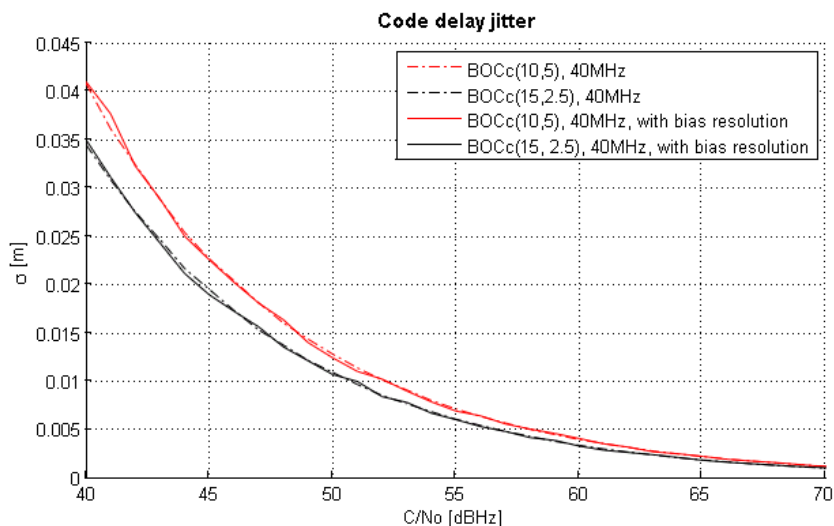


Figure 6-8: Code delay jitter of $\text{BOCcos}(10,5)$ and $\text{BOCcos}(15, 2.5)$ for an RF frontend bandwidth of 40 MHz, with and without bias removal.

The standard deviation of the code delay estimation for these scenarios is then compared against the jitter of the same variable when this technique is in use (considering both averaging and filtering of the bias estimation). From results depicted in Figure 6-8, no degradation in terms of C/N_0 is introduced with this bias resolution technique for the simulated cases. This statement can be

extended to all simulated scenarios to the publishing date, provided that effective filtering/averaging is performed on the bias estimation (see Figure 6-3).

6.8 *On the Practicality of This Measure*

It is interesting to note that this technique is very well implementable by using hardware/software resources already present within the navigation receiver, only in use during the acquisition of SVs, and does not require major redesign. In fact this statement has been kept as a development premise during the design of this code bias resolution approach.

To implement this operation, N_{corr} additional correlators and an FFT/IFFT module of length N_{fft} are required for every receiver tracking channel. Although all these elements are already available, the use of supplementary resources will increase the overall power consumption up to an extent still supported by batteries found in aeronautical or vehicle navigation applications.

By sequentially applying this technique to a single channel at a time (as already considered in the reported simulation results), the overall power consumption is reduced to a level compatible with personal navigation applications. Obviously, a trade-off between reaction time to code bias and power consumption should be resolved in this case.

6.9 *Chapter Summary*

As shown, the frequency-domain code delay bias resolution technique presented in this contribution, allows a receiver compatible with BOCcos(10,5) and/or BOCcos(15,2.5) to instantaneously approximate the value of an eventual bias in the code delay estimation, and to promptly resolve this condition.

Included simulations have proven that this technique behaves adequately in an AWGN channel, approximating and promptly eliminating systematic errors in the code delay estimation. However, exhaustive studies and optimizations of all parameters with realistic satellite channels in L-band are necessary to achieve fully reliable operation. This optimization and further performance comparison with advanced techniques will be documented in the future.

Also in the future, the author plans to treat a simplified, efficient and more practical version of this technique (already under development at the time of writing) in order to improve the applicability and the effective use of on-receiver resources.

CHAPTER 7

TRADE-OFF BETWEEN DILUTION OF PRECISION AND INTERFERENCE LEVEL ON A COMPATIBLE RECEIVER WITHIN A COMBINED GPS+GALILEO SCENARIO

7.1 Preface

As discussed in Chapter 4, a broad range of interference sources can degrade the quality of the positioning observables obtained by a given navigation receiver. In the classical literature, a number of techniques have been developed to block such interfering signals within the RF frontend or to counteract their effects on the tracking and acquisition operations of the receiver. However, none of them aim to minimize the probability of these disrupting and/or harmful signals to actually access the hardware of the receiver through the antenna.

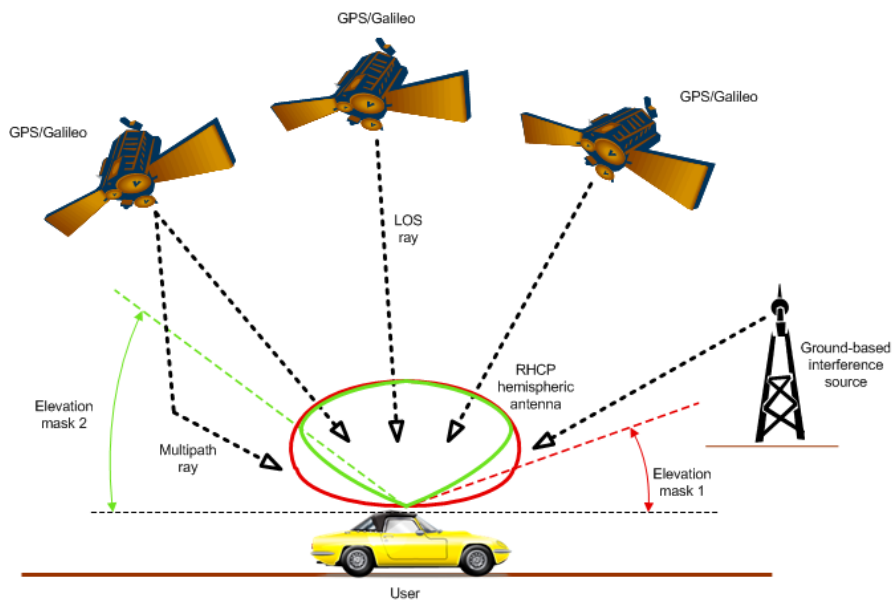


Figure 7-1: Concept of the proposed antenna-based protection measure.

In an attempt to fill this literature gap, this chapter develops on the possibility to use an antenna with an elevation masking angle higher than 15° for a GPS+Galileo receiver while keeping dilutions of precision and code delay tracking jitters equal or better than shown within a unique GPS constellation with a receiver antenna with a cut-off angle⁴⁴ of 15°. This measure, based on the concept depicted in Figure 7-1 and not treated in the present literature as per the author's

⁴⁴ An antenna with a cut-off angle of 15° provides a GPS minimal global availability of 4 satellites.

knowledge, is targeted to reduce the vulnerability to ground-based non-navigation interference sources, and to multipath in urban canyons.

7.2 Study Logic

Given the complexity of this study, a two-part logic is graphically introduced in Figure 7-2 to keep a clear set of objectives throughout the complete development in this chapter.

In a first stage of this logic, a preliminary study is conducted to assess the feasibility of the reported measure for a single user located within the city of Graz, Austria. This phase of the study has the aim to produce suitable methodologies and scenarios, and to select reasonable figures of merit for simulation scenario comparison.

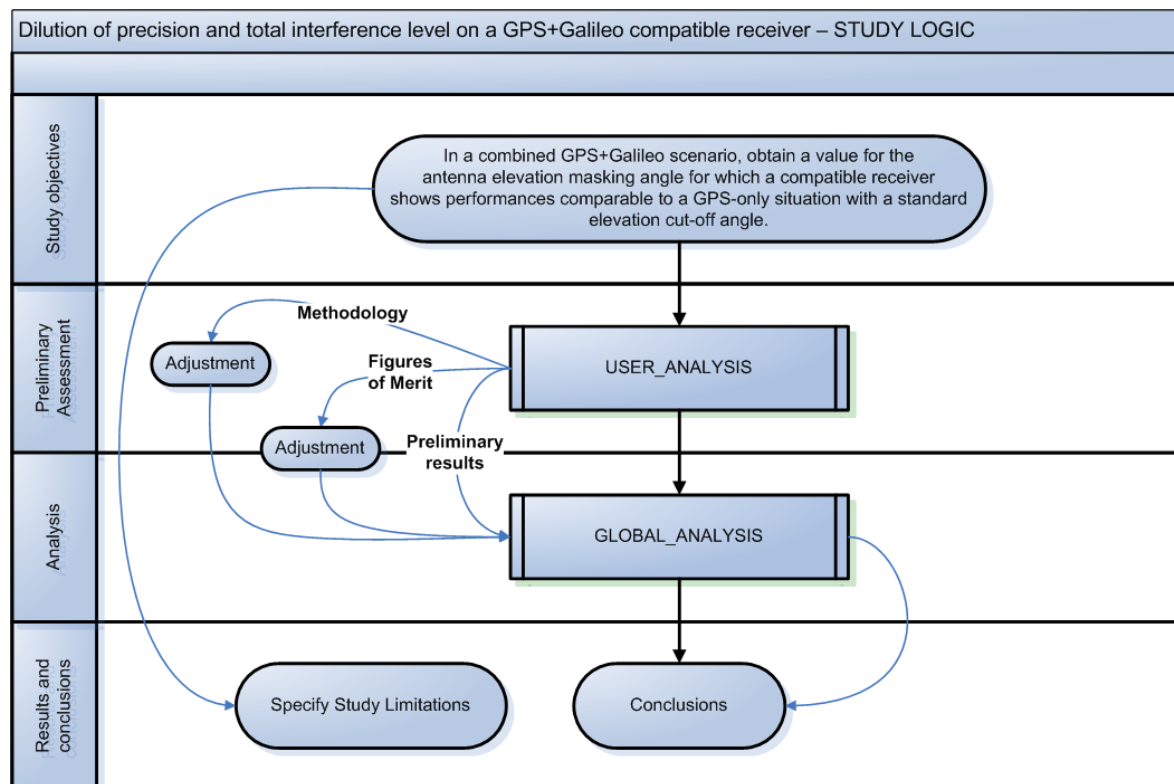


Figure 7-2: Applicable study logic for the developments in Chapter 7.

Upon completion of the first phase, the applicability of this measure is evaluated for users in arbitrary positions above the globe. In connection with the experience gathered during Phase 1, preliminary methodologies and figures of merit are adjusted and conveniently extended to account for both the statistical and geographical fitting of scenarios.

Finally, the combination of results from Phases 1 and 2 are expected to lead to a number of conclusions within the study limitations listed in the introduction of every phase.

7.3 *Part 1: Preliminary Study over Graz, Austria*

7.3.1 Background

In the following, a number of theoretical concepts necessary for the developments in this first phase are refreshed to establish a consistent knowledge base, and several precisions made according to the author's objectives.

Regarding the study limitations, as a general premise in this contribution special interest is drawn to measures applicable to mass-market GNSS receivers. Due to this fact, only CDMA systems based on Time-of-arrival (TOA) range determination are considered, excluding those systems that require receivers with an active role (the Chinese COMPASS is therefore excluded of the analysis – see 2.2.4–). Besides, the discussion here provided has been limited to eventual receivers combining GPS and Galileo, as this is, for evident political reasons, the most likely future scenario for the mentioned market segment over Europe unless the modernization of GLONASS brings the system to the CDMA scene (see 2.2.2 for details on this possibility).

The architecture of the navigation user receiver applicable in this context comprises a mono or multiband RF frontend, a baseband processing stage with capability for multiple and simultaneous satellite acquisition and tracking from both Galileo and GPS constellations, and an application module that allows the transparent combination of pseudorange observables and navigation data from both systems into the PVT solution. Furthermore, assuming a limited number of tracking channels in the user receiver, a satellite selection method based on the best combined geometry is here considered, and this assumption consistently applied in the evaluation of the dilution of precision in subsequent sections.

With regard to the antenna, the masking angle is assumed a characteristic of the receiver antenna pattern and not a soft limit imposed at processing time to discard low elevation satellites after the demodulation of the navigation data. Therefore, the final goal of this contribution is the proposal of a valid measure against non-navigation related interferences to be implemented on the antenna itself.

7.3.2 Procedure

The validation of the technique here developed consists, in this phase, on the characterization of the dilution of precision observed by a receiver under GPS or Galileo isolated constellations or a GPS+Galileo combined system. In the same range of conditions and for a single receiver baseband processing arm tracking a GPS or Galileo satellite, the GNSS-related interference⁴⁵ level and the eventual degradation of the code delay tracking performance need to be obtained. All these

⁴⁵ The author is aware of the implications of a study limited to GPS and Galileo systems, as in the reality (see Figure 2-1) all signals radiated by other GNSS (i.e. the Russian GLONASS, or the Chinese COMPASS, among the most relevant) and regional augmentations (the North American WAAS, the European EGNOS and the Japanese MSAS, the Japanese QZSS or the Indian GAGAN -towards the global system IRNSS-) will contribute to the degradation of the receiver channel tracking performance. In future evolutions of this work, other spread spectrum GNSS interference sources will be considered to be expected in the future multiconstellation system, and the measure here proposed extended for a more realistic scenario.

quantities are required over time for a single user position, and for several values given to the design parameter (the receiver antenna masking angle).

All necessary data is obtained through a software simulator consistent with the design in section 5.2 that contains embedded models of the GPS and Galileo space segments, the signal propagation environment and the receiver performance. This simulator can be parametrically configured for the studies in both phases in this chapter.

Within this simulator, GPS and Galileo constellations are theoretically modelled according to [Ref. 7]. On one hand, GPS is simulated as a constellation of 37 active satellites (extended from the nominal 24 in order to represent a worst-case scenario where all vehicles in space are active), irregularly spaced within 6 orbital planes with nominal orbital inclination 55° and semi-major axis equal to 26,560 Km. Galileo, on the other hand, is modelled using a Walker Delta Pattern⁴⁶ $56^\circ:27/3/1$ constellation (27 active satellites, equally spaced 40° in 3 orbital planes, with nominal inclination 56° , no spare satellites modelled) with a nominal semi-major axis equal to 29,601 Km. Given the nature of the data models in use, it is considered adequate to run a simulated time equal to or higher than the maximum of the orbital revolution periods (11 hours and 58 minutes for GPS, 14 hours and 5 minutes for Galileo) rather than the ground track repeat periods (1 and 10 sidereal days, respectively for GPS and Galileo). In this case, 48 hours are considered, to allow reliable statistics to be formed.

Omitting the shadowing effects caused by the Earth topography, the visibility and dilution of precision are computed over time from all the satellites above a flat horizon for a receiver antenna with an elevation masking angle equal to 0° . Several values of the cut-off angle are sequentially applied to these baseline data and fed into the next steps of the processing, this is, the determination of the interference level, the computation of the effective post-correlation carrier-to-noise power density ratio, and the code delay tracking evolution of the receiver channel in terms of its jitter.

For a single baseband channel in the receiver and in a basic scenario in which no pulsed interferes are defined, the relevant formulation and procedure for the calculation of the interference levels I_{ref} and I_{int} and the post-correlation effective carrier-to-noise power density at the receiver channel tracking the i -th target satellite, $(C/N_o)_{eff}^i$, can be found in section 5.2.7. Note that in phase 1 spectral separation constant values are used for every pair of signals.

Once $(C/N_o)_{eff}^i$ is determined over time for the user position, and as a function of the receiver architecture and its parametrical configuration, the accuracy of the pseudorange estimation from the user to the i -th target satellite is obtained through interpolation of the characteristics of the code delay tracking jitter σ^i versus $(C/N_o)_{eff}^i$. This characteristic is determined through a GNSS receiver channel simulator coded according to the semi bit-true simulation technique reported in 5.3.3.

The complete procedure is iterated for several values of the elevation masking angle for the scenarios presented in the following sections.

⁴⁶ Notation introduced by J. Walker in [Ref. 61].

7.3.3 Definition of Scenarios

Four scenarios are to be configured and sequentially loaded into the simulator for processing. These scenarios are designed to provide information about the dilution of precision and the receiver performance degradation under isolated GPS or Galileo isolated constellations, and a combined GPS+Galileo system:

| General | |
|---|---|
| User Id | Graz, Austria |
| User coordinates | 47.0833°N 15.3667°E |
| User height | 500.0 m |
| Simulated duration | 48 hours |
| Time resolution | 120 seconds |
| Atmospheric attenuation | 0.5 dB |
| GPS constellation (Active for scenarios 1, 3 & 4) | |
| Constellation modelling | As previously defined in 7.3.2. |
| Transmitted signals | GPS L1 C/A, GPS L1 P(Y), GPS L1 M, GPS L1 C |
| Transmitted power | 12.8 (16.8) dBW @ GPS L1 C/A, 14.3 dBW @ GPS L1 P(Y), 19.5 dBW @ GPS L1 M, 15.6 dBW @ GPS L1 C |
| Satellite antenna gain | Interpolated from realistic antenna patterns for Block II F satellites. Maximum gain: 14.9 dBi |
| Galileo constellation (Active for scenarios 2, 3 & 4) | |
| Constellation modelling | As previously defined in 7.3.2. |
| Transmitted signals | Galileo E1A, Galileo E1B |
| Transmitted power | 17.3 dBW @ Galileo E1A, 14.6 (15.5) dBW @ Galileo E1B |
| Satellite antenna gain | Interpolated from realistic antenna patterns foreseen for Galileo satellites. Maximum gain: 16.2 dBi |
| Receiver | |
| N_o | -201.5 dBW/Hz (in all cases) |
| RF frontend bandwidth | GPS channels (scenarios 1/3): 2.5 MHz Galileo channels (scenarios 2/4): 24.5 MHz |
| Tracked signal | GPS L1 C/A (scenarios 1/3), Galileo E1B (scenarios 2/4) |
| Antenna | Hemispherical RHCP antenna. Mask angles: 0° to 30° Maximum gain: 4.5 dBi |

Table 7-1: Relevant configurations for the simulation scenarios of Phase 1.

1. **Scenario 1:** In this scenario, the receiver channel is assumed to track any GPS PRN on L1 C/A, considering an isolated GPS constellation. I_{ref} is then constituted by all transmissions on L1 P, L1 M and L1 C, and from all GPS satellites other than the tracked PRN on L1 C/A.

2. **Scenario 2:** signal tracked from any Galileo PRN, under a single Galileo constellation. In this scenario, I_{ref} is from the addition of contributions from E1A, and from all Galileo satellites other than the tracked PRN on E1BC.
3. **Scenario 3:** signal tracked from any GPS PRN, under a combined GPS+Galileo constellation. Here, I_{ref} is constituted by all transmissions on L1 P, L1 M and L1 C, and from all GPS satellites other than the tracked PRN on L1 C/A. I_{int} is obtained from all Galileo satellites transmitting E1A and E1BC signals.
4. **Scenario 4:** signal tracked from any Galileo PRN, under a combined GPS+Galileo constellation. I_{int} is constituted by all transmissions on GPS L1 C/A, L1 P, L1 M and L1 C and I_{ref} is obtained from all Galileo satellites transmitting E1A, from all Galileo SV on E1BC signals, other than the tracked PRN.

To complement the scenario definition, Table 7-1, summarizes relevant configurations valid in the frame of the mass-market positioning and navigation business, with the tracked signals supporting open services in all cases.

Furthermore, the constant spectral separation coefficients necessary to compute I_{ref} and I_{int} in all cases have been determined by applying the method outlined in section 5.2.6 to PSDs generated compliant with references [Ref. 6] and [Ref. 3], to estimate the worst-case SSC. For this reason, all values in Table 7-2 are considered conservative. Note that in this phase the SSC values are taken constant with the Doppler difference in order to accelerate the progress of this phase. More accurate Doppler dependent values will be considered in phase 2.

| | Galileo E1B | GPS L1 C/A |
|-------------|-------------|------------|
| Galileo E1A | -103.3 | -107.9 |
| Galileo E1B | -64.9 | -67.5 |
| GPS L1 C/A | -67.8 | -50.3 |
| GPS L1 P(Y) | -70.4 | -70.1 |
| GPS L1 M | -82.5 | -86.9 |
| GPS L1 C | -64.9 | -67.6 |

Table 7-2: SSC values considered within Table 7-1 (in dB/Hz)

Also note in Table 7-1 the following convention: power values in red are used when the corresponding signal is considered interference, values in black, as a contrast, are used when the signal is targeted by the considered receiver.

7.3.4 Satellite Visibility of GPS and Galileo Constellations

From satellite and user positions obtained as results during the analysis of scenarios 1 to 3, time evolutions and statistical figures to characterize the visibility of satellites, $N(p, t)$, are extracted for GPS, Galileo, and for a combined GPS+Galileo constellation, for the user antenna elevation masking

angles listed in Table 7-1. Again, for such analysis no topography on Earth is considered, ignoring shadowing and signal blockage other than for those satellites below the antenna elevation masking angle selected in every case.

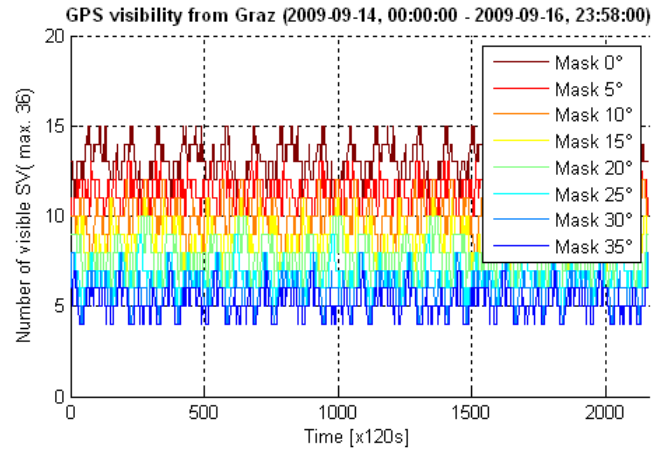


Figure 7-3: Satellite visibility for scenario 1 (user in Graz).

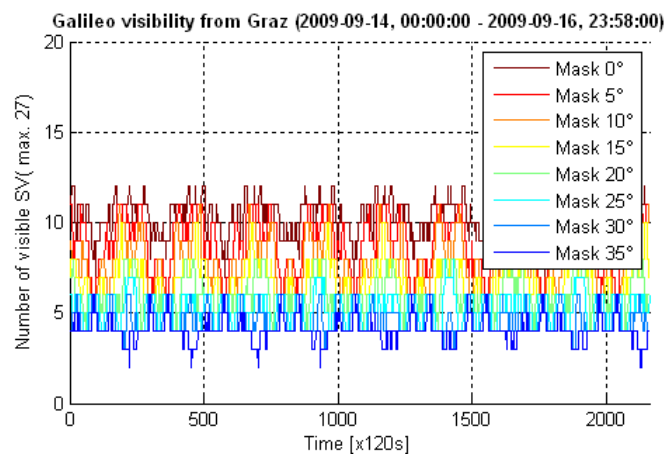


Figure 7-4: Satellite visibility for scenario 2 (user in Graz).

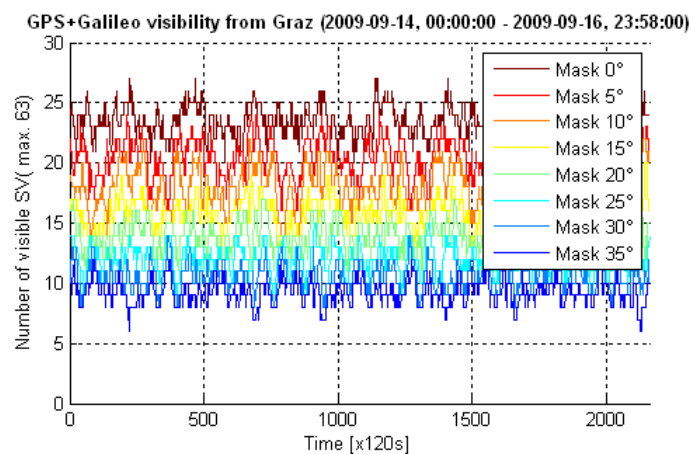


Figure 7-5: Satellite visibility for scenarios 3 and 4 (user in Graz).

The 3 figures in page 123 represent the temporal evolution of the visibility of GPS, Galileo and GPS+Galileo constellations from a user in Graz. The corresponding statistical figures, with depicted minimum, maximum and mean over time and as a function of the antenna masking angle are displayed below.

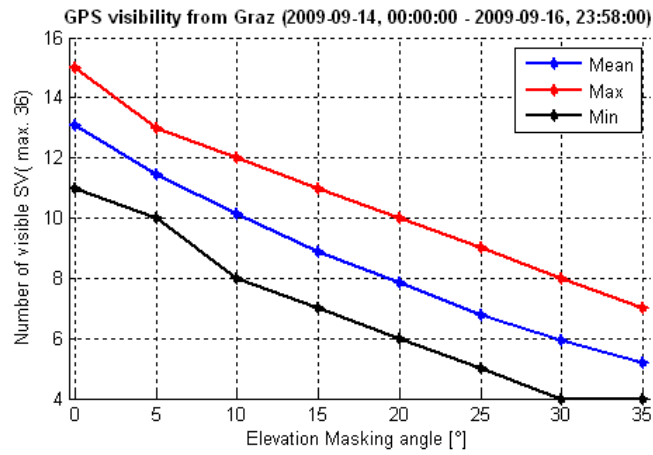


Figure 7-6: Maximum, minimum and mean values of visibility for scenario 1 (user in Graz).

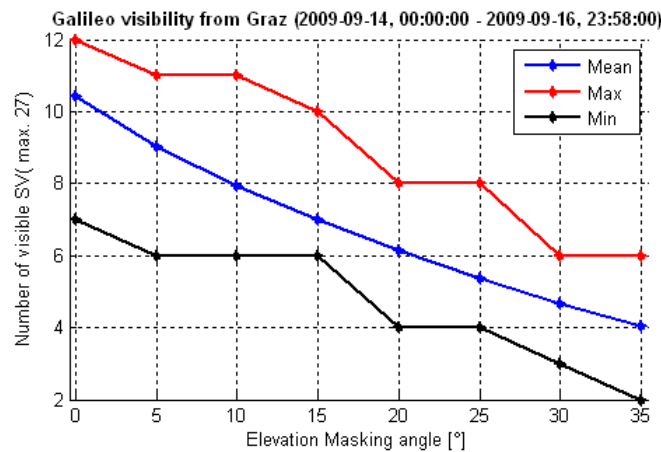


Figure 7-7: Maximum, minimum and mean values of visibility for scenario 2 (user in Graz).

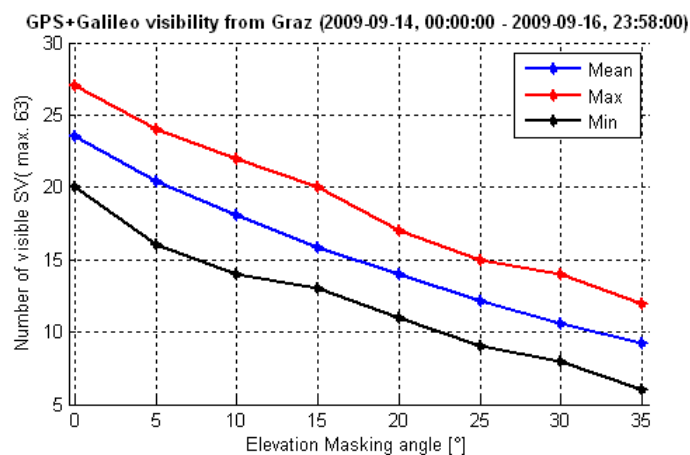


Figure 7-8: Maximum, minimum and mean values of visibility for scenarios 3 and 4 (user in Graz).

Observe that an equivalent mean number of visible satellites is obtained for a standard 10° receiver antenna elevation masking angle under a GPS constellation, and for a receiver under a GPS+Galileo system with an antenna cut-off angle between 30° and 35° .

Note that the visibility correspondence is not a sufficient criterion for scenario equivalence. However, this analysis is included to assess that a minimum number of 4 satellites are in all cases visible to produce the positioning solution.

7.3.5 Determination of GDOP for GPS, Galileo and Combined Constellations

Once again taking the satellite positions previously obtained, the instantaneous evolution of the geometric dilutions of precision is computed for the considered user position and for all possible combinations of 4 satellites out of $N(p,t)$. From all these combinations, the best instantaneous values are then kept and representative statistics depicted in the figures below.

Note that in this case, maximum, minimum and mean values are not sufficient to statistically represent the GDOP distribution for a given user position, for it cannot be considered a symmetrical Gaussian bell. In this case, the percentiles 95 and 98 are included in order to describe the asymmetry of the distribution.

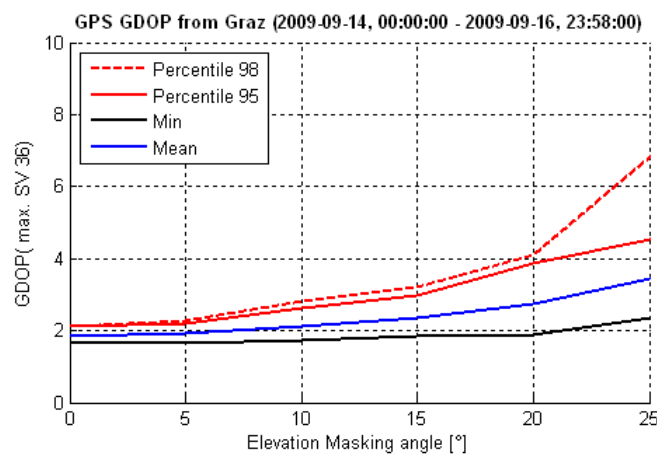


Figure 7-9: GDOP in a GPS-only scenario, for elevation cut-off angles between 0° and 25° (user in Graz).

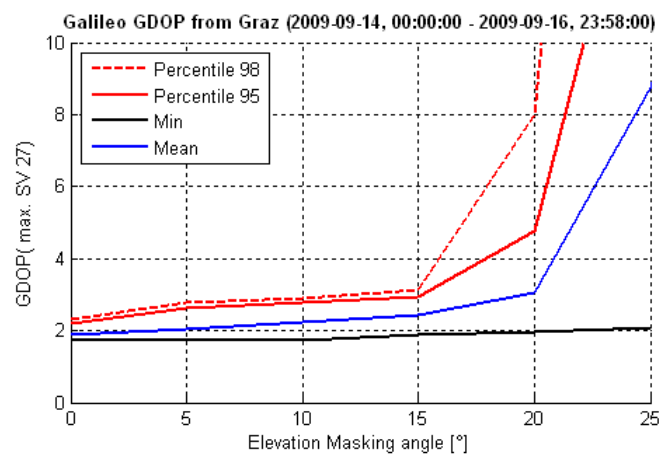


Figure 7-10: GDOP in a Galileo-only scenario, for elevation cut-off angles between 0° and 25° (user in Graz).

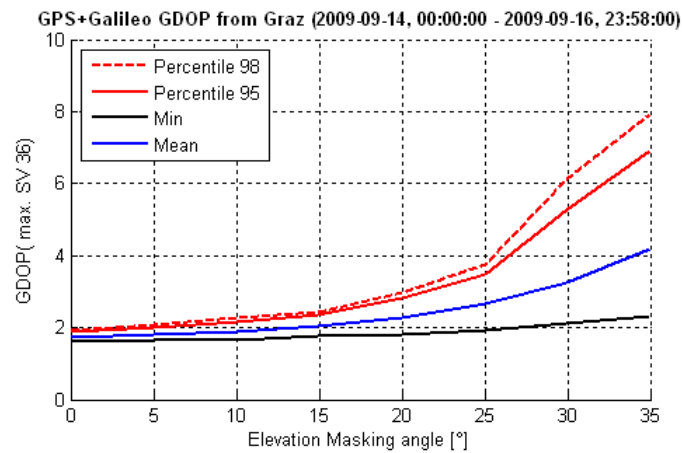


Figure 7-11: GDOP in a GPS+Galileo scenario, for elevation cut-off angles between 0° and 35° (user in Graz).

Note the evident imbalance of GPS and Galileo in terms of GDOP (Figure 7-9 and Figure 7-10), obviously caused by the number of simulated SV in every constellation. With this configuration, it is evident that the same mean GDOP in a single GPS constellation above 10° is obtained for 20° cut-off angle within a GPS+Galileo system (Figure 7-11). Note that this range of values becomes now the driver of the study, for it is more limiting than the one obtained in terms of visibility in the previous section.

In the following section, the gain in performance of a receiver channel tracking either GPS or Galileo satellites is determined when the user antenna elevation masking angle is increased from the standard 10° to the new 20°.

7.3.6 GNSS-Induced Interference Levels From and to GPS and Galileo

A step towards the final conclusion is here given, with the computation of desired and interfering powers within all scenarios in Table 7-1. Besides, the degradation in terms of C/N_0 is also presented, and the pertinent discussion included.

Regarding the plots offered below, it is worth to clarify that each of them display statistical quantities (desired and interfering power spectral densities, $(C/N_0)_{\text{eff}}$, C/N_0 degradation, and other parameters) averaged for all active channels at the receiver tracking every visible satellite at any particular time shot from the user position. Besides, note that all figures in this section display mean values, with standard deviations represented as error lines.

As a necessary intermediate result towards the determination of the Figure 7-12 and Figure 7-13 respectively display the mean power level received from all visible satellites in GPS and Galileo constellations as a function of the design parameter. Higher standard deviation values are observed for low elevation masking angles due to the fact that SVs in a broader range of elevations are included in the calculations.

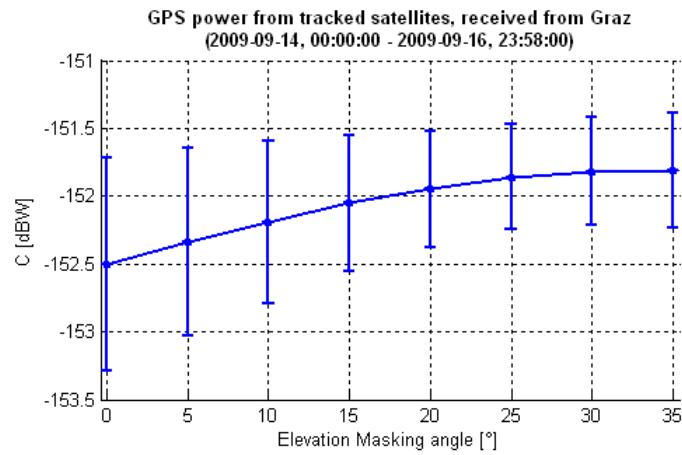


Figure 7-12: Mean desired power received from the GPS constellation.

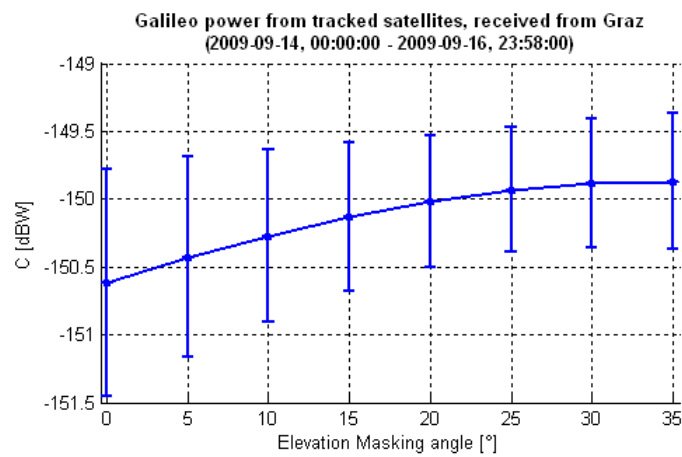
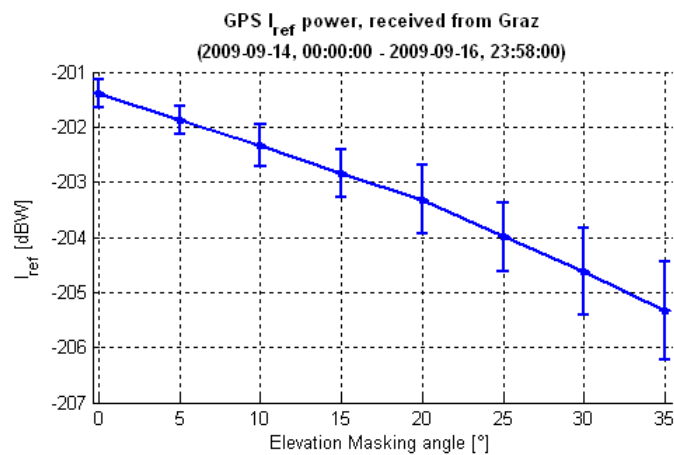


Figure 7-13: Mean desired power received from the Galileo constellation.

The instantaneous received power levels considered to produce the statistics in the figures above are used to calculate the effective interfering power spectral densities, I_{int} and I_{ref} , as seen by receiver channels tracking GPS and Galileo satellites within the defined scenarios.

Figure 7-14: Mean I_{ref} received from the GPS system in scenario 1.

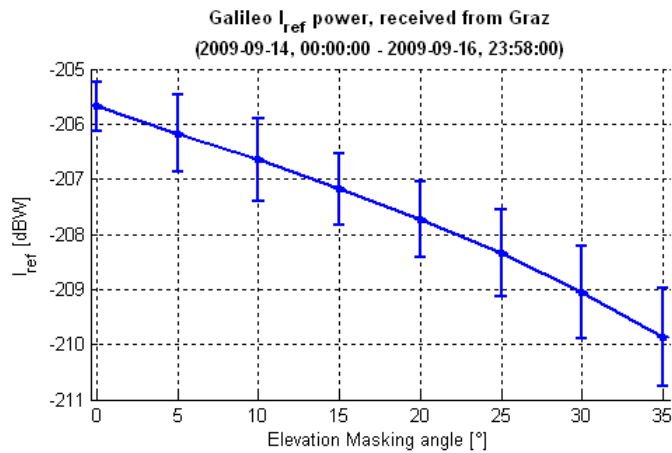


Figure 7-15: Mean I_{ref} received from the Galileo system in scenario 2

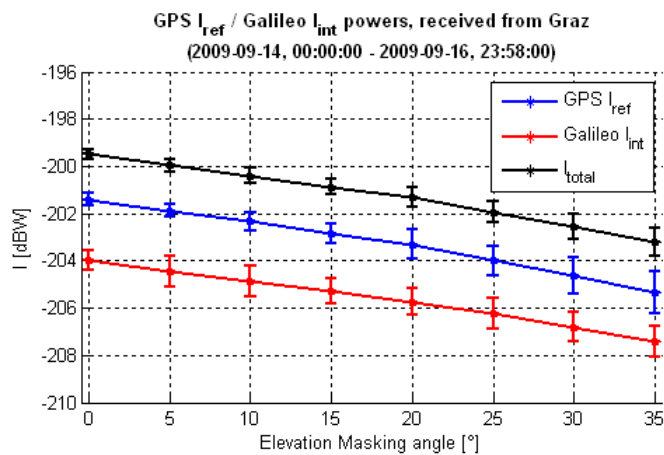


Figure 7-16: Mean I_{ref}/I_{int} received from GPS and Galileo constellations for scenario 3.

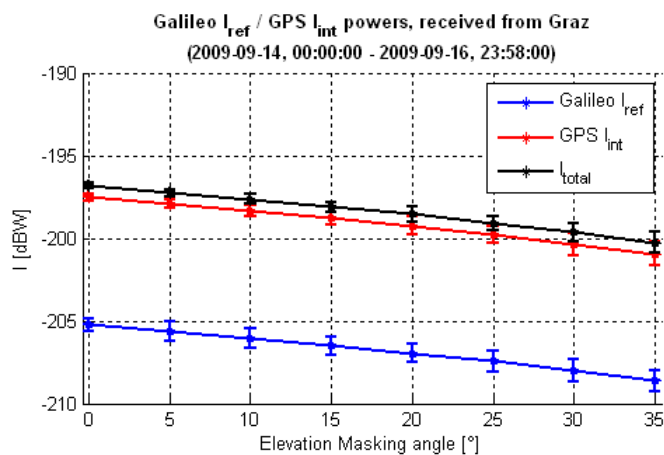


Figure 7-17: Mean I_{ref}/I_{int} received from Galileo and GPS constellations, for scenario 4.

As shown for scenario 1 in Figure 7-14, the mean total interfering power spectral density at 10° for GPS is of -202.4 dBW/Hz. This value is lower than the corresponding figures displayed for scenarios 3 and 4 (Figure 7-16 and Figure 7-17) for a cut-off angle of 20° (angle value consistent with the partial conclusion of the previous section).

However, given the non-linear characteristic of the receiver channel tracking jitter versus the total interfering power level, in the following statistical evolutions of $(C/N_o)_{\text{eff}}$ and the code delay tracking jitters for GPS and Galileo receiver channels are derived from the time series of I_{int} and I_{ref} obtained here for all scenarios.

7.3.7 Receiver Performance Degradation Due to Interferences for All Scenarios

The power levels received from every satellite (characterized in Figure 7-13) yield the dependency of the C/N_o versus the masking angle value in the figures below, as estimated by every receiver channel for both GPS and Galileo satellites.

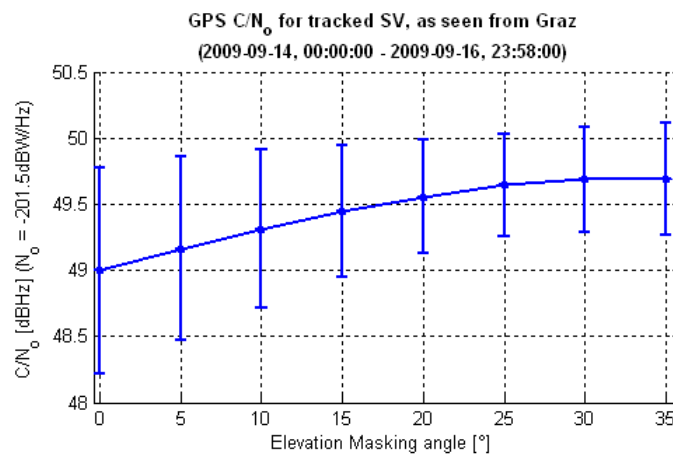


Figure 7-18: Mean C/N_o seen by a GPS receiver channel, applicable to scenarios 1&3.

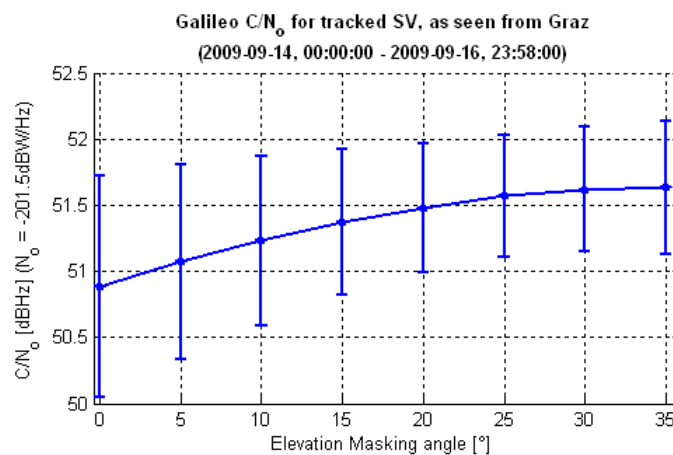


Figure 7-19: Mean C/N_o seen by a Galileo receiver, applicable to scenarios 2&4.

Taking the received desired powers in Figure 7-13 and interfering power spectral densities shown for Scenarios 1, 3 and 4 in Figure 7-14, Figure 7-16 and Figure 7-17, the $(C/N_o)_{\text{eff}}$ is then computed according to equation 5-13 with $\mu_s = 0$ dB, and results displayed in the 3 figures in page 130.

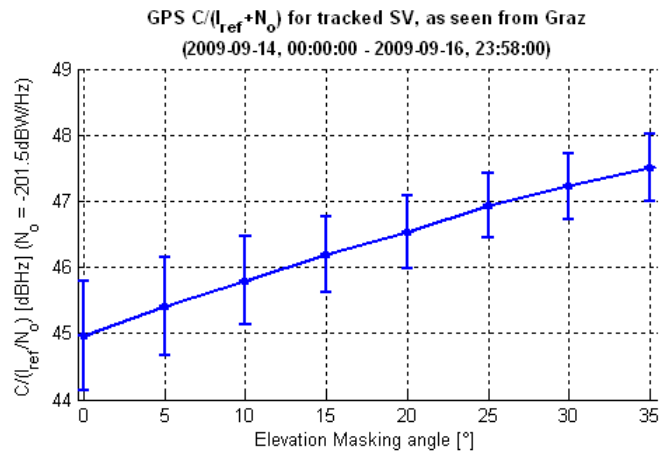


Figure 7-20: Mean $(C/N_0)_{\text{eff}}$ seen by a GPS receiver channel in scenario 1.

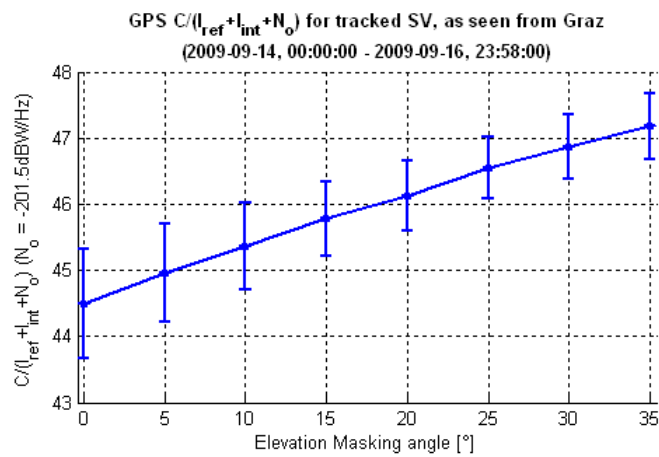


Figure 7-21: Mean $(C/N_0)_{\text{eff}}$ seen by a GPS receiver channel in scenario 3.

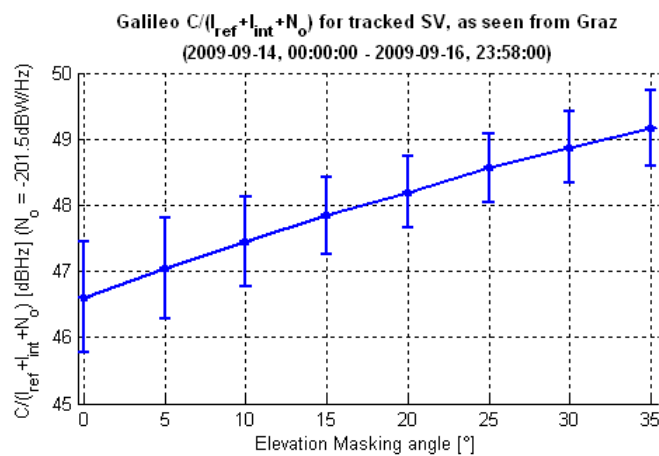


Figure 7-22: Mean $(C/N_0)_{\text{eff}}$ seen by a Galileo receiver channel in scenario 4.

From Figure 7-20, it turns out that the $(C/N_0)_{\text{eff}}$ value at 10° is 45.75 dBHz when a GPS-only scenario is considered. For the combined GPS+Galileo future scenario, the readings on Figure 7-21 and Figure 7-22 at 20° is of 46.10 and 48.24 dBHz respectively for GPS and Galileo tracking channels.

As the last stage in this development, the $\Delta\sigma$ offered for Galileo receiver tracking channels within the hypothetical compatible receiver considered during the whole contribution. For this purpose, GPS receiver channels are here modelled to track a BPSK(1), with an RF frontend bandwidth consistent with the SSC values in Table 7-2. Additionally, an Early Minus Late Power (EMLP) discriminator with an Early-Late (EL) spacing of 0.5 chips and a code loop bandwidth equal to 1 Hz are selected. Concerning the Galileo tracking channels, these are configured compatible with CBOCsin(6,1,1), also with an EMLP discriminator with a 0.5-chip EL spacing, and 5 Hz of code loop bandwidth. Again, the RF bandwidth has been selected consistent with the computed SSC values.

From these configurations and the time series obtained for the $(C/N_o)_{\text{eff}}$, the code delay tracking jitters for scenarios 1, 3 and 4 are depicted below.

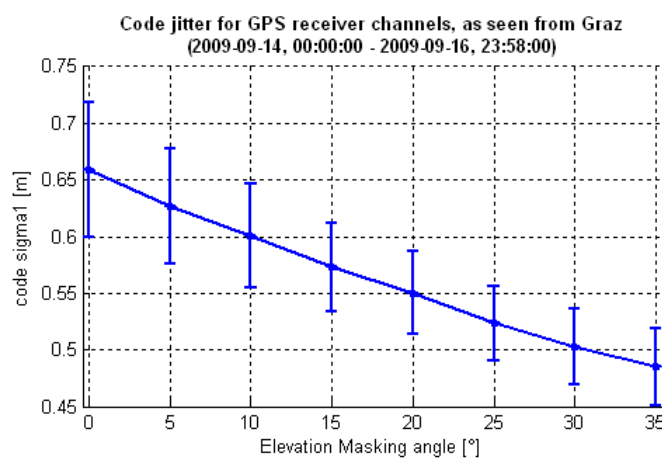


Figure 7-23: Jitter of the code delay estimate for a typical GPS receiver channel tracking L1 C/A in scenario 1.

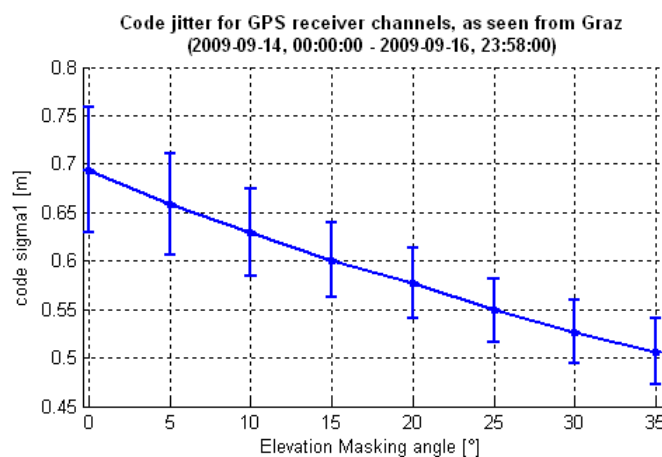


Figure 7-24: Jitter of the code delay estimate for a typical GPS receiver channel tracking L1 C/A in scenario 3.

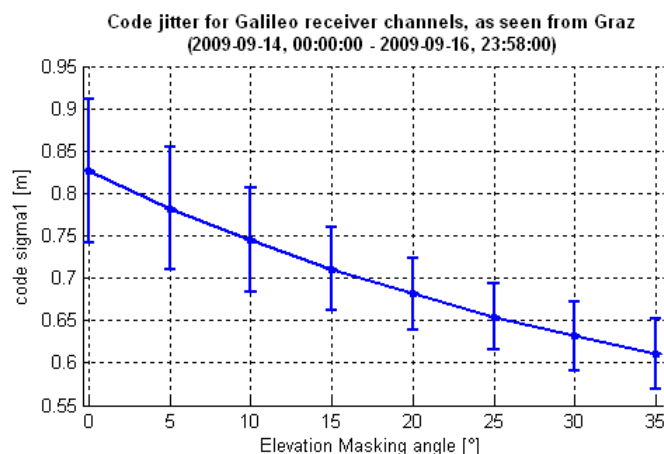


Figure 7-25: Jitter of the code delay estimate for a typical Galileo receiver channel tracking E1B in scenario 4.

From the previous figures, depicting the code jitter for GPS and Galileo tracking channels in scenarios 1, 3 and 4, it is observed that the precision of the code delay estimate in Scenario 1 for 10° masking angle (0.6 m) is approximately obtained for a 20° elevation cut-off angle in Scenarios 3 and 4 (0.57 and 0.68 m respectively) when the described receiver architectures are in use.

7.3.8 Lessons Learned From Phase 1

From these results and the plots depicted during this development phase, it is evident that a dichotomy appears when determining the dilution of precision and the receiver code delay tracking jitter as a function of the elevation masking angle at the antenna. From the user position, in statistical terms, the interference power level (and hence the code delay tracking jitter) rises for decreasing values of the design parameter while the geometry of visible satellites improves. This statement describes a one-dimensional optimization problem for which a closed numerical solution has been searched in the first part of this chapter.

The methodology adopted during this development phase proposes independent scenario comparisons for GDOP and code delay tracking jitter at the receiver for a user in Graz, Austria. From this method, and under the described simulation settings and constraints, it is observed that a receiver antenna with an elevation masking angle smaller or equal to 20° in a GPS+Galileo scenario provides a mean GDOP which is lower or equal to the observations for a receiver antenna of 10° under a GPS constellation. In other words, a cut-off angle higher than 20° in a combined GPS+Galileo constellation shows degraded satellite geometry relative to 10° under a GPS-only constellation.

Concerning the precision of the code delay tracking, simulation results yield values of 0.57 and 0.68 m respectively for GPS and Galileo channels in a receiver under the combined constellation and with an antenna of cut-off angle equal to 20°. Note that these values present minimal sub-meter divergence relative to 0.6 m, which is the expected code delay tracking jitter for the reference case (10° under a GPS constellation).

Table 7-3 includes a summary of statistical results obtained within this first phase of the study, for the reference case, and a compatible receiver under a GPS+Galileo constellation, with elevation masking angles of 20° and 35°. This table includes results taken from previous figures for the three

scenarios, on visibility, GDOP, mean total interfering power, $(C/N_o)_{\text{eff}}$ and code delay tracking jitter when GPS and Galileo satellites are targeted.

| | | GPS(10°) | GPS+Galileo(20°) | GPS+Galileo(35°) |
|---|----------------|--------------|------------------|------------------|
| Mean visibility [1] ⁽ⁱ⁾ | | 8/10/12 | 11/14/17 | 6/9/11 |
| Mean GDOP [1] ⁽ⁱⁱ⁾ | | 1.95/2.1/2.9 | 1.96/2.16/3 | 2.3/4.12/6.92 |
| Mean I_{total} [dBW/Hz] ⁽ⁱⁱⁱ⁾ | GPS | -202.4/0.8 | -201.4/0.82 | -203.1/1.2 |
| | Galileo | | -198.6/0.9 | -200.1/0.92 |
| Mean $(C/N_o)_{\text{eff}}$ [dBHz] ⁽ⁱⁱⁱ⁾ | GPS | 45.75/1.35 | 46.10/1.15 | 47.25/1.0 |
| | Galileo | | 48.24/1.1 | 49.17/1.15 |
| Mean code jitter [m] ⁽ⁱⁱⁱ⁾ | GPS | 0.6/0.09 | 0.57/0.08 | 0.51/0.07 |
| | Galileo | | 0.68/0.09 | 0.61/0.08 |

Note: the format of the data included in this table is as follows:

- ⁽ⁱ⁾ min/mean/max
- ⁽ⁱⁱ⁾ min/mean/percentile95
- ⁽ⁱⁱⁱ⁾ mean/std

Table 7-3: Summary of numeric results obtained in Phase 1.

These numeric results show that in a future GPS+Galileo an elevation masking angle of 20° can be used with satellite geometry and receiver tracking precision comparable to the figure observed for GPS only with 10°. Additionally, they prove that the convergence of the problem is possible at least for a user within the city of Graz, a condition that is considered promising enough to proceed with a worldwide analysis to assess the validity of these conclusions for receivers all over the Globe.

From the experience gathered, several minor adjustments to the simulation settings will be made in Phase 2 to obtain more realistic results.

- The GPS constellation will be simulated with 24 active space vehicles instead of 37. This measure is expected to have an impact on both interfering power level and satellite geometry.
- The spectral separation between signals, considered in a first approach constant in scenarios 1 to 4, will be extended to account for its dependency with the relative Doppler frequency shift due to the movement of signal sources relative to the receiver.

Regarding the figures of merit used during Phase 1, they are designed to give an indication of the similarity between two scenarios defined for a single user. In Phase 2, in order to simultaneously account for time and geographic scenario fitting, these figures of merit will be conveniently adapted to worldwide scenarios.

7.4 Part 2: Assessment of the Worldwide Applicability of the Proposed Measure

The methodology developed in 7.3 has been used to evaluate the validity of an increase in the user antenna cut-off angle for a single user located in Graz (Austria) within a GPS+Galileo scenario, in order to enhance the robustness of the GNSS receiver to ground-based interfering signals and multipath.

A similar strategy is now applied to assess the general applicability of the measure outlined above from a worldwide point of view. In order to make the scenarios in use more realistic, a number of refinements listed in 7.3.8 have been introduced here.

7.4.1 Modifications on the Original Procedure

As previously mentioned, the procedure described in 7.3.2 is considered here a baseline. In this second phase, the Galileo constellation is simulated as in phase 1 (27 active satellites, equally spaced 40° in 3 orbital planes, with nominal inclination 56° , and nominal semi-major axis equal to 29,601 Km), while the GPS constellation is modelled as 24 active satellites irregularly spaced within 6 orbital planes with nominal orbital inclination 55° and semi-major axis equal to 26,560 Km. Note that in this case, the number of GPS space vehicles has been reduced to a nominal value.

Also in this phase, the spectral separation between signals is mathematically derived as a function of the Doppler frequency shift due to the relative movement between space vehicles, through a more computationally efficient method outlined in 5.2.6. The results of these computations are stored in look-up tables, which are used to interpolate the instantaneous evolution of the SSC's in all cases from the simulated velocity difference between given pairs of tracked and interfering satellites.

Besides these modifications, the estimation of the dilution of precision and the receiver channel code delay tracking jitter is consistent with the baseline procedure. Concerning the figures of merit, in order to simultaneously ensure both the statistical and geographical adjustment of every defined GPS+Galileo scenario relative to the reference case, equations 7-1 to 7-4 introduce a number of non-linear figures of merit computed from time statistics over K grid points, that present a zero-crossing for those values of the antenna cut-off angle θ separately fulfilling each equivalence criteria (respectively on visibility –symbolized as V –, PDOP and the tracking precision due to noise and interfering power levels). Equation 7-4, obtained from the combination of F_{PDOP}^θ and F_σ^θ , is intended to be used to draw a compromise GPS+Galileo scenario equivalent to the reference case in terms of PDOP and σ_{int} due to noise and interference.

$$F_{Vis}^\theta = \sum_{k=1}^K \left[\overline{V_{GPS+Gal}^\theta(k)} - \overline{V_{GPS}^{10^\circ}(k)} \right] \quad 7-1$$

$$F_{PDOP}^\theta = \sum_{k=1}^K \left[\overline{PDOP_{GPS+Gal}^\theta(k)} - \overline{PDOP_{GPS}^{10^\circ}(k)} \right] \quad 7-2$$

$$F_{\sigma}^{\theta} = \sum_{k=1}^K \left[\overline{\sigma_{GPS+GAL}^{\theta}}(k) - \overline{\sigma_{GPS}^{10^{\circ}}}(k) \right] \quad 7-3$$

$$F_{Comb}^{\theta} = F_{\sigma}^{\theta} \cdot F_{PDOP}^{\theta} \quad 7-4$$

These figures of merit are in the following independently studied for the scenarios under consideration as a function of the antenna cut-off angle (θ).

7.4.2 Definition of Worldwide Scenarios

Following the numbering started in 7.3.3, this section covers and defines the scenarios used for the worldwide assessment. I_{ref} and I_{int} are defined as in section 5.2.7.

1. **Scenario 5:** In this worldwide scenario, the target receiver channel is assumed to track the signal component L1 C/A from a given GPS PRN, considering a GPS constellation only. I_{ref} is then constituted by all transmissions on L1 P, L1 M and L1 C, and from all GPS satellites other than the tracked PRN on L1 C/A. In this case, the bandwidth of the receiver frontend is fixed to 2.5 MHz.
2. **Scenario 6:** In this case, a receiver with an RF frontend bandwidth of 24.5 MHz⁴⁷ is assumed to track the L1 C/A signal component transmitted by a particular GPS PRN, under a combined GPS+Galileo constellation. Here, I_{ref} is constituted by all transmissions on L1 P, L1 M and L1 C, and from all GPS satellites other than the tracked PRN on L1 C/A. I_{int} is obtained from all Galileo satellites transmitting E1A and E1BC signal components.
3. **Scenario 7:** Similarly, a channel in the same receiver of Scenario 6 is supposed to track the E1B signal component from a single Galileo PRN, under a combined GPS+Galileo constellation. I_{int} is constituted by all transmissions on GPS L1 C/A, L1 P, L1 M and L1 C and I_{ref} is obtained from all Galileo satellites transmitting E1A and from all Galileo SV transmitting on E1BC signals, other than the tracked PRN.

Table 7-4 summarizes the configurations listed above, and allow for a higher degree of detail regarding time and space extent of the simulations, transmitted power levels, satellite and user antenna patterns, and others. Once again in this case, red values in this table are only used when the corresponding signal is considered interference.

Besides, Annex B of this document develops on the link budget computation applied to these scenarios, and serves to assess that the selected values of transmitted powers and satellite antenna gains in Table 7-4 are compliant with the minimum received power levels specified in the most up-to-date GPS and Galileo ICDs.

⁴⁷ This RF frontend bandwidth has been selected for Scenarios 6 and 7 as a compromise, being 24.5 MHz (see Table 2-11) suitable for the simultaneous tracking of GPS L1 C/A and Galileo E1BC signals. The Doppler evolutions of all required SSCs within these scenarios are to be computed using this value.

| General | |
|---|--|
| Type of analysis | Worldwide |
| Longitude range | 180°W to 180°E, in steps of 5° |
| Latitude range | 90°S to 90°N, in steps of 5° |
| User height | 0 m (sea level) |
| Simulated duration | 48 hours |
| Time resolution | 120 seconds |
| Atmospheric attenuation | 0.5 dB, constant with elevation |
| GPS constellation (Active for scenarios 5, 6 & 7) | |
| Constellation modelling | As previously defined in 7.3.2, with the amendments in 7.4.1. |
| Transmitted signals | GPS L1 C/A, GPS L1 P(Y), GPS L1 M, GPS L1 C _D , GPS L1 C _P |
| Transmitted power | 12.8 (16.8) dBW @ GPS L1 C/A, 14.3 dBW @ GPS L1 P(Y), 19.5 dBW @ GPS L1 M, 12.6 dBW @ GPS L1 C _D , 12.6 dBW @ GPS L1 C _P |
| Satellite antenna gain | Interpolated from a realistic antenna pattern for Block II F satellites. Maximum gain: 14.9 dBi |
| Galileo constellation (Active for scenarios 6 & 7) | |
| Constellation modelling | As previously defined in 7.3.2. |
| Transmitted signals | Galileo E1A, Galileo E1B, Galileo E1C |
| Transmitted power | 17.3 dBW @ Galileo E1A, 14.6 (15.5) dBW @ Galileo E1B, 14.6 dBW @ Galileo E1C |
| Satellite antenna gain | Interpolated from realistic antenna pattern, foreseen for Galileo satellites. Maximum gain: 16.2 dBi |
| Receiver | |
| N_o | -201.5 dBW/Hz (in all cases) |
| RF frontend bandwidth | 2.5 MHz (Scenario 5) and 24.5 MHz (Scenarios 6 & 7) |
| Tracked signal | GPS L1 C/A (scenarios 5 & 6), Galileo E1B (scenarios 7) |
| Antenna | Hemispherical RHCP antenna. Mask angles: 0°, 10°, 20°, 30° Maximum gain: 4.5 dBi |

Table 7-4: Relevant configurations for the worldwide simulation scenarios for Phase 2.

7.4.3 Estimation of the Spectral Separation between Signals

For every signal combination, the Doppler dependent spectral separation coefficients are determined following the steps listed below.

7.4.3.1 Selected Power Spectral Densities

After the scenario definition, the necessary PSDs are selected and generated, taking into account not only the modulation type but also the spreading code and data rate for the specific signal. These PSDs are an input to the spectral separation determination, following the approach documented in 5.2.6. Note that, as specific PRN codes for GPS L1 P, GPS L1 M and Galileo E1A are not defined and documented in public ICDs (given the confidential nature of this information), the SSCs involving these signal components are computed from the envelope power spectral densities exposed in

Annex A rather than from the fine structured PSDs. For this reason, fine structured and envelope PSDs are presented in the following for the sake of completeness.

In Figure 7-26, the fine structured PSDs of the disclosed signal components used within this section are depicted, all of them generated according to [Ref. 44]. From left to right and from top to bottom, the following list summarizes the descriptions for all PSDs:

- a) **GPS L1 C/A, PRN 1:** modulated as a BPSK(1), with a ranging code 1,023 chips long, a code rate of 1.023 Mcps and a data rate of 50 sps. Produced for compliance with [Ref. 3], for the spreading code corresponding to PRN 1.
- b) **GPS L1 C/A, PRN 2:** similar to the previous PSD, produced for compliance with [Ref. 3] for the spreading code corresponding to PRN 2.
- c) **GPS L1 C_D, PRN 1:** BOCsin(1,1) modulated, with a primary code of 10,230 chips, a code rate of 1.023 Mcps and a data rate of 100 sps. Generated according to specifications in [Ref. 4] for the spreading code of PRN 1.
- d) **GPS L1 C_p, PRN 1:** BOCsin(1,1) modulated, with a primary code of 10,230 chips, a code rate off 1.023 Mcps and no data modulation (pilot channel). Generated according to specifications in [Ref. 4] for the spreading code PRN 1.
- e) **Galileo E1B, PRN 1:** CBOCsin(6,1,1/11) modulated, with primary and secondary codes of 4,092 chips and 1 chip respectively, a code rate of 1.023 Mcps and a data rate of 250 sps. Generated according to specifications in [Ref. 6] for the spreading code PRN 1.
- f) **Galileo E1B, PRN 2:** similar to the previous PSD, generated according to specifications in [Ref. 6] for the spreading code PRN 2.
- g) **Galileo E1C, PRN 1:** CBOCsin(6,1,1/11) modulated, with a primary and secondary codes of 4,092 and 25 chips respectively, a code rate of 1.023 Mcps and no data modulation (pilot channel). Generated according to specifications in [Ref. 6] for the spreading code PRN 1.

Additionally, Figure 7-27 shows the envelope PSDs for all signals in the analysis, described as follows from left to right and top to bottom, and with their generation compliant with Annex A:

- a) **GPS L1 C/A, envelope:** modulated as a BPSK(1).
- b) **GPS L1 P, envelope:** modulated as a BPSK(10).
- c) **GPS L1 M, envelope:** modulated as a BOCsin(10,5).
- d) **GPS L1 C_D, envelope:** BOCsin(1,1) modulated.
- e) **GPS L1 C_p, envelope:** BOCsin(1,1) modulated.
- f) **Galileo E1A, envelope:** modulated as BOCcos(15,2.5).
- g) **Galileo E1B, envelope:** CBOCsin(6,1,1/11) modulated.
- h) **Galileo E1C, envelope:** CBOCsin(6,1,1/11) modulated.

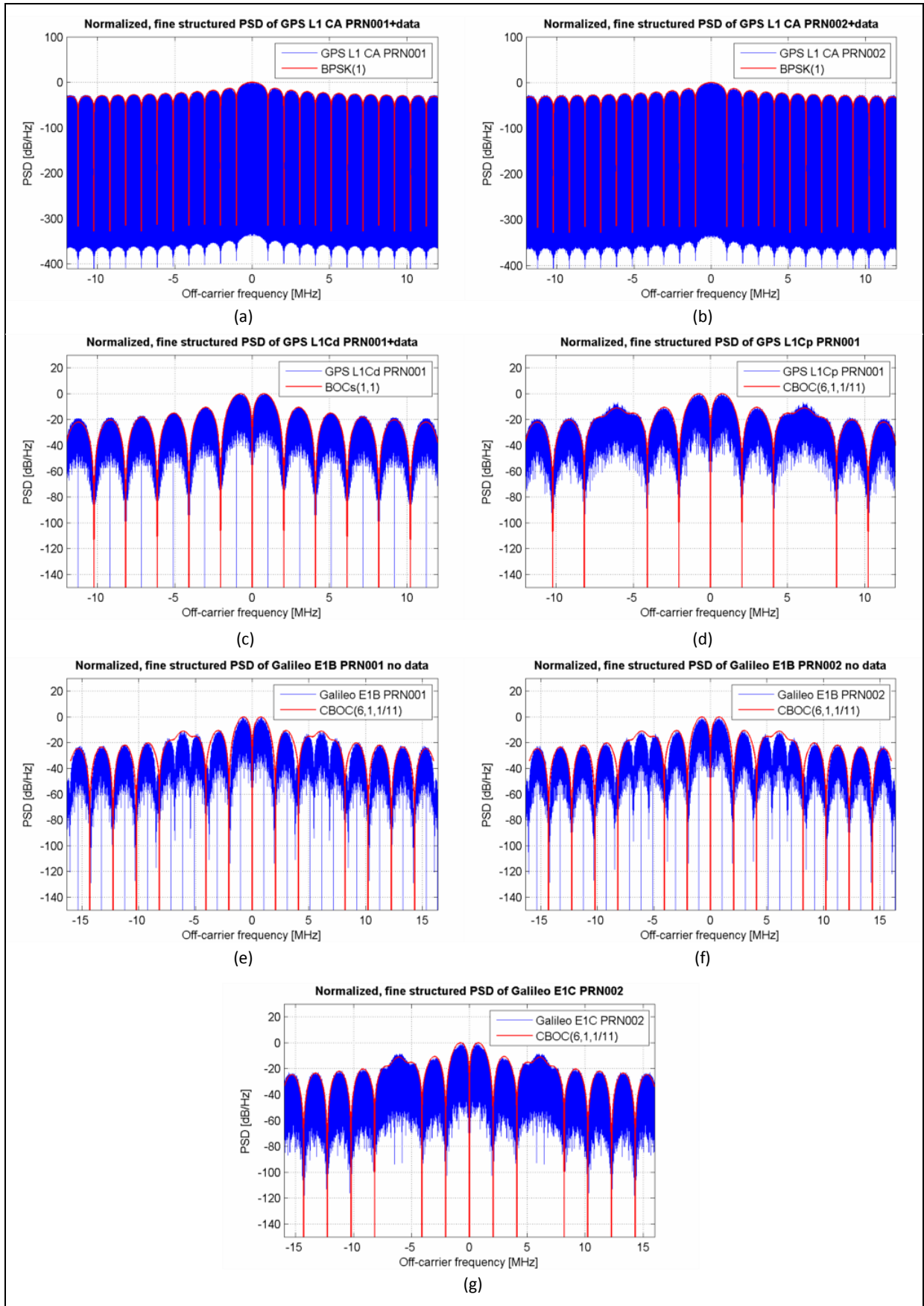


Figure 7-26: Fine structured PSDs used within simulations in this section.

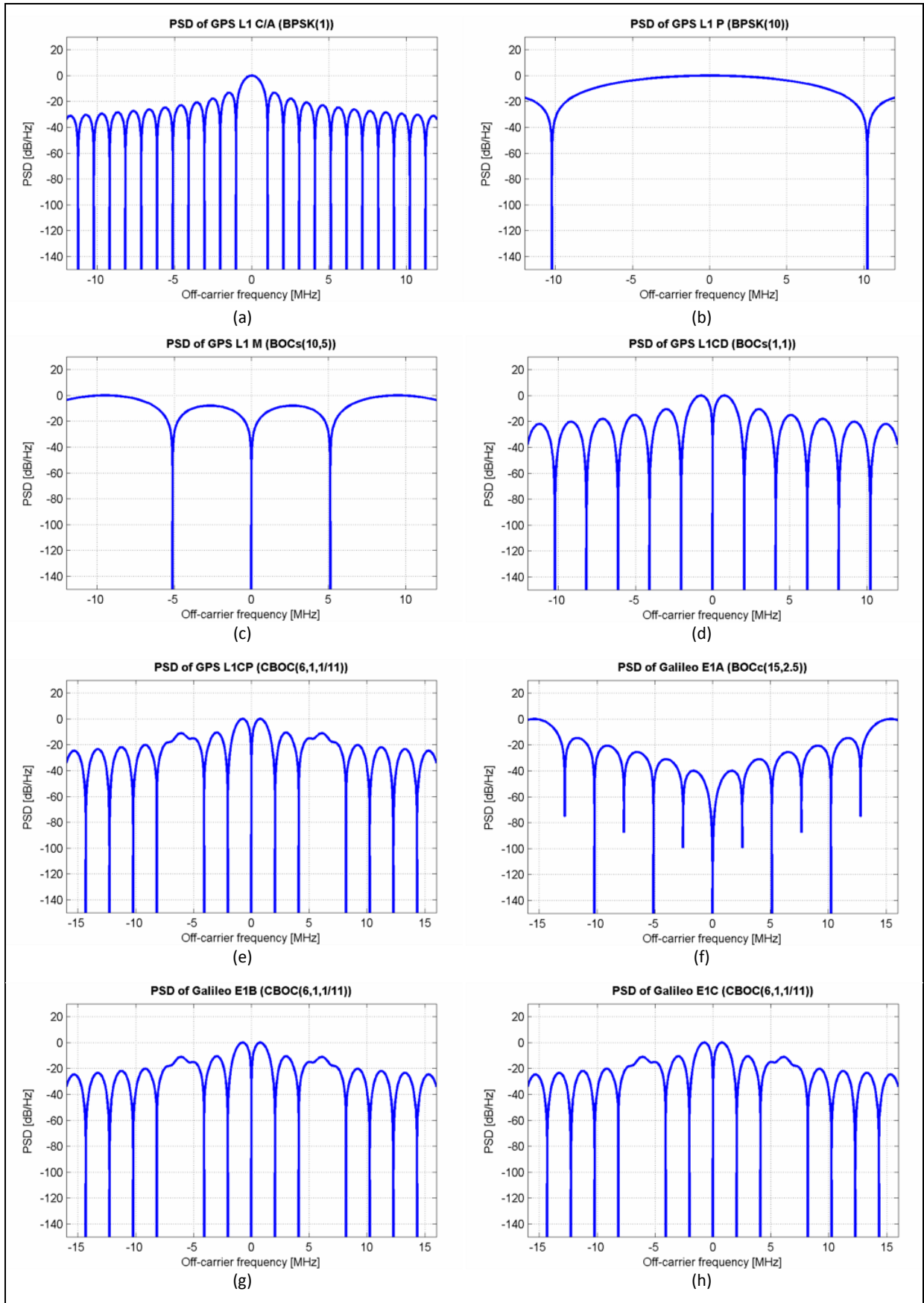


Figure 7-27: Envelope PSDs used within simulations in this section.

7.4.3.2 Range of Values for the Doppler Offset in GPS and Galileo

As a preliminary step for a consistent and reasoned computation of the spectral separation between signals within all scenarios (by default, a function of the Doppler frequency offsets differences between signal sources), it is appropriate to estimate the statistical distribution of the Doppler offset differences for the constellations defined in Table 7-4, over all simulated time and a worldwide extent. For this purpose, however, the simulated scenario in Table 7-4 has been run over 24 hours, with a grid resolution of 10° , being this configuration suitable for this matter.

Results of this preliminary analysis are depicted in the figures below (and summarized in Table 7-5 in page 141), which show cumulative distribution functions (CDF) for the Doppler differences for every combination of signals sources in the scenario, this is, GPS to GPS, Galileo to Galileo, GPS to Galileo, and Galileo to GPS. Additionally, Table 7-5 serves to summarize the range of Doppler difference values to be considered during the estimation of SSCs in 7.4.3.3.

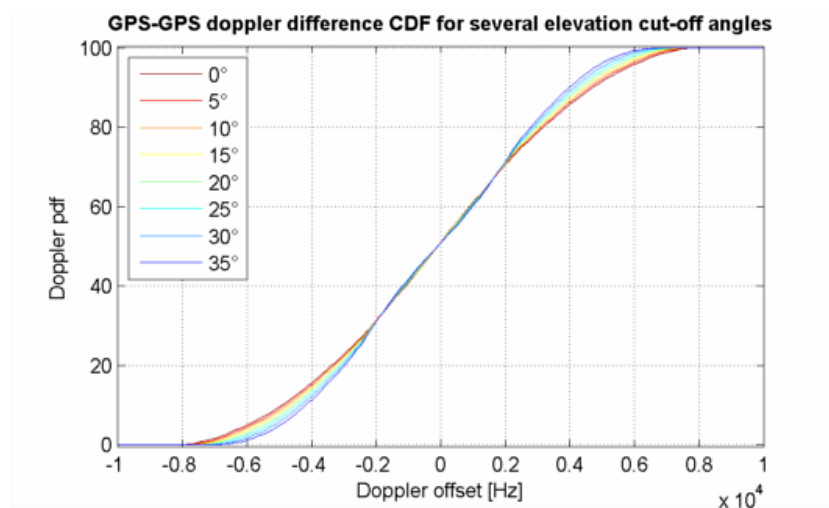


Figure 7-28: CDF of the Doppler offset difference between satellites of the GPS constellation as specified in Table 7-4.

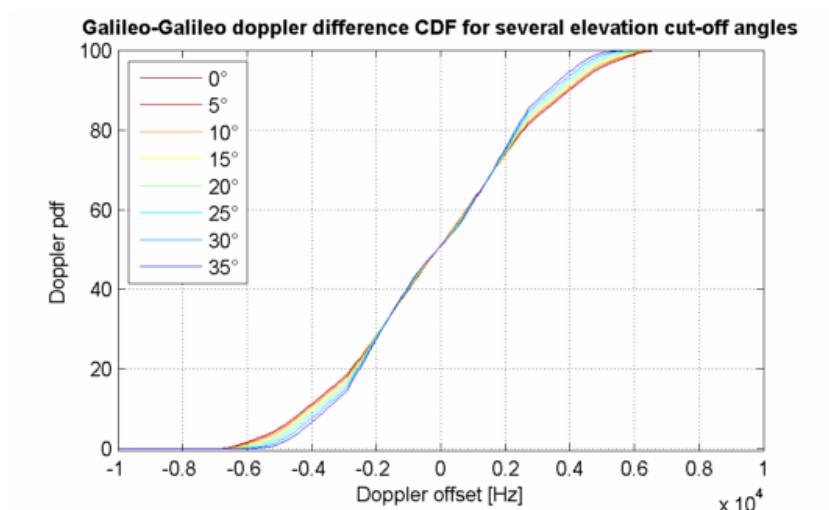


Figure 7-29: CDF of the Doppler offset difference between satellites of the Galileo constellation as specified in Table 7-4.

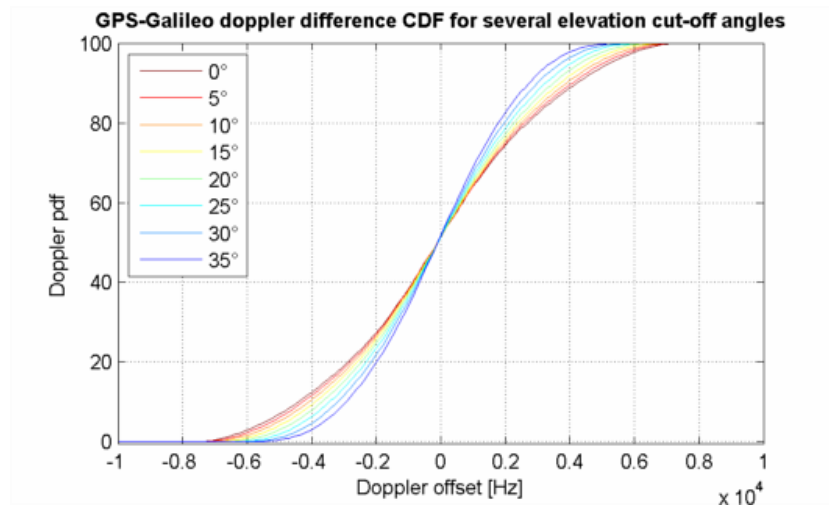


Figure 7-30: CDF of the Doppler offset difference between satellites of GPS and Galileo constellations as specified in Table 7-4.

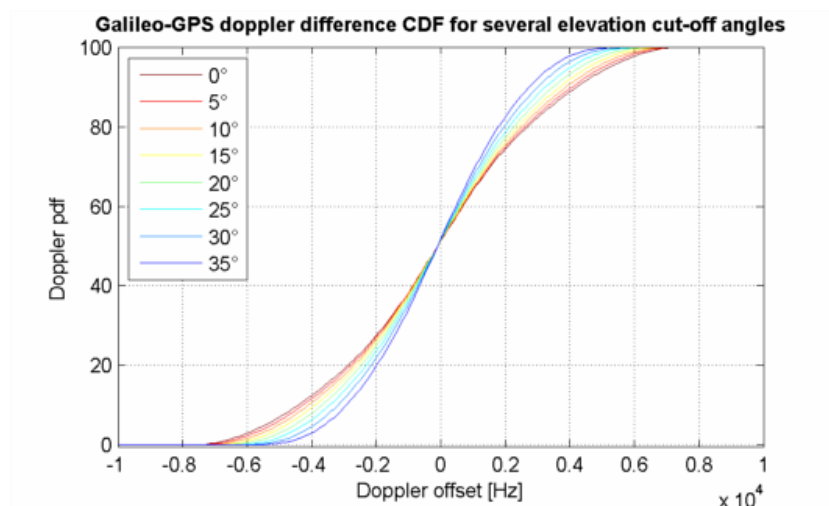


Figure 7-31: CDF of the Doppler offset difference between satellites of Galileo and GPS constellations as specified in Table 7-4.

| | Lower limit of Doppler difference [Hz] | Upper limit of Doppler differences [Hz] |
|-------------------|--|---|
| GPS – GPS | -8,008.59 | 8,008.59 |
| Galileo – Galileo | -6,816.91 | 6,816.91 |
| GPS – Galileo | -7,438.24 | 7,434.42 |
| Galileo – GPS | -7,434.42 | 7,438.24 |

Table 7-5: Doppler difference boundaries obtained from the simulations reported above.

7.4.3.3 Frequency Dependence of the Relevant Spectral Separation Coefficients

From the PSDs defined before, and depending on the availability of fine structured definitions, the SSCs are computed as a function of the Doppler difference through the technique developed in 5.2.6 for scenarios 5 to 7, and results displayed in Figure 7-32 and Figure 7-33.

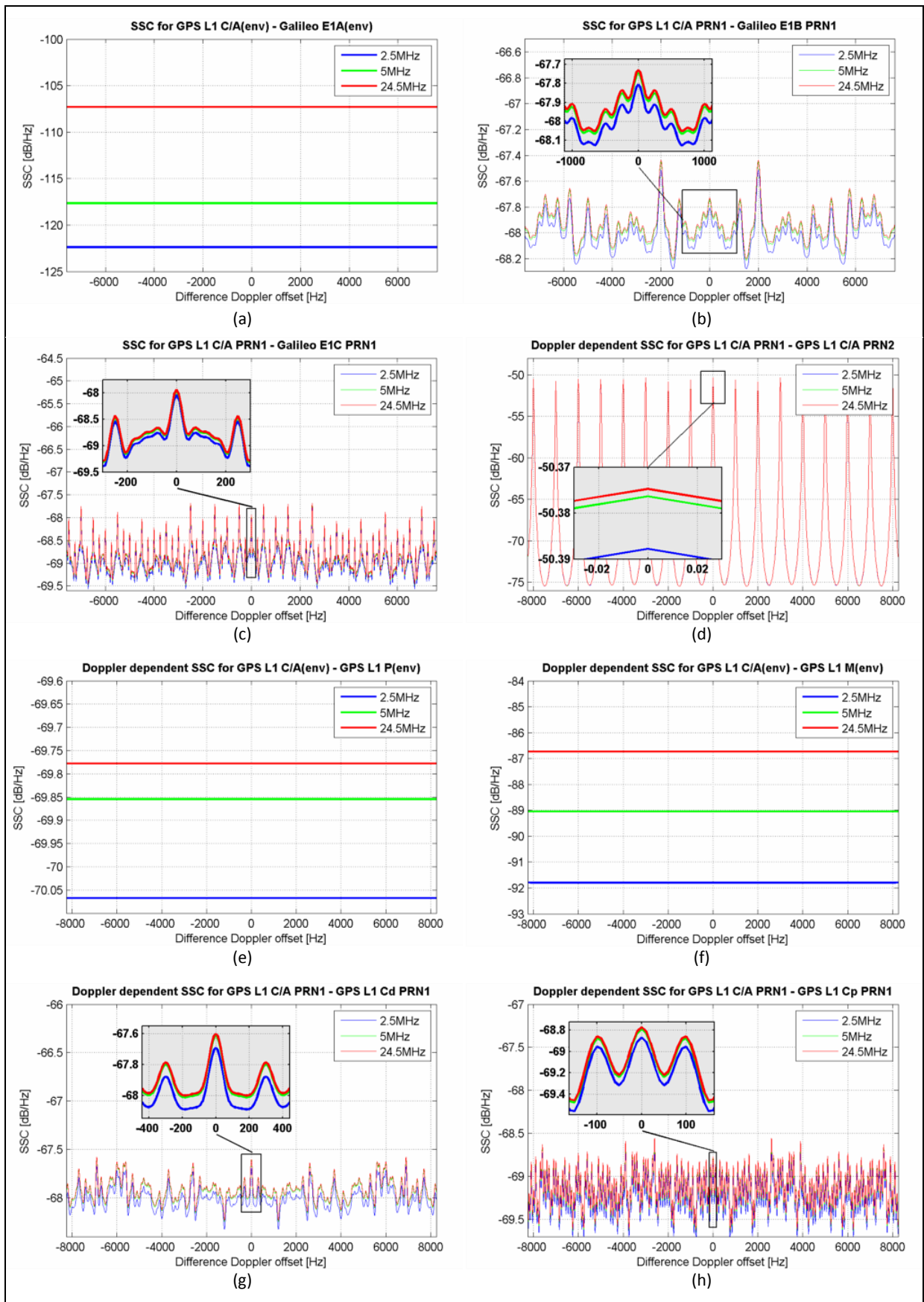


Figure 7-32: SSCs computed for scenarios 5, 6 & 7, with GPS L1 C/A as the desired signal.

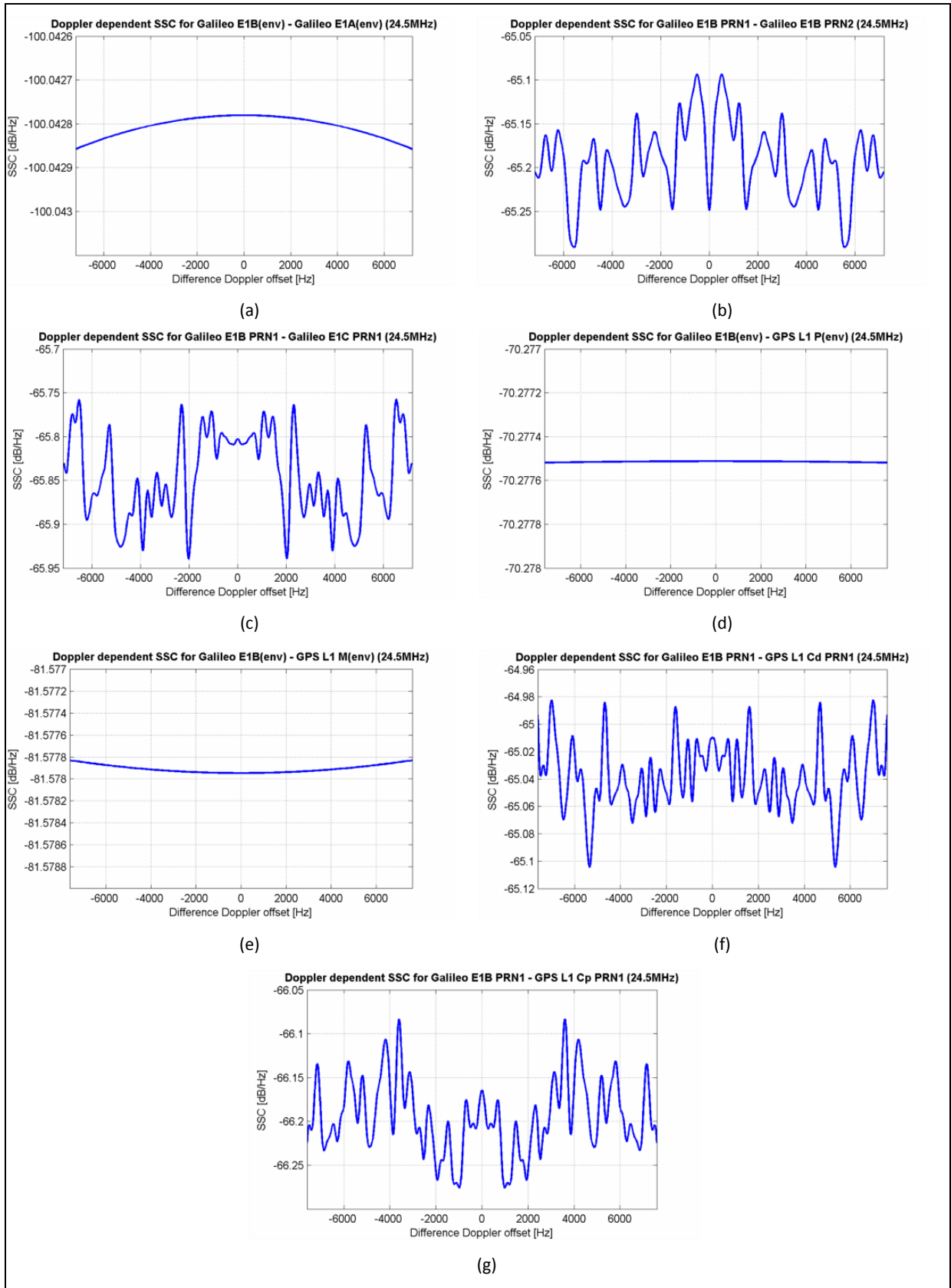


Figure 7-33: SSCs computed for scenario 7, with Galileo E1B as the desired signal.

Given these results, the estimated SSCs used in subsequent simulations of this chapter are summarized in the tables below, where constant values are assumed when the spectra of both signals are represented through the envelope of their PSDs. Doppler dependent quantities are assumed otherwise.

Note that Doppler dependent SSCs are interpolated at runtime in all noted cases for the sake of accuracy, despite the reduced dynamic range of the spectral separation evolutions represented above (in all cases but in Figure 7-32-d).

| <i>2.5 MHz RF frontend bandwidth</i> | | GPS L1 C/A | |
|--------------------------------------|-------------------------------|---------------------------|----------------------|
| | | GPS L1 C/A, PRN 1 | GPS L1 C/A, envelope |
| Galileo E1A | Galileo E1A, envelope | | -122.40 |
| Galileo E1B | Galileo E1B, PRN 1 | Figure 7-32-b, blue trace | |
| Galileo E1C | Galileo E1C, PRN 1 | Figure 7-32-c, blue trace | |
| GPS L1 C/A | GPS L1 C/A, PRN 2 | Figure 7-32-d, blue trace | |
| GPS L1 P(Y) | GPS L1 P, envelope | | -70.07 |
| GPS L1 M | GPS L1 M, envelope | | -91.80 |
| GPS L1 C_D | GPS L1 C _D , PRN 1 | Figure 7-32-e, blue trace | |
| GPS L1 C_P | GPS L1 C _P , PRN 1 | Figure 7-32-f, blue trace | |

Table 7-6: SSC values estimated for scenario 5.

| <i>24.5 MHz RF frontend bandwidth</i> | | GPS L1 C/A | |
|---------------------------------------|-------------------------------|--------------------------|----------------------|
| | | GPS L1 C/A, PRN 1 | GPS L1 C/A, envelope |
| Galileo E1A | Galileo E1A, envelope | | -107.30 |
| Galileo E1B | Galileo E1B, PRN 1 | Figure 7-32-b, red trace | |
| Galileo E1C | Galileo E1C, PRN 1 | Figure 7-32-c, red trace | |
| GPS L1 C/A | GPS L1 C/A, PRN 2 | Figure 7-32-d, red trace | |
| GPS L1 P(Y) | GPS L1 P, envelope | | -69.78 |
| GPS L1 M | GPS L1 M, envelope | | -86.73 |
| GPS L1 C_D | GPS L1 C _D , PRN 1 | Figure 7-32-e, red trace | |
| GPS L1 C_P | GPS L1 C _P , PRN 1 | Figure 7-32-f, red trace | |

Table 7-7: SSC values estimated for scenario 6.

| <i>24.5 MHz RF frontend bandwidth</i> | | Galileo E1B | |
|---------------------------------------|-------------------------------|--------------------------|-----------------------|
| | | Galileo E1B, PRN 1 | Galileo E1B, envelope |
| Galileo E1A | Galileo E1A, envelope | | -100.04 |
| Galileo E1B | Galileo E1B, PRN 2 | Figure 7-33-b | |
| Galileo E1C | Galileo E1C, PRN 1 | Figure 7-33-c | |
| GPS L1 C/A | GPS L1 C/A, PRN 1 | Figure 7-32-b, red trace | |
| GPS L1 P(Y) | GPS L1 P, envelope | | -70.28 |
| GPS L1 M | GPS L1 M, envelope | | -81.58 |
| GPS L1 C_D | GPS L1 C _D , PRN 1 | Figure 7-33-f | |
| GPS L1 C_P | GPS L1 C _P , PRN 1 | Figure 7-33-g | |

Table 7-8: SSC values estimated for scenario 7.

7.4.4 Determination of Visibility for GPS and GPS+Galileo Constellations

The analysis of F_{Vis}^{θ} , corresponding to the scenario fitting in terms of satellite visibility, shows that equivalent minimal visibilities are observed for Scenario 5 (10°), and Scenario 6 (33.5°). In a graphical fashion, this conclusion can be assessed through the plots in Figure 7-35.

Note that this information serves to assess that in all cases at least four satellites in view are available to compose the PVT solution at receiver application level.

7.4.5 Determination of PDOP for GPS and GPS+Galileo Constellations

In a similar way, by analyzing the evolution of the adimensional figure of merit F_{PDOP}^{θ} (depicted in Figure 7-34), it is observed that a sign change occurs for a user antenna cut-off angle of 16.5° . Therefore, it can be inferred that the overall PDOP of a GPS+Galileo scenario with θ lower than 16.5° is smaller than for a GPS-only constellation, with a cut-off angle of 10° .

The visual equivalence in terms of mean PDOP of GPS and GPS+Galileo constellations, with θ respectively equal to 10° and 15° or 20° is depicted in Figure 7-36.

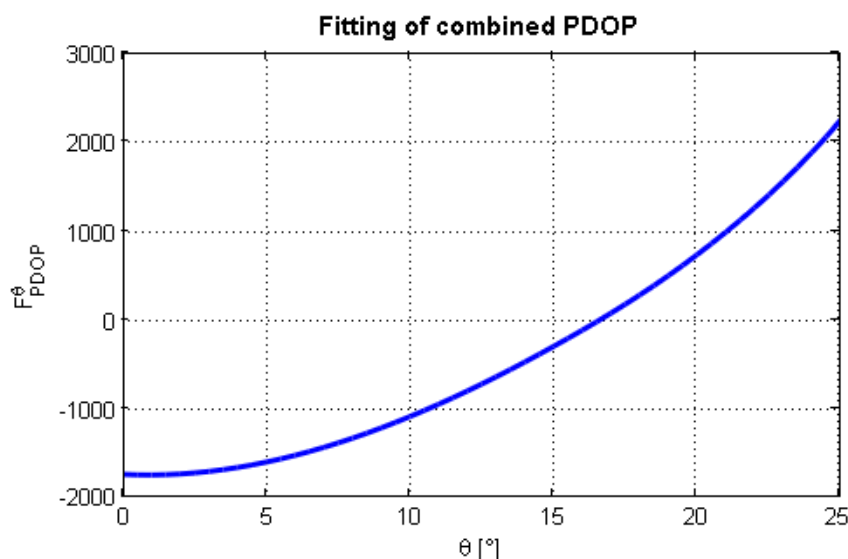


Figure 7-34: Scenario fitting for combined GPS+Galileo PDOP, relative to GPS-only with θ equal to 10° .

7.4.6 Effective C/N_0 Due to GNSS-Induced Interference Level

The following step in the developed methodology consists on the computation of the post-correlation $(C/N_0)_{eff}$. Such operation involves the determination of the receiver power from every satellite, and the discrimination of the interference power spectral densities I_{ref} and I_{int} . Figure 7-37 depicts the geographical distributions for the mean $(C/N_0)_{eff}$ in several scenarios.

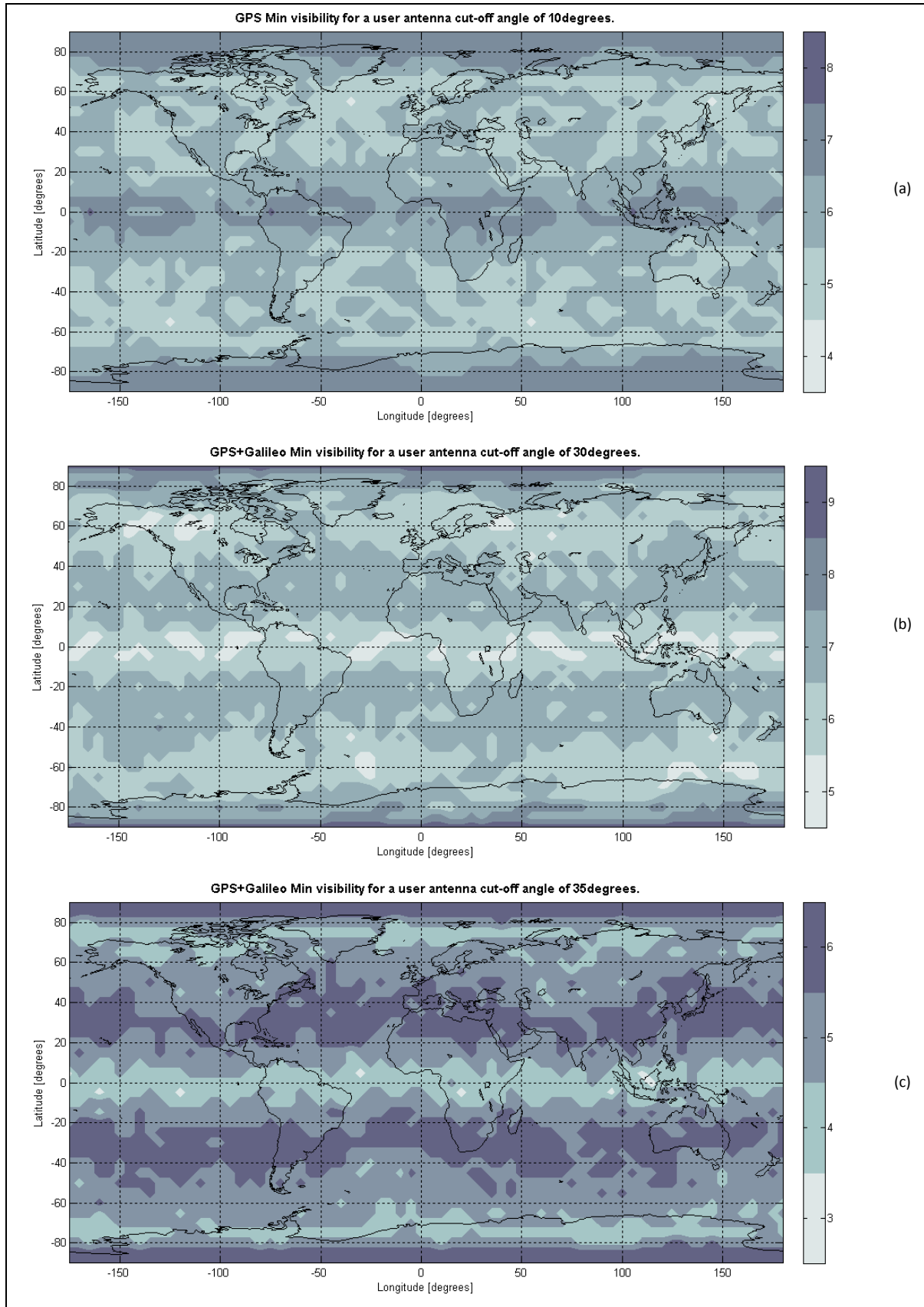


Figure 7-35: Minimal visibility obtained for (a) scenario 5 with 10° elevation masking angle, and scenario 6 with (b) 30° and (c) 35°.

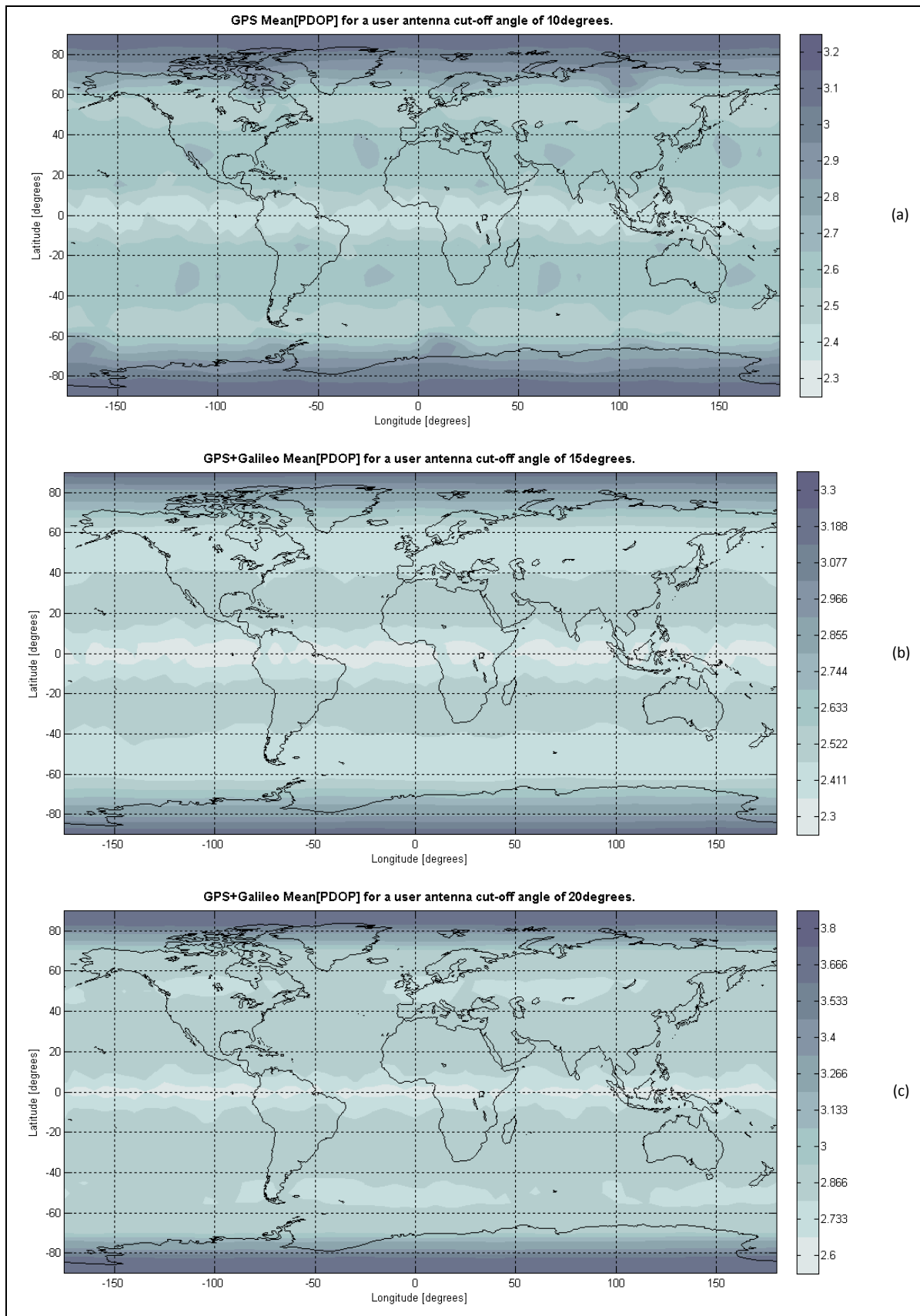


Figure 7-36: Mean PDOP obtained for (a) scenario 5 with 10° elevation masking angle, and scenario 6 with (b) 15° and (c) 20°.

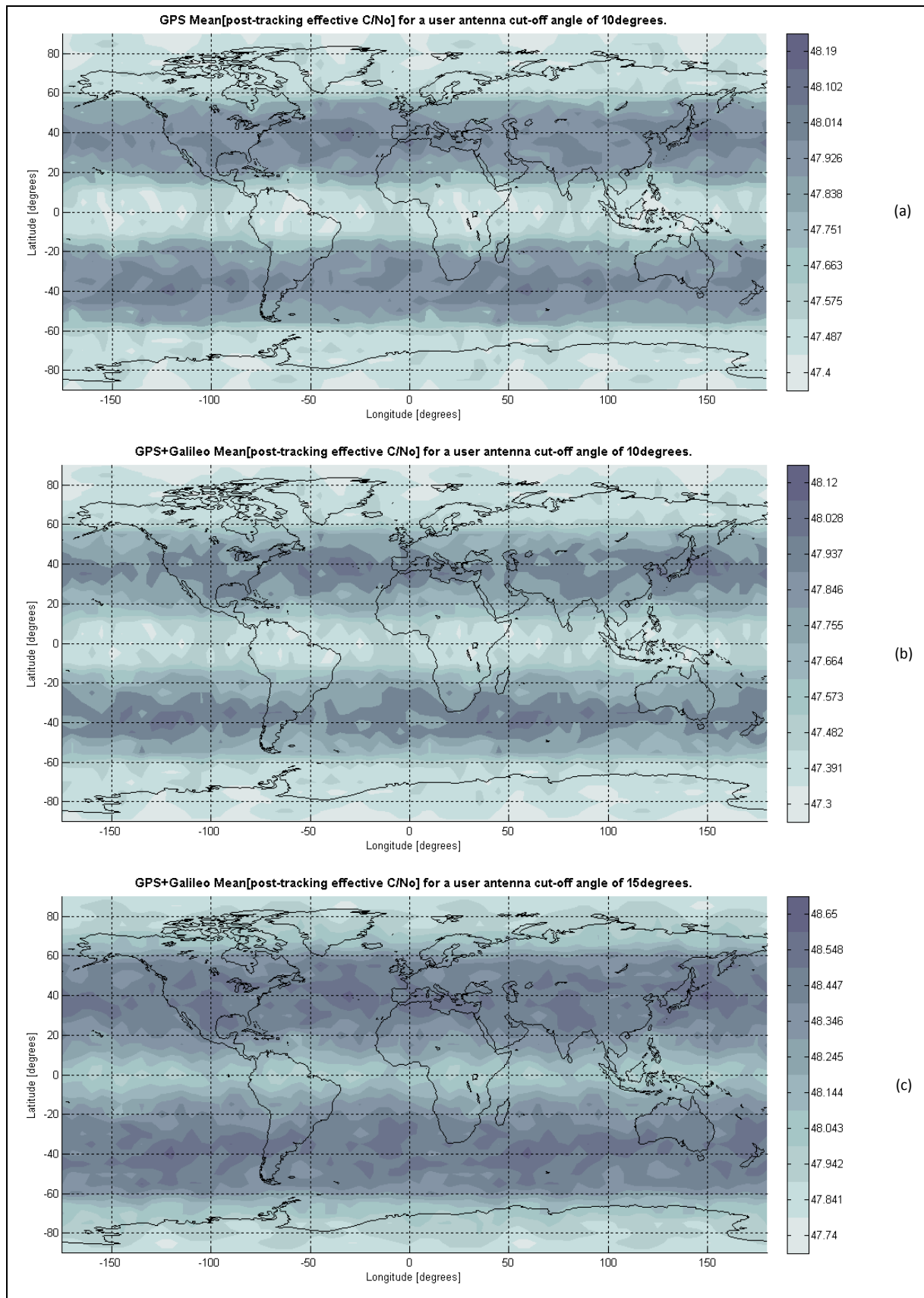


Figure 7-37: Mean $(C/N_0)_{\text{eff}}$ obtained for (a) scenario 5 with 10° elevation masking angle, and (b) scenario 6 with 10° and 15° (c).

7.4.7 Receiver Performance Degradation Due to GNSS-Related Interferences Sources

In this phase, the architecture and parametric configuration of GPS and Galileo baseband receiver channels has been defined as illustrated in Table 7-9, and the Early-Late spacing optimized in every case from the plots in Figure 7-38 and Figure 7-39. These reference figures, produced through the semi bit-true software simulators described in 5.3, provide the variation of the code delay tracking jitter of the proposed architectures when the Early-Late correlator spacing is swept from 0.01 to 0.6 chips.

| | GPS (Scenario 5) | Galileo (Scenarios 6 & 7) |
|---------------------------------|------------------|-----------------------------|
| Tracked Signal | BPSK(1) | CBOCs _{in} (6,1,1) |
| RF frontend bandwidth | 2.5 MHz | 24.5 MHz |
| Code delay discriminator | EMLP | EMLP |
| Early-Late spacing | 0.35 chips | 0.1 chip |
| Code Integration time | 0.02 s | 0.004 s |
| Code loop bandwidth | 5 Hz | 5 Hz |

Table 7-9: Parametric configuration of GPS and Galileo receiver channels for Phase 2.

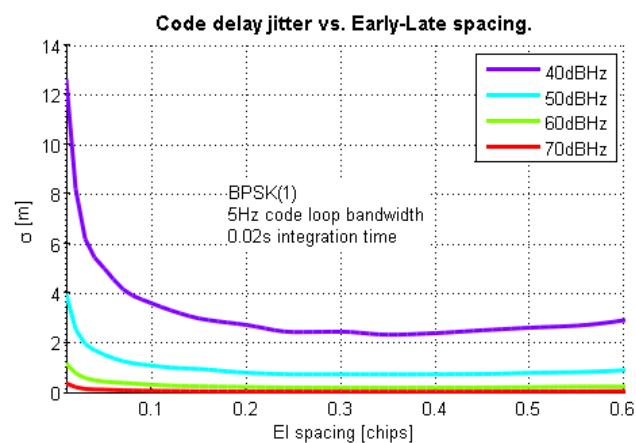


Figure 7-38: Code delay jitter versus the Early-Late spacing on the discriminator for a GPS receiver channel with 2.5 MHz RF frontend bandwidth.

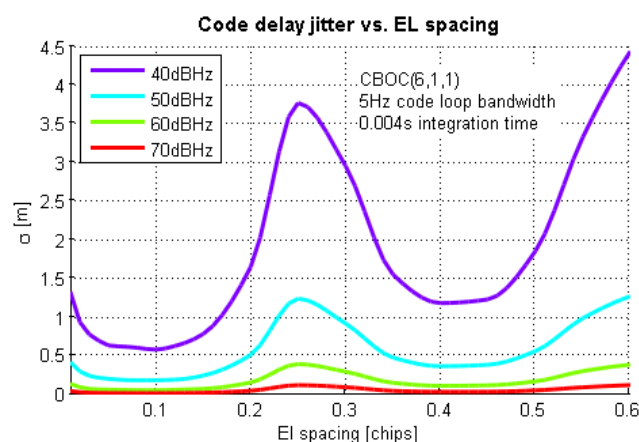


Figure 7-39: Jitter of the estimated code delay versus the Early-Late spacing on the discriminator for a Galileo receiver channel with 24.5 MHz RF frontend bandwidth.

Assuming in all cases that the code delay tracking processes in GPS and Galileo receiver channels are of Gaussian distribution and entirely independent, the variance of the code delay estimation in a GPS+Galileo scenario is obtained as the addition of separated variances for GPS and Galileo.

$$\sigma_{\text{int}_{GPS+GAL}} = \sqrt{\sigma_{\text{int}_{GPS}}^2 + \sigma_{\text{int}_{GAL}}^2} \quad 7-5$$

In other words, for a given θ value, the combined standard deviation of the code delay estimation in a GPS+Galileo receiver can be computed as shown in 7-5 according to the behaviour of the receiver channels configured above, and the time series of $(C/N_o)_{\text{eff}}$ previously obtained in section 7.4.6. The resulting values for $\sigma_{\text{int}_{GPS+GAL}}^{\theta}$ are then feed into F_{σ}^{θ} to obtain the evolution in Figure 7-40, to illustrate that a GPS+Galileo scenario with a user antenna elevation masking angle higher than 13° shows a code delay tracking error lower than a GPS-only scenario with $\theta = 10^{\circ}$.

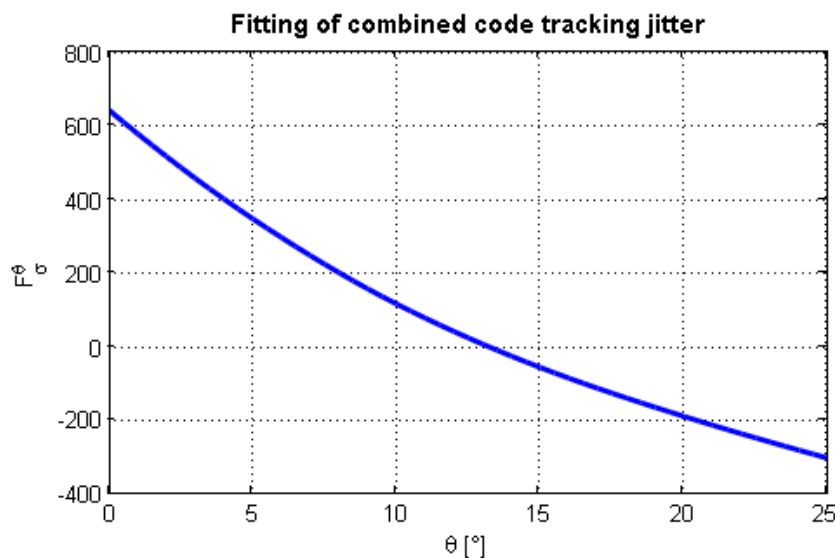


Figure 7-40: Scenario fitting for combined GPS+Galileo tracking code error, relative to GPS-only with θ equal to 10° . Units of vertical axis in meters.

7.4.8 Scenario Equivalence Based on Combined Code Tracking Jitter and PDOP

As a last step towards a conclusion in this study, the shaded area in Figure 7-41 marks a compromise range of θ within which both the PDOP and the code delay tracking error of a GPS+Galileo scenario are lower than the same parameters in a GPS-only situation.

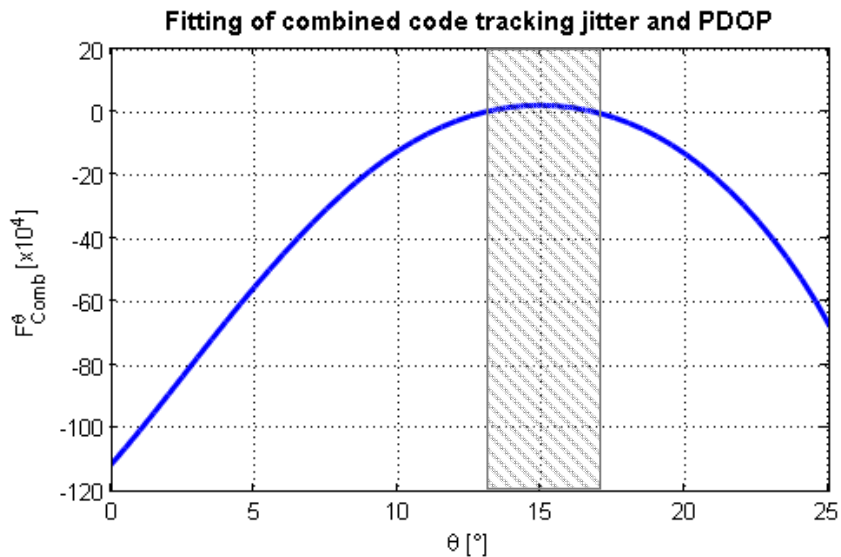


Figure 7-41: Scenario fitting for combined GPS+Galileo tracking code error and PDOP, relative to GPS-only with θ equal to 10° .

With all this information in view, it is stated that the user antenna elevation masking angle could be increased in 6.5° within a GPS+Galileo receiver in order to obtain performances equivalent to a GPS-only scenario with $\theta = 10^\circ$ in terms of PDOP and code delay tracking jitter. Gain values in the same range are observed following the same methodology if a GPS-only constellation with θ equal to 5° and 15° is taken as the reference scenario (see Table 7-10).

| GPS-only, θ [$^\circ$] | GPS+Galileo, θ [$^\circ$] | $\Delta\theta$ [$^\circ$] |
|---------------------------------|------------------------------------|-----------------------------|
| 5 | 11.34 | 6.34 |
| 10 | 16.65 | 6.65 |
| 15 | 23.23 | 8.23 |

Table 7-10: Study results summarized for several values of the reference masking angle in a GPS-only case.

Note, however, that this partial conclusion does not include the elevation dependency⁴⁸ of the residual error left behind during the compensation of the ionospheric/tropospheric delay at the receiver, and that a homogeneous atmospheric attenuation in elevation has been considered all throughout the development. Consequent improvements to account for these factors are left to a future review of this contribution.

7.5 Chapter Summary

As a summary, in the second phase of this study it has been shown through simulation techniques applied to specific worldwide scenarios, that a user receiver antenna with an elevation

⁴⁸ The pseudorange residual error due to the ionosphere/troposphere is exponentially decreasing with the satellite elevation, and presents a submeter magnitude for elevations above 15° [Ref. 7].

cut-off masking angle of 23.3° sees, on an arbitrary position in a GPS+Galileo scenario, equivalent satellite geometry compared to a 15° cut-off masking angle in a GPS-only situation. Additionally, the same receiver shows a code delay tracking jitter equivalent to the value observed in the reference scenario.

Therefore, in a future GPS+Galileo scenario, this simple and economic measure on the antenna design would provide additional robustness against ground-based interfering signals arriving below 23.3° of elevation. A point worth to emphasize here is that, due to the big amount of parameters and the enormous number of possible scenario variations, the conclusions here presented only apply to this very particular case. However, a methodology has been introduced for the determination of an optimal configuration with a worldwide applicability, in contrast with the local study presented in Phase 1. This methodology will be enhanced in a future release to use HDOP and σ_{URE} as equivalence criteria between scenarios, and valid figures of merit developed for these criteria to be applied.

An additional future step considered as a natural extension of this study is a mobile measurement campaign in navigation bands, to obtain realistic figures for dilution of precision and the total interference level for both GPS and Galileo, and the most likely direction of arrival of multipath and ground-based interfering signals in different scenarios. These data would then be used to validate the simulation conditions and results here exposed, and to quantify the gain in performance given by the increased value of the design parameter as a final consolidation of our findings

As a final detail, the author wants to emphasize that, due to the lack of definitive information on Galileo, signals, receiver bandwidth, and transmitted power levels, the values here included have been rationally estimated for analysis purposes only, and should not be considered official.

CHAPTER 8

GENERAL CONCLUSIONS AND FUTURE LINES OF WORK

In all developments within this PhD dissertation, an unambiguous framework has been kept in mind, clearly oriented towards the detailed understanding of the most likely future global situation in terms of satellite-based navigation and positioning. In this respect, it is clear that in a near future a combined multiconstellation system composed of GPS, GLONASS, Galileo, and COMPASS constellations will provide improved visibility and satellite geometry to a compatible user GNSS receiver.

Although the technology is already available, it is important to bear in mind that the difficulty to internationally coordinate the design of such a receiver, together with the derived political and strategic concerns, might eventually reduce the compatibility of such devices to two systems (e.g. GPS+Galileo, GPS+GLONASS or GLONASS+COMPASS), specially for tactical and safety-of-life applications. Even in this case, the improved satellite visibility of the multiconstellation will also raise the intersystem interference level as seen by the receiver, which will cause a further degradation of the receiver performance and eventually of the service given to the user.

In order to improve the navigation experience for the final user of a navigation receiver, seen as the focus of the industrial and commercial developments in the field, this PhD dissertation has analyzed two reasonable, feasible, and low cost measures to improve both the accuracy and the precision of the positioning solution. At this point, and assuming the impossibility to affect the design or performances of nor the space neither the ground segments of the target satellite-based navigation systems, receiver-based measures have been selected.

In a first stage, a theoretical study of error sources on the PVT solution determination has been introduced, with special attention to the effect of interfering signals on the precision of the positioning. In order to characterize potential GNSS-related sources, a study with global extent has been conducted to define the SIS and the orbital modelling of all present and planned GNSS and SBAS. For completeness, an exhaustive list of documented non-GNSS related signals sources in L-, S-, and C-bands has been compiled to produce a realistic picture of the interference environment in which an arbitrary GNSS receiver may be located.

Always through a practical approach supported with software simulations, the author of this thesis has confirmed the feasibility to use, within the multiconstellation scenario, a user receiver antenna with an elevation masking angle higher than 15° while keeping performances already observed in the current GNSS scene. In terms of the combined intersystem interference level and DOP, it has been shown that scenario equivalence is observed for a user receiver with an antenna elevation masking angle of 15° under a GPS-only constellation, and for the dual system receiver with

an antenna cut-off angle of 23.23° under a GPS+Galileo combined constellation. This result can very well be applied as a low cost measure to increase the robustness of non-handheld mass-market receivers to ground-based external interferences and to multipath rays with low elevation of arrival. Even in a slightly more elaborate measure, two antennas of 15° and 23° respective elevation masking angles can be automatically switched into a given GNSS receiver depending on the scenario conditions.

The results and methodologies of this study, particularized/tailored for a user in Graz, Austria, and extended with a worldwide scope, have been published in the proceedings of international radionavigation conferences under the following references:

Fernandez-Prim D., Dilution of precision and interference level on a compatible receiver within a combined GPS+Galileo scenario: A comparative study and conclusions. 13th World Congress of the International Association of Institutes of Navigation (IAIN), October 27-30, 2009, Stockholm, Sweden.

Fernandez-Prim D., Dilution of precision and total interference level on a GPS+Galileo compatible receiver. A global perspective. IEEE/ION Positioning, Location and Navigation Symposium (PLANS) 2010, May 4-6, 2010, Indian Wells, California (USA).

Additionally, and in order to resolve the possible appearance of bias in the satellite-to-user pseudorange estimation from the tracked code delay, an innovative multigate, FFT-based technique has been developed to rise an alarm in case a systematic error is observed and to automatically resolve this condition for receivers compatible with modern subcarrier-based modulations. Concerning the practicality of this measure, it has been noted that the number of required FFT/IFFT modules and the additional correlator count required for its implementation are already present within a classical receiver channel structure, and idle for modes other than satellite acquisition. Furthermore, by sequentially applying this technique to a single channel at a time (i.e. applied to each channel at a rate equal to the bias update rate, which is lower than the loop integration time), the overall power consumption can be sensitively reduced to a level compatible with personal navigation applications. The behaviour of a receiver channel implementing this method has been determined through software simulations, which show virtually no degradation of the code delay tracking performance in terms of jitter, and a maximum bias detection and recovery time of 2 bias update periods when tracking BOCcos(15, 2.5).

The design and performance of this technique have been published in the proceedings of the *IEEE/ION Positioning, Location and Navigation Symposium 2010*, under the following references:

Fernandez-Prim D., A robust bias detection method in the frequency domain for code delay estimation applied to modern navigation modulations. IEEE/ION Positioning, Location and Navigation Symposium (PLANS) 2010, May 4-6, 2010, Indian Wells, California (USA).

In this PhD dissertation the software simulations have not only been used as a tool for all developments but have also been subject of study and improvement. To this respect, a precise and more computationally effective method has been developed to estimate the maximal SSC between navigation signals by exploiting the frequency periodicity of this quantity derived from the presence of spectral lines in the PSD of such signals. In the case where both navigation signals have proportional spreading code durations referred to a common fundamental frequency, it has been

shown that peak values of the SSC between two given signals (i.e. the only points to be computed to estimate the worst-case spectral separation) occur at natural integer multiples of the greatest common divisor of the two signals' inverse spreading code duration.

This SSC computation approach has been accepted and published in the proceedings of the *ION GNSS 2008* conference, under the following references:

*Fernandez-Prim D. et al., **Determination of the spectral separation between signals and its effect on the GNSS receiver performance. A more pragmatic approach.** ION GNSS 2008, September 2008, Savannah, Georgia (USA).*

Finally, a modified semi bit-true scheme based on the interpolation of precomputed cross-correlation functions has been defined to achieve shorter simulation times in the AWGN performance determination of baseband GNSS receiver channels with non-coherent code delay discriminators and multipath reflection delays higher than the chipping period of the tracked signal.

In my opinion, being the author of this PhD dissertation, the logical future evolution of the work in this document will be directed to the enhancement of validation studies for the proposed techniques and methods, the inclusion of more realistically modelled signal sources (as already defined within this document), and the definition of even more realistic simulation scenarios. Furthermore, understanding that modelled signals and receiver structures in software simulations are accurate up to a limited extent, real world measurement and study campaigns would be required to certify that the validity of all these proposals is sufficient to be integrated in real commercial products. Depending on budget, these will be my desired lines of work and interests for the future.

ANNEX A

ENVELOPE PSD OF COMMON MODULATION TYPES IN CURRENT SATELLITE NAVIGATION SYSTEMS

A.1 BPSK

The PSD of BPSK(n), where $f_c = n \cdot f_o$ is the spreading code rate, and f_o is the fundamental frequency of the system, corresponds to equation in A-1 [Ref. 9]. This expression is also valid for non-integer values of n .

$$G_{BPSK(n)}(f) = (f_c) \cdot \left(\frac{\sin\left(\frac{\pi f}{f_c}\right)}{\pi f} \right)^2 \quad \text{A-1}$$

For illustration purposes, here included (Figure A-1) the comparison between PSDs of BPSK(1) and BPSK(10).

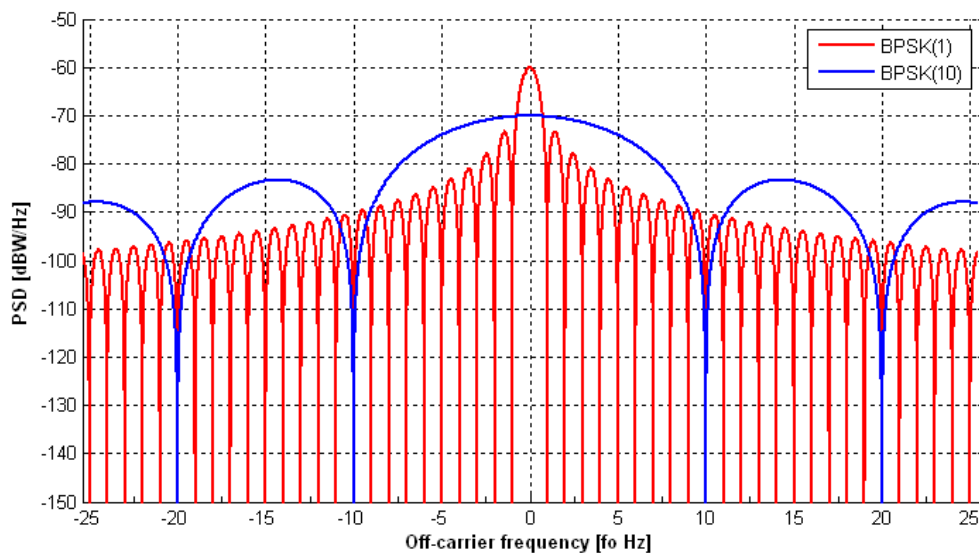


Figure A-1: Compared PSDs of BPSK(1) and BPSK(10), normalized to power 1W over a bandwidth of 52 MHz.

A.2 BOC

A.2.1 BOCsin

The Binary Offset Carrier modulation, with 'sine-like' subcarrier displays the PSD in equation A-2 [Ref. 44]:

$$G_{BOCs(n,m)}(f) = \begin{cases} (f_c) \cdot \left(\frac{\sin\left(\frac{\pi f}{f_s}\right) \cdot \sin\left(\frac{\pi f}{f_c}\right)}{\pi f \cdot \cos\left(\frac{\pi f}{f_s}\right)} \right)^2 & k \text{ even} \\ (f_c) \cdot \left(\frac{\sin\left(\frac{\pi f}{f_s}\right) \cdot \cos\left(\frac{\pi f}{f_c}\right)}{\pi f \cdot \cos\left(\frac{\pi f}{f_s}\right)} \right)^2 & k \text{ odd} \end{cases} \quad \text{A-2}$$

Where $f_c = m \cdot f_o = \frac{1}{T_c} = \frac{1}{k \cdot T_s}$ is the spreading code rate (in Hz), $f_s = n \cdot f_o = \frac{1}{2 \cdot T_s}$ is the subcarrier frequency (also in Hz), and $k = \frac{T_c}{T_s} = \frac{2 \cdot n}{m}$.

Figure A-2 compares the PSDs of BOCsin(1,1) and BOCsin(2,5) signals.

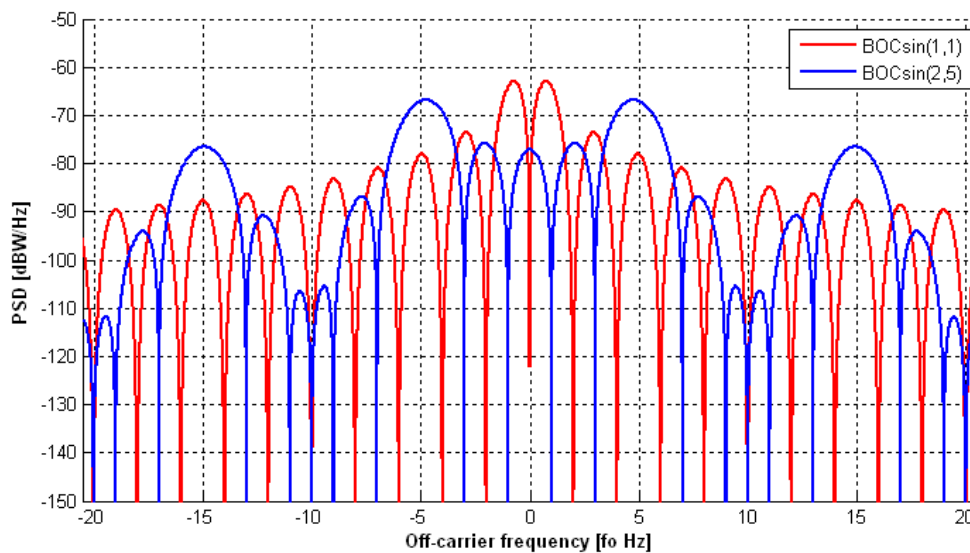


Figure A-2: Compared PSDs of BOCsin(1,1) and BOCsin(2,5), normalized to power 1W over a bandwidth of 42 MHz.

A.2.2 BOCcos

In a similar fashion, the PSD of a Binary Offset Carrier signal with ‘cosine-like’ subcarrier is here obtained and introduced in equation A-3 [Ref. 44]:

$$G_{BOC(n,m)}(f) = \begin{cases} \left(f_c \cdot \frac{\sin\left(\frac{\pi f}{f_c}\right)}{\pi f \cdot \cos\left(\frac{\pi f}{f_s}\right)} \left[\cos\left(\frac{\pi f}{f_s}\right) - 1 \right] \right)^2 & k \text{ even} \\ \left(f_c \cdot \frac{\cos\left(\frac{\pi f}{f_c}\right)}{\pi f \cdot \cos\left(\frac{\pi f}{f_s}\right)} \left[\cos\left(\frac{\pi f}{f_s}\right) - 1 \right] \right)^2 & k \text{ odd} \end{cases} \quad \text{A-3}$$

Again, with $f_c = m \cdot f_o = \frac{1}{T_c} = \frac{1}{k \cdot T_s}$ the spreading code rate (in Hz), $f_s = n \cdot f_o = \frac{1}{2 \cdot T_s}$ the subcarrier frequency (also in Hz), and $k = \frac{T_c}{T_s} = \frac{2 \cdot n}{m}$.

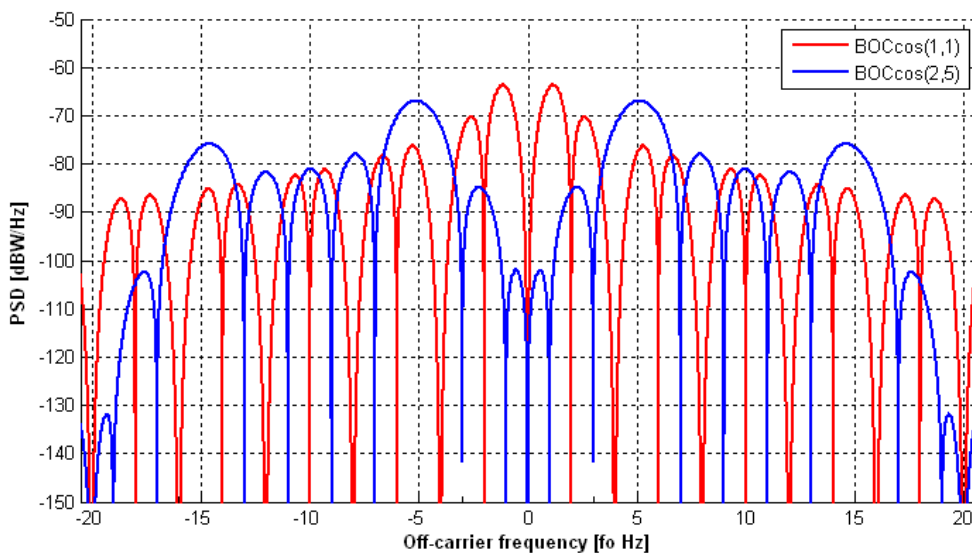


Figure A-3: Compared PSDs of BOCcos(1,1) and BOCcos(2,5), normalized to power 1W over a bandwidth of 42 MHz.

A PSD comparison for BOCcos(1,1) and BOC(2,5) is shown in Figure A-3. Additionally, Figure A-4 puts side by side the PSDs of BOC(1,1) with ‘sine’ and ‘cosine’ subcarriers.

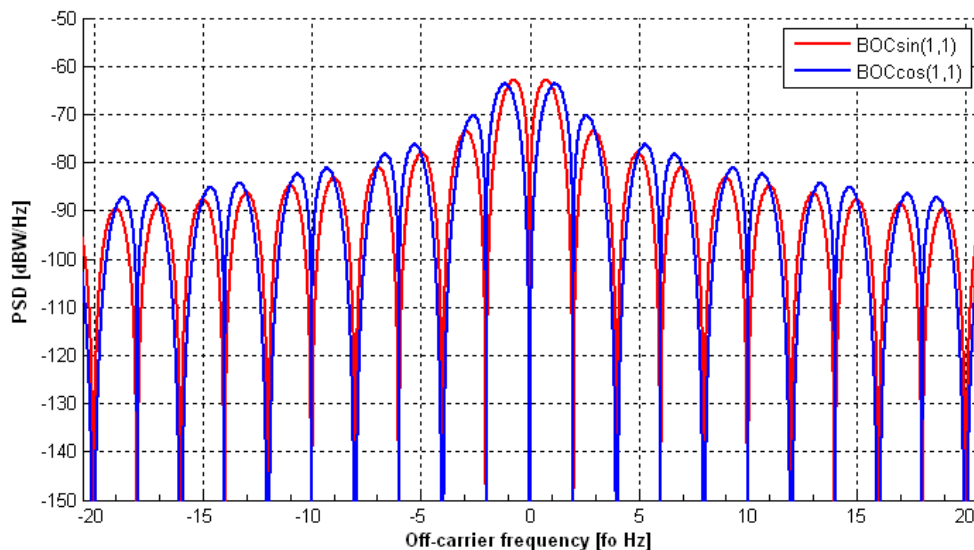


Figure A-4: Compared PSDs of BOCsin(1,1) and BOCcos(1,1), normalized to power 1W over a bandwidth of 42 MHz.

A.3 AltBOC

A.3.1 Constant Envelope

The Alternate Binary Offset Carrier modulation, with constant envelope presents the PSD in equation A-4 [Ref. 44], where $f_c = m \cdot f_o = \frac{1}{T_c} = \frac{1}{k \cdot T_s}$ is the spreading code rate in Hz,

$f_s = n \cdot f_o = \frac{1}{2 \cdot T_s}$ is the subcarrier frequency in Hz, and $k = \frac{T_c}{T_s} = \frac{2 \cdot n}{m}$.

$$G_{AltBOC(n,m)}(f) = \begin{cases} \frac{f_c}{2 \cdot (\pi f)^2} \cdot \frac{\left(\sin\left(\frac{\pi f}{f_c}\right) \right)^2}{\cos\left(\frac{\pi f}{f_s}\right)} \cdot \begin{bmatrix} \cos^2\left(\frac{\pi f}{f_s}\right) - \cos\left(\frac{\pi f}{f_s}\right) - \\ 2 \cdot \cos\left(\frac{\pi f}{f_s}\right) \cdot \cos\left(\frac{\pi f}{2 \cdot f_s}\right) + 2 \end{bmatrix} & k \text{ even} \\ \frac{f_c}{2 \cdot (\pi f)^2} \cdot \frac{\left(\cos\left(\frac{\pi f}{f_c}\right) \right)^2}{\cos\left(\frac{\pi f}{f_s}\right)} \cdot \begin{bmatrix} \cos^2\left(\frac{\pi f}{f_s}\right) - \cos\left(\frac{\pi f}{f_s}\right) - \\ 2 \cdot \cos\left(\frac{\pi f}{f_s}\right) \cdot \cos\left(\frac{\pi f}{2 \cdot f_s}\right) + 2 \end{bmatrix} & k \text{ odd} \end{cases} \quad \text{A-4}$$

Figure A-5 compares the PSDs of AltBOC (15,10) and AltBOC(5,2) signals, with constant envelope.

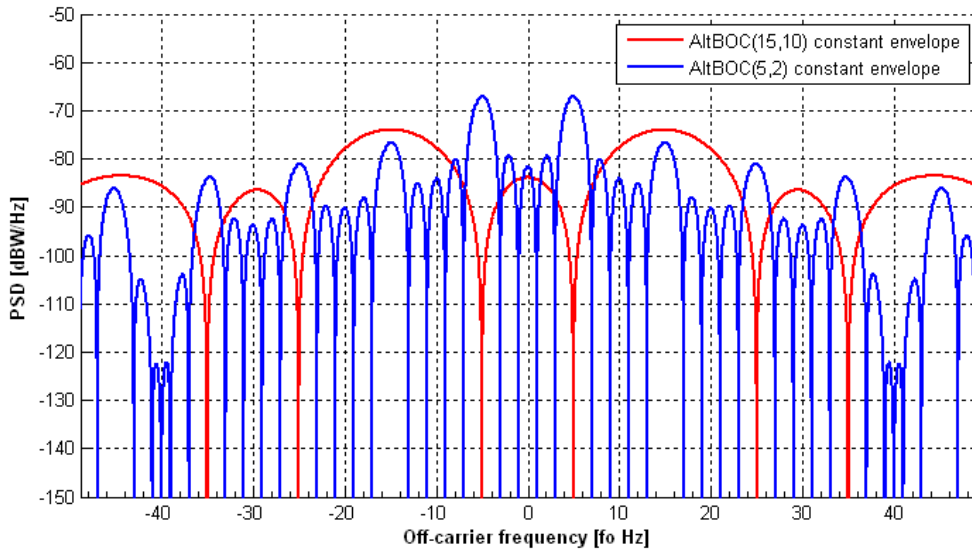


Figure A-5: Compared PSDs of AltBOC(15,10) and AltBOC(5,2) (constant envelope), normalized to power 1W over a bandwidth of 100 MHz.

A.3.2 Non-constant Envelope

In a similar way, the Alternate Binary Offset Carrier modulation, with non-constant envelope presents the PSD in equation A-5 [Ref. 44], where $f_c = m \cdot f_o = \frac{1}{T_c} = \frac{1}{k \cdot T_s}$ is the spreading code rate in Hz, $f_s = n \cdot f_o = \frac{1}{2 \cdot T_s}$ is the subcarrier frequency in Hz, and $k = \frac{T_c}{T_s} = \frac{2 \cdot n}{m}$.

$$G_{AltBOC(n,m)}(f) = \begin{cases} \frac{f_c}{(\pi f)^2} \cdot \frac{\left(\frac{\sin\left(\frac{\pi f}{f_c}\right)}{\cos\left(\frac{\pi f}{f_s}\right)} \right)^2 \left[1 - \cos\left(\frac{\pi f}{f_s}\right) \right]}{\left(\frac{\sin\left(\frac{\pi f}{f_c}\right)}{\cos\left(\frac{\pi f}{f_s}\right)} \right)^2 \left[1 - \cos\left(\frac{\pi f}{f_s}\right) \right]} & k \text{ even} \\ \frac{f_c}{(\pi f)^2} \cdot \frac{\left(\frac{\cos\left(\frac{\pi f}{f_c}\right)}{\cos\left(\frac{\pi f}{f_s}\right)} \right)^2 \left[1 - \cos\left(\frac{\pi f}{f_s}\right) \right]}{\left(\frac{\cos\left(\frac{\pi f}{f_c}\right)}{\cos\left(\frac{\pi f}{f_s}\right)} \right)^2 \left[1 - \cos\left(\frac{\pi f}{f_s}\right) \right]} & k \text{ odd} \end{cases} \quad \text{A-5}$$

Figure A-6 compares the PSDs of AltBOC(15,10) and AltBOC(5,2) signals, with non-constant envelope, and Figure A-7 displays the differences between AltBOC(15,10) with constant and non-constant envelopes.

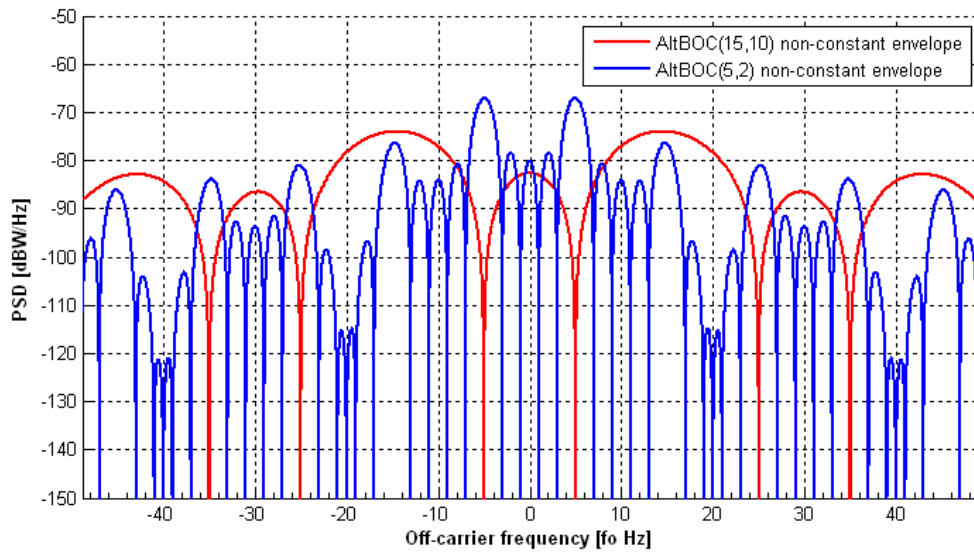


Figure A-6: Compared PSDs of AltBOC(15,10) and AltBOC(5,2) (non-constant envelope), normalized to power 1W over a bandwidth of 100 MHz.

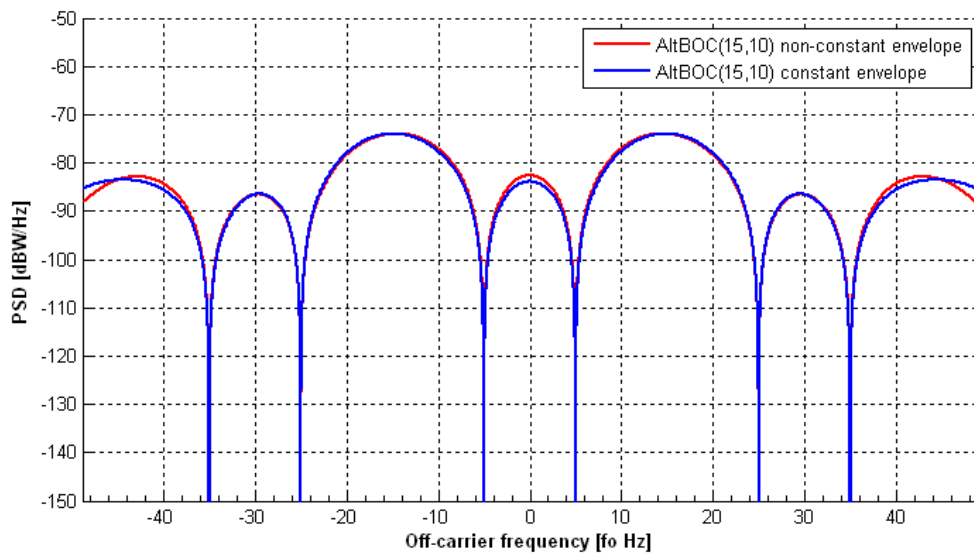


Figure A-7: Compared PSDs of AltBOC(15,10) with constant and non-constant envelope, normalized to power 1W over a bandwidth of 50 MHz.

A.4 MBOC

The PSD of MBOC signals is obtained from the combination of two differently weighted BOC signals with equal subcarrier phasing (equation A-6, [Ref. 44] and [Ref. 45]).

$$G_{MBOCs(n,m,x)}(f) = (1-x) \cdot G_{BOCs(m,m)}(f) + x \cdot G_{BOCs(n,m)}(f) \quad \text{A-6}$$

$$G_{MBOCc(n,m,x)}(f) = (1-x) \cdot G_{BOCc(m,m)}(f) + x \cdot G_{BOCc(n,m)}(f)$$

Note that x in equation A-6 controls the balance of power towards high frequencies, as depicted in Figure A-8 and Figure A-9 for 'sine' and 'cosine' phasing.

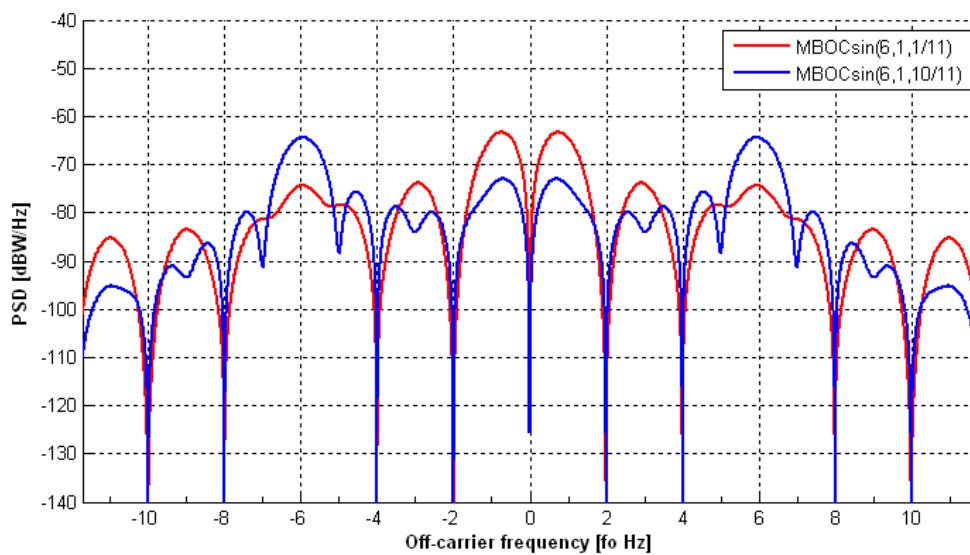


Figure A-8: Compared PSDs of MBOCsin(6,1,1/11) and MBOCsin(6,1,10/11), normalized to power 1W over a bandwidth of 24 MHz.

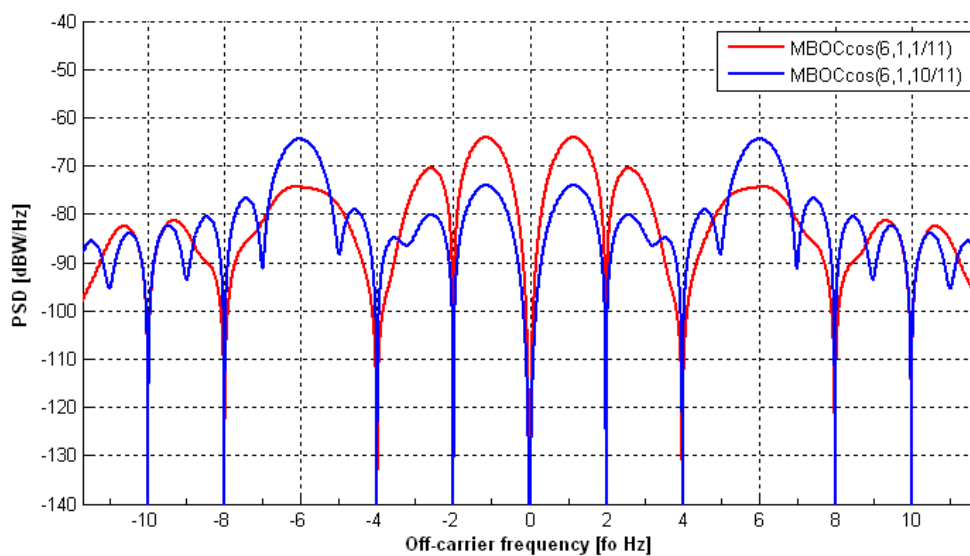


Figure A-9: Compared PSDs of MBOCcos(6,1,1/11) and MBOCcos(6,1,10/11), normalized to power 1W over a bandwidth of 24 MHz.

Figure A-10 depicts the effect of subcarrier phasing on the MBOC power spectral density.

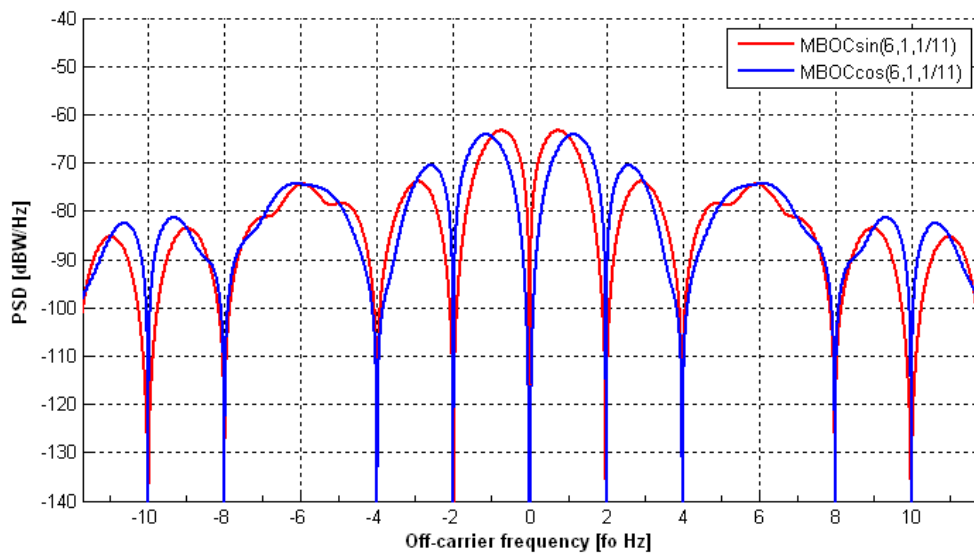


Figure A-10: Compared PSDs of MBOCsin(6,1,1/11) and MBOCcos(6,1,1/11), normalized to power 1W over a bandwidth of 24 MHz.

ANNEX B

REPRESENTATIVE CLEAR SKY LINK BUDGETS FOR GPS AND GALILEO CONSTELLATIONS

B.1 Statistic of the Satellite-to-User Range

From the constellation definitions used in Chapter 7, the following subsections represent the probability density function and boundary values of the simulated satellite-to-user ranges for GPS and Galileo constellations, for a number of user receiver antenna elevation masking angles.

B.1.1 GPS

Figure B-1 depicts the distribution of values for the range to any GPS satellite, obtained through simulation for arbitrary users on locations worldwide, and for antenna cut-off angles from 0° to 35°. A probability peak is observed for a range equal to 21,658,291 m.

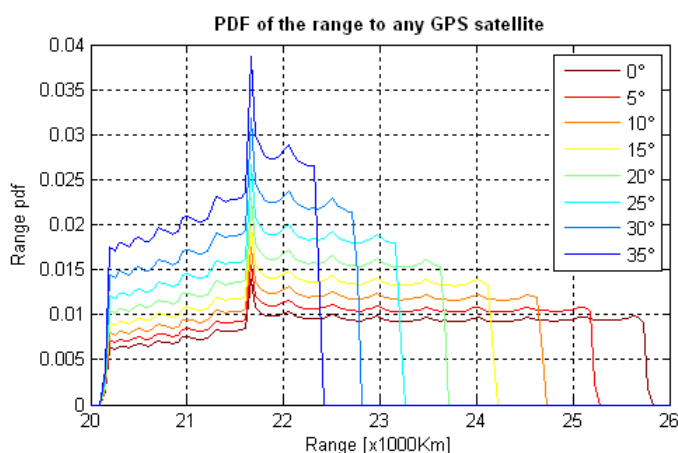


Figure B-1: Probability distribution function of satellite-to-user range for the GPS constellation.

For all considered cut-off angles, Table B-1 summarizes in its first column on the right the maximum distance between an arbitrary user and any GPS satellite, observed through statistics all over the Globe. These worst-case values will be used to obtain the maximum free space loss in following sections.

| Antenna elevation masking angle [°] | Minimum range [m] | Maximum range [m] |
|-------------------------------------|-------------------|-------------------|
| 0 | 20,181,564 | 25,806,642 |
| 5 | | 25,256,934 |
| 10 | | 24,722,778 |
| 15 | | 24,207,904 |
| 20 | | 23,715,878 |
| 25 | | 23,249,446 |
| 30 | | 22,810,866 |
| 35 | | 22,402,280 |

Table B-1: Boundary values for the satellite-to-user range for the GPS constellation.

B.1.2 Galileo

Similarly, Figure B-2 shows the probability distribution function for the distance to any Galileo satellite from any point on the Earth. These values have already been obtained through simulation, for elevation masking angles in the range [0°, 35°]. In this case, the probability peak is observed for a range equal to 24,572,864 m, and the maximum distance between an arbitrary user on the Globe and any Galileo satellite is summarized in the first column on the right of Table B-2. Again, these worst-case values will be applied to compute the maximum free space loss in following sections.

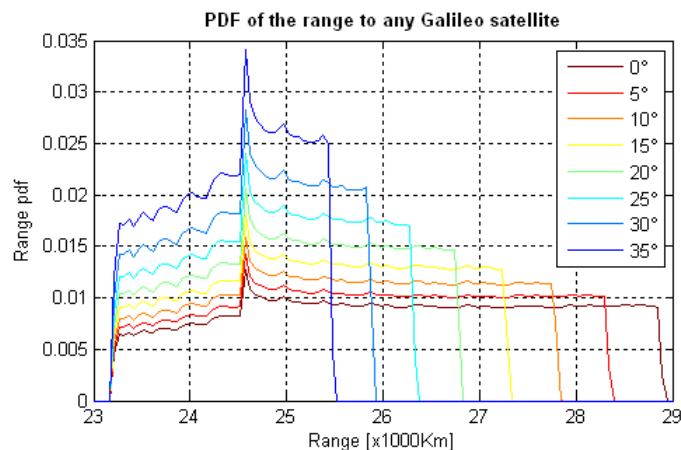


Figure B-2: Probability distribution function of satellite-to-user range for the Galileo constellation.

| Antenna elevation masking angle [°] | Minimum range [m] | Maximum range [m] |
|-------------------------------------|-------------------|-------------------|
| 0 | 23,221,864 | 28,928,410 |
| 5 | | 28,378,144 |
| 10 | | 27,842,492 |
| 15 | | 27,324,910 |
| 20 | | 26,828,818 |
| 25 | | 26,357,156 |
| 30 | | 25,912,484 |
| 35 | | 25,497,336 |

Table B-2: Boundary values for the satellite-to-user range for the Galileo constellation.

B.2 Free Space Loss Determination

GPS and Galileo constellations have been previously characterised in terms of the satellite-to-user range. These values are to be used to compute the Free Space Loss in equation B-1, where c is the speed of light, d is the satellite-to-user range, and f_c is the navigation signal carrier. Note that this expression is compatible with the definition in equation 3-6.

$$L_{fs} = 20 \cdot \log_{10} \left(\frac{4\pi \cdot d \cdot f_c}{c} \right) \quad \text{B-1}$$

The results on L_{fs} will then be used in section B.3 to obtain the minimum received power level from GPS and Galileo satellites from signal components on 1,575.42 MHz.

B.2.1 Computation for GPS Carriers

The figure and tables below contain the values for the Free Space Loss for GPS carriers (L1, L2 and L5), computed for the minimum and maximum satellite-to-user range, and for a set of user antenna cut-off angles.

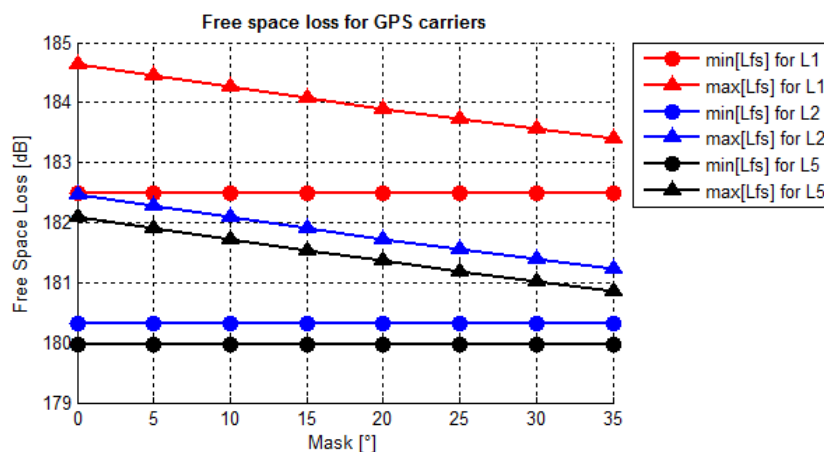


Figure B-3: Evolution of GPS free space loss for several values of the user antenna cut-off angle.

| Antenna elevation masking angle [°] | Minimum L_{fs} [dB] | Maximum L_{fs} [dB] |
|-------------------------------------|-----------------------|-----------------------|
| 0 | 182.496 | 184.631 |
| 5 | | 184.444 |
| 10 | | 184.259 |
| 15 | | 184.076 |
| 20 | | 183.897 |
| 25 | | 183.725 |
| 30 | | 183.559 |
| 35 | | 183.402 |

Table B-3: Free space loss computed for L1 carrier in GPS.

| Antenna elevation masking angle [°] | Minimum L_{fs} [dB] | Maximum L_{fs} [dB] |
|-------------------------------------|-----------------------|-----------------------|
| 0 | 180.33 | 182.46 |
| 5 | | 182.28 |
| 10 | | 182.09 |
| 15 | | 181.91 |
| 20 | | 181.73 |
| 25 | | 181.56 |
| 30 | | 181.39 |
| 35 | | 181.24 |

Table B-4: Free space loss computed for L2 carrier in GPS.

| Antenna elevation masking angle [°] | Minimum L_{fs} [dB] | Maximum L_{fs} [dB] |
|-------------------------------------|-----------------------|-----------------------|
| 0 | 179.96 | 182.09 |
| 5 | | 181.91 |
| 10 | | 181.72 |
| 15 | | 181.54 |
| 20 | | 181.36 |
| 25 | | 181.19 |
| 30 | | 181.02 |
| 35 | | 180.87 |

Table B-5: Free space loss computed for L5 carrier in GPS.

B.2.2 Computation for Galileo Carriers

Similar data is obtained for the Galileo carriers (E1, E5a, E5b and E6), and displayed in the figure and tables below.

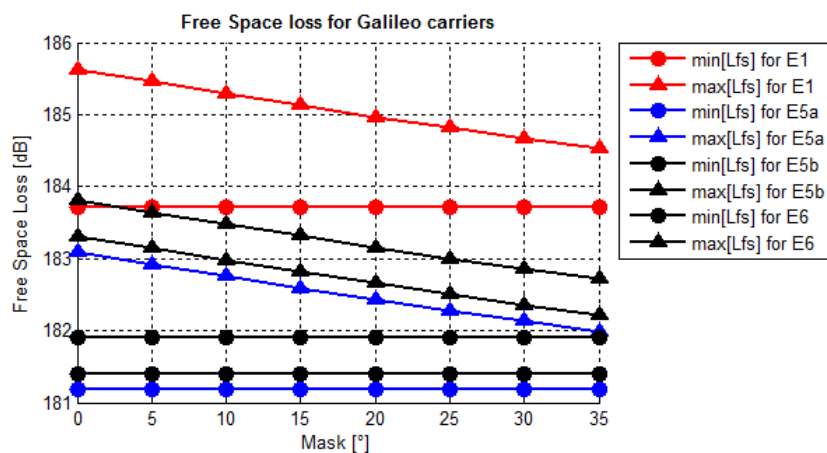


Figure B-4: Evolution of Galileo free space loss for several values of the user antenna cut-off angle.

| Antenna elevation masking angle [°] | Minimum L_{fs} [dB] | Maximum L_{fs} [dB] |
|-------------------------------------|-----------------------|-----------------------|
| 0 | 183.71 | 185.62 |
| 5 | | 185.46 |
| 10 | | 185.29 |
| 15 | | 185.13 |
| 20 | | 184.97 |
| 25 | | 184.81 |
| 30 | | 184.67 |
| 35 | | 184.53 |

Table B-6: Free space loss computed for E1 carrier in Galileo.

| Antenna elevation masking angle [°] | Minimum L_{fs} [dB] | Maximum L_{fs} [dB] |
|-------------------------------------|-----------------------|-----------------------|
| 0 | 181.18 | 183.09 |
| 5 | | 182.92 |
| 10 | | 182.75 |
| 15 | | 182.59 |
| 20 | | 182.43 |
| 25 | | 182.28 |
| 30 | | 182.13 |
| 35 | | 181.99 |

Table B-7: Free space loss computed for E5a carrier in Galileo.

| Antenna elevation masking angle [°] | Minimum L_{fs} [dB] | Maximum L_{fs} [dB] |
|-------------------------------------|-----------------------|-----------------------|
| 0 | 180.18 | 182.32 |
| 5 | | 182.13 |
| 10 | | 181.95 |
| 15 | | 181.76 |
| 20 | | 181.58 |
| 25 | | 181.41 |
| 30 | | 181.25 |
| 35 | | 181.09 |

Table B-8: Free space loss computed for E5b carrier in Galileo.

| Antenna elevation masking angle [°] | Minimum L_{fs} [dB] | Maximum L_{fs} [dB] |
|-------------------------------------|-----------------------|-----------------------|
| 0 | 180.68 | 182.82 |
| 5 | | 182.63 |
| 10 | | 182.45 |
| 15 | | 182.26 |
| 20 | | 182.09 |
| 25 | | 181.91 |
| 30 | | 181.75 |
| 35 | | 181.59 |

Table B-9: Free space loss computed for E6 carrier in Galileo.

B.3 Received powers from GPS and Galileo constellations

Equation B-2 serves to characterize, in terms of the received power level P^{Rx} , the downlink through which GPS and Galileo satellites broadcast the navigation signals. In this equation, P^{Tx} is the transmitted power from the satellite in a particular signal component, G^{Tx} and G^{Rx} are respectively the satellite antenna and the user receiver antenna gains, and L_{fs} is the free space loss as previously defined.

$$P^{Rx} = P^{Tx} + G^{Tx} - L_{fs} + G^{Rx} \quad \text{B-2}$$

The transmitted powers and satellite antenna gains considered for the scenario definitions in Chapter 7 are reproduced in Table B-10 and Table B-11 for convenience, and used to assess that the minimum received power level computed from the link budget in previous developments in this thesis is compliant with the specifications in GPS and Galileo ICDs.

| | L1 C/A | L1 P | L1 M | L1 C _d / L1 C _p |
|-------------------------------------|--------|------|------|---------------------------------------|
| Transmitted Power [dBW] | 12.8 | 14.3 | 19.5 | 12.6 |
| Satellite antenna gain [dBi] | 14.9 | | | |

Table B-10: Transmitted power levels and satellite antenna gain for the GPS signal components in L1.

| | E1A | E1B / E1C |
|-------------------------------------|------|-----------|
| Transmitted Power [dBW] | 17.3 | 14.6 |
| Satellite antenna gain [dBi] | 16.2 | |

Table B-11: Transmitted power levels and satellite antenna gain for the Galileo signal components in E1.

The tables below display, in Clear Sky conditions, minimum received signal strength levels (given in power units) from GPS and Galileo satellites transmitting on 1,575.42 MHz, as seen by an on-ground user receiver with a hemispherical antenna of 0 dBi and ideally matched to the transmitted RHCP polarization.

| Antenna elevation masking angle [°] | L1 C/A [dBW] | L1 P [dBW] | L1 M [dBW] | L1 C _d / L1 C _p [dBW] |
|-------------------------------------|--------------|------------|------------|---|
| 0 | -157.53 | -156.03 | -150.83 | -157.73 |
| 5 | -157.34 | -155.84 | -150.64 | -157.54 |
| 10 | -157.16 | -155.66 | -150.46 | -157.36 |
| 15 | -156.98 | -155.48 | -150.28 | -157.18 |
| 20 | -156.80 | -155.30 | -150.10 | -157.00 |
| 25 | -156.62 | -155.12 | -149.92 | -156.82 |
| 30 | -156.46 | -154.96 | -149.76 | -156.66 |
| 35 | -156.30 | -154.80 | -149.60 | -156.50 |

Table B-12: Minimum received power on GPS L1 for an on-ground user receiver with an RHCP antenna of 0 dBi.

| Antenna elevation masking angle [°] | E1A [dBW] | E1B / E1C [dBW] |
|--|--------------|--------------------|
| 0 | -152.12 | -154.82 |
| 5 | -151.96 | -154.66 |
| 10 | -151.79 | -154.49 |
| 15 | -151.63 | -154.33 |
| 20 | -151.47 | -154.17 |
| 25 | -151.31 | -154.01 |
| 30 | -151.17 | -153.87 |
| 35 | -151.03 | -153.73 |

Table B-13: Minimum received power on Galileo E1 for an on-ground user receiver with an RHCP antenna of 0 dBi.

Note that the obtained values are compatible with the specifications in Table 2-3 and Table 2-12. In all cases, the computed minimum power level is higher than the specifications by a given difference. This safety margin is introduced to compensate for the atmospheric attenuation (not accounted for in this estimation) and the roll-off of the satellite antenna gain (only the peak gain has been used).

These data confirm the validity of the values for transmitted powers and satellite antenna gains selected by the author in the developments of Chapter 7. However, and once more, due to the lack of definitive information on Galileo, signals, receiver bandwidth, and power levels, the values here included have been rationally estimated for analysis purposes only, and should not be considered official.

LIST OF REFERENCES

- [Ref. 1] ARINC Engineering Services, *GPS SPS Performance Standard, 4th Ed.*, (<http://pnt.gov/public/docs/2008/spsps2008.pdf>), September 2008. Accessed on October 8, 2008.
- [Ref. 2] ARINC Engineering Services, *Navstar GPS Space Segment /User Segment L5 Interfaces IS-GPS-705rev.A*, (<http://www.gps.gov/technical/icwg/IS-GPS-705A.pdf>), 2010. Accessed on August 23, 2010.
- [Ref. 3] ARINC Engineering Services, *Navstar GPS Space Segment/Navigation User Interfaces IS-GPS-200rev.E* (<http://www.gps.gov/technical/icwg/IS-GPS-200E.pdf>), 2010. Accessed on August 23, 2010.
- [Ref. 4] ARINC Engineering Services, *Navstar GPS Space Segment/User Segment L1C Interfaces, Draft IS-GPS-800rev.A* (<http://www.gps.gov/technical/icwg/IS-GPS-800A.pdf>), 2010. Accessed on August 23, 2010.
- [Ref. 5] Coordination Scientific Information Centre, *Global Navigation Satellite System GLONASS - Interface Control Document ver. 5.1*, (http://rniikp.ru/en/pages/about/publ/ICD_GLONASS_eng.pdf), Moscow, 2008. Accessed on April 24, 2010.
- [Ref. 6] European Space Agency/European GNSS Supervisory Authority, *Galileo Signal In Space Interface Control Document, OS SIS ICD, Issue 1, Revision 3*, (http://ec.europa.eu/enterprise/policies/satnav/galileo/files/galileo_os_sis_icd_revised_3_en.pdf), 2010. Accessed on August 23, 2010.
- [Ref. 7] Hofmann-Wellenhof B., Lichtenegger H. and Wasle E. *GNSS - Global Navigation Satellite Systems. GPS, GLONASS, Galileo and more – 1st Ed.* SpringerWienNewYork, 2008.
- [Ref. 8] Gibbons, G., *Russia Approves CDMA Signals for GLONASS, Discussing Common Signal Design*, Inside GNSS News, 28 April 2008, (<http://www.insidegnss.com/node/648>). Accessed on May 18, 2008.
- [Ref. 9] Kaplan E.D. and Hegarty C.J., *Understanding GPS - Principles and Applications – 2nd Ed.* Artech House, 2006.
- [Ref. 10] Radio Technical Commission for Maritime Services, *RTCM Recommendation Standards For Differential GNSS Service ver. 2.3*, 2001.
- [Ref. 11] Zinoviev Alexei E., *Using GLONASS in Combined GNSS Receivers: Current Status*. Proceedings of ION GNSS 18th International Technical Meeting of the Satellite Division. - Long Beach, CA, 2005. - pp. 1046-1057.
- [Ref. 12] The White House, Office of the Press Secretary, *Statement by the President regarding the United States' decision to stop degrading the Global Positioning System Accuracy*,

- May 1, 2000. (<http://www.navcen.uscg.gov/?pageName=gpsSelectiveAvailability>). Accessed on August 23, 2010.
- [Ref. 13] The EGNOS Operations Helpdesk, *The EGNOS Geo Footprint*, (<http://194.224.177.81/Webportal/Egnos/Pages/Home.page>). Accessed on October 19, 2008
- [Ref. 14] *Minimum Operational Performance Standards for Global Positioning System/Wide Area Augmentation System Airborne Equipment, DO-229C, RTCA*, November 2001
- [Ref. 15] *International Standards and Recommended Practices, Aeronautical Telecommunications, Annex 10 to the Convention on International Civil Aviation*, vol. I, ICAO.
- [Ref. 16] Kinal, G.V. and Ryan, F., *Satellite-Based Augmentation Systems: The Need for International Standards*, 1999, *The Journal of Navigation*, 52 , pp 70-79
- [Ref. 17] Federal Aviation Administration, *WAAS Fact Sheets*, (http://www.faa.gov/about/office_org/headquarters_offices/ato/service_units/techops/navservices/gnss/library/factsheets/#q2). Accessed on October 26, 2008
- [Ref. 18] European Space Agency, *EGNOS Signal In Space through the internet*, (<http://www.egnos-pro.esa.int/sisnet/index.html>), Accessed on October 26, 2008.
- [Ref. 19] Manabe H., JCAB, *Status of MSAS –MTSAT Satellite-based Augmentation system–*, Presentation at ION GNSS 2008, September 17, 2008, Savannah, Georgia (USA)
- [Ref. 20] Chuang Shi, *COMPASS/Beidou Satellite Navigation System*, Presentation at ICG 2008 (<http://www.unoosa.org/pdf/icg/2008/expert/2-1a.pdf>, accessed on October 28, 2008), July 19, 2008, Montreal, Canada
- [Ref. 21] *Interface Specification for QZSS (IS-QZSS) ver1.2 with revision marks, March 19, 2010*, JAXA, (http://qzss.jaxa.jp/is-qzss/IS-QZSS_12Draft_E.pdf). Accessed on April 27, 2010
- [Ref. 22] Terada K., JAXA, *Quasi-Zenith Satellite System (QZSS). Program Update*, Presentation at ION GNSS 2008, September 17, 2008, Savannah, Georgia (USA)
- [Ref. 23] Official website of Argos System, (http://www.argos-system.org/welcome_en.html). Accessed on April 13, 2009
- [Ref. 24] Official website of COSPAS-SARSAT System, (<http://www.cospas-sarsat.org/>). Accessed on April 13, 2009
- [Ref. 25] Official website of the International DORIS Service, (<http://ids.cls.fr/>). Accessed on April 13, 2009
- [Ref. 26] *Doris, The space surveyor*, (<http://www.aviso.oceanobs.com/en/doris/index.html>), Accessed on April 13, 2009
- [Ref. 27] Kibe S., Indian Space Research Organization, *GAGAN and IRNSS, Presentation by*, Third Meeting of the International Committee on Global Navigation Satellite Systems (ICG-3),

organized jointly by the US State Department and the Jet Propulsion Laboratory, Pasadena, USA, December 8-12, 2008
(<http://www.oosa.unvienna.org/pdf/icg/2008/icg3/07.pdf>). Accessed on May 16, 2009

- [Ref. 28] *COMPASS View on Compatibility and Interoperability*, Presentation by Yuanxi Yang, China National Administration of GNSS and Applications, ICG Workshop on GNSS Interoperability, United Nations Office at Vienna, Vienna, Austria, July 30-31, 2009, (<http://www.oosa.unvienna.org/pdf/icg/2009/workgroupinterop/04.pdf>). Accessed on August 12, 2009
- [Ref. 29] Kolodziejcki K.R., Betz J.W., *Effect of Non-White Gaussian Interference on GPS Code Tracking*, MTR 99B0000021R1, The MITRE Corporation, June 1999.
- [Ref. 30] *A coordination methodology for RNSS inter-system interference estimation*. ITU-R M.1831, International Telecommunication Union, October 2007.
- [Ref. 31] Bastide F., Akos D., Akos C., Roturier B., *Automatic Gain Control (AGC) as an Interference Assessment Tool*, ION GPS/GNSS 2003.
- [Ref. 32] Proakis J. G., *Digital Communications, 4th Ed.*, McGraw-Hill, 2001
- [Ref. 33] Holmes J.K., *Code Tracking Loop Performance Including the Effects of Channel Filtering and Gaussian Interference*, U.S. ION Annual Meeting, June 26-27, 2000, San Diego California (USA)
- [Ref. 34] Holmes J.K., *Non-coherent Late Minus Early Power Code Tracking Performance With Front End Filtering*, ION GPS 97, September 16-19, 1997, Kansas City, Missouri
- [Ref. 35] Betz J.W., *Effect of Narrowband Interference on GPS Code Tracking Accuracy.*, ION NTM 2000, 2000, Anaheim, CA.
- [Ref. 36] Soualle F., Burger Th. B., *Impact of Galileo Spreading Code Selection and Data Rate onto Navigation Signal Interference*, ION GPS/GNSS 2003, September 9-12, 2003, Portland, OR.
- [Ref. 37] Betz J.W., Titus B.M., *Intersystem and Intrasystem Interference with Signal Imperfections*, The MITRE Corporation – Technical Paper, January 2004.
- [Ref. 38] Wallner S. et al., *Interference Computations Between GPS and GALILEO*, ION GNSS 2005, September 13-16, 2005, Long Beach, CA.
- [Ref. 39] Klobuchar, J., *Ionospheric time-delay algorithm for single frequency GPS users*, IEEE Trans. Aerospace and Electronic Systems, 23, 325-332, 1987
- [Ref. 40] *Assessment of Radio Frequency Interference Relevant to the GNSS L5/E5A Frequency Band*, RTCA/DO-292, Radio Technical Commission for Aeronautics, July 2004.
- [Ref. 41] *EFIS: ERO Frequency Information System*, (<http://www.efis.dk/>), Accessed on July 7, 2009.

- [Ref. 42] TADIL J. *Introduction To Tactical Digital Information Link J and Quick Reference Guide*. USA Army, Marine Corps, Navy and Air Force, June 2000.
- [Ref. 43] *Quantification of the potential threat to Galileo from man-made Noise sources (QGN/001/WP3/D3)*. Report prepared by University of Leeds, UK, and Luleå University of Technology, Sweden, 2006
- [Ref. 44] Wasle E., Seybold J., Hofmann-Wellenhof B., *GNSS Signal Generation for Interference Analysis*, International Symposium on Certification of GNSS Systems and Services - CERGAL 2009, Oberpfaffenhofen, March 18 – 19, 2009.
- [Ref. 45] Avila-Rodriguez J.A. et al., *The MBOC Modulation - A Final Touch for the Galileo Frequency and Signal Plan*, InsideGNSS, issue of September / October 2007.
- [Ref. 46] Balanis C.A., *Modern Antenna Handbook*, John Wiley & Sons, 2008.
- [Ref. 47] Holmes J.K., *Spread Spectrum Systems for GNSS and Wireless Communications*, Artech House Boston-London, 2007.
- [Ref. 48] *Instruction Book, Field Maintenance, ARSR-4 System, Type FA-10331*, Technical Instruction TI-6340.23, Baltimore MD: Westinghouse Electric Corporation, December 1999
- [Ref. 49] Revniviykh S., *GLONASS Status and Progress*, Presentation at 4th International Committee on GNSS, September 2009, St. Petersburg (The Russian federation) (<http://www.oosa.unvienna.org/pdf/icg/2009/icg-4/01.pdf>). Accessed on April 2010)
- [Ref. 50] Ashby N. , *Relativity in the Global Positioning System*. Living Reviews in Relativity, (<http://www.livingreviews.org/Articles/Volume6/2003-1ashby/>). Accessed on November 11, 2009
- [Ref. 51] Fine P., Wilson W., *Tracking Algorithm for GPS Offset Carrier Signals*, ION NTM 1999, January 1999, San Diego CA.
- [Ref. 52] Fante R.L., *Unambiguous Tracker for GPS Binary-Offset-Carrier Signals*, The MITRE Corporation – Technical Paper, April 2003.
- [Ref. 53] Hodgart M.S., Blunt P.D., Unwin M., *Double Estimator. A new receiver principle for tracking BOC Signals*, Inside GNSS, Spring 2008.
- [Ref. 54] Skournetou D., Lohan E.S., *Discontinuity-based Code Delay Estimator for GNSS Signals*, IEEE ASMS 2008, September 2008.
- [Ref. 55] De Latour A. et al., *New BPSK, BOC and MBOC Tracking Structures*, ION ITM 2009, January 2009, Anaheim CA.
- [Ref. 56] ITU, *ITU-R Radio Regulations*, Edition 2008, Geneva, Switzerland.
- [Ref. 57] Arthur J. D., *The Emerging Role Of The U.S. Army In Space*, National Defense University Press, 1985.

- [Ref. 58] Betz J.W., Kolodziejski K.R., *Generalized theory of code tracking with an Early-Late Discriminator. Part I: Lower bound and coherent processing*, IEEE Transactions on Aerospace and Electronics Systems, Vol. 45, No. 4, October 2009.
- [Ref. 59] Betz J.W., Kolodziejski K.R., *Generalized theory of code tracking with an Early-Late Discriminator. Part II: Noncoherent processing and numerical results*, IEEE Transactions on Aerospace and Electronics Systems, Vol. 45, No. 4, October 2009.
- [Ref. 60] Avila-Rodriguez J.A. et al., *Revised Combined Galileo/GPS Frequency and Signal Performance Analysis*, Proceedings of ION 2005, September 2005, Long Beach, California, USA.
- [Ref. 61] Walker J. G., *Satellite constellations*, Journal of the British Interplanetary Society, vol. 37, pp. 559-571, 1984.
- [Ref. 62] Ai, Guo-Xiang et al., *A Positioning System based on Communication Satellites and the Chinese Area Positioning System (CAPS)*, Chinese Journal of Astronomy and Astrophysics, vol. 8, no. 6, pp. 611 – 630, 2008.
- [Ref. 63] Lu, Xiaochun et al., *Signal structure of the Chinese Area Positioning System*, Science in China Series G: Physics, Mechanics and Astronomy, Volume 52, Issue 3, pp.412-422, 2009.
- [Ref. 64] Ostermeier J., *Test of DME/TACAN Transponders. Application Note*, Rohde & Schwarz, March 2009.
- [Ref. 65] *Bluetooth Specifications Version 4.0*, December 2009, (<http://www.bluetooth.com>), Accessed on July 4, 2010.
- [Ref. 66] Bensky, A., *Wireless Positioning Technologies and Applications*, Artech House, 2008.
- [Ref. 67] Proakis J. G., Salehi M. *Communication Systems Engineering, 2th Ed.*, Prentice Hall, 2002.
- [Ref. 68] *WiMAX Forum[®] Air Interface Specifications*, September 2010, (http://www.wimaxforum.org/sites/wimaxforum.org/files/technical_document/2010/09/WMF-T23-005-R015v04-RSP.pdf). Accessed on November 11, 2010.

